Measurement of morphological modifications of cell population using lensless imaging.

Srikanth Vinjimore Kesavan

CELL CULTURE MONITORING BY MEANS OF LENSFREE VIDEO MICROSCOPY

SUIVI DE CULTURE CELLULAIRE PAR IMAGERIE SANS LENTILLE

Thesis for the degree of Doctor of Philosophy

Etablissement d'inscription: UNIVERSITE CERGY-PONTOISE
Ecole doctorale: ED SI - Sciences et Ingénierie
Spécialité: Physique – Cergy

Submitted by **Srikanth VINJIMORE KESAVAN**

Prepared in the laboratory of
Laboratoire Imagerie et Systèmes d'Acquisition (LISA), CEA, Grenoble

Jury Members:

Dr. Cédric ALLIER (PhD Supervisor)
Commissariat à l'Energie Atomique et aux Energies Alternatives, France
Dr. Bernard CHALMOND (PhD Director)
Université de Cergy-Pontoise
CMLA, École normale supérieure de Cachan, France
Dr. Jean-Marc DINTEN (Chief of lab 'LISA' and Examinateur)
Commissariat à l'Energie Atomique et aux Energies Alternatives, France
Dr. Antoine DELON (Rapporteur)
Université Joseph Fourier, France
Dr. Manuel THERY (Rapporteur)
Commissariat à l'Energie Atomique et aux Energies Alternatives, France
Dr. Xavier GIDROL (Examinateur)
Commissariat à l'Energie Atomique et aux Energies Alternatives, France
Dr. Pierre ROCHETEAU (Examinateur)
Institut Pasteur, France
Dr. Spencer SHORTE (Examinateur)
Institut Pasteur, France

To my parents, my grandparents, my sister, and my wife.

ACKNOWLEDGEMENTS

From March 1, 2011, the day I started my master's internship, until the end of my PhD, Cédric Allier has been an exceptional supervisor. He has always been there for friendly chats, for discussions, questions, suggestions, critical evaluation, motivation, and encouragement, while providing independence and freedom at the same time. He always stayed positive even during the initial stages when we contaminated the incubator and killed all the cells. He encouraged me irrespective of the outcome of the experiments. His passion for science and open-minded approach to learn new things has certainly had a positive impact on my PhD work. He has been the best mentor I have ever had and I have learnt a lot from him. I cannot express my gratitude enough to Cédric for being as exceptional as he had been for the past 3.5 years and certainly this acknowledgements section would not be enough. If I supervise a PhD student someday, I have a real-life experience of how a PhD supervisor should be.

I thank both Jean-Marc Dinten and Bernard Chalmond for being exceedingly considerate and supportive. They provided critical evaluation of the work, Jean-Marc from an 'imaging' point of view, and Bernard from 'statistics' point of view. They always appreciated the work, which motivated me to go further. The telephonic conferences with Bernard have always given me a fresh perspective on the results.

I looked forward to every day of my PhD. I never once felt stressed or pressured or exhausted, and this was mainly due to the support from Cédric, Jean-Marc, and Bernard.

Fabrice is the courageous researcher who gave me the incubator in his lab to test lensfree imaging system. He was so brave that even after the initial contamination that lensfree imaging caused, he gave us another chance. My first exposure to cell culture and cell biology was through Fabrice. He was very friendly and aside from very interesting discussions about cell biology, he also taught me important French and Spanish phrases that cannot be written here. But, I would definitely remember those phrases and would use them wisely.

Discussions involving lensfree imaging have always been fascinating. For this, and for all the help that they offered during my PhD, I thank the 'Lensfree team' and all those who use lensfree system, including Thomas Bordy, Sophie Morel, Fabien Momey, Olivier Cioni, Lionel Herve, Jean-Guillaume Coutard, Samy Strola. I also thank Rolland Sauze for the software support and Henry Grateau for design and fabrication. My special thanks to Thomas from whom I learnt about fabrication of the system and instrumentation, and also to Fabien for all those image processing and data visualization techniques that he taught me. Fabien played a major role in the article that was published in Nature Scientific Reports, without his support, the article couldn't have gotten its weightage and credibility. My wishes to Anthony Berdeu who joined the team recently.

I thank the entire lab of LISA (current lisa members and alumni), for its warmth and support especially Sophie Morel and Veronica Sorgato who gave me 40 cents for coffee, which gave me the motivation to stay late and finish the cell migration chapter of this PhD thesis. I thank Veronique Duvocelle, secretary of LISA, for being so helpful and kind, without her, the administrative processes would have been so very difficult. I thank Lionel and his wife for giving their house to host my 'pot de marriage'.

The success of my PhD work is mainly because of our collaborators, which include, Fabrice Navarro, Mathilde Menneteau, Eric Sulpice, Xavier Gidrol, Delphine Freida, Nathalie Picollet, Monica Dolega, Fabien Abeille (who taught me cell culture techniques and collaborated with me for the PNIPAM project), Vincent Haguet, Patricia Obeid, our collaborators from Institut Pasteur, from Grenoble Institute of Neurosciences (Boudewijn

Vander Sanden, Charles Di Natale). My knowledge in biology comes from constant even stupid questions that I asked each one of them, to which they have responded with patience every single time.

I cannot express my gratitude enough to my parents, my grandparents, my sister and my wife, so I dedicate this PhD dissertation to them. My wife's incredible support on the day of the defense allowed me to solely concentrate on my presentation, when she took care of all the rest. I also thank my 'Atthai' who tutored me during my school days.

Special thanks to all my friends, especially to my brother-in-law and my friend Mithun, and my friend Vinoth, who gave me support and breaks when I needed the most.

This PhD work was possible only because of the support from everyone that I mentioned here and also support from those that I might have missed to mention.....

TABLE OF CONTENTS

ABSTRACT.....I

ABBREVIATIONS.....III

LIST OF FIGURES.....IV

1 INTRODUCTION.....1

2 DEVELOPMENT OF LENSFREE VIDEO MICROSCOPE.....9

2.1 LENSFREE IMAGING.....10

2.1.1 Principle.....10

2.1.2 Design and development.....11

2.2 LENSFREE IMAGING FOR CELL.....15

2.3 LENSFREE VIDEO MICROSCOPE.....16

2.3.1 Hardware considerations.....17

2.3.2 Software – Holographic reconstruction.....24

2.3.2.1 Software – Holographic reconstruction of adherent cells.....27

3 CELL CULTURE MONITORING.....35

3A. MONITORING CELL-SUBSTRATE ADHESION AND CELL SPREADING.....37

3A.1 INTRODUCTION.....38

3A.2 RESULTS.....40

3A.2.1 Cell-substrate adhesion.....40

3A.2.2 Cell spreading.....44

3A.3 DISCUSSION.....49

3A.4 METHODS.....53

3B MONITORING CELL DIVISION AND DETERMINATION OF CELL DIVISION ORIENTATION.....60

3B. 1 INTRODUCTION.....61

3B.2 RESULTS.....63

3B.2. 1 Detection of dividing cells.....63

3B.2.2 Comparison with EdU proliferation assay.....67

3B.2.3 Inhibiting cell proliferation using ActinomycinD.....69

3B.2.4 Monitoring cell proliferation kinetics.....71

3B.2. 5 Application to Other Cell Types Including Primary Cells.....73

3B.2. 6 Determination of cell division orientation.....74

3B.3 DISCUSSION.....76

3B.4 METHODS.....80

3C MONITORING CELL DIFFERENTIATION.....88

3C.1 INTRODUCTION.....89

3C.1.1 Adipogenic differentiation.....90

3C.1.2 Neuronal differentiation.....91

3C.2 RESULTS.....92

3C.2.1 Adipogenic differentiation.....92

3C.2.2 Neuronal differentiation.....98

3C.3 DISCUSSION.....101

3C.4 METHODS.....103

3D MONITORING CELL DEATH.....107

3D.1 INTRODUCTION.....108

3D.2 RESULTS.....110

3D.2.1 Cell death of U2OS cells.....112

3D.2.2 Cell death of human Mesenchymal Stem Cells (hMSCs) 116

3D.2.3 Other cell types and substrates.....120

3D.3 DISCUSSION.....122

3D.4 METHODS.....123

3E CELL MIGRATION AND ITS ALTERATIONS.....127

3E.1 CELL MIGRATION ON 2D SUBSTRATES.....129

3E.2 CELL MIGRATION ON 3D SUBSTRATES: Network formation between 3D acini structures.....137

3E.3 EXPLORATORY MIGRATION: 3D/2D INTERFACE.....143

3E.4 REVERSIBLE AND IRREVERSIBLE ALTERATION IN CELL MIGRATION..... 144

3E.4.1 Cell migration and division.....145

3E.4.2 Cell migration and differentiation.....146

3E.4.3 Cell migration and death.....149

3E.4.4 Quiescence and cell migration.....153

3E.5 DISCUSSION.....160

4 CASE STUDIES.....163

4.1 TEMPERATURE MEDIATED CELL DETACHMENT–USING PNIPAM GRAFTED SUBSTRATES.....165

4.1.1 Introduction.....165

4.1.2 Results.....167

4.1.3 Discussion.....170

4.1.4 Methods.....172

4.2 3D CELL CULTURE: RWPE1 CELL POLARITY.....175

4.2.1 Introduction.....175

4.2.2 Results.....176

4.2.3 Discussion.....178

4.2.4 Methods.....179

4.3 3D CELL CULTURE: ENDOTHELIAL NETWORK FORMATION.....180

4.3.1 Introduction.....180

4.3.2 Results.....180

4.3.3 Discussion.....183

4.3.4 Methods.....184

4.4 NORMAL AND REDUCED TEMPERATURES IN NORMOXIC AND ANOXIC CONDITIONS.....185

4.4.1 Introduction.....185

4.4.2 Results.....185

4.4.2.1 Myoblasts at standard culture conditions (37°C, 20% 0_2) 187

4.4.2.2 Myoblasts at 4°C, 0% 0_2.....190

4.4.3 Discussion.....192

5. CONCLUSION AND FUTURE PERSPECTIVES 196

ANNEX.....206

ABSTRACT

Biological studies always start from curious observations. This is exemplified by description of cells for the first time by Robert Hooke in 1665, observed using his microscope. Since then the field of microscopy and cell biology grew hand in hand, with one field pushing the growth of the other and vice-versa. From basic description of cells in 1665, with parallel advancements in microscopy, we have travelled a long way to understand sub-cellular processes and molecular mechanisms. With each day, our understanding of cells increases and several questions are being posed and answered. Several high-resolution microscopic techniques are being introduced (PALM, STED, STORM, etc.) that push the resolution limit to few tens of nm, taking us to a new era where 'seeing is believing'. Having said this, it is to be noted that the world of cells is vast, with information spread from nanometers to millimeters, and also over extended time-period, implying that not just one microscopic technique could acquire all the available information. The knowledge in the field of cell biology comes from a combination of imaging and quantifying techniques that complement one another.

Majority of modern-day microscopic techniques focuses on increasing resolution which, is achieved at the expense of cost, compactness, simplicity, and field of view. The substantial decrease in the field of observation limits the visibility to a few single cells at best. Therefore, despite our ability to peer through the cells using increasingly powerful optical instruments, fundamental biology questions remain unanswered at mesoscopic scales. A global view of cell population with significant statistics both in terms of space and time is necessary to understand the dynamics of cell biology, taking in to account the heterogeneity of the population and the cell-cell variability. Mesoscopic information is as important as microscopic information. Although the latter gains access to sub-cellular functions, it is the former that leads to high-throughput, label-free measurements. By focusing on simplicity, cost, feasibility, field of view,

and time-lapse in-incubator imaging, we developed 'Lensfree Video Microscope' based on digital in-line holography that is capable of providing a new perspective to cell culture monitoring by being able to capture the kinetics of thousands of cells simultaneously. In this thesis, we present our lensfree video microscope and its applications for in-vitro cell culture monitoring and quantification.

We validated the system by performing more than 20,000 hours of real-time imaging, in diverse conditions (e.g.: 37°C, 4°C, 0% O2, etc.) observing varied cell types and culture conditions (e.g.: primary cells, human stem cells, fibroblasts, endothelial cells, epithelial cells, 2D/3D cell culture, etc.). This permitted us to develop label-free cell based assays to study the major cellular events – cell adhesion and spreading, cell division, cell division orientation, cell migration, cell differentiation, network formation, and cell death. The results that we obtained respect the heterogeneity of the population, cell to cell variability (a raising concern in the biological community) and the massiveness of the population, whilst adhering to standard cell culture practices - a rare combination that is seldom attained by existing real-time monitoring methods.

We believe that our microscope and associated metrics would complement existing techniques by providing wide field of view with micrometric resolution.

ABBREVIATIONS

FOV	Field of View
ROI	Region of Interest
siRNA	Small interfering RNA
ECIS	Electric Cell Substrate Impedance Sensing
CCD	Charge-Coupled Device
CMOS	Complementary Metal–Oxide–Semiconductor
LED	Light Emitting Diode
hMSC	Human Mesenchymal Stem Cells
PIV	Particle Image Velocimetry
BME	β-mercaptoethanol
PNIPAM	Poly(N-isopropylacrylamide)
LCST	Lower Critical Solution Temperature
ATRP	Atom Transfer Radical Polymerization
EMT	Epithelial Mesenchymal Transition

LIST OF FIGURES

CHAPTER 1	
Figure 1.1	Standard lens-based time-lapse microscope
Figure 1.2	Schematic diagram of typical flow cytometer setup
Figure 1.3	Schematic diagram of Electric Cell Substrate Impedance Sensing
CHAPTER 2	
Figure 2.1.1	Principle of in-line holography introduced by Gabor.
Figure 2.1.2	Digital in-line holography Setup used by Xu et al.
Figure 2.1.3	Lensless digital holographic microscope setup by Repetto et al.
Figure 2.1.4	Modified lensfree imaging design using CMOS imaging sensor
Figure 2.3.1	Lensfree video microscope prototypes
Figure 2.3.2	Temperature increase and frequency of imaging
Figure 2.3.3	Parallel real-time imaging inside standard incubator
Figure 2.3.4	Different cell types in different conditions – imaged by lensfree video microscope.
Figure 2.3.5	Full FOV lensfree image
Figure 2.3.6	Schematic diagram explaining holographic reconstruction method 1
Figure 2.3.7	Schematic diagram explaining holographic reconstruction method 2
Figure 2.3.8	Holographic reconstruction
Figure 2.3.9	Comparison of reconstructed lensfree image and lens-based microscopic image
CHAPTER 3A	
Figure 3A.1	Change in lensfree holographic pattern during cell-substrate adhesion
Figure 3A.2	Discrimination of floating and adhering cells
Figure 3A.3	Floating and adherent cells imaged by lensfree and lens-based microscopes

Figure 3A.4	Cell-substrate adhesion kinetics of hMSCs and Primary human fibroblasts
Figure 3A.5	Quantification of cell-substrate adhesion and spreading
Table 3A.6	Overview of different cell-substrate adhesion assays
Figure 3A.7	Cell-cell variability in cell-substrate adhesion and spreading
Figure 3A.8	Age-dependent cell-substrate adhesion kinetics
Figure 3A.9	Pattern recognition of floating cells
Figure 3A.10	Gray-level detection of adherent cells
Table 3A.11	Validation of automated cell count
CHAPTER 3B	
Figure 3B.1	Changes in cell shape and adhesion during cell division
Figure 3B.2	Detection of dividing cells
Table 3B.3	Validation of automated detection of dividing cells
Figure 3B.4	Comparison with standard EdU proliferation assay
Figure 3B.5	Effect of ActinomycinD on cell proliferation
Table 3B.6	Effect of ActinomycinD on cell proliferation –EdU Proliferation assay
Figure3B.7	Cell proliferation kinetics
Figure 3B.8	Kinetics of cell proliferation of different cell types.
Figure 3B.9	Cell division orientation
Figure 3B.10	Unsuccessful cell division
Figure 3B.11	Applicability to other cell types
Figure 3B.12	Increased temporal resolution
Figure 3B.13	Automated detection of cell division orientation
CHAPTER 3C	
Figure 3C.1	Adipogenic differentiation and associated changes
Figure 3C.2	Neuronal differentiation and associated changes

Figure 3C.3	hMSC and differentiated adipocyte
Figure 3C.4	Adipogenic differentiation of single hMSC
Figure 3C.5	Gray-level based detection of differentiated and non-differentiated cells
Figure 3C.6	Comparison with standard lens-based microscopic images.
Figure 3C.7	Reconstruction and segmentation of differentiated adipocytes.
Figure 3C.8	Kinetics of adipogenic differentiation
Figure 3C.9	Different stages of adipogenic differentiation
Figure 3C.10	Time-lapse lens-based microscopic image of neuronal differentiation
Figure 3C.11	Neuronal differentiation of a single hMSC
Figure 3C.12	Kinetics of neuronal differentiation
Figure 3C.13	Mesenchymal stem cell differentiation to other types
CHAPTER 3D	
Table 3D.1	Cell viability assays
Figure 3D.2	Cell death observed by lensfree video microscopy
Figure 3D.3	Comparison with lens-based microscopy
Figure 3D.4	Cell death – human Osteo Sarcoma (U2OS) cells
Figure 3D.5	Cell death –hMSCs
Figure 3D.6	Change in gray value during cell death of hMSCs
Figure 3D.7	Cell death of DU145 and PC3 cells
Figure 3D.8	Cell death of NIH3T3 cells
Figure 3D.9	Cell death on micro-patterns
CHAPTER 3E	
Figure 3E.1	Random cell migration of NIH3T3 cells on 2D substrate
Figure 3E.2	Random cell migration of a single neuron cells on 2D substrate
Figure 3E.3	Circular cell migration: RWPE1 cells on 2D substrate

Figure 3E.4	Directed rectilinear cell migration of keratinocytes on 2D substrate
Figure 3E.5	Directed migration on 2D substrate – Wound healing
Figure 3E.6	Cell velocity in relation to confluence
Figure 3E.7	Cell migration at confluence – RPE1 cells.
Figure 3E.8	Cell migration at confluence - hMSCs
Figure 3E.9	Velocity as a function of length of the cells, aspect-ratio of the cells, and adhesion of the cells.
Figure 3E.10	Directed migration on 3D –acini network formation.
Figure 3E.11	Formation of network between 4 acini structures
Figure 3E.12	Failed Connection
Figure 3E.13	Formation of network between 3acini structures
Figure 3E.14	Multiple branching
Figure 3E.15	Close-gap branching
Figure 3E.16	Trajectories
Figure 3E.17	Exploratory migration
Figure 3E.18	Cell migration and cell division
Figure 3E.19	Myoblasts cell migration during cell division
Figure 3E.20	Reduction in cell velocity during neuronal differentiation
Figure 3E.21	Reduction in area of cell body during neuronal differentiation
Figure 3E.22	Chronograph cell differentiation
Figure 3E.23	Cell migration and cell death - Fibroblasts
Figure 3E.24	Cell migration and cell death - hMSCs
Figure 3E.25	Cell size and cell adhesion during cell death
Figure 3E.26	Chronograph – cell death
Figure 3E.27	Single migrating hMSC during cell death
Figure 3E.28	Scratch assay

Figure 3E.29	Computational analysis
Figure 3E.30	Wound area measurement
Figure 3E.31	Rate of wound healing at different temperatures
CHAPTER 4	
Figure 4.1.1	Time-taken to descend below LCST
Figure 4.1.2	Percentage of cell detachment
Figure 4.1.3	Static contact angle variation with respect to temperature
Figure 4.1.4	Loss of cell detachment efficiency
Figure 4.1.5	PNIPAM grafting procedure
Figure 4.1.6	Protocol schematic of a cell detachment experiment
Figure 4.2.1	Lensfree imaging of 3D cell culture
Figure 4.2.2	Discriminating acini and spheroids from lensfree holographic patterns
Figure 4.2.3	Growth of acini
Figure 4.3.1	HUVEC angiogenesis observed using lensfree video microscope
Figure 4.3.2	Analysis of HUVEC angiogenesis
Figure 4.3.3	Analysis of the kinetics of HUVEC network
Figure 4.4.1	Single fibers
Figure 4.4.2	Proliferation of satellite cells that exit from single fibers
Figure 4.4.3	Myoblast trajectories
Figure 4.4.4	Cell migration of myoblast
Figure 4.4.5	Cell migration of myoblast
Figure 4.4.6	Proliferation of myoblasts at 37°C Normoxia
Figure 4.4.7	Cell migration and cell shrinking of myoblasts at 4°C anoxia.
Figure 4.4.8	Cell detachment of myoblasts at 4°C anoxia.
Figure 4.4.9	Cell proliferation of myoblasts at 4°C anoxia

1. INTRODUCTION

Imaging is an inherent part of biology. Microscope allows researchers to peer through cells and sub-cellular structures. Rapid advancements have occurred in the field of microscopy over the past decade and several super resolution microscopy techniques that break the diffraction barrier first stated by Abbe in 1873, have been reported (Betzig et al., 2006; Egner & Hell, 2005; Hell, 2007; Hess, Girirajan, & Mason, 2006; Rust, Bates, & Zhuang, 2006; Schermelleh, Heintzmann, & Leonhardt, 2010; Sengupta, Van Engelenburg, & Lippincott-Schwartz, 2012). Super-resolution techniques overcame, more precisely circumvented, the Abbe diffraction limit by using tailored illumination, nonlinear fluorophore responses, or by using single molecule localization (Schermelleh et al., 2010; Sengupta et al., 2012). Modern day microscopic techniques have reached spatial and lateral resolution close to few tens of nm, popularizing the phrase 'Seeing is Believing'. However, increase in resolution is achieved at the expense of cost, compactness, simplicity and importantly field of view (FOV). Hence, despite increased resolution, to perform in-vitro quantification (e.g.: quantification of cell proliferation, etc.) flow cytometry is preferred over microscopy.

In-vitro quantification is about providing information about the status of the cells (quiescent, dying, proliferating, etc.). This is the preliminary step towards understanding complex cellular mechanisms, for example, to assess effectiveness of drugs, siRNAs, to control cell behavior, and to test the compatibility of materials. It is therefore an inevitable step well before in-vivo testing. Modern-day lens-based microscopes are not commonly used to perform in-vitro quantification mainly due to lack of (or difficulty in obtaining) spatial and temporal information.

Spatial information or field of view (FOV) is often traded off for resolution. Typical FOV with 20X magnification can visualize few single cells at best. Even with a lower magnification of 10X, only few tens of cells (or couple of hundreds at best) are observed. Hence the global view, which is necessary to understand the entirety of the population, is lost. Temporal information, on the other hand, is lost due to the inability to perform real-time monitoring. This is because, cells cannot stay alive outside the incubator for extended period of time. The incubator provides ambient environmental conditions needed for the viability of cells (humidity, %02, %CO2, and temperature). Microscopes cannot be placed inside the standard incubator mainly due to their bulkiness, and elevated temperature and humidity inside the incubator. In order to observe the dynamics of cell culture, using lens-based microscopes, a personnel intervention is required at static time-points, which apart from being labor-intensive, raises concerns about sterility, and incapacity to follow same cell at single cell level. As a response, to perform continuous live-cell imaging, time-lapse microscopy was introduced. Lens-based time-lapse microscopes maintain suitable culture environment, by housing an environmental chamber **(Fig. 1.1)**. As a consequence, the cost and bulkiness of the microscope is increased manifold times, along with the complexity in manipulating culture dishes during the experiment while the FOV remains restricted. Further, mostly standard video microscopes necessitate labeling for clear visualization and quantification. This raises concerns related to cytotoxicity, bias introduced by labeling (Marx, 2013), photo-toxicity, and photo-bleaching. These factors limit the use of standard video microscope for in-vitro quantification.

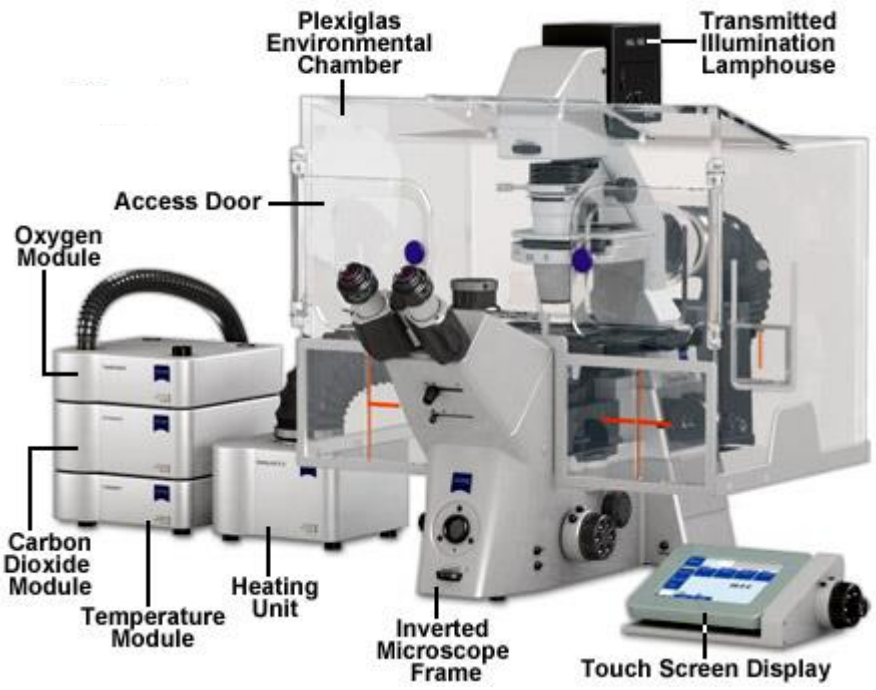

Figure 1.1: Standard lens-based time-lapse microscope. Standard lens-based time-lapse microscope setup housing an environmental chamber connected to external CO2, O2 and temperature modules to provide ambient cell culture conditions.

(Courtesy: http://zeisscampus.magnet.fsu.edu/)

Therefore, researchers are forced to resort to marker-dependent flow cytometry assays, which monopolize in-vitro quantification. A flow cytometer performs automated quantification, and provides information about the state of the cell, depending on the uptake (or not) of expensive biomarkers, by the cells. The technique analyses entire cell populations and provides high-throughput information **(Fig. 1.2)**. However, markers are indispensable for quantification using flow cytometry. Though several markers that do not affect the cells are being introduced, most of the currently used markers are cytotoxic and are also suspected to be introducing bias in measurements (Marx, 2013). Also, another major limitation with the technique is the need for the cell population to be harvested for end-point analysis. Therefore, in most cases, the cell population is lost, along with the continuity of quantification, rendering the assays invasive and non-continuous.

The only way to perform continuous measurement using flow cytometry is by conducting several measurements at different time points using cultures that are subjected to same treatment. The end result is an extrapolation of data obtained from different time points. However, the data cannot be called continuous since the population is not the same.

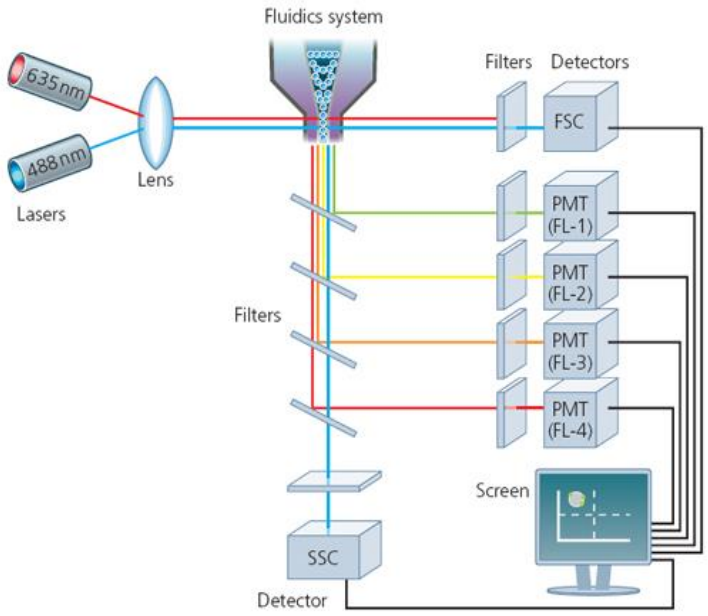

Figure 1.2: Schematic diagram of typical flow cytometer setup. The fluidics system passes the cell population one-by-one through the laser. Based on light scattering, the uptake of markers (or not) by the cell is quantified. (Courtesy: www.abdserotec.com)

In order to overcome the limitations and to perform label-free, real-time continuous measurements, several techniques are being introduced. One of the well popularized techniques is ECIS – Electric Cell Substrate Impedance Sensing **(Fig. 1.3)**. The technique takes advantage of the fact that the cell membranes are strong insulators. By measuring the substrate impedance changes, presence or absence of cells and also the surface area covered by cells are quantified. Using this information, the status of the cell culture is determined leading to several label-free assays (Arias, Perry, & Yang, 2010; Diemert et al., 2012; Hondroulis, Liu, & Li, 2010; Hong, Kandasamy, Marimuthu, Choi, & Kim, 2011; Michaelis, Wegener, & Robelek, 2013). Nevertheless, it is an indirect approach. First, the

obtained parameters are surrogate measurements of substrate impedance changes. Second, the measurement is restricted to cell population and is not usually extended to the level of single cells. Third, the cells are not visualized which represents a huge loss of information in the era of HCA. Though various techniques that are being introduced, as alternatives provide higher resolution and feasibility, they face one or combination of the limitations mentioned above (Marrison, Räty, Marriott, & O'Toole, 2013).

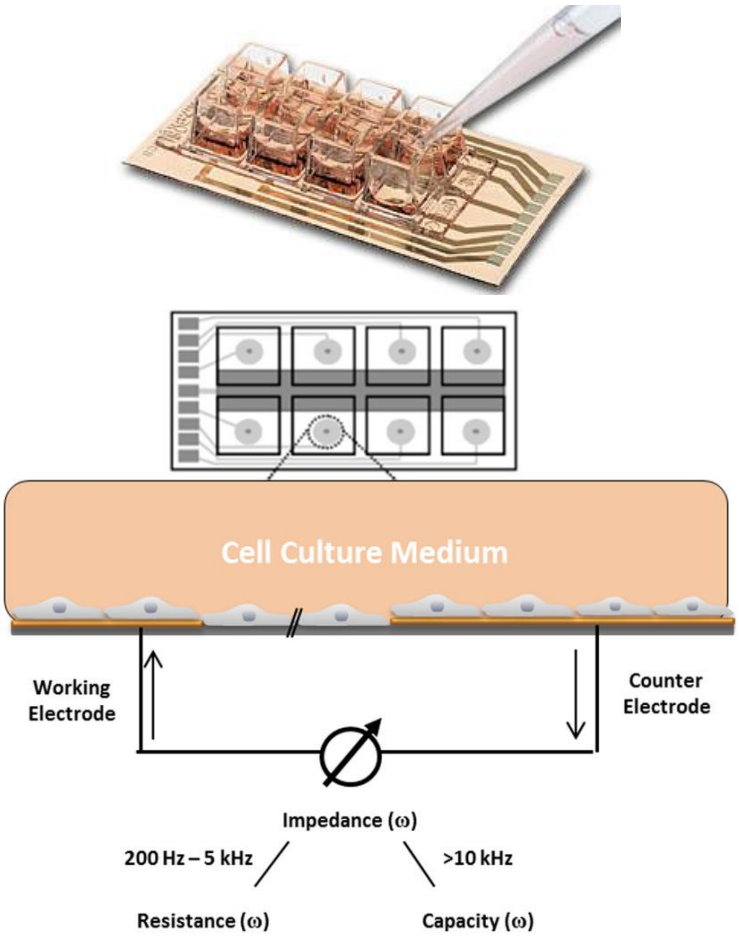

Figure 1.3: Schematic diagram of Electric Cell Substrate Impedance Sensing. The setup comprises of gold electrode surfaces and culture wells built around the gold electrode surfaces. (Courtesy: www.biophysics.com)

An apt alternative platform should combine the advantages of all the three major techniques (time-lapse microscopy, flow cytometry, ECIS) mentioned above. That is, the platform, (i) should be readily applicable to cell culture imaging inside standard incubator, (ii) should be able to provide label-free information about the status of cell population and single cells in real-time, (iii) should provide high-throughput information thereby respecting the heterogeneity of the population.

This thesis presents the development and validation of such an imaging platform – 'Lensfree Video Microscope'. We detail the principle of our imaging platform – Digital Inline holography introduced by Gabor in 1940. Followed by, the development of our 'Lensfree Video Microscope' capable of performing real-time monitoring inside the standard incubator (chapter 2).

Further, we illustrate the applicability of our platform to cell culture monitoring by performing high-throughput monitoring of major cell functions such as cell-substrate adhesion, cell spreading, cell division, cell division orientation, cell migration, cell differentiation, and cell death (chapter 3).

Along with the ability to monitor cell culture inside standard incubator, we further illustrate the versatility of our platform, by performing case studies in diverse conditions, which include, 3D cell culture imaging, cell culture monitoring at 4°C, in anoxia, cell detachment monitoring due to change in temperature (chapter 4).

REFERENCES

Arias, L. R., Perry, C. a, & Yang, L. (2010). Real-time electrical impedance detection of cellular activities of oral cancer cells. *Biosensors & bioelectronics*, *25*(10), 2225–31. doi:10.1016/j.bios.2010.02.029

Betzig, E., Patterson, G. H., Sougrat, R., Lindwasser, O. W., Olenych, S., Bonifacino, J. S., … Hess, H. F. (2006). Imaging intracellular fluorescent proteins at nanometer resolution. *Science (New York, N.Y.)*, *313*(5793), 1642–5. doi:10.1126/science.1127344

Diemert, S., Dolga, a M., Tobaben, S., Grohm, J., Pfeifer, S., Oexler, E., & Culmsee, C. (2012). Impedance measurement for real time detection of neuronal cell death. *Journal of neuroscience methods*, *203*(1), 69–77. doi:10.1016/j.jneumeth.2011.09.012

Egner, A., & Hell, S. W. (2005). Fluorescence microscopy with super-resolved optical sections. *Trends in cell biology*, *15*(4), 207–15. doi:10.1016/j.tcb.2005.02.003

Hell, S. W. (2007). Far-field optical nanoscopy. *Science (New York, N.Y.)*, *316*(5828), 1153–8. doi:10.1126/science.1137395

Hess, S. T., Girirajan, T. P. K., & Mason, M. D. (2006). Ultra-high resolution imaging by fluorescence photoactivation localization microscopy. *Biophysical journal*, *91*(11), 4258–72. doi:10.1529/biophysj.106.091116

Hondroulis, E., Liu, C., & Li, C.-Z. (2010). Whole cell based electrical impedance sensing approach for a rapid nanotoxicity assay. *Nanotechnology*, *21*(31), 315103. doi:10.1088/0957-4484/21/31/315103

Hong, J., Kandasamy, K., Marimuthu, M., Choi, C. S., & Kim, S. (2011). Electrical cell-substrate impedance sensing as a non-invasive tool for cancer cell study. *The Analyst*, *136*(2), 237–45. doi:10.1039/c0an00560f

Marrison, J., Räty, L., Marriott, P., & O'Toole, P. (2013). Ptychography--a label free, high-contrast imaging technique for live cells using quantitative phase information. *Scientific reports*, *3*, 2369. doi:10.1038/srep02369

Marx, V. (2013). Is super-resolution microscopy right for you? *Nature methods*, *10*(12), 1157–63. doi:10.1038/nmeth.2756

Michaelis, S., Wegener, J., & Robelek, R. (2013). Label-free monitoring of cell-based assays: Combining impedance analysis with SPR for multiparametric cell profiling. *Biosensors & bioelectronics*, *49C*, 63–70. doi:10.1016/j.bios.2013.04.042

Rust, M. J., Bates, M., & Zhuang, X. (2006). imaging by stochastic optical reconstruction microscopy (STORM), *3*(10), 793–795. doi:10.1038/NMETH929

Schermelleh, L., Heintzmann, R., & Leonhardt, H. (2010). A guide to super-resolution fluorescence microscopy. *The Journal of cell biology*, *190*(2), 165–75. doi:10.1083/jcb.201002018

Sengupta, P., Van Engelenburg, S., & Lippincott-Schwartz, J. (2012). Visualizing cell structure and function with point-localization superresolution imaging. *Developmental cell*, *23*(6), 1092–102. doi:10.1016/j.devcel.2012.09.022

CHAPTER 2

DEVELOPMENT OF LENSFREE VIDEO MICROSCOPE

Pg. 9	**LENSFREE IMAGING** **Principle, Design and development**
Pg. 15	**LENSFREE IMAGING FOR CELL IMAGING**
Pg. 16	**LENSFREE VIDEO MICROSCOPE** **Hardware considerations**
Pg. 24	**LENSFREE VIDEO MICROSCOPE** **Software – Holographic reconstruction**

2. DEVELOPMENT OF LENSFREE VIDEO MICROSCOPE

2.1 LENSFREE IMAGING

2.1.1 Principle

Although major part of research is focused towards increasing the resolution of microscopes down to few tens of nm (Betzig et al., 2006; Egner & Hell, 2005; Hell, 2007; Schermelleh, Heintzmann, & Leonhardt, 2010; Sengupta, Van Engelenburg, & Lippincott-Schwartz, 2012), a significant part is also devoted towards finding alternatives to bulkiness, cost, complexity, limited field of view associated with most of the microscope setups. Lensfree imaging, based on digital in-line holography, is one of the few significant alternatives. The very first idea of using digital inline holography to image objects was proposed by D. Gabor, in 1948 (Gabor, 1948). Light from the point source, in this case a pinhole, illuminates the object which is a few mm away from the point source. The light scattered by the object and the light that directly passes from the source to the imaging sensor forms a holographic pattern on the imaging sensor (CCD or CMOS) which is a few cm away from the point source **(Fig. 2.1.1)**. The holographic pattern obtained by the imaging sensor must be back-propagated to reconstruct the image of the object. Unlike, conventional holography, a separate reference wave is not used. The light that is not scattered by the sample acts as the reference wave.

2.1.2 Design and development

After the introduction of the technique by Gabor, digital in-line holography to study biological objects (Single cell of D. brightwellii ~60µm long) was first reported by Xu et al. in 2001 (Xu, Jericho, Meinertzhagen, & Kreuzer, 2001). It featured Laser and a pinhole (Diameter ~ 2µm) as point source. Similar to the setup demonstrated by Gabor, the object was placed close to the source of illumination (1-6mm) and far from CCD (3-7cm) **(Fig. 2.1.2)**.

In 2004, Repetto et al. also demonstrated a similar setup **(Fig. 2.1.3)**, named 'Lensless digital holographic microscope' (Repetto, Piano, & Pontiggia, 2004) . In place of a laser, the setup featured LED, objective lens (20X) and pinhole as point source. Since the objective lens used for illumination, does not contribute to image formation, the system is considered to be lens-less. Using this configuration, they demonstrated imaging of 10µm latex beads.

In both the cases, the diameters of the pinholes used were between 1µm and 10µm, and the point source-to-object and object-to-CCD distances were in ranges of 0.8 - 6.3mm and 3 - 6.9cm respectively. The CCD used by both Repetto et al., and Xu et al. had pixel sizes close to 9µm. In order to achieve resolution greater than 9µm, the number of fringes captured by CCD should be as large as possible resulting in a configuration where the object is far was from the CCD. This configuration magnified the hologram acquired from the object facilitating high-resolution reconstruction.

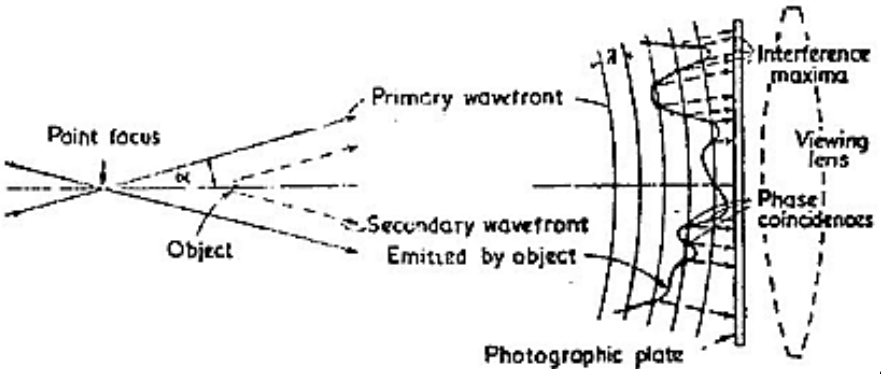

Fig 2.1.1: Principle of in-line holography introduced by Gabor. The primary wavefront from the source of illumination and secondary wavefront scattered by the object interfere to form holographic pattern on the photographic plate. Schematic diagram reproduced from (Gabor, 1948).

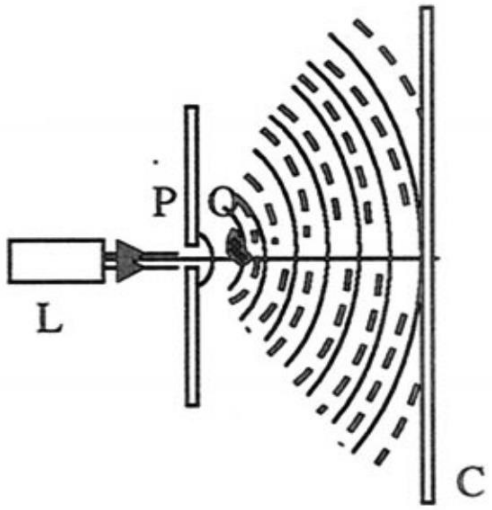

Figure 2.1.2: Digital in-line holography Setup used by Xu et al. Laser 'L' along with pinhole 'P' acts as point source of illumination. Object 'O' is placed a few mm (1-6mm) away from the point source and a few cm away from the CCD 'C' (3-6cm). Continuous lines indicate the reference wave and dotted lines indicate the scattered wave from the object. Single cell of D. brightwellii was imaged using this setup. Figure reproduced from (Xu et al., 2001).

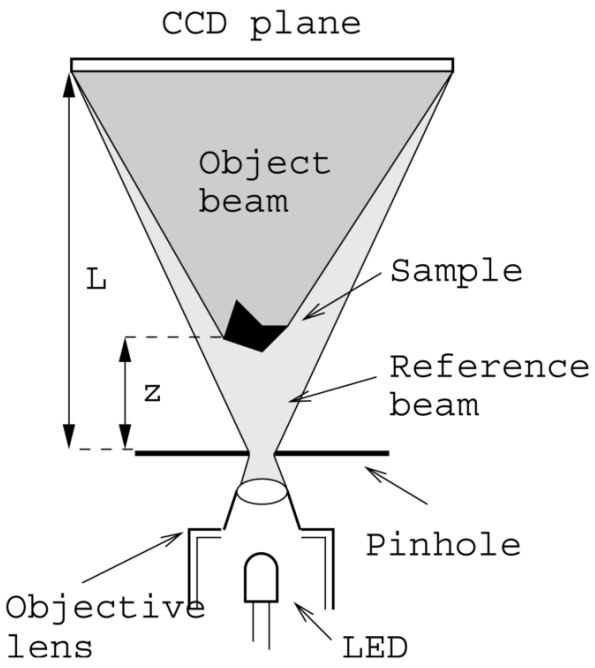

Figure 2.1.3: Lensless digital holographic microscope setup reported by Repetto et al. The setup uses LED, objective lens and pinhole as source of illumination. Sample is placed at distance 'z' from the source of illumination and the CCD is placed at distance 'L', from the source of illumination. The values of 'z' and 'L' are approximately 2mm and 23 mm respectively. 10μm latex beads were imaged using the setup. Figure reproduced from (Repetto et al., 2004).

It is to be noted that placing the object close to the source of illumination (distances from 1-6mm) restricted the field of observation. This lead to a modified design from A. Ozcan et al., in 2007, where the object was placed far away from the point source (~5cm), in other words, closer to the imaging sensor (~1mm) **(Fig. 2.1.4)**. The CCD was replaced by CMOS imaging sensor, with reduced pixel size of 2.2μm. Also, the diameter of the pinhole was increased to ~100μm. In this geometry, the FOV increases to 24mm^2, but the resolution is decreased due to the reduction in the number of fringes recorded by the imaging sensor. However, the latter is counterbalanced by the development of CMOS imaging sensor, in recent years, resulting in a pixel size ~ 2μm or even less.

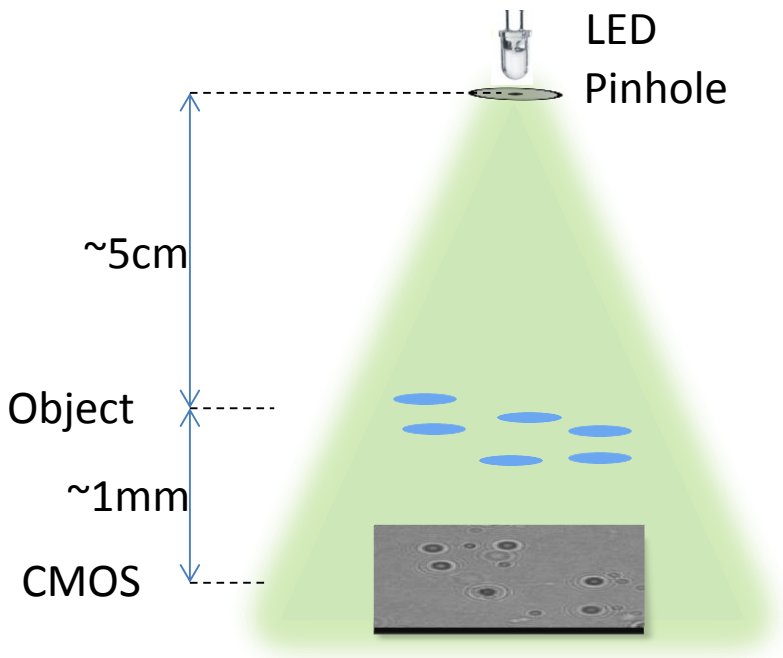

Figure 2.1.4: Modified lensfree imaging design using CMOS imaging sensor. Lensfree microscopy setup consisting of LED, pinhole (150µm diameter), and CMOS imaging sensor. Unlike the setup used by Xu et al., and Repetto et al., the Object is placed very close to the imaging sensor (1mm), far away from (~5cm) the source of illumination, and CMOS replaces CCD.

The applications of lensfree imaging system reported by Ozcan et al. chiefly targeted diagnostics in resource-poor settings (Biener et al., 2011; Coskun et al., 2013; Mudanyali, Oztoprak, Tseng, Erlinger, & Ozcan, 2010; Seo, Su, Tseng, Erlinger, & Ozcan, 2009; Su, Seo, Erlinger, & Ozcan, 2009). The resolution of the system is micrometric (~ 2 µm), only restricted by the pixel size (2.2 µm) of the imaging sensor. The resolution limit is efficiently surpassed to detect bacteria and virus by using a thin-wetting film on top of the object to create a lensing effect (Allier, Hiernard, Poher, & Dinten, 2010; Hennequin et al., 2013; Mudanyali et al., 2013).

With only 3 major components, LED, pinhole and CMOS sensor, the fabrication cost of the setup (~1000$) became negligible in comparison with lens-based microscopes, and the

field-of-view had increased manifold times (from < $5mm^2$ to $24mm^2$). These characterizations established lensfree imaging as a pragmatic response to bulkiness and cost of lens-based microscopes.

2.2 LENSFREE IMAGING FOR CELLS

The use of lensfree imaging platform for cell imaging and for characterization of cells was demonstrated significantly (Isikman, 2012; Navruz et al., 2013; Ozcan & Demirci, 2008; Seo et al., 2010; Su, Erlinger, Tseng, & Ozcan, 2010; Su et al., 2009; Weidling, Isikman, Greenbaum, Ozcan, & Botvinick, 2012). However, in all the cases, experiments were performed outside the incubator and cells were imaged at static time-points within microscopic slides.

Inside standard incubator, Kim et al. demonstrated real-time detection of cardiotoxicity using lensfree imaging inside standard incubator, by measuring the variances of beating cardiomyocytes (Kim et al., 2011). However, the period of observation was very short lasting ~ 2 hours. In addition, global variation in the image was measured, but without extending to the level of single cells. G. Zheng et al. demonstrated 'ePetri', a system based on lensfree shadow imaging to monitor cell culture in real-time (Zheng, Lee, Antebi, Elowitz, & Yang, 2011). The method described in the article is closer to the standard cell culture practices allowing extended continuous monitoring inside standard incubator. In order to circumvent the problem holographic reconstruction (refer section 2.3.2) and to increase the resolution beyond the pixel size of the imaging sensor, shadow imaging was employed, where the cells were cultured directly on the imaging sensor (removing the protective cap of the imaging sensor). The system allows continuous monitoring over a large field of view (24 mm^2), with sub-micrometric resolution. However, the system

requires preparation of a PDMS culture well within the sensor. Customization of the sensor along with skillful integration and pre-coating of the sensor with fibronectin are necessary steps. In addition, a nutrient filled fluid was used instead of normal growth substrate for better acquisition. G. Jin et al. reported a lensfree imaging device for real-time cell culture monitoring (Jin et al., 2012). Since the observation was performed outside the standard incubator, ambient conditions were provided to the cells by integrating oxygen permeable PDMS wall sandwiching the cover glass, custom-built heating block and an uninterrupted flow of CO_2 independent media. These requirements increase the complexity while performing necessary manipulation (change of culture media, addition of drugs, etc.) of cell culture during the experiments.

2.3 LENSFREE VIDEO MICROSCOPE

Majority of the above mentioned studies mainly focus on competing with lens-based microscopy in terms of resolution. This restricts lensfree imaging to static time point imaging of cells or mandate utilization of engineered approaches to perform short duration real-time monitoring. These approaches largely compromise the simplicity and applicability of lensfree imaging to cell culture monitoring over extended time-period. In all the methods described above, cell culture protocols were largely modified in order to meet the demands of lensfree imaging, and in order to attain resolution comparable with lens-based microscopes. However, by focusing on the contrary, we developed a lensfree video microscope **(Fig. 2.3.1)** that adheres to the standard cell culture practices. Our lensfree video microscope and associated cell based assays based on image reconstruction and processing, are entirely compatible with the standard practices of cell culture, accommodating most commonly used culture dishes (culture dishes of different diameter, T-flasks, multi-well plates). The culture dish is simply placed on the device

installed permanently inside the incubators **(Fig. 2.3.3)**, without considering distance to sensor, without preparing sample within slides or a dedicated chamber. Hence we do not compromise with the standard practices in cell culture laboratories and the overall simplicity of lensfree microscopy.

Our lensfree video microscope consists of a 12-bit APTINA MT9P031 CMOS RGB imaging sensor with a pixel size of 2.2µm, measuring 5.7 × 4.3 mm, and light-emitting diode (LED) (dominating wavelength 525nm) with a pinhole of 150µm. In a typical experiment, the lensfree video microscope is placed inside the incubator and the culture dish containing the cells is placed on lensfree video microscope. Illumination is provided by the LED along with the pinhole from a distance of ~5cm.

2.3.1 Hardware considerations

To build a video microscope installable inside the standard incubator, we confronted major complications e.g. contamination of the cell culture, temperature stability and poor illumination condition due to diffusion in the culture medium. Our first prototype **(Fig. 2.3.1a)** caused major concerns due to a non-bio-compatible material, Polyoxymethylene (Delrin) used in the exterior casing, which emitted formaldehyde at very low concentration, yet enough to cause cell death. Another concern is that the imaging sensor and the associated circuit board get heated while being switched on continuously (up to 45°C from ~ 20°C in ~10 minutes). It is to be noted that the temperature inside the incubator is already at 37°C. Within initial 5 minutes the temperature of the imaging sensor and the circuit board (in continuous mode) surpasses 40°C. As a result, the temperature of the culture dish placed in contact with the imaging sensor increases, consequently resulting in cell death. Also, this causes evaporation of the culture media and subsequent condensation on the lid of the culture dish. In order to diminish the

heating, (i) the imaging sensor is switched on only during image acquisitions (typically for 3 seconds), (ii) proper ventilation by a fan to minimize the temperature increase during acquisitions. These measures greatly minimized the heating, nullifying the evaporation of the culture media. Measurement of increase in temperature is shown while the lensfree video microscope acquires images with temporal resolution of 20 minutes **(Fig. 2.3.2a)** As it can observed, the temperature on the sensor rises up to 37.9°C during image acquisitions (lasting typically 3 seconds), while the temperature inside the incubator is stable at 37.2°C. Immediately after image acquisition the temperature on the imaging sensor starts the descent and reaches 37.4°C in ~8 minutes. However, the temperature increase inside the culture dish is lesser compared to the temperature increase on the imaging sensor. On an average, there is only a less than 0.1°C difference between the temperature inside the petri dish and the temperature inside the incubator. However, if the frequency of imaging is increased to 1 image every 10 minutes **(Fig. 2.3.2b)** or every 5 minutes **(Fig. 2.3.2c)**, a temperature difference of greater than 0.3°C is observed between the petri dish and the incubator. Hence, our lensfree video microscope can offer only a limited temporal resolution of 15 minutes. For applications that require increased temporal resolution, a modification in the lensfree video microscopy setup is done to include a Peltier element to maintain the surface temperature of the imaging sensor at 37°C **(Fig. 2.3.1c)**. This setup provides an increased temporal resolution of 10 seconds whilst maintaining the surface temperature at 37°C. Here, the temperature inside the culture dish placed on the imaging sensor is equal to the temperature inside the incubator **(Fig. 2.3.2d)**. With this setup we have performed 1-minute longitudinal imaging of BJ cells inside standard incubator. However, using Peltier element is not satisfactory due to the cost involved (~5000$ Keithley Source-Measurement Unit AT 2510), and also due to the initial calibration (~3 hours) that is required to bring the

imaging sensor temperature to a stable 37°C. Hence in our fourth prototype, we removed the Peltier element and replaced with a heat sink **(Fig. 2.3.1d)**. Using this system, we obtain a temporal resolution of 15 minutes, which is suitable for myriad applications pertaining to cell biology, which can be seen in the following sections of the report (chapters 3, 4).

We validated the robustness and versatility of our lensfree video microscope by performing real-time imaging of different cell types (e.g.: endothelial, fibroblast, epithelial, stem/cancer/primary cells, etc.), different culture conditions (2D/3D), different substrates (standard culture dish, micro-patterned, polymer coated substrates) and different conditions **(Fig. 2.3.4)**. For example, we have performed real-time monitoring at,

1. ~25°C (room temperature)

2. 37°C, 20% O_2, 5% CO_2 and 95% relative humidity (inside the incubator, values to be verified)

3. 4°C in normoxia

4. 4°C in anoxia

More than 20,000 hours of imaging in different conditions combined with FOV of 24mm^2 **(Fig. 2.3.5)**, enabled us to perform label-free quantification of the major cell functions in real-time, using image reconstruction and image processing. This includes cell adhesion, cell spreading, cell proliferation, cell division orientation, cell migration, cell differentiation, and cell death.

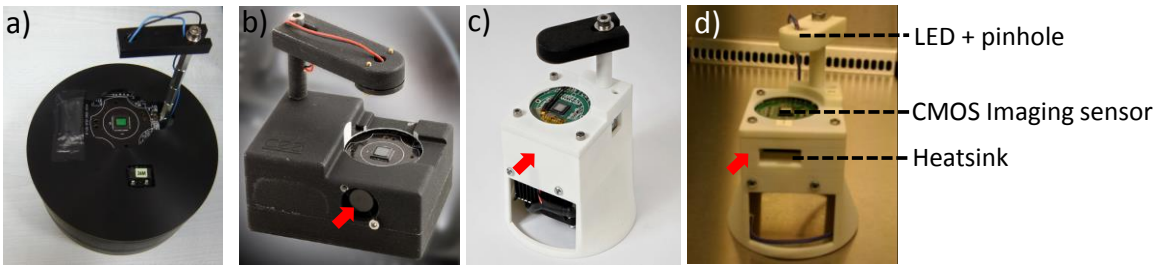

Figure 2.3.1: Lensfree video microscope prototypes.

(a) First lensfree video microscope prototype with a non-biocompatible exterior casing (Delrin - Polyoxymethylene).

(b) Second prototype of lensfree video microscope, with a fan for ventilation (red arrow mark). Achievable temporal resolution is 15 minutes. The sensor is switched off in between image acquisitions.

(c) Third prototype with Peltier element (red arrow), and an achievable temporal resolution close to 10 seconds. The imaging sensor is always on.

(d) Lensfree video microscope where Peltier element is replaced by a heat-sink (red arrow), and opening for cross ventilation. The sensor is switched off in between acquisitions. Achievable temporal resolution is 15 minutes. All prototypes measure ~10cm in height.

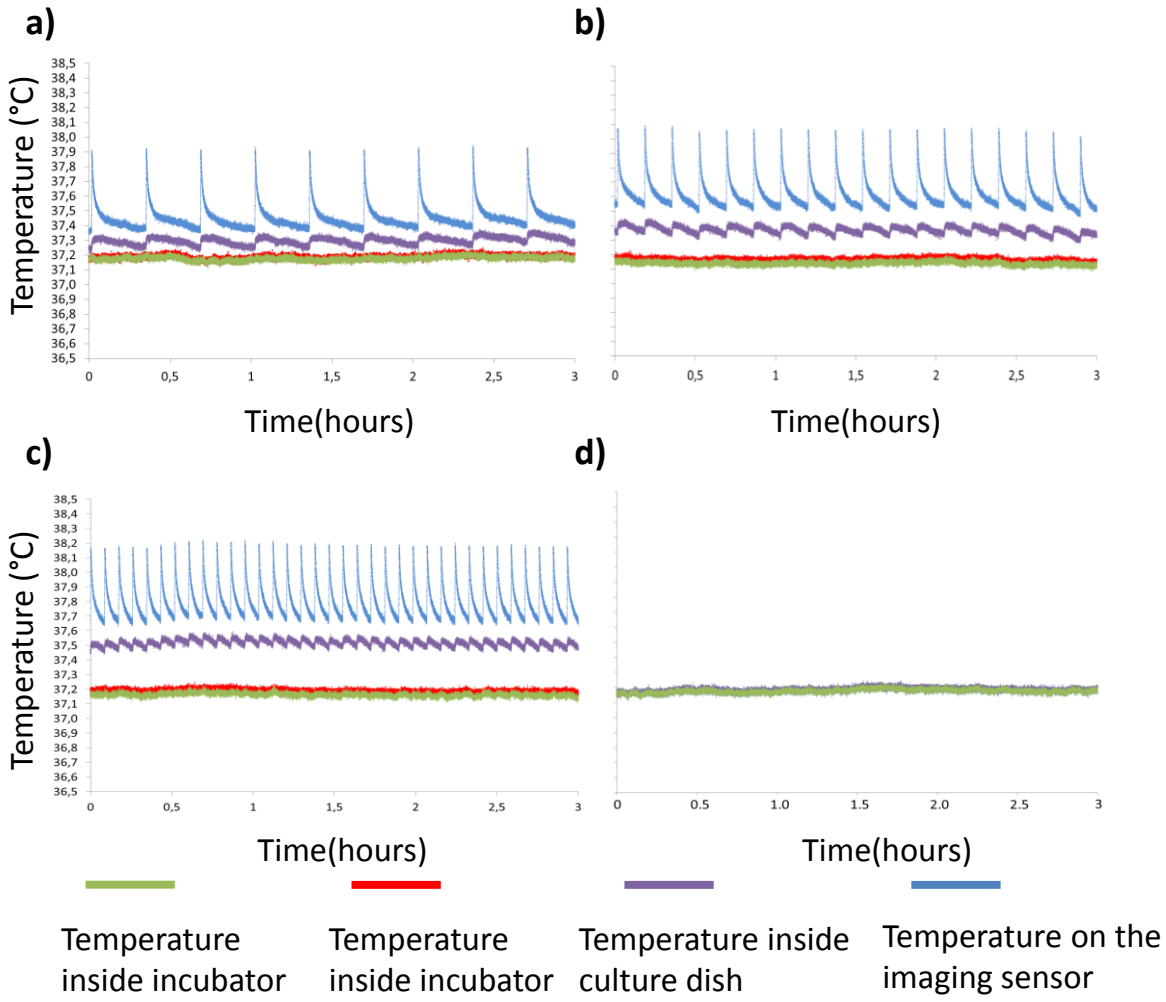

Figure 2.3.2: Temperature increase and frequency of imaging

4 temperature sensors were used for evaluation. Two temperature sensors were placed inside the incubator at different points (lines green, red). The other 2 temperature sensors were placed inside the culture dish (line purple) and on top of the imaging sensor (line blue).

(a), (b), (c): Temperature increase during image acquisitions is observed for temporal resolutions of 20 minutes, 10 minutes, and 5 minutes respectively.

(d) Temperature stability of the lensfree video microscope, with integrated temperature control. It is to be noted that the temperature inside the culture dish placed on the system and the temperature inside the incubator do not vary.

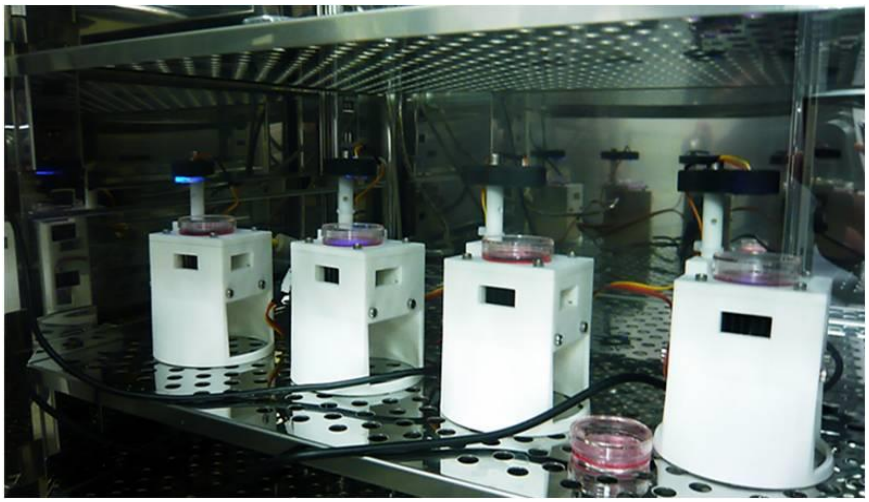

Figure 2.3.3: Parallel real-time imaging inside standard incubator. Four Lensfree video microscopes installed inside a standard incubator performing parallel monitoring of 35mm diameter culture dishes. The image acquired is transmitted to a laptop placed outside the standard incubator.

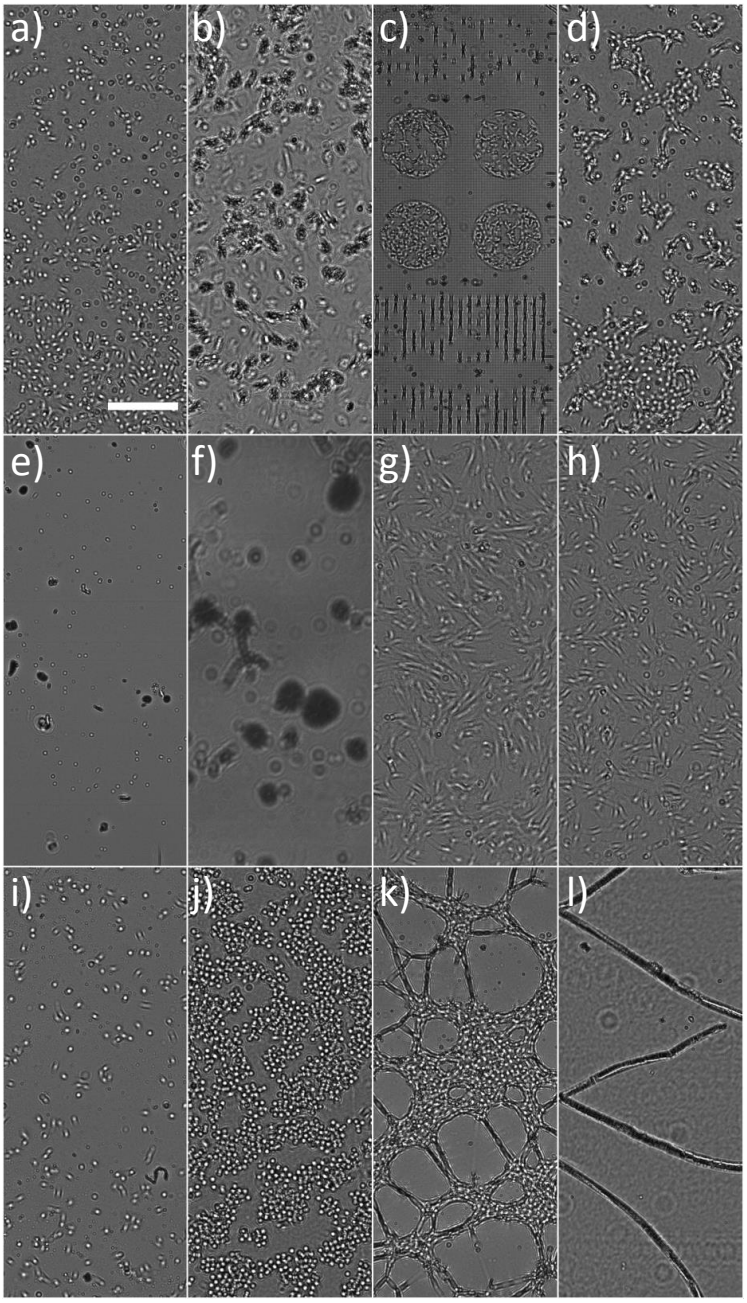

Figure 2.3.4: Different cell types in different conditions – imaged by lensfree video microscope. (a) PC3, (b) Adipocytes differentiated from hMSCs, (c) NIH3T3 cells on Cytoo™ micro-patterns, (d) PNT2, (e) satellite cells in anoxia at 4°C, (f) 3D culture of RWPE, (g) hMSCs, (h) Primary human fibroblasts, (i) U87, (j) MCF10A, (k) Network formation in 3D culture by Huvec endothelial cells, (l) single muscle fibers extracted from muscle tissue. Scale bar 500 µm.

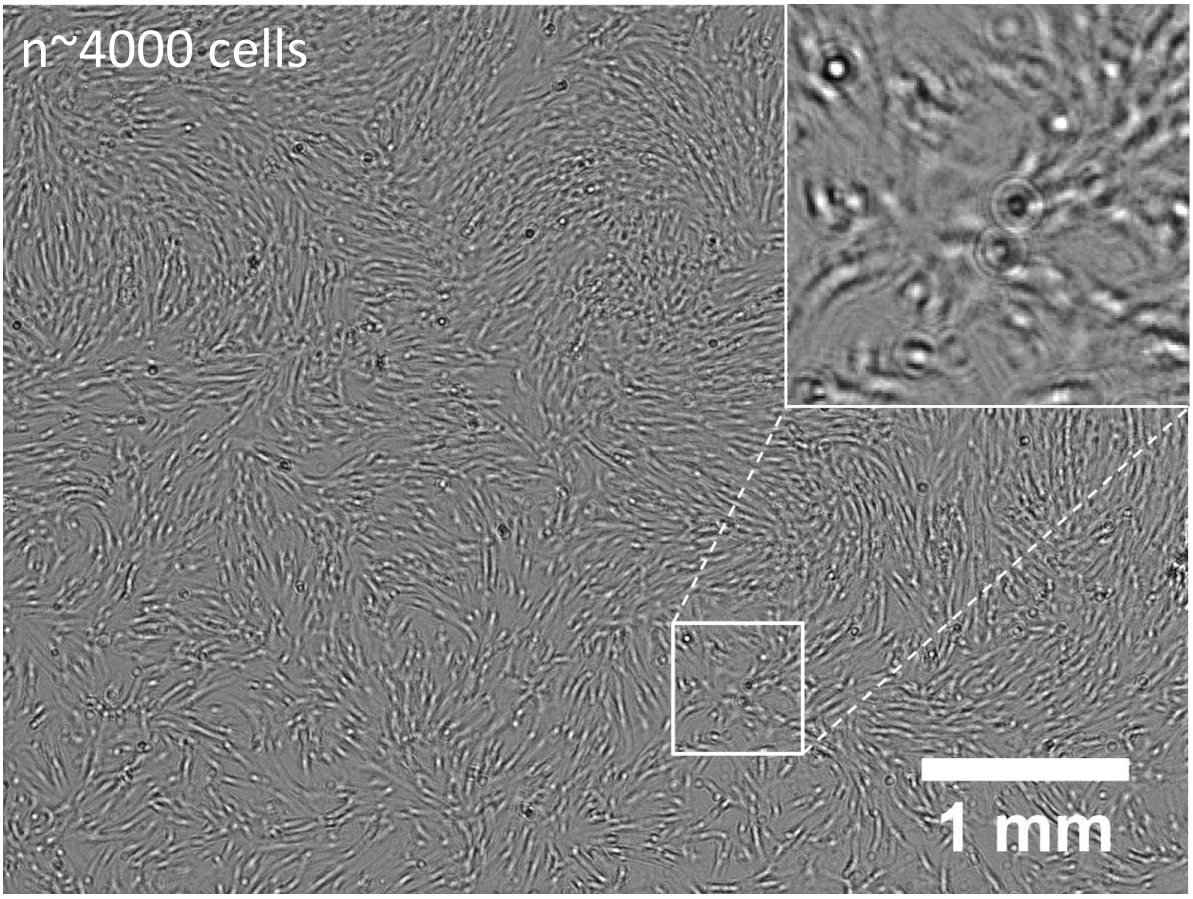

Figure 2.3.5: Full FOV lensfree image. Image illustrating the FOV of our lensfree video microscope. The image contains ~4000 human mesenchymal stem cells. Digitally magnified region on top right shows the single cells inside the population.

2.3.2 Software – Holographic reconstruction

As mentioned earlier, images acquired by CMOS imaging sensor are holographic patterns resulting from the interaction of the object with light. Although information about the status of single cells and cell population can be obtained from the raw image (following sections), holographic reconstruction is required to obtain the exact image of the cell. The holographic pattern can be reconstructed following the computational methods described in (Denis, Fournier, Fournel, & Ducottet, 2005; Mudanyali, Tseng, et al., 2010)

From fig. 2.1.4, fig. 2.3.1, it can be understood that a pinhole is used in order to create plane waves at the object plane. Therefore, it is to be noted that the reconstruction is performed assuming a plane-wave illumination. The object at a distance 'Z' (considering 'Z' as the physical distance between the object and the sensor) scatters the illuminated light through free space, the scattered light and the light from the source interfere to form holographic pattern on the sensor. This holographic pattern can be written as,

$$h_z = \frac{1}{j\lambda z} e^{j2\pi\frac{z}{\lambda}} \exp\left(j\pi \frac{x^2 + y^2}{\lambda z}\right)$$

(1)

Where,

h_z is the holographic pattern of the object formed on the sensor, at a distance Z.

J is the unitary imaginary number,

x, y, z are the spatial variables, and

λ (nm)denotes the wavelength of the source

Fresnel approximation is employed to relate the reconstructed complex amplitude at distance 'Z' with the hologram using transmittance t.

$$A_z(x, y) = t(x, y) * h_z(x, y) \tag{2}$$

The transmission coefficients $t(x, y)$ of equation (2), is defined with respect to the absorption coefficients $a(x, y)$ as,

$$t(x, y) = 1 - a(x, y) \tag{3}$$

It is to be noted that the amplitude cannot be recorded directly by the sensor and it is the squared modulus of the complex amplitude of the incident field which is recorded on the sensor, that is,

$$I = |A_z|^2 \tag{4}$$

Equation (4) can be written using (1), (2), and (3) as,

$$I = 1 - a * h_z - a^* * h_z^* + |a * h_z|^2 \tag{5}$$

Removing the non-linear term as suggested by (Denis, Fournier, Fournel, & Ducottet, 2005), and using the duality property of Fresnel transform (6), we arrive at equation (7),

$$\begin{aligned} h_z^* * h_z &= h_{-z} * h_z \\ h_z * h_z &= h_{2z} \end{aligned} \tag{6}$$

$$I * h_{-z} = -a - a^* * h_{-2z} \tag{7}$$

$$\begin{aligned} U &= 1 - I * h_{-z} \approx \left(1 - e^{j2\pi\frac{z}{\lambda}} \cdot a^* * h_z^* - e^{-j2\pi\frac{z}{\lambda}} \cdot a * h_z\right) * h_{-z} \\ U &\approx e^{j2\pi\frac{-z}{\lambda}} - e^{j2\pi\frac{z}{\lambda}} \cdot a^* * h_z^* * h_{-z} - e^{-j2\pi\frac{z}{\lambda}} \cdot a * h_z * h_{-z} \\ U &\approx e^{j2\pi\frac{-z}{\lambda}} - e^{j2\pi\frac{z}{\lambda}} \cdot a^* * h_{-z} * h_{-z} - e^{-j2\pi\frac{z}{\lambda}} \cdot a \\ U &\approx e^{j2\pi\frac{-z}{\lambda}} \left(1 - a - e^{j2\pi\frac{2z}{\lambda}} \cdot a^* * h_{-2z}\right) \end{aligned} \tag{8}$$

From the above equation (8) we can determine the amplitude U(x,y,z) and phase φ(x,y,z).

$$U(x, y, z) = abs(U) = abs(1 - I * h_{-z}) = abs(a + e^{j2\pi\frac{z}{\lambda}}.a^{*} * h_{-2z}) \quad (9)$$

$$\varphi(\mathrm{x}, \mathrm{y}, \mathrm{z}) = \arg(U) = \arg(I * h_{-z}) \quad (10)$$

2.3.2.1 Software – Holographic reconstruction of adherent cells

The above equation contains both the complex amplitude, and the twin image. The influence of the twin image, or in other words, the spatial separation of the twin image and the real image is related to the distance between the object and the sensor. If the object is placed close to the sensor, like in our setup, the signal from the twin-image is highly similar to the signal from the real image. However, the influence of the twin image can be reduced by iterative techniques(Denis et al., 2005; Fienup, 1982). The elimination of twin-image can be performed by iterative propagation, (1), between the object plane and the sensor plane, (2) on either side of the plane of the sensor between the object plane and the plane symmetrical to the plane of the sensor. The methods necessitate an automated threshold based mask.

The first method **(Fig. 2.3.6)** consists of following steps, (1) The hologram is back-propagated by using Fresnel function (h_{-z}) to obtain the amplitude and phase of the object **(Fig. 2.3.6a)**, (2) The obtained information is filtered using a mask to enhance the contrast between the signal of interest and the twin-image **(Fig. 2.3.6b)**, which is propagated to the imaging sensor plane by using Fresnel function (h_z) **(Fig. 2.3.6c)**, along with the acquired phase information (3) This image now replaces the initially acquired amplitude signal, (4) The result is now propagated again to the object plane by h_{-z} to have a better approximation of the object, (5) the steps 3, and 4 are repeated until convergence **(Fig. 2.3.6d, e)**.

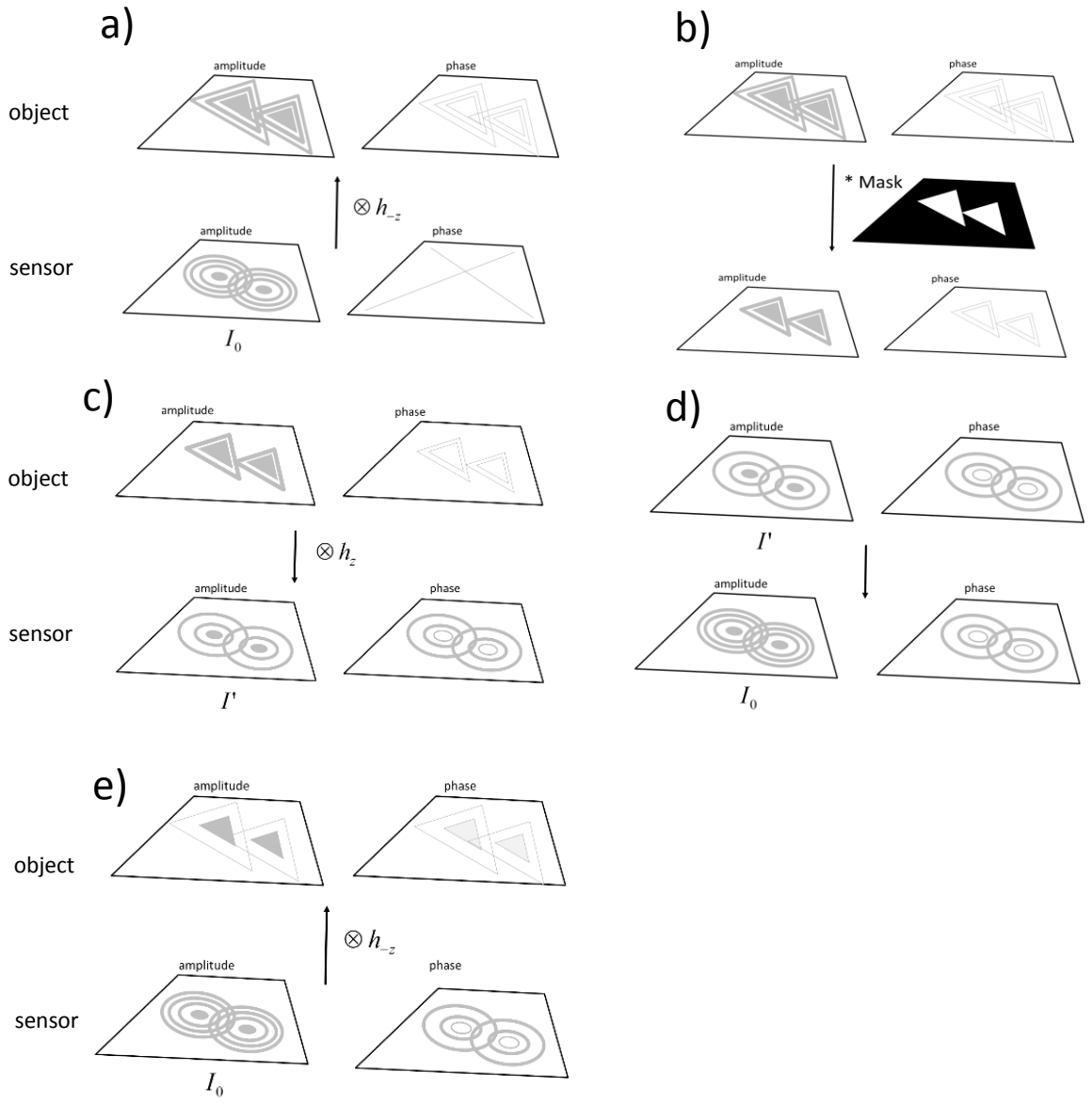

Figure 2.3.6: Schematic diagram explaining holographic reconstruction method 1.

The steps involved in second methods are as follows, (1) the acquired signal is propagated by h_{-Z} , from the imaging sensor plane to the object plane to obtain an initial approximation of the amplitude and phase of the object **(Fig. 2.3.7a)**, (2) a mask is generated **(Fig. 2.3.7b)**, and on the contrary to the first algorithm, in this case, the mask is used to enhance the contrast of the twin-image and not the signal of interest. The obtained result is propagated, h_{2Z} giving us an estimation of the object based on the relation, object = twin image * h_{2Z} **(Fig. 2.3.7c)**, (3) the obtained information is filtered

using a mask to enhance the difference in signal between the object and the twin image residue, (4) the result is propagated by h_{-2Z} to further enhance the signal, (5) the steps (2) to (4) are repeated iteratively until possible convergence **(Fig. 2.3.7d,e)**. This algorithm can be summarized in a separation of the twin image and the object on either sides of the imaging sensor plane **(Fig. 2.3.7f)**.

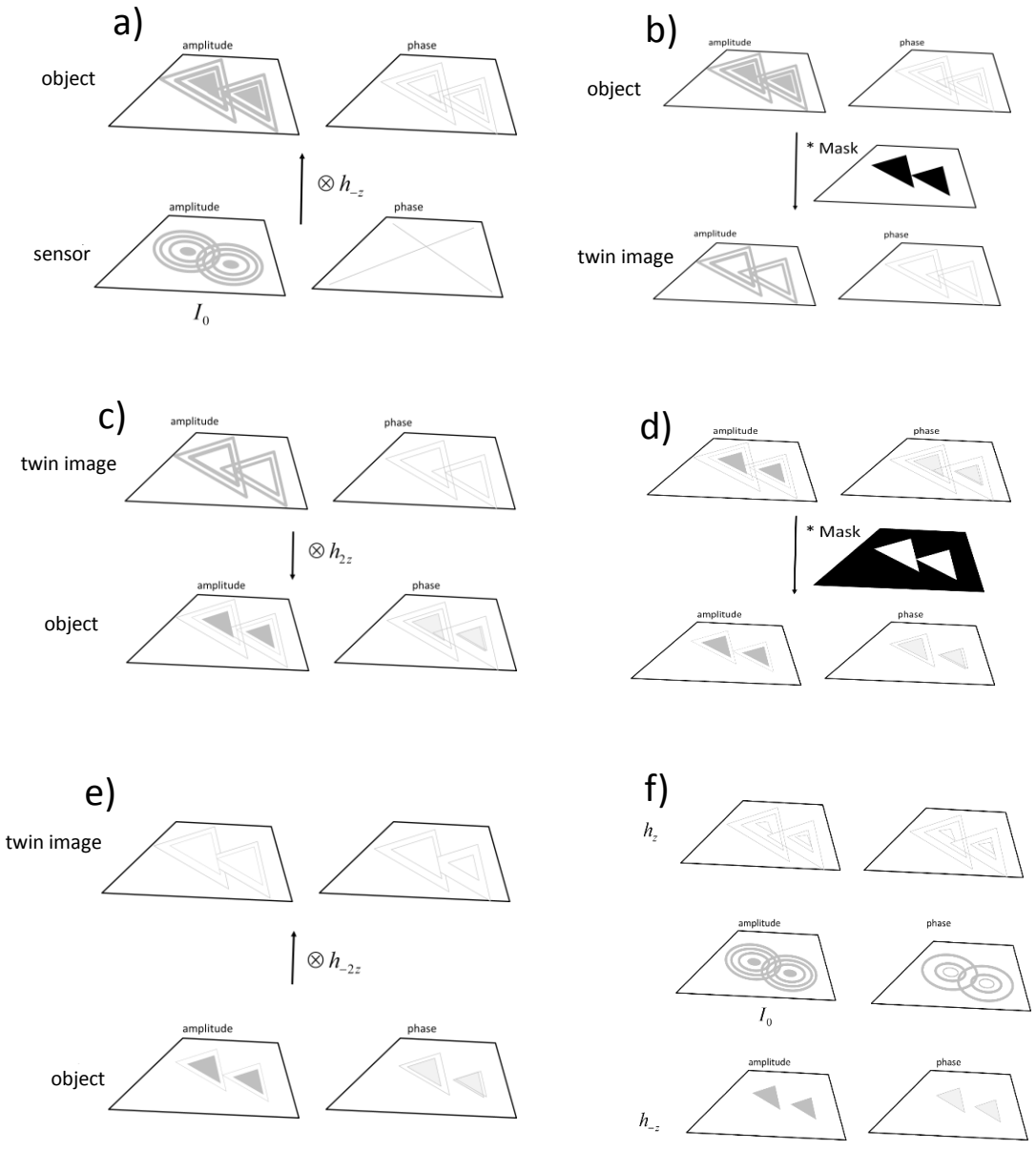

Figure 2.3.7: Schematic diagram explaining holographic reconstruction method 2.

The two reconstruction methods give us similar results **(Fig. 2.3.8)**. Initial back projection gives amplitude and phase reconstruction accompanied by the twin-image **(Fig. 2.3.8b,c)**. A mask is generated **(Fig. 2.3.8d),** to enhance the contrast of the original signal. The filtered image is propagated to the imaging sensor plane. After iterative steps (as mentioned in method 1), we obtain the final amplitude and phase images **(Fig. 2.3.8e,f)**. Edge detection of the reconstructed image is used to outline the reconstructed image for better visualization **(Fig. 2.3.8g)**. In this case, we used 15 iterations were performed. However, we find that with the reconstruction methods listed here, the selection of an appropriate mask is more important to obtain a better reconstruction. A comparison between lensfree reconstruction and lens-based microscopic image (10X) is shown in **Fig. 2.3.9**. Our Lensfree video microscopy prioritized simplicity and adherence to standard cell culture practices over resolution. As a result, resolution of our setup is limited (~5μm). However, the shape of the cell is well reconstructed and correlates well with the lens-based microscopic image **(Fig. 2.3.9, yellow arrows)**. In some cases, the pseudopodia are well reconstructed **(Fig. 2.3.9, green arrows),** however when the pseudopodia are thin (< 5μm), the information is not recovered from reconstruction **(Fig. 2.3.9, red arrows)**. In order to remove the twin-image, an automated mask is used as mentioned earlier. The signal obtained from fine pseudopodia is similar to that of the twin-image, which causes the loss of information when the image is filtered by the mask. A better reconstruction method without the use of mask might recover the weak signal arising from the fine pseudopodia, and also could eliminate the effects of cross-talk arising from closely spaced cells. This work remains a future perspective. Nonetheless, the shape of the cells is well reconstructed, and in chapters 3, 4, we demonstrate that many important measurements can be performed with the resolution of our images, without requiring sub-cellular resolution or fluorescence.

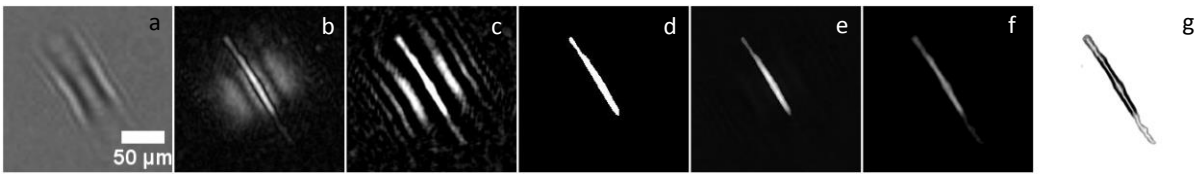

Figure 2.3.8: Holographic reconstruction. (a) raw lensfree hologram, (b,c) amplitude and phase obtained from single Fresnel back projection at Z = 700µm, (c) automated mask, (d,e) final amplitude and phase reconstruction after iterations of steps 3, 4 mentioned in method 1, (g) edge detection for better visualization.

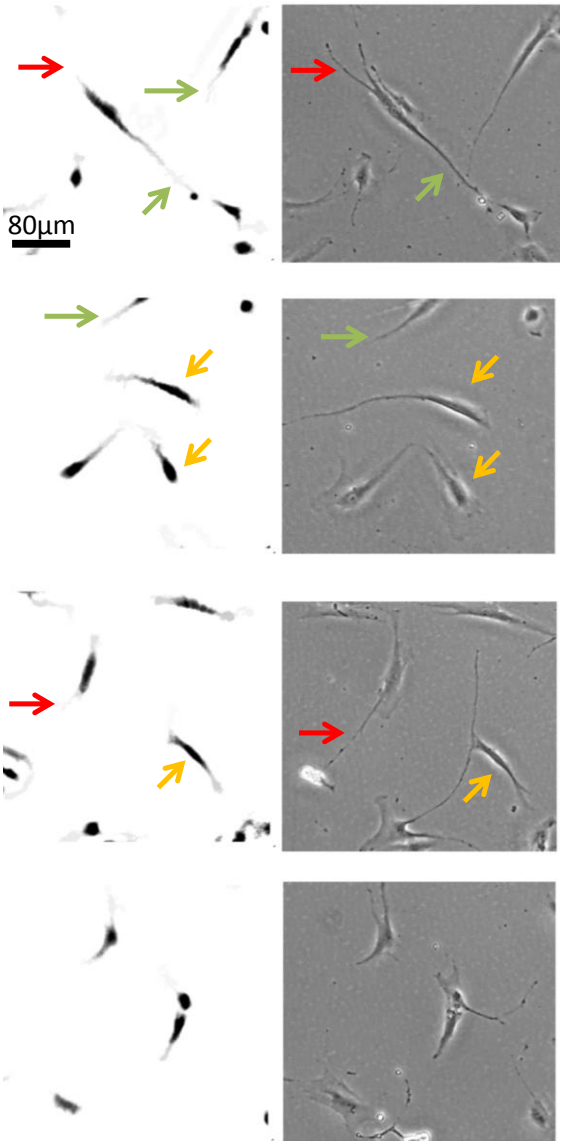

Fig. 2.3.9: Comparison of reconstructed lensfree image (left) and lens-based microscopic image (10X) (right). Yellow arrows indicate examples of cell shape that correlate well with the microscopic image. Green arrows indicate the pseudopodia that are imaged using lensfree video microscope. Red arrows show the finer details that are not imaged by lensfree video microscope. It is to be noted that in all the cases; the cell shape obtained by lensfree video microscope and lens-based microscope correlates well.

REFERENCES

Allier, C. P., Hiernard, G., Poher, V., & Dinten, J. M. (2010). Bacteria detection with thin wetting film lensless imaging. *Biomedical optics express*, *1*(3), 762–770. doi:10.1364/BOE.1.000762

Betzig, E., Patterson, G. H., Sougrat, R., Lindwasser, O. W., Olenych, S., Bonifacino, J. S., … Hess, H. F. (2006). Imaging intracellular fluorescent proteins at nanometer resolution. *Science (New York, N.Y.)*, *313*(5793), 1642–5. doi:10.1126/science.1127344

Biener, G., Greenbaum, A., Isikman, S. O., Lee, K., Tseng, D., & Ozcan, A. (2011). Combined reflection and transmission microscope for telemedicine applications in field settings. *Lab on a chip*, *11*(16), 2738–43. doi:10.1039/c1lc20169g

Coskun, A. F., Wong, J., Khodadadi, D., Nagi, R., Tey, A., & Ozcan, A. (2013). A personalized food allergen testing platform on a cellphone. *Lab on a chip*, *13*(4), 636–40. doi:10.1039/c2lc41152k

Denis, L., Fournier, C., Fournel, T., & Ducottet, C. (2005). Twin-image noise reduction by phase retrieval in in-line digital holography. (M. Papadakis, A. F. Laine, & M. A. Unser, Eds.)*Wavelets XI, SPIE's Symposium on Optical Science and Technology, San Diego : United States (2005)*, 59140J–59140J–14. doi:10.1117/12.617405

Egner, A., & Hell, S. W. (2005). Fluorescence microscopy with super-resolved optical sections. *Trends in cell biology*, *15*(4), 207–15. doi:10.1016/j.tcb.2005.02.003

Fienup, J. R. (1982). Phase retrieval algorithms : a comparison. *Applied Optics*, *21*(15).

Gabor, D. (1948). A New Microscopic Principle. *Nature*, *161*, 777–778.

Hell, S. W. (2007). Far-field optical nanoscopy. *Science (New York, N.Y.)*, *316*(5828), 1153–8. doi:10.1126/science.1137395

Hennequin, Y., Allier, C. P., McLeod, E., Mudanyali, O., Migliozzi, D., Ozcan, A., & Dinten, J.-M. (2013). Optical Detection and Sizing of Single Nanoparticles Using Continuous Wetting Films. *ACS nano*, (9), 7601–7609. doi:10.1021/nn403431y

Isikman, S. O. G. A. M. B. W. O. S. T.-W. O. A. (2012). Lensfree computational microscopy tools for cell and tissue imaging at the point-of-care and in low-resource settings. *Anal Cell Pathol(Amst).*, *35*(4), 229–247. doi:10.3233/ACP-2012-0057.Lensfree

Jin, G., Yoo, I.-H., Pack, S. P., Yang, J.-W., Ha, U.-H., Paek, S.-H., & Seo, S. (2012). Lens-free shadow image based high-throughput continuous cell monitoring technique. *Biosensors & bioelectronics*, *38*(1), 126–31. doi:10.1016/j.bios.2012.05.022

Kim, S. B., Bae, H., Cha, J. M., Moon, S. J., Dokmeci, M. R., Cropek, D. M., & Khademhosseini, A. (2011). A cell-based biosensor for real-time detection of cardiotoxicity using lensfree imaging. *Lab on a chip*, *11*(10), 1801–7. doi:10.1039/c1lc20098d

Mudanyali, O., Mcleod, E., Luo, W., Greenbaum, A., Coskun, A. F., Hennequin, Y., & Allier, C. P. (2013). Wide-field optical detection of nanoparticles using on-chip microscopy and self-assembled nanolenses, *254*(February), 2013. Retrieved from http://dx.doi.org/10.1038/nphoton.2013.49

Mudanyali, O., Oztoprak, C., Tseng, D., Erlinger, A., & Ozcan, A. (2010). Detection of waterborne parasites using field-portable and cost-effective lensfree microscopy. *Lab on a chip*, *10*(18), 2419–23. doi:10.1039/c004829a

Mudanyali, O., Tseng, D., Oh, C., Isikman, S. O., Sencan, I., Bishara, W., … Ozcan, A. (2010). Compact, light-weight and cost-effective microscope based on lensless incoherent holography for telemedicine applications. *Lab on a chip*, *10*(11), 1417–1428. doi:10.1039/c000453g

Navruz, I., Coskun, A. F., Wong, J., Mohammad, S., Tseng, D., Nagi, R., … Ozcan, A. (2013). Smart-phone based computational microscopy using multi-frame contact imaging on a fiber-optic array. *Lab on a chip*, *13*(20), 4015–23. doi:10.1039/c3lc50589h

Ozcan, A., & Demirci, U. (2008). Ultra wide-field lens-free monitoring of cells on-chip. *Lab on a chip*, *8*(1), 98–106. doi:10.1039/b713695a

Repetto, L., Piano, E., & Pontiggia, C. (2004). Lensless digital holographic microscope with light-emitting diode illumination. *Optics letters*, *29*(10), 1132–4. Retrieved from http://www.ncbi.nlm.nih.gov/pubmed/15182009

Schermelleh, L., Heintzmann, R., & Leonhardt, H. (2010). A guide to super-resolution fluorescence microscopy. *The Journal of cell biology*, *190*(2), 165–75. doi:10.1083/jcb.201002018

Sengupta, P., Van Engelenburg, S., & Lippincott-Schwartz, J. (2012). Visualizing cell structure and function with point-localization superresolution imaging. *Developmental cell*, *23*(6), 1092–102. doi:10.1016/j.devcel.2012.09.022

Seo, S., Isikman, S. O., Sencan, I., Mudanyali, O., Su, T., Bishara, W., … Ozcan, A. (2010). High-Throughput Lens-Free Blood Analysis on a Chip, *82*(11), 4621–4627. doi:10.1039/C000453G.(10)

Seo, S., Su, T.-W., Tseng, D. K., Erlinger, A., & Ozcan, A. (2009). Lensfree holographic imaging for on-chip cytometry and diagnostics. *Lab on a chip*, *9*(6), 777–87. doi:10.1039/b813943a

Su, T.-W., Erlinger, A., Tseng, D., & Ozcan, A. (2010). Compact and light-weight automated semen analysis platform using lensfree on-chip microscopy. *Analytical chemistry*, *82*(19), 8307–12. doi:10.1021/ac101845q

Su, T.-W., Seo, S., Erlinger, A., & Ozcan, A. (2009). High-throughput lensfree imaging and characterization of a heterogeneous cell solution on a chip. *Biotechnology and bioengineering*, *102*(3), 856–68. doi:10.1002/bit.22116

Weidling, J., Isikman, S. O., Greenbaum, A., Ozcan, A., & Botvinick, E. (2012). Lens-free computational imaging of capillary morphogenesis within three-dimensional substrates. *Journal of biomedical optics*, *17*(12), 126018. doi:10.1117/1.JBO.17.12.126018

Xu, W., Jericho, M. H., Meinertzhagen, I. a, & Kreuzer, H. J. (2001). Digital in-line holography for biological applications. *Proceedings of the National Academy of Sciences of the United States of America*, *98*(20), 11301–5. doi:10.1073/pnas.191361398

Zheng, G., Lee, S. A., Antebi, Y., Elowitz, M. B., & Yang, C. (2011). The ePetri dish, an on-chip cell imaging platform based on subpixel perspective sweeping microscopy (SPSM). *Proceedings of the National Academy of Sciences of the United States of America*, *108*(41), 1–6. doi:10.1073/pnas.1110681108

CHAPTER 3

CELL CULTURE MONITORING

Pg. 37	**MONITORING CELL-SUBSTRATE ADHESION AND CELL SPREADING**
Pg. 61	**MONITORING CELL DIVISION AND DETERMINATION OF CELL DIVISION ORIENTATION**
Pg. 88	**MONITORING CELL DIFFERENTIATION**
Pg. 107	**MONITORING CELL DEATH**
Pg. 127	**CELL MIGRATION AND ITS ALTERATIONS**

Collaborators

F. Navarro, CEA, Grenoble (3B, 3D, 3E)
M. Menneteau, CEA, Grenoble (3B, 3D, 3E)
F. Mittler, DSV, Biomics, CEA, Grenoble (3B)
D. Freida ,DSV, Biomics, CEA, Grenoble (3A, 3B, 3C, 3D, 3E)
E. Sulpice, DSV, Biomics, CEA, Grenoble (3D)
N. PicolletD'Hahan, DSV, Biomics, Grenoble (3E)
M. Dolega, DSV, Biomics, CEA, Grenoble (3E)
S. Gerbaud, DSV, Biomics, CEA, Grenoble (3E)
F. Kermarrec, DSV, Biomics, CEA, Grenoble (3E)
X. Gidrol, DSV, Biomics, CEA, Grenoble (3A, 3B, 3C, 3D, 3E)
B. David Watine, Imagopole, Institut Pasteur (3A, 3B)
N. Dubrulle, Imagopole, Institut Pasteur (3A, 3B)
S. Shorte, Imagopole, Institut Pasteur (3A, 3B)
P. Rocheteau, Institut Pasteur (3E)

3. CELL CULTURE MONITORING

Cell culture monitoring implies not just time-lapse cell imaging, but identifying the status of the cells during the period of monitoring. From our lensfree video microscope images, we extract information about the status of the single cells and the entire population, using specifically devised metrics. This chapter contains 5 major parts (A through E) detailing the quantification of major cell functions, which includes cell-substrate adhesion and spreading, cell division and orientation of cell division, cell differentiation, cell migration, and cell death. All these major cell functions were visualized from the perspective of lensfree video microscope, and were quantified in real-time using image reconstruction/ analysis, without utilization of any markers.

CHAPTER 3A

MONITORING CELL-SUBSTRATEADHESION AND CELL SPREADING

Pg. 38	**EXISTING CELL ADHESION ASSAYS**
Pg. 40	**DETECTION OF CELL-SUBSTRATE ADHESION**
Pg. 44	**QUANTIFICATION OF CELL SPREADING** **Kurtosis and Aspect-ratio**

3A. MONITORING CELL-SUBSTRATE ADHESION AND CELL SPREADING

3A.1 INTRODUCTION

Most of the cells are adherent to the substrate in nature, with few exceptions such as hematopoietic cells. Cell - substrate adhesion and spreading are complex processes involving various molecular actors and signaling pathways. These processes are categorized into passive and active events. Passive event is the initial contact and adhesion of a cell with the substrate followed by the active event which involves in actin polymerization and myosin contraction. The ability of a cell to attach and spread has important consequences (Cuvelier et al., 2007; McGrath, 2007). Cell-substrate adhesion is key to wound healing, tissue differentiation, etc. Study of cell - substrate adhesion and spreading is therefore inevitable to study the processes of a cell life, tumor cell adhesion, stem cell differentiation (depending on mechanical constraints) (Engler, Sen, Sweeney, & Discher, 2006), compatibility of biomaterials, etc. In spite of its importance, cell adhesion assays are either laborious or expensive.

One of the most commonly used quantification assays, to find if the cells have adhered to the substrate, is the plate-and-wash assay. The assay involves washing of non-attached cells after certain period of time followed by cell plating. The remaining adherent cells are counted manually. The main advantage of this assay is that it is simple. However, the assay is not reliable. Both washing and quantification steps performed manually induce unquantifiable bias that is subjected to the operator, accounting for extremely low repeatability. Though apparatus such as spinning disk and flow chambers are used to provide uniform shear stress for washing non-attached cells and automated counting is

used remove the bias introduced by manual counting, the assay remains labor-intensive, insensitive to cell-cell variability, and most of all, end-point. Other relatively less employed techniques involve high-cost microscopy platforms to measure the detachment force of a single cell by exerting a pulling force (Burmeister, Olivier, Reichert, & Truskey, 1998; Friedrichs, Helenius, & Muller, 2010; Hug, Prenosil, & Morbidelli, 2001; Sund & Axelrod, 2000). These measurements provide accurate information on the cell-substrate adhesion force of single cells in the order of nN. However, they require complex, delicate, high-cost experimental setup and at best the cell-substrate adhesion force of only a few single cells in a population is measured. Several assays that circumvent the limitations faced by the above-mentioned techniques are being developed of late (Asphahani et al., 2008; Connors & Heino, 2005; Friedrichs et al., 2013; Hong, Kandasamy, Marimuthu, Choi, & Kim, 2011; Huang, Cheng, Antensteiner, Lin, & Vogler, 2013; Mölder et al., 2008; Warrick, Young, Schmuck, Saupe, & Beebe, 2013). However, most of the approaches are not straight-forward and they mandate the use of one or a combination of the following: microfluidic platforms (Warrick et al., 2013) , impedance readers (Asphahani et al., 2008), microscopy (Mölder et al., 2008; Warrick et al., 2013), and cytometry (Connors & Heino, 2005).

To state if a cell has adhered to the substrate, a straight-forward approach is required that readily identifies the floating, just adhered and well-spread cells, and that can monitor cells in culture. Owing to its principle and simplicity, lensfree video microscope provides a platform to readily identify the three broad stages mentioned above.

3A.2 RESULTS

3A.2.1 Cell-substrate adhesion

The process of cell-substrate adhesion captured by means of lensfree video microscope is seen in **Fig. 3A.1**. Lensfree hologram of a floating cell is similar to airy pattern **(Fig. 3A.1a at t0).**The zero-order (center of the holographic pattern) is darker, with relatively lower gray values: less than 75 gray-levels (with the maximum value of 255 gray-levels and background of ~50 gray-levels), and several interference rings are observed. As the cell gradually adheres to the substrate, there is an increase in the gray value **(Fig 3A.1)**. In contrast to the lensfree hologram obtained from a floating cell **(t0)**, there is a 2 to 3-fold increase in the zero-order gray value as the cell adheres to the substrate **(Fig 3A.1: t0 + 10m)**: typically values greater than 200 gray-levels (considering a background value of ~50 gray-levels).

Therefore, by using gray value differentiation and pattern recognition, floating cells and adherent cells can be detected, counted, and quantified **(Fig. 3A.2, Fig. 3A.4, methods)**. The percentage of floating and adherent cells is obtained at each time point thus providing the kinetics of cell adhesion. As proof of concept, we monitored cell-substrate adhesion kinetics of hMSCs and primary human fibroblasts **(Fig. 3A.4).** In the case of hMSCs, 90% of population adhered to the substrate in 5h30m±30m (S.D. N=3 experiments). Whereas, cell substrate adhesion of primary human fibroblasts was slower, and adhesion of 90% of the population was achieved in 8h40m±40m (S.D. N=3 experiments). We observed that the adhesion kinetics of both hMSCs and primary human fibroblasts followed the same trend. That is, immediately after plating, the percentage of cell adhesion increased rapidly **(Fig. 3A.4, Region A)** until reaching a certain value (adhesion of ~60% of the population)

after which the adhesion rate became slower **(Fig. 3A.4, Region B)**. After ~95% of cell substrate adhesion, a plateau was reached **(Fig. 3A.4, Region C)**.

The change in gray value due to adhesion to the substrate is not particular to a cell type. All the adhering cells exhibit a similar change **(Fig. 3A.3)**. Also, the difference is clearly evident from the lensfree image compared to lens-based image **(Fig. 3A.3)**.

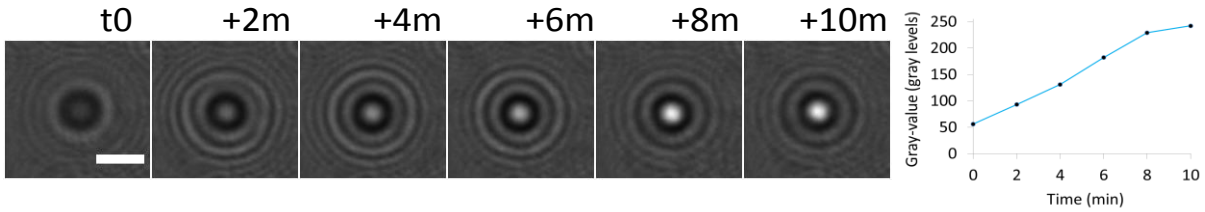

Figure 3A.1: Change in lensfree holographic pattern during cell-substrate adhesion. Time-lapse lensfree video microscope images showing cell substrate adhesion of a single primary human fibroblast. The gradual adhesion to the substrate is observed from t0+2m until t0 + 10m shown by the increase in the gray value. The image at t0 shows the floating cell. At t = t0+10m, the cell is well adhered to the substrate shown by the increase in the zero-order gray value from ~50 to ~245 gray-levels. Scale bar 50µm. Time t0 denotes the cell just before the commencement of substrate adhesion, and not to be confused with cell seeding time.

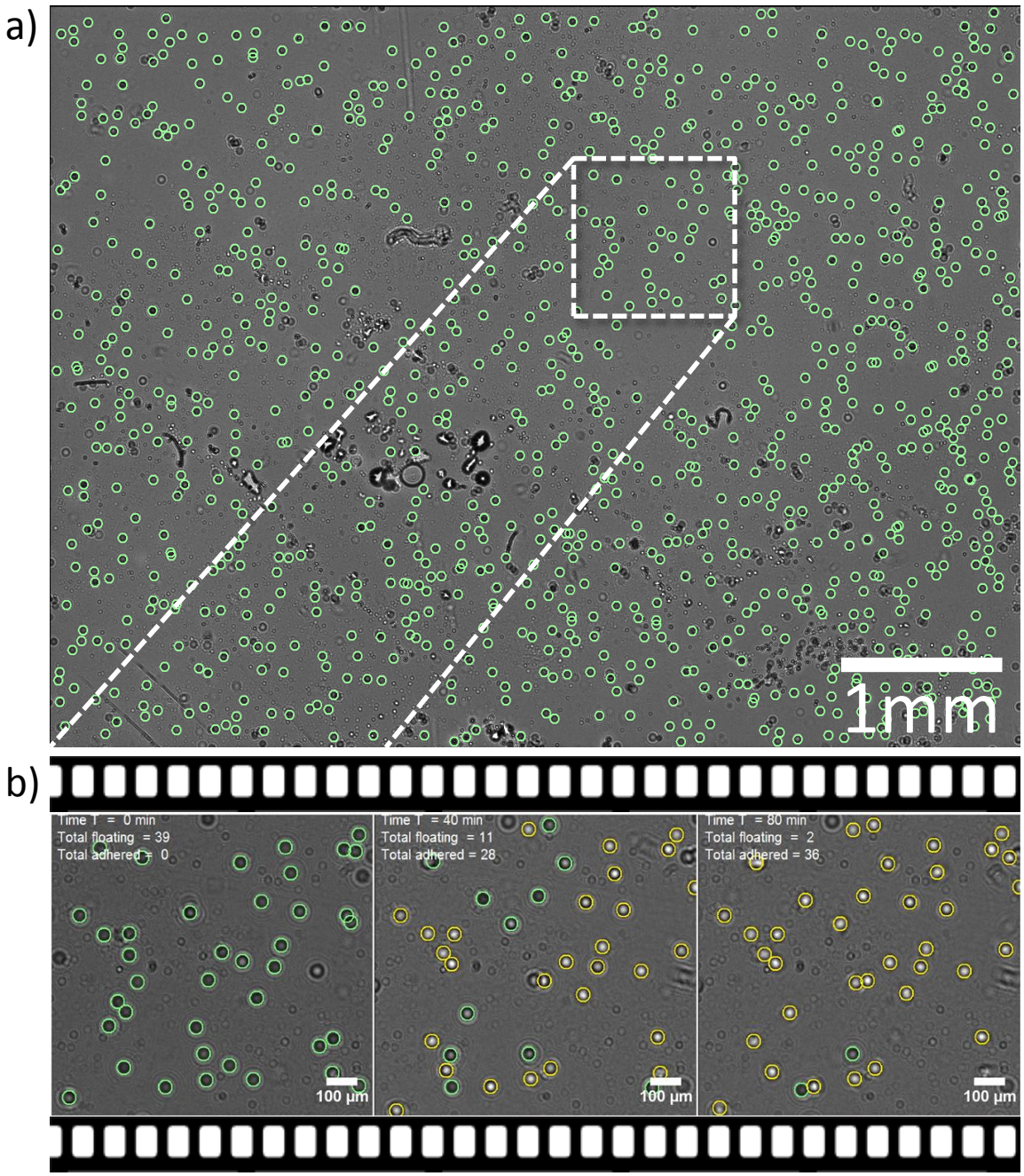

Figure: 3A.2: Discrimination of floating and adhering cells

(a) Full FOV image, obtained immediately after cell plating, shows the pattern recognition of floating cells (recognized patterns encircled in green).

(b) Time lapse lensfree video microscope images, of the region of interest, showing cell substrate adhesion, over time, of kidney cells from Cercopithecus aethiops. Floating cells and adherent cells are detected based on pattern recognition, and gray value differentiation respectively. Note that initially at t = t0 min, all the cells were floating and almost all the cells adhered to the substrate within 1 hour. Floating cells are encircled in green, and the adhered cells are encircled in yellow. Note that the images represent only a chosen region of interest and not the entire field of view of lensfree video microscope.

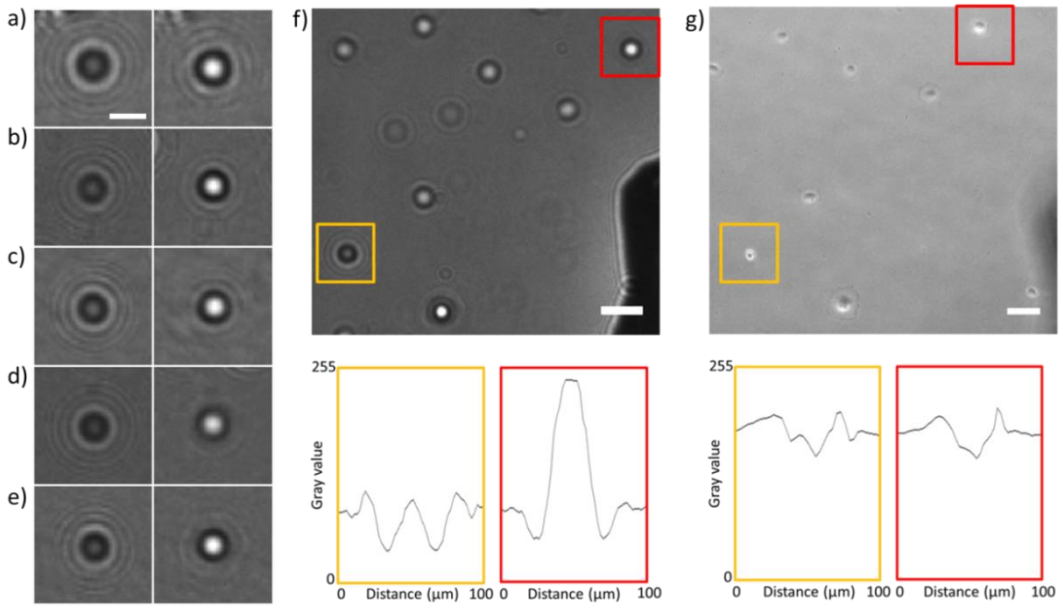

Figure 3A.3: Floating and adherent cells imaged by lensfree and lens-based microscopes.

(a,b,c,d,e) shows the applicability of the approach to different cell types. (a,b,c,d,e: U87, U20S, human Mesenchymal Stem Cells, MCF10A, RPE1 respectively). Scale bar 50µm.

(f,g) shows the same region of interest of cell population of hMSCs observed using lensfree video microscope and lens-based microscope. The yellow and red boxed regions and corresponding gray value profiles shows that the difference in gray value of floating and adhered cells is more prominent in lensfree video microscopic image compared to that of a lens-based microscope. Scale bar 100 µm.

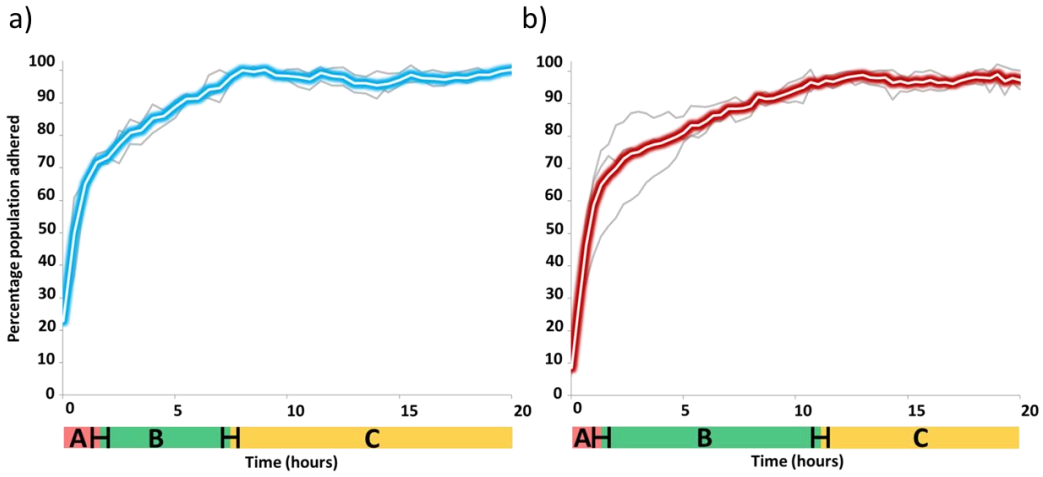

Figure 3A.4: Cell-substrate adhesion kinetics of hMSCs and Primary human fibroblasts.

(a), (b) Cell substrate adhesion kinetics of hMSCs and primary human fibroblasts respectively (N = 3 experiments). In the case of hMSCs, 90% of population adhered to the substrate in 5h30m ± 30m (S.D., N=3 experiments). Whereas, cell substrate adhesion of

primary human fibroblasts was slower, and 90% adhesion was achieved after 8h40m ±40m (S.D., N=3 experiments). Region A denotes rapid adhesion immediately after plating. Region B denotes the decrease in the adhesion rate after ~ 60% of the population adhered to the substrate, while region C shows the plateau after nearly 95% of the cells adhered to the substrate. The error bars in the regions are from standard deviation of cell-substrate adhesion percentage determined from every frame of 3 independent experiments (in both cases) of cell populations containing ~2000 cells.

3A.2.2 Cell spreading

Following the 'passive event' of initial adhesion with the substrate, the cells proceeded to the 'active event' of spreading. By using appropriate metrics to extract information from both raw **(Fig. 3A.5a)** and reconstructed **(Fig. 3A.5b)** images, in addition to merely distinguishing floating and adherent cells, we monitored the kinetics of the entire process of cell adhesion and spreading. The metrics that we propose are kurtosis from the raw image and aspect-ratio obtained after holographic reconstruction of the raw lensfree holograms.

Though during the initial cell-substrate contact, the intensity change in the raw image is predominant **(Fig. 3A.5a t = t0+1h00m)**, the change becomes subtle during the process of cell spreading **(Fig. 3A.5a t0+1h30m until t0+4h).** However, variation can be measured by computing kurtosis of the lensfree hologram obtained from the cells **(methods)**. Kurtosis is a way to determine whether the gray value distribution of an image is almost peaked or flat. First, we plotted the changes in kurtosis, with respect to time, obtained from 10 adhering primary human fibroblasts. From Fig. **3A.5c,** it can be observed that, typically the kurtosis of a floating cell is between 4 a.u. and 8 a.u. describing a rather flat gray value distribution. The distribution is peaked, due to the sharp change in the zero-order gray value during the initial attachment of the cell to the substrate: 3-6 fold increase in kurtosis is seen, with values going up to 40 a.u. As the cell spreads, the

zero-order gray value decreases resulting in a flat distribution. Kurtosis descends gradually attaining a value of 10 ± 3 a.u. (S.D., n = 10 cells) and remains stable.

By determining the rise time and decay time of mean kurtosis **(Fig. 3A.5c blue)**, we systematically characterized the kinetics of cell adhesion and spreading. Rise time is defined as the time taken for a response to rise from 10% to 90% of the final value. In other words, rise time corresponds to the increase in kurtosis resulting from cell substrate adhesion **(Fig. 3A.5c, region A)**. Decay time is defined as the time taken for a response to fall from 90% to 10% of the final value. Therefore, decay time corresponds to the time taken for the cells to spread **(Fig. 3A.5c, region B)**. Here, the rise time was 40 minutes **(Fig. 3A.5c, region A, t = 0h00m to t = 0h40m)** and the decay time of 6 hours commenced at t = 2h20m and lasted until t = 8h20m **(Fig. 3A.5c, region B)**. This shows that, on an average (n = 10 cells), the time taken for the cells to adhere to the surface was 40 minutes and to spread was 6 hours.

We extended this measurement to the entire population and compared the cell spreading time of hMSCs and primary human fibroblasts **(Methods)**. This resulted in scatter plots **(Fig. 3A.5e,g)**, in each case containing more than 100,000 measurements obtained from nearly 5,000 cells (N = 3 experiments) followed over a period of 20 hours. We calculated the rise time and decay time for the mean curves of the scatter plots **(white dotted line, Fig. 3A.5e,g)**, to obtain initial cell adhesion time and cell spreading time respectively.

Initial adhesion time was similar for both hMSCs and primary human fibroblasts with values of 1h00m ± 20m (S.D., N = 3 experiments) and 1h00m ± 30m (S.D., N = 3 experiments) respectively **(Fig. 3A.5 e, g : region A)**. For hMSCs, cell spreading started at t = 2h00m ± 30m (S.D., N = 3 experiments) and lasted until 11h00m ± 30m (S.D., N = 3

experiments) **(Fig. 3A.5e: region B)**. For primary human fibroblasts, cell spreading started at t = 1h20m ± 20m (S.D., N = 3 experiments) and lasted until 8h20m ± 40m (S.D., N = 3 experiments) **(Fig. 3A.5g: region B).**

The second method consists in calculating the aspect-ratio of the cells from the reconstructed image **(Fig. 3A.5b)**. Aspect-ratio is the ratio of the minor axis length to the major axis length of the ellipse which best fits the shape of the cell segmented from the reconstructed image **(Methods)**. The aspect-ratio takes a value between 0.0 a.u. and 1.0 a.u, with 1.0 being perfectly circular and< 0.1 being highly elongated. When a cell first contacts the surface, it is circular in shape with an aspect-ratio between 0.9 a.u and 1.0 a.u. As the cell spreads to adopt a more elliptical shape, the aspect-ratio decreases.

The time dependent change in the aspect-ratio of single spreading cells (n = 10 single cells) is shown in **Fig. 3A.5d**. The aspect-ratio was calculated only after the cells adhered to the substrate. Consequently, the absence of the initial values **(Fig. 3A.5d, t=0h00m and t=0h20m)** indicates that the cells were afloat. The decay time of the mean **(Fig. 3A.5d, blue)** corresponds to average cell spreading time of 10 single cells. The decay time obtained is 6h20m starting from t = 1h00m, until t = 7h20m.

Further, we measured the aspect-ratio for the entire population of hMSCs and primary human fibroblasts **(Fig. 3A.5f, h)**. The aspect-ratio measurement was performed after nearly 50% cells adhered to the substrate (in our experiments, t = 0h40m for primary human fibroblasts and t = 0h30m for hMSCs). Due to substantial diversity of the population, the mean aspect-ratio only reached a maximum of ~0.8 a.u. (instead of a value > 0.9 a.u.) even during the initial stages of adhesion. Although, from the scatter plots **(Fig. 3A.5f,h)** it can be observed that more than 50% of the population had an aspect-ratio

value greater than 0.8 a.u. at the beginning. HMSCs started to spread at 1h30m ± 30m (S.D., N = 3 experiments) and were almost completely spread by 13h00m ± 1h (S.D., N = 3 experiments) denoted by a stable aspect-ratio value of 0.3 – 0.2 a.u. **(Fig.3A.5f: Region B).** In the case of primary human fibroblasts, cell spreading started at t = 1h40m ± 20m (S.D., N = 3 experiments) and lasted until 10h40m ± 1h (S.D., N = 3 experiments) **(Fig.3A.5h: Region B)**.

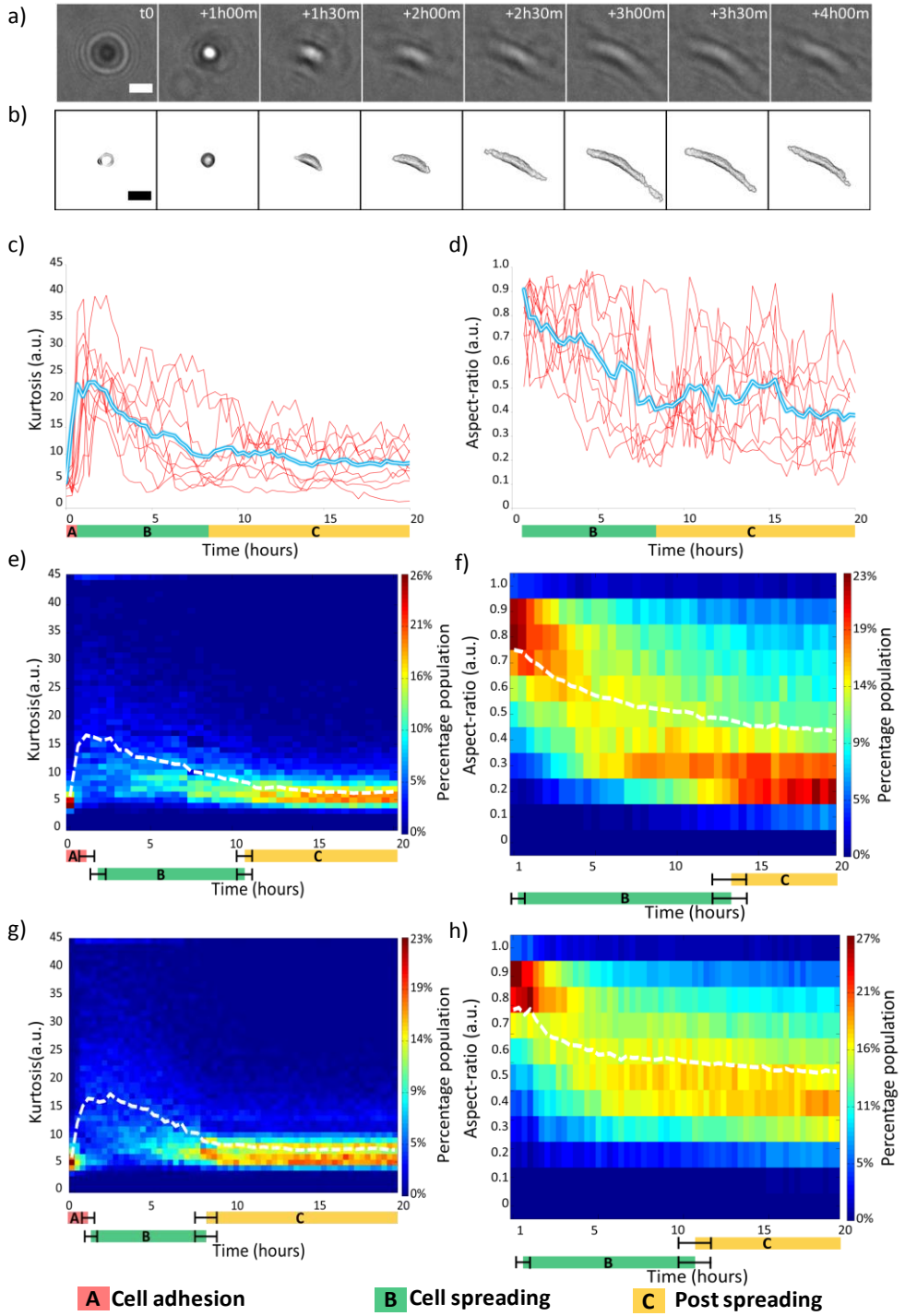

Figure 3A.5: Quantification of cell-substrate adhesion and spreading.

(a) Time lapse images of raw lensfree holograms of adhering primary human fibroblast cell. Scale bar 50µm.

(b) Lensfree holographic reconstruction and segmentation of (a). Scale bar 50µm. Note that at t0, since the cell was afloat, the distance between the cell and the imaging sensor was larger compared to the subsequent frames. However, this difference was not considered while performing holographic reconstruction.

(c) Kurtosis measurement of 10 cells along with the mean (blue). Rise time of the mean corresponds to the average time taken for the cells to adhere to the substrate (region A) and the decay time corresponds to the average time taken for the cells to spread (region B). Region C denotes stable kurtosis values post cell spreading.

(d) Aspect-ratio measurement of 10 cells along with the mean (blue). The absence of values at t = 0h00m and t = 0h20m denotes that the cells were afloat. The decay time corresponds to the average time taken for cell spreading (Region B)

(e,g) Scatter plots containing ~100,000 kurtosis values of n ~ 5000 primary human fibroblasts and hMSCs from N = 3 experiments, respectively. The mean is plotted in white dotted line. Region A denotes the initial adhesion of cells to the substrate, region B denotes time taken for the cells to spread, and region C shows the stability of the kurtosis values post cell spreading.

(f,h) Scatter plots of ~100,000 aspect-ratio values obtained from primary human fibroblasts and hMSCs over N = 3 experiments respectively, along with the mean (in white dotted line). Region B shows the time taken for cell spreading.

In figure e,f,g,h, error margin in regions A, B, and C, is the standard deviation resulting from N = 3 experiments, i.e., the variation in the time taken for the cells to adhere and spread depending on the experiment, calculated by respective methods.

3A.3 DISCUSSION

Friedrichs et al. reviewed the commonly used techniques to study cell-substrate adhesion (**Table 3A.6**, (Friedrichs et al., 2013)). None of the existing methods offer the advantage of performing real-time observation and monitoring the same cell population over extended time period, to obtain information on both cell-substrate adhesion and cell spreading. Also, almost all the methods require careful prior calibration based on cell type, substrate, etc.

The metrics we established to measure cell adhesion and spreading are kurtosis and aspect-ratio. To our knowledge, label-free, real-time, high-throughput, and direct method that can quantify both cell adhesion and cell spreading has not been reported before. Especially, our method does not require personnel intervention and is capable of visualizing both single cells and large population. The cell-cell variability is well preserved

and respected using lensfree video microscope **(Fig. 3A.7)**. Though both the metrics provided similar results, one might be more sensitive compared to the other depending on the cell type, cell density, etc. In the case of extremely high cell density (3×10^5 cells per 35mm culture dish or more), interference of neighboring cells may decrease the accuracy of kurtosis measurements whereas, the aspect-ratio measurement will remain unbiased. The aspect-ratio measurement depends on the accuracy of lensfree holographic reconstruction and segmentation. As a result, the aspect-ratio measurement is noisy compared to kurtosis measurement. By enhancing the quality of holographic reconstruction, and also by integrating cell tracking, this noise could be reduced. As proof of concept, we compared cell-substrate adhesion and spreading of hMSCs and primary human fibroblasts. Though there was not a significant difference, it ensures that our platform and metrics can be used in a similar way to compare several substrates, cell types, effect of drugs, etc. As an example, we conducted a brief study to show the age-dependent difference in cell-substrate adhesion **(Fig. 3A.8)**. We compared cells obtained from 20-29 year old, and 60-69 year old healthy female donors. We observed that, for the same seeding density of ~20,000 cells, the cell-substrate adhesion of cells obtained from 20-29 year old donors was faster than that of 60-69 year old donors. In the case of 20-29 year old donors, 90% of the population adhered to the substrate in less than 6 hours. Whereas, in the case of 60-69 year old, a period of nearly 16 hours was required post seeding for 90% of the population to adhere to the substrate.

Our method can efficiently differentiate floating, adhered and spread cells. However, with the current setup, it is not possible to measure the force exerted by the cells on the substrate. Nevertheless, the compatibility of any substrate (for cell adhesion and spreading) can be easily tested with our method depending on the affinity that the cells

exhibit towards the substrate by adhering and spreading on the substrate. This will be the subject of a case study discussed in chapter 4.1: Temperature mediated cell detachment. Also, our method can provide preliminary information about the status of adhesion along with location of the cells down to single cell level, which might be useful for further adhesion strength measurement using AFM related techniques.

Assay	Type of force application	Read-out	Pro/Contra
Plate-and-wash assay	Uneven/unknown shear force	Ratio of attached/non-attached cells	+ Economic + Simple – Low reproducibility – No quantitative data – Relative measure of initial adhesion only
Spinning –disc assay	Shear forces (linear force gradient)	Disc radius at which 50% of the cells remain attached (shear forces estimated)	+ High reproducibility + High throughput + Wide applicable force range – No exact force quantification – Shear forces cell-shape dependent – Not commerciably available
Flow chamber	Shear force (laminar flow)	Ratio of attached / non-attached cells Analysis of rolling cells (binding frequency, arrest time)	+ Simple setup + Commercially available + Widely applicable force range – No exact force quantification – Shear forces cell shape dependent
Centrifugation assay	Shear force (centrifugal force)	Ratio of post-spin to pre-spin cells	+ High reproducibility + High throughput + Wide applicable force range – Shear forces cell shape dependent – Multiple runs at different speeds required – Not commecially available
Step pressure technique	Pulling force(suction)	Cell detachment at certain suction pressure	– Restricted to high forces – Low force resolution – Cell shape changes during aspiration
Biomembrane force-probe	Pulling force	Detachment force (0.1 pN–1 nN)	+ High force resolution + Good temporal control – Cell shape changes during aspiration
Optical tweezers	Pulling force	Detachment force (0.1–200 pN)	+ High force resolution – Complex experimental setup – Restricted to low detachment forces
AFM–SCFS	Pulling force	Cell detachment force (10 pN–100 nN)	+ High force resolution + Large range of applicable forces + Good control of contact conditions + Commercially available – Time and cost intensive

Table 3A.6: Overview of different cell-substrate adhesion assays. Table illustrating the most commonly used techniques to study cell-substrate adhesion reproduced from Friedrichs et al. (Friedrichs et al., 2013) (Permission in Annex)

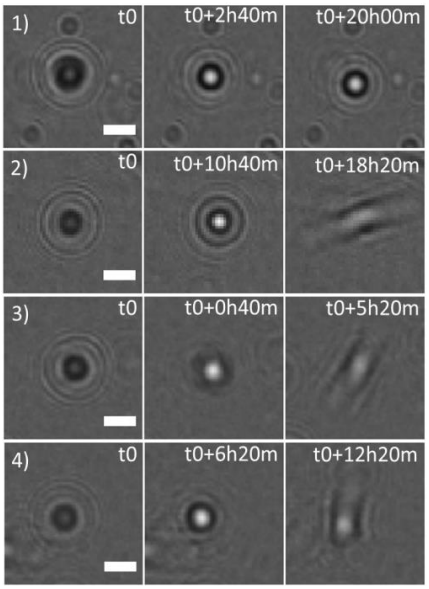

Figure 3A.7: Cell-cell variability in cell-substrate adhesion and spreading. Time-lapse images of 4 random hMSCs from the same population show cell-cell variability in time taken for the cells to adhere to the substrate and spread. In each case t0 is the same and it denotes the time of cell plating. Note that cell 1 did not spread on the substrate even after 20h post plating, while cell 3 spread within t0+5h20m. Scale bar 50 μm.

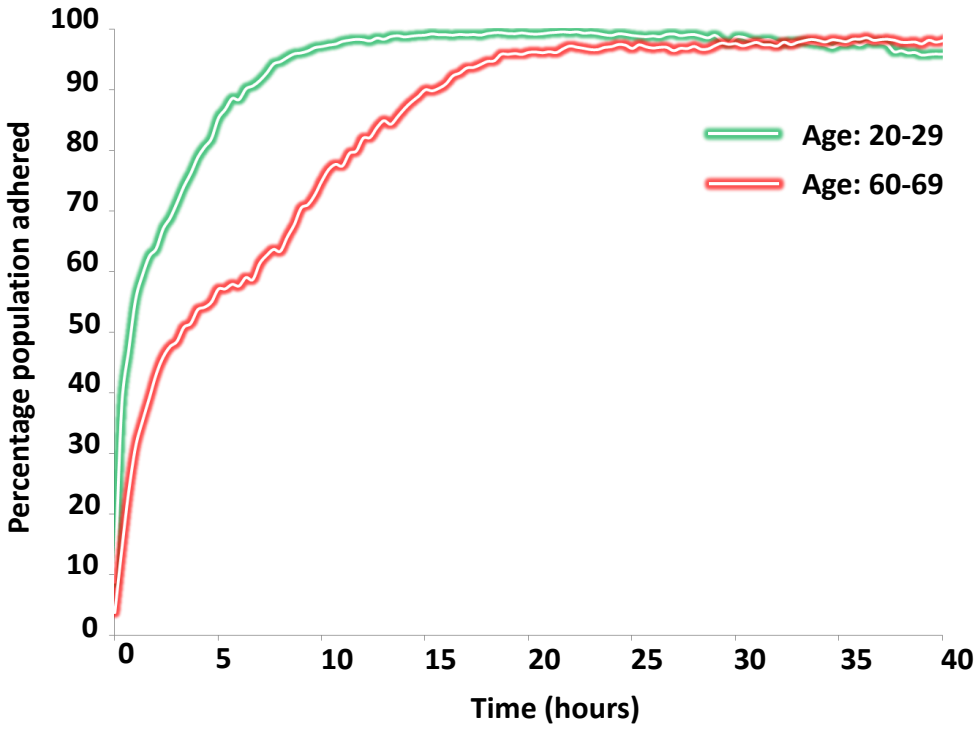

Figure 3A.8: Age-dependent cell-substrate adhesion kinetics. Cell substrate adhesion of cells obtained from 20-29 year old and 60-69 year old female healthy donors. For 90% of the population to adhere to the substrate, a difference of nearly 10 hours is observed between 2 cell populations (data from single experiment, n~2000 cells).

3A.4 METHODS

3A.4.1 Computational methods

3A.4.1.1 Pattern recognition of floating cells

A typical pattern of a floating cell is chosen to act as a template and is matched against the full field of view raw image **(Fig. 3A.9)**. Pattern recognition was performed using normalized cross-correlation function available in Matlab. Signal processing uses cross-correlation for feature detection between 2 signals. If cross-correlation is applied for template matching of images, the cross-correlation coefficients would be,

$$c(u,v) = \sum_{x,y} f(x,y)t(x-u,y-v) \tag{1}$$

However, in equation (1),the probable variation in intensity between the template and the image is not taken in to account. Therefore in image processing, normalized cross-correlation is used, where the template and the images are normalized by subtracting the mean and dividing by standard deviation. This leads to the normalized cross-correlation coefficients,

$$c(u,v) = \frac{\sum_{x,y}\left[f(x,y) - \overline{f}u,v\right]\left[t(x-u,y-v) - \bar{t}\right]}{\left\{\sum_{x,y}\left[f(x,y) - \overline{f}u,v\right]^2 \sum_{x,y}\left[t(x-u,y-v) - \bar{t}\right]^2\right\}^{0.5}} \tag{2}$$

Where, f(x,y) is the image and t(u,v) is the template (Lewis, 1995).

The resulting matrix has normalized cross-correlation coefficients between -1 and +1. Those values that are below a certain threshold are eliminated, considering being

irrelevant. Note: The threshold used for our analysis is 0.55 (lowest and the highest being -1 and +1 respectively).

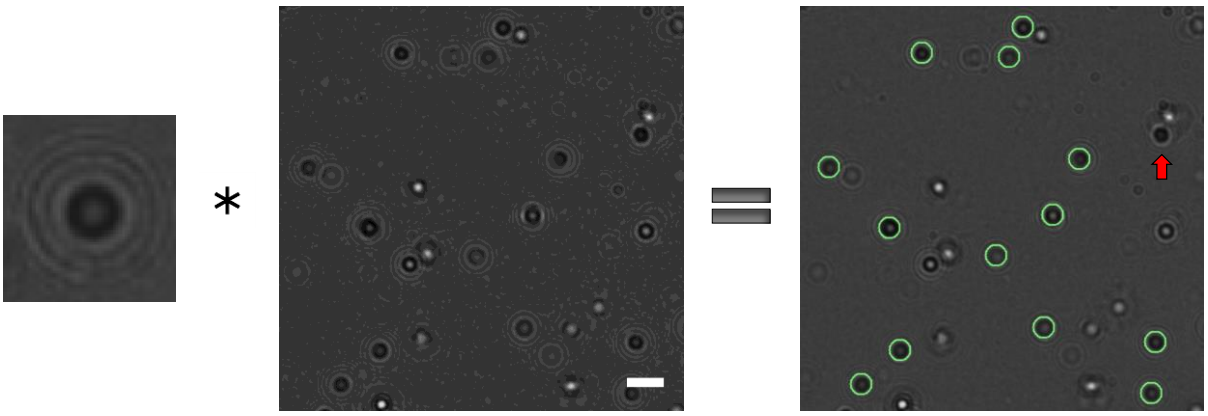

Figure 3A.9: Pattern recognition of floating cells. A typical pattern is chosen to act as the template (far left) which is matched against the raw image (centre) to find corresponding hits (far right). It can be observed that all the floating cells are well detected except for one denoted by red arrow. Scale bar 100µm.

3A.4.1.2 Detection of adherent cells

The increased average gray value of adherent cells is taken advantage of, in order to differentiate the floating and the adherent cells. The acquired raw (full field of view) image has pixel intensity values ranging from 0 to 255 gray-levels. Those pixels that have a value above a certain threshold (30% more than the mean background gray value) are assigned a value of 1, and those below are assigned a value of 0. Then by using area, solidity and eccentricity the small debris and noise due to edge diffraction are removed **(Fig. 3A.10)**. Eccentricity is the ratio of the distance between the foci of the ellipse and its major axis length. The value is between 0 and 1. (0 and 1 are degenerate cases; an ellipse whose eccentricity is 0 is actually a circle, while an ellipse whose eccentricity is 1 is a line segment). Solidity is computed as Area/ConvexArea (primarily used to remove the edge diffraction from floating objects).

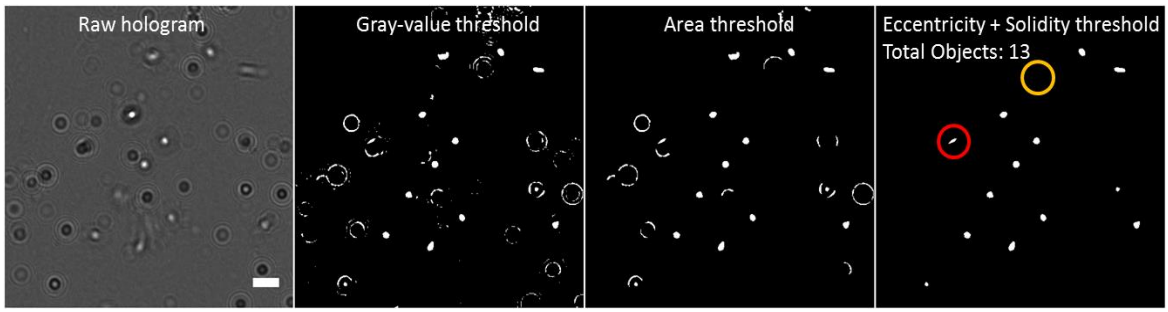

Figure 3A.10: Gray-level detection of adherent cells. Based on gray value differentiation, objects that are above 30% of the background gray value are detected, from the raw image. Smaller debris are removed by applying appropriate threshold on the area of the object. By applying threshold on eccentricity and solidity, noise from edge diffraction is removed. The remaining objects are considered to be adhered cells. In this case, one floating cell is wrongly identified as adhered (red circle) and one cell is left undetected (yellow circle). Scale bar: 100um.

We calculated the F1 measure in order to validate the automated detection of both floating and adherent cells. F1 measure is defined as the harmonic mean of Precision and Sensitivity. Precision or positive predictive value is defined as TP/(TP + FP), while recall or sensitivity is defined as TP/(TP + FN), where TP, FP, and FN are True Positives, False Positives, and False Negatives respectively. The F1 measure obtained is close to 0.95 based on 1352 cells from 10 random images from different experiments and cell types. The positive predictive value is more than 0.95 indicating that more than 95% of the detected objects correspond to cells **(Table 3A.11)**. F1 measure was particularly used since the true negatives cannot be determined in this case.

Total no. of cells (Manual count)	Automated count	True Positives (TP)	False Positives (FP)	False Negatives (FN)	Precision (P) [TP/(TP+FP)]	Recall (R) [TP/(TP+FN)]	F1 Measure [2PR/(P+R)]
1352	1353	1299	54	82	0.96	0.94	0.95

Table 3A.11: Validation of automated cell count. For the validation of automated cell count, 10 random images, of size 1050µm * 1050µm from different independent experiments and different cell types, were considered. Automated cell count was compared against manual cell count.

3A.4.1.3 Kurtosis

Kurtosis value indicates whether the gray-value distribution of an image is peaked or broad. Region of interest measuring 165 µm * 165 µm is segmented (from the raw image) surrounding the centroid of the detected cells. Kurtosis of the region of interest is computed using the Matlab function 'kurtosis'. For each ROI, kurtosis is computed on the gray values of the pixels present in the ROI.

3A.4.1.4 Measurement of aspect-ratio

Adherent cells are segmented from the reconstructed image by applying appropriate threshold on the higher gray-levels in accordance with their characteristic patterns. Then artifacts and debris, e.g. too small or too big objects, are removed from the obtained binary image with a threshold based on the mean size of the objects present. Aspect-ratio, which is calculated on the segmented cells, is the ratio of the minor axis length to the major axis length of the ellipse which best fits the shape of the segmented cells.

3A.4.2 Cell culture methods

Healthy donors' bone marrow (BM) samples were obtained from filters used during BM processing for allogeneic transplantation. Bone marrow samples were harvested from washed filters used during BM graft processing for allogeneic transplantation after healthy donor informed consent according to approved institutional guidelines

(Assistance Publique – Hôpitaux de Paris, Paris, France). HMSCs were isolated and expanded as previously described (Arnulf et al., 2007). Briefly, the hMSCs were cultured at the initial density of $5x10^4$ cells/cm2 in Minimum Essential Medium-α (Invitrogen) supplemented with 10% Fetal Calf Serum (PAA), Glutamax-I (2mM; Invitrogen), basic fibroblast growth factor (1ng/mL; R&D Systems) antibiotic/antimycotic (1%, Invitrogen). After 24-48 hours, non-adherent cells were removed and medium was changed. Adherent cells were then trypsinized, harvested, and cultured by seeding $5x10^3$ cells/cm^2. Cultures were fed every 2 to 3 days and trypsinized every 5 days. In all experiments, hMSCs were used at passage 3 to 7.

Primary cultures of human fibroblasts were prepared from skin biopsies performed on healthy donors. The cells were established in DME-Glutamax (Invitrogen) supplemented with 20% Fetal Calf Serum and used at passage 2 using standard operating procedures.

To monitor cell adhesion, ~ 20000 cells were added to a standard 35mm culture dishes and the culture dishes were immediately positioned on lens free video microscopes inside a standard incubator.

REFERENCES

Arnulf, B., Lecourt, S., Soulier, J., Ternaux, B., Lacassagne, M.-N., Crinquette, a, … Larghero, J. (2007). Phenotypic and functional characterization of bone marrow mesenchymal stem cells derived from patients with multiple myeloma. *Leukemia*, *21*(1), 158–63. doi:10.1038/sj.leu.2404466

Asphahani, F., Thein, M., Veiseh, O., Edmondson, D., Kosai, R., Veiseh, M., … Zhang, M. (2008). Influence of cell adhesion and spreading on impedance characteristics of cell-based sensors. *Biosensors & bioelectronics*, *23*(8), 1307–13. doi:10.1016/j.bios.2007.11.021

Burmeister, J. S., Olivier, L. a, Reichert, W. M., & Truskey, G. a. (1998). Application of total internal reflection fluorescence microscopy to study cell adhesion to biomaterials. *Biomaterials*, *19*(4-5), 307–25. Retrieved from http://www.ncbi.nlm.nih.gov/pubmed/9677147

Connors, W. L., & Heino, J. (2005). A duplexed microsphere-based cellular adhesion assay. *Analytical biochemistry*, *337*(2), 246–55. doi:10.1016/j.ab.2004.10.044

Cuvelier, D., Théry, M., Chu, Y.-S., Dufour, S., Thiéry, J.-P., Bornens, M., … Mahadevan, L. (2007). The universal dynamics of cell spreading. *Current biology : CB*, *17*(8), 694–9. doi:10.1016/j.cub.2007.02.058

Engler, A. J., Sen, S., Sweeney, H. L., & Discher, D. E. (2006). Matrix elasticity directs stem cell lineage specification. *Cell*, *126*(4), 677–89. doi:10.1016/j.cell.2006.06.044

Friedrichs, J., Helenius, J., & Muller, D. J. (2010). Quantifying cellular adhesion to extracellular matrix components by single-cell force spectroscopy. *Nature protocols*, *5*(7), 1353–61. doi:10.1038/nprot.2010.89

Friedrichs, J., Legate, K. R., Schubert, R., Bharadwaj, M., Werner, C., Müller, D. J., & Benoit, M. (2013). A practical guide to quantify cell adhesion using single-cell force spectroscopy. *Methods (San Diego, Calif.)*, *60*(2), 169–78. doi:10.1016/j.ymeth.2013.01.006

Hong, J., Kandasamy, K., Marimuthu, M., Choi, C. S., & Kim, S. (2011). Electrical cell-substrate impedance sensing as a non-invasive tool for cancer cell study. *The Analyst*, *136*(2), 237–245. doi:10.1039/c0an00560f

Huang, Q., Cheng, A., Antensteiner, M., Lin, C., & Vogler, E. a. (2013). Mammalian cell-adhesion kinetics measured by suspension depletion. *Biomaterials*, *34*(2), 434–41. doi:10.1016/j.biomaterials.2012.09.073

Hug, T. S., Prenosil, J. E., & Morbidelli, M. (2001). Optical waveguide lightmode spectroscopy as a new method to study adhesion of anchorage-dependent cells as an indicator of metabolic state. *Biosensors & bioelectronics*, *16*(9-12), 865–74. Retrieved from http://www.ncbi.nlm.nih.gov/pubmed/11679265

Lewis, J. P. (1995). Fast Normalized Cross-Correlation Template Matching by Cross-Correlation. *Industrial Light and Magic*, 1–11.

McGrath, J. L. (2007). Cell spreading: the power to simplify. *Current biology : CB*, *17*(10), R357–8. doi:10.1016/j.cub.2007.03.057

Mölder, a, Sebesta, M., Gustafsson, M., Gisselson, L., Wingren, a G., & Alm, K. (2008). Non-invasive, label-free cell counting and quantitative analysis of adherent cells using digital holography. *Journal of microscopy*, *232*(2), 240–7. doi:10.1111/j.1365-2818.2008.02095.x

Sund, S. E., & Axelrod, D. (2000). Actin dynamics at the living cell submembrane imaged by total internal reflection fluorescence photobleaching. *Biophysical journal*, *79*(3), 1655–69. doi:10.1016/S0006-3495(00)76415-0

Warrick, J. W., Young, E. W. K., Schmuck, E. G., Saupe, K. W., & Beebe, D. J. (2013). High-content adhesion assay to address limited cell samples. *Integrative biology : quantitative biosciences from nano to macro*, *5*(4), 720–7. doi:10.1039/c3ib20224k

CHAPTER 3B

MONITORING CELL DIVISION AND DETERMINATION OF CELL DIVISION ORIENTATION

Pg. 61	**EXISTING CELL PROLIFERATION ASSAYS**
Pg. 63	**MITOTIC CELL ROUNDING AND PATTERN RECOGNITION OF DIVIDING CELLS**
Pg. 67	**COMPARISON TO EdU PROLIFERATION ASSAY**
Pg. 71	**CELL PROLIFERATION KINETICS** **Effects of ActinomycinD**
Pg. 74	**CELL DIVISION ORIENTATION** **Long-axis rule**

3B. MONITORING CELL DIVISION AND DETERMINATION OF CELL DIVISION ORIENTATION

3B. 1 INTRODUCTION

Cell division is one of the main events determining cell fate. Cell proliferation rate can reveal important information on perturbation of the cell cycle, and is used routinely in a variety of biomedical research areas including oncology, and drug discovery. Current cell proliferation assays quantify proliferation either directly by incorporating a modified nucleotide (BrdU/ EdU) to the newly synthesized DNA (at S phase of cell cycle) (Gratzner, 1982; Salic & Mitchison, 2008; Siegers, Schaer, Hirsiger, & Schindler, 1974) or indirectly by measuring parameters such as total ATP/ DNA content (Ansar Ahmed, Gogal, & Walsh, 1994; Crouch, S.P.M., Kozlowski, R., Slater, K.J. & Fletcher, 1993; Jones, Gray, Yue, Haugland, & Singer, 2001), metabolic rate (Al-Nasiry, Geusens, Hanssens, Luyten, & Pijnenborg, 2007; Berridge, Herst, & Tan, 2005), substrate impedance changes (Giaever & Keese, 1984; Hong, Kandasamy, Marimuthu, Choi, & Kim, 2011; Upadhyay & Bhaskar, 2000; Xiao, Lachance, Sunahara, & Luong, 2002), etc. Most of the direct techniques are static end point assays. Hence, they do not allow the measurement of cell proliferation kinetics - a critical parameter to test the time-dependent effect of various drugs/ agents on cell proliferation. Other limitations include dependency on markers, being cumbersome and sample destructive. Indirect techniques are unsatisfactory as strong assumptions are needed to correlate surrogate measurements with single cell division. The simplest way to measure cell proliferation rate would be to count individual cell divisions in a cell population as and when it occurs. Only very few methods have been

proposed so far to quantify/analyze cell division on the basis of time-lapse imaging (Harder et al., 2009; Held et al., 2010; Kemper et al., 2013; Sigoillot et al., 2011; Tyson, Garbett, Frick, & Quaranta, 2012). However, the limitations include limited field of view (FOV), high cost, decreased feasibility of the approach, photo-toxicity, and photo-bleaching.

We used lensfree video microscopy platform along with associated image analysis techniques, to detect and number dividing cells. The method that we introduce, coined 'lensfree video proliferation assay' is based on continuous and high-throughput recording of cells in culture using lensfree video microscopy combined with automated detection of dividing cells among a population of thousands of cells at glance. Unlike currently used proliferation assays, cell division is directly detected without the need for surrogate measurements, exogenous contrast agents or fluorescent dyes. Further, it is practical and highly amenable to facilitate high-throughput inasmuch as it: i) does not require cell harvesting, and ii) provides continuous direct live imaging data to follow cell proliferation kinetics as they happen in thousands of cells yielding robust statistics outright. We compared our method to most commonly used proliferation assay – EdU proliferation assay, and we also followed the effect of ActinomycinD (ActD) – a well-known cell proliferation inhibitor.

By following cell populations treated with different concentrations of ActD, we show that despite significant difference in concentration (2.5μg/ml, 5 μg/ml and 10 μg/ml) inhibition of cell proliferation is rapid and rigorous, with ~80% reduction in number of cell divisions in less than 3 hours post cell treatment.

In addition to detection and numbering of dividing cells, we also demonstrated the ability of our platform to determine the orientation of cell division. We calculated the difference in longest-axis of the cell prior to cell division and the cell division axis of 299 dividing human Mesenchymal Stem Cells (hMSCs). We observed that, without any constraints, mostly cells divide along their longest-axis as stated by the popular long-axis rule (Hertwig, 1884).

3B.2 RESULTS

3B.2. 1 Detection of dividing cells

The automated detection of dividing cells using lensfree video-microscopy is based on the changes in shape and adhesion that mitotic cells undergo, which is reflected in the raw holographic image. Before dividing into two daughter cells, almost all mammalian cells undergo dramatic shape transformation from being flat during interphase to being round during M-phase, typifying a process termed “mitotic cell rounding.” This is usually accompanied by a reduction in cell-substrate adhesion. A schematic drawing illustrating changes in cell shape and substrate adhesion during division is presented in **Fig.3B.1**. Upon entering mitosis, the complex actin network is completely deconstructed and re-formed (Théry & Bornens, 2006). Hence, at metaphase, during mitosis, the cells adopt a round shape and a decreased adhesion to the substrate (Baker & Garrod, 1993; Boucrot & Kirchhausen, 2008; Clark & Paluch, 2011; Stenman, Wartiovaara, & Vaheri, 1977; Suzuki & Takahashi, 2003). This helps in efficient and stable bipolar spindle formation and is thus vital to ensure a proper cell division (Théry & Bornens, 2008). Almost all proliferating animal cells undergo these changes before cytokinesis. While extensive research is focused on understanding the underlying mechanism of the driving force(s) leading to cell rounding (Cramer & Mitchison, 1997; Heng & Koh, 2010; Kunda, Pelling,

Liu, & Baum, 2008; Lancaster et al., 2013; Maddox & Burridge, 2003; Stewart et al., 2011), these changes have not been widely exploited as a signature of mitotic cells. By contrast, lensfree video proliferation assay exploits the change in cell shape and cell adhesion as natural markers to detect dividing cells.

To exemplify the approach time-lapse images of holographic pattern obtained from a dividing NIH3T3 cell, observed using the lensfree video microscope, is shown in **Fig. 3B.1.** At T=T0 the cell is elongated and adhered to the substrate with larger zero-order gray value. There is a sharp change in the holographic pattern obtained from the cell at T= T0 + 20 min. The zero-order gray value reaches descends (from > 150 gray-levels to ~ 30 gray-levels with a background value of ~70 gray-levels) denoting reduction in cell-substrate adhesion. The daughter cells are observed at T = T0 + 100 min.

All the cells that experience rounding and reduction in cell-substrate adhesion during division, exhibit a similar holographic pattern **(as in Fig. 3B.1 T = T0 + 20 min).** Thereafter cells that are in the process of division are identified among several thousand neighboring cells by pattern recognition (FOV of the image 24mm^2) (**Fig. 3B.2**).

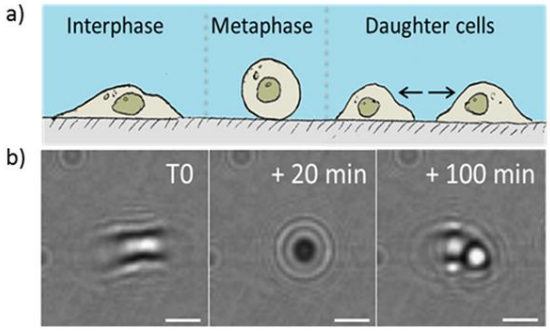

Figure 3B.1: Changes in cell shape and adhesion during cell division.

(a) Schematic drawing showing the change in cell shape and cell-substrate adhesion during cell division exemplifying a process called 'mitotic cell rounding'.

(b) Cell rounding and reduction in cell-substrate adhesion preceding the separation of daughter cells is clearly observed in the hologram obtained from the NIH3T3 cell at T = T0 + 20 min. The two daughter cells are seen at T = T0 + 100 min. Scale bar 50μm.

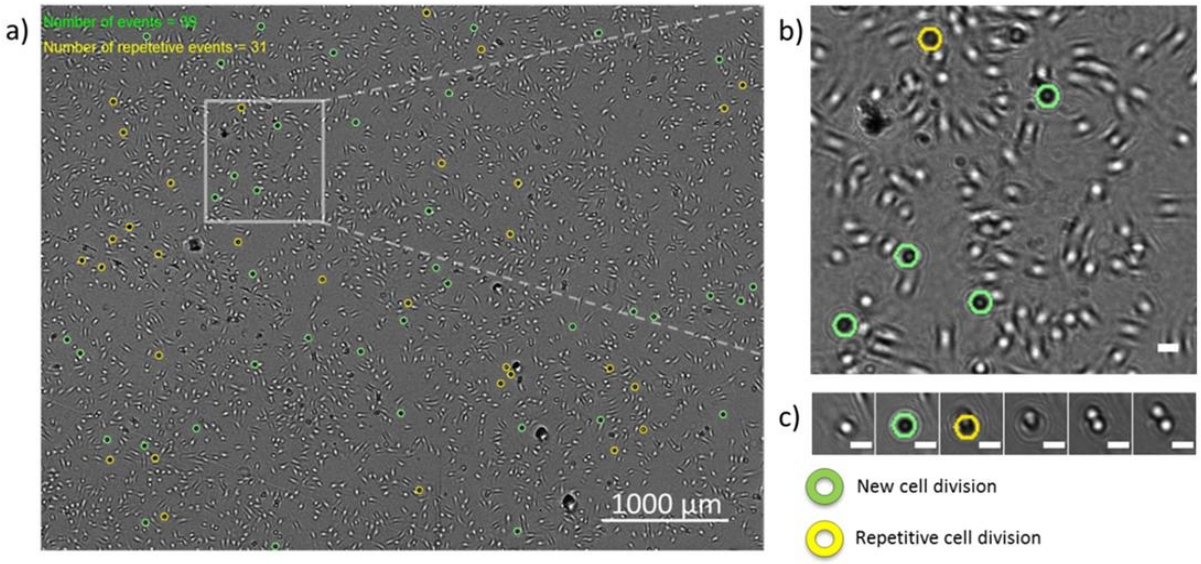

Figure 3B.2: Detection of dividing cells.

(a) Number of cells exhibiting the pattern corresponding to cell division is detected, using pattern recognition, in a full FOV image of 24mm², spanning across several thousand cells. New cell divisions are encircled in green while repetitive cell divisions (cells that were round from the previous image) are encircled in yellow.

(b) Magnified region of interest showing cells that are encircled in green and yellow amongst adherent (non-circled bright holographic pattern) neighboring cells. Scale bar 50μm.

(c) Time-lapse images showing a single cell exhibiting the pattern corresponding to cell division in subsequent temporal images (temporally separated by 20 min). Initially the cell is encircled in green and later in yellow. Scale bar 50μm.

We have verified the accuracy of the automated detection of patterns by manually detecting the patterns and by following it in the subsequent temporal images to ensure the occurrence of cell division (note that the cell displacement is negligible during cell division: chapter 3E.4.1). Since true negatives cannot be determined in this case, we calculated the F1 measure (F1 measure is defined as the harmonic mean of precision and

sensitivity. Refer 3A.4.1.2) based on true positives, false positives and false negatives. True positives constitute accurate automated detection of patterns from cells which further divide in the subsequent temporal images. False positives constitute erroneous detection of patterns which either were not from cells or were from cells that did not divide in the subsequent temporal images. False negatives are the cell divisions that were missed. The F1 measure is close to 0.87 on a scale of 0 to 1, with 1 being the best score. The measurement was based on 7 random sequences of 9 images that are temporally separated by 20 minutes, of dimension 1900µm x 1425µm, from different independent experiments **(Table 3B.3)**.

Validation of pattern recognition of dividing cells							
No. of dividing cells (Manual count)	Automated count	True Positives (TP)	False Positives (FP)	False Negatives (FN)	Precision (P) [TP/(TP + FP)]	Recall (R) [TP/(TP + FN)]	Fl Measure [2PR/{P + R)]
176	173	156	17	20	0,90	0,84	0,87
Validation of automated cell count: Number of cells present in an image (dividing + nondividing)							
Total no. of cells (Manual count)	Automated count	True Positives (TP)	False Positives (FP)	False Negatives (FN)	Precision (P) [TP/(TP + FP)]	Recall (R) [TP/(TP + FN)]	Fl Measure [2PR/(P + R)]
1177	1152	1118	34	59	0,97	0,94	0,95

Table 3B.3: Validation of automated detection of dividing cells. For the validation of pattern recognition of dividing cells, seven random sequences of nine images (temporal resolution 20min) of dimension 1900 X 1425 µm from different experiments were considered. Automated detection was compared to manual detection. For the validation of cell count, 10 random images of dimension 1196 X 1050 µm from random independent experiments were considered. Automated detection was compared to manual detection. Precision or positive predictive value is defined as TP/(TP+FP), while recall or sensitivity is defined as TP/(TP+FN), where TP, FP, and FN are true positives, false positives, and false negatives respectively. F1 measure is the harmonic mean of precision and sensitivity.

3B.2.2 Comparison with EdU proliferation assay

In order to validate the method, it was directly compared to the standard EdU proliferation assay. Cells were imaged using the lensfree video microscope inside

standard incubator during the EdU incubation period of 2.5 hours. The acquired images were subjected to pattern recognition. A total of 9 images were acquired per experiment. Number of cells undergoing division was calculated for each image and was summed. In order to compare the results obtained with the two assays, the total number of dividing cells calculated with the lensfree video proliferation assay was divided by the average total number of cells that were present in the images, to yield the percentage of dividing cells. Automated detection of the total number of cells (in division and non-dividing cells) was based on binary conversion of the image and an appropriate threshold to remove noise, using the same method as described in chapter 3A.4.1.2. Number of cells from random images was manually calculated to verify the accuracy of automated detection. Six independent experiments were performed. It was observed **(Fig. 3B.4a)** that the proliferation rate (percentage of dividing cells) obtained using our method is 18 ± 5 % (S.D. N = 6 experiments), whereas the proliferation rate obtained using EdU proliferation assay is 33.8 ± 6 % (for the EdU incubation period of 2.5 hours). The difference in the results could be due to false positives from EdU proliferation assay or false negatives from lensfree video proliferation assay (or both). EdU proliferation assay detects the cells that are in the initial stage of cell division (S-phase). False positives may occur in EdU proliferation assay if a cell that is marked during the S phase is stopped from dividing at the G2-M checkpoint **(Fig. 3B.4b)** due to improper replication of DNA. Indeed the cells are allowed to pass through the checkpoints only after they have repaired DNA damages (Melo & Toczyski, 2002; Murray, 1992; O'Connell, Nancy, & Carr, 2000). Whereas, lensfree video proliferation assay detects the cells that are in the final process of cell division (M-phase) and is unbiased by the G2-M checkpoint. However, false negatives may occur if holographic signature corresponding to mitosis is not well detected. Also, the temporal resolution of the experiments performed was 20 minutes; this may have also limited the

detection efficiency causing false negatives. Nevertheless, the standard deviation of the proliferation rate measurement over N=6 experiments is 5% showing the consistency of the method, comparable to that of EdU proliferation assay. Further, the impact of a cell proliferation inhibitor is clearly depicted in the results obtained by the method (Following section 3B.2.3).

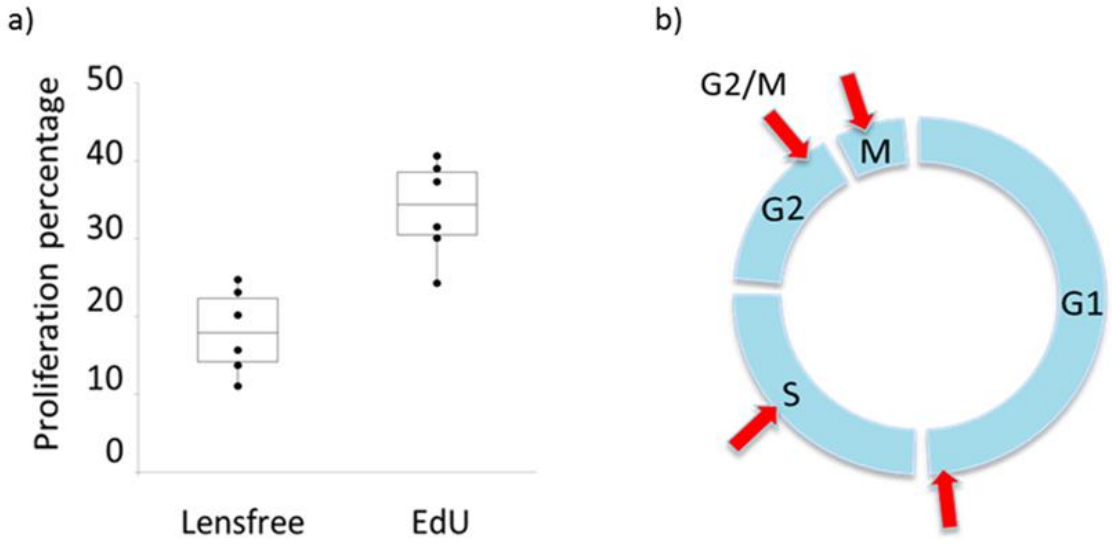

Figure 3B.4: Comparison with standard EdU proliferation assay. Percentage proliferation rate measured by lensfree video proliferation assay and EdU proliferation assay. Data points obtained from six independent experiments are shown. The horizontal line in the plot marks the median. Error bar S.D., 6 independent experiments. (b) Cell cycle showing different checkpoints at various stages (marked by red arrow). EdU proliferation assay detects cells that are in the initial stage of division (S phase), whereas lensfree video proliferation assay detects cells that are in the final stage of cell division (M phase).

3B.2.3 Inhibiting cell proliferation using ActD

The rate of cell proliferation may be altered by various stimulating or inhibiting conditions or agents. We further assessed our methods by measuring the influence of ActD, which is well known for inhibiting cell proliferation (Hollstein, 1973; Sobell, 1985). ActD was added to culture plates at predetermined concentrations of 0µg/ml (control), 5µg/ml and 10µg/ml. Following the administration of the drug, the culture plates were imaged in parallel using 3 lensfree video microscopes for 6.5 hours. Images were acquired every 20 minutes, and the obtained images were subjected to pattern recognition to calculate the number of dividing cells. It is noteworthy that manipulation of the culture plates during the addition of the drug triggered the detachment of a few cells that also gave rise to a holographic pattern similar to the one corresponding to cell division. In order to avoid the interference of these floating cells in the calculation, the initial three images following the addition of the drug were not considered for measurement.

Number of dividing cells was calculated for a total of 324 images obtained from 6 independent experiments, with 108 images per condition (control, 5µg/ml, and 10µg/ml). As shown in the graphs **(Fig. 3B.5)**, the number of dividing cells was, on an average, between 30 and 40 per image for untreated cells, and a total of 625 ± 66 (S.D. N = 6 experiments) cells divided during the experiment time frame. On the contrary, the number of dividing cells was reduced to less than 5 per image for cell cultures treated with 5µg/ml and 10µg/ml of ActD, within the initial 3 hours following the addition of the drug. Only 48 ± 17 and 34 ± 15 (S.D. N =6 experiments) cells divided in cell populations treated with the drug at concentrations of 5µg/ml and 10µg/ml, respectively. Thus the impact of the presence of the drug on the number of dividing cells is demonstrated but with little or no variation of the effect at different concentrations of the drug.

We verified the results obtained by lensfree video proliferation assay using EdU proliferation assay. The average percentage of dividing cells for the control was 45 ± 4% (S.D. N= 6 experiments) during the 2.5-hour EdU incorporation time. On the complete contrary, average percentage population of dividing cells in the presence of the ActD (5µg/ml and 10µg/ml) was close to zero **(Table 3B.6)**. Hence similar to the results obtained by lensfree video proliferation assay, no difference could be observed between the two drug concentrations.

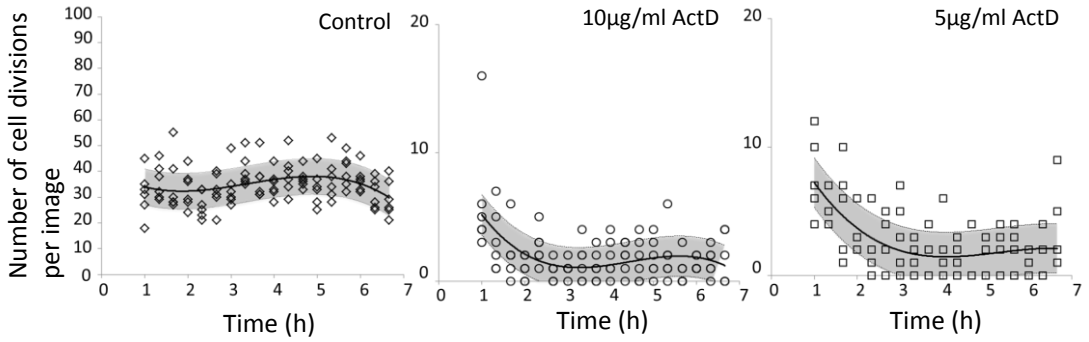

Figure 3B.5: Effect of ActD on cell proliferation. Number of dividing cells calculated for 3 different conditions from 6 independent experiments are plotted. Trendline of polynomial order 3 of mean is shown. The number of cell divisions in an image is between 30 and 40 in the case of control whereas, in the case of 10µg/ml ActD and 5µg/ml ActD, the number of cell divisions per image is reduced to less than 5 denoting a strong influence of the drug.

	Control			5 µg/ml ActD			10 µg/ml ActD		
Independent Experiments 00	Total number of events	Number of dividing cells	Percentage of dividing cells	Total number of events	Number of dividing cells	Percentage of dividing cells	Total number of events	Number of dividing cells	Percentage of dividing cells
1	10,000	4113	43.3	10,000	18	0.2	10,000	6	0.1
2	10,000	3856	41.3	10,000	3	0.0	10,000	1	0.0
3	10,000	4249	45.0	10,000	14	0.1	10,000	14	0.1
4	10,000	4629	49.1	10.000	1	0.0	10,000	8	0.1
5	10,000	4879	51.7	10,000	13	0.1	10,000	3	0.0
6	10,000	3876	42.2	10,000	4	0.0	10,000	0	0.0

Table 3B.6: The table depicts the results obtained from FACS analysis. EdU-incorporated cells were analyzed using a BD LSR II two lasers flow cytometer (BD Biosciences). The red laser (633 nm) is used for the detection of Alexa Fluor® 647. Sample measurements were performed with DIVA® software (BD Biosciences). Cell debris and aggregates were excluded from the analysis using an appropriate threshold (~30000). Based on the results obtained from 6 independent experiments, the average percentage of dividing cells for the control (untreated with ActD) was 45 ± 4 % (S.D. N = 6 experiments) during the 2.5 hour EdU incorporation time. On the complete contrary, average percentage population of dividing cells in the presence of the ActD (5µg/ml and 10µg/ml) was close to zero (with ~10 dividing cells in 10000 events). Hence similar to the results obtained by lensfree video proliferation assay, though drastic difference is seen between cells exposed to ActD and those which were not, no difference could be observed in the influence of the drug at two concentrations.

3B.2.4 Monitoring cell proliferation kinetics

The most expected contribution from any cell proliferation assay, and the least met with, is to give an accurate description of the kinetics of cell proliferation and its variations. By monitoring cell cultures before and after the addition of ActD, we are able to show how lensfree video proliferation assay meets this critical requirement. To give an accurate description of the kinetics of cell proliferation and its variations, influenced by different concentrations of ActD, cell cultures were monitored before (4.5 hours) and immediately after the addition of ActD (for 4.5 hours) at smaller concentrations (compared to previously used 5µg/ml and 10µg/ml) of 2.5µg/ml, 1 µg/ml and 0.5 µg/ml (**Fig. 3B.7**). In the case of 2.5µg/ml, the average total number of cell divisions (for a period of 4.5 h) before and after the addition of the drug were, 433 ± 112 and 63 ± 7 (S.D. N = 4 experiments) respectively. The average total number of dividing cells was reduced by ~80%. As expected, when the concentration was further reduced to 1µg/ml and 0.5µg/ml, the effect was less pronounced. The average total number of cell divisions before the addition for 1.0µg/ml and 0.5µg/ml were 310 ± 35 and 327 ± 18 (S.D. N = 4 experiments) respectively. After the addition of the drug, the average total number of dividing cells was reduced by ~50% in both the cases (128 ± 34 and 131 ± 14 for 1µg/ml and 0.5µg/ml

respectively). These results demonstrate a rapid effect of ActD on cell proliferation at 2.5µg/ml, compared to a more gradual effect at 1µg/ml and 0.5 µg/ml. Nonetheless, in all the concentrations, at ~5 hours following the addition of ActD, the number of cell divisions reduced by > 70%.

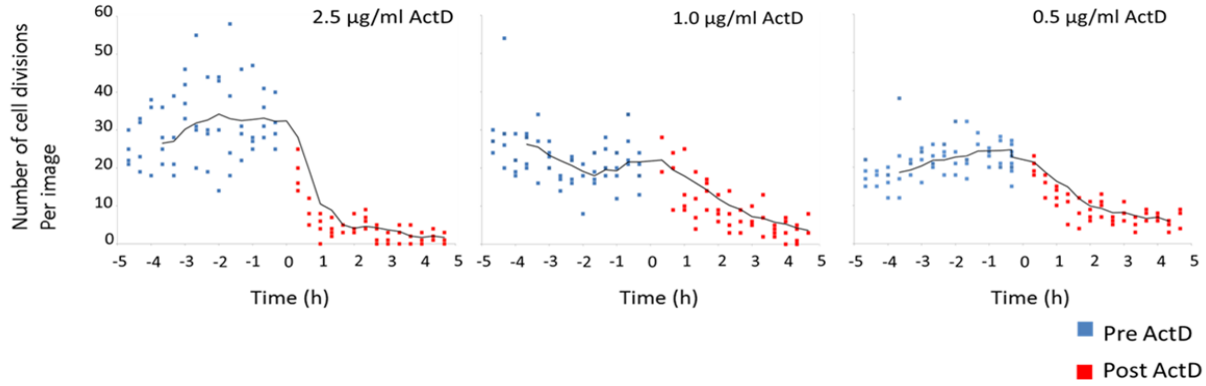

Figure 3B.7: Cell proliferation kinetics. Cell cultures subjected to different concentrations of ActD, were monitored for a period of ~9 hours before and after the addition of ActD. Time T = 0h marks the addition of the drug. Trend line of order 4 of the mean number of cell divisions per image plummets immediately following the addition of the drug in the case of 2.5µg/ml, whereas, a more gradual decrease is observed in the cases of 1.0 µg/ml and 0.5 µg/ml. In the case of 2.5µg/ml, the average total number of cell divisions (for a period of 4.5 h) before and after the addition of the drug were, 433 ± 112 and 63 ± 7 (S.D. N = 4 experiments) respectively. The average total number of dividing cells was reduced by ~80%. However, when the concentration was further reduced to 1 µg/ml and 0.5 µg/ml, the effect was less pronounced. The average total number of cell divisions before the addition of the drug for 1.0 µg/ml and 0.5 µg/ml were 310 ± 35 and 327 ± 18 (S.D. N = 4 experiments) respectively. While after the addition of the drug, the average total number of dividing cells was reduced by ~50% in both the cases (128 ± 34 and 131 ± 14 for 1µg/ml and 0.5µg/ml respectively). These results demonstrate a rapid effect of ActD on cell proliferation at 2.5µg/ml, compared to the less intense effect at 1µg/ml and 0.5µg/ml.

3B.2.5 Application to other cell types including primary cells

To test the versatility of the lensfree video proliferation assay, we followed the proliferation kinetics of other cell types: primary human fibroblasts (343), immortalized human fetal fibroblasts (Nemo-/-) and Vero cells. Cells were allowed to adhere to the substrate for 4 hours following cell plating. We calculated the percentage of cell division or proliferation rate. Percentage of cell proliferation is the ratio of number of dividing cells

to average total number of cells calculated from images acquired over a period of 2.5 hours. We followed the kinetics for over 12 hours. A moving average of the percentage of dividing cells (with a period of ~2.5 hours) was plotted. It could be inferred **(Fig. 3B.8)** that the percentage of dividing cells for immortalized cell line 'Nemo -/-' is higher compared to Vero and primary human fibroblasts (343). The difference is expected since the Nemo cells are immortalized compared to the other 2.

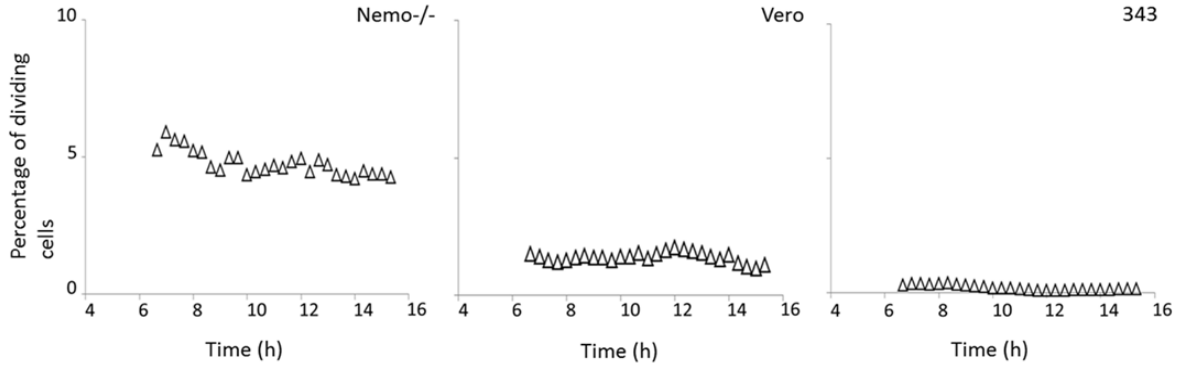

Figure 3B.8: Kinetics of cell proliferation of different cell types. The kinetics of cell division of 3 cell types, Nemo-/- (immortalized fetal fibroblasts), Vero (kidney cells from Cercopithecus aethiops), and 343 (primary human fibroblasts) were followed for a period of 16 hours. Cells were first allowed to attach to the substrate during 4 hours after plating. Percentage of dividing cells is the ratio of total number of dividing cells to average total number of cells obtained from images acquired over a period of 2.5 hours (20-minute interval image acquisitions). Moving average (of the percentage of dividing cells) with a period of 2.5 hours is depicted in the graph. 2.5 hour period was chosen to be in accordance with the comparative study performed with EdU proliferation assay in figure 3a. Since 343 cells took more time to adhere to the substrate, the few initial values of 343 are higher. Note that the percentage of dividing cells in immortalized Nemo -/- cells is higher compared to Vero and primary human fibroblasts (343) cells. In the case of 343 cells, only very few cell divisions (less than 5) were observed in an image and hence the percentage is very low.

3B.2.6 Determination of cell division orientation

The detection of patterns to identify dividing cells is performed on the raw image. We noted that reconstructing the images obtained from a dividing cell **(Fig. 3B.9)**, did not enhance the detection of the dividing cell. Again pattern recognition had to be employed and the signal was not enhanced in any way. However, holographic reconstruction permitted further examination of cell division process. i.e., it allowed capturing the orientation of cell division.

The orientation of cell division controls the fate of the daughter cells and therefore has important consequences. 'Long-axis rule' states that cells divide along their longest-axis prior to cell division, claiming that only the shape of the cell has an effect on the orientation of cell division. However, several other factors such as environment, stress, cortical cues, etc., which directly influence the orientation of cell division are being identified(Gillies & Cabernard, 2011; Minc, Burgess, & Chang, 2011; Théry & Bornens, 2006; Théry et al., 2005). Extensive research is being carried out to discover other factors that may influence the orientation of cell division.

As a proof of principle, we determined the difference in angles between the longest axis and the axis of cell division of dividing hMSCs over a period of 4 days **(Fig. 3B.9, methods)**. The longest axis of the cell was determined from the reconstructed images obtained prior to mitotic cell rounding **(Fig. 3B.9a, at t0+0h40m: longest axis denoted by dotted yellow line)** and the cell division axis was determined from the image following cell-rounding **(Fig. 3B.9a, b at t = t0+1h40m: cell division axis denoted by red dotted line)**.

In total, we analyzed 299 cell divisions from 208 images obtained over a period of 3 days. From the rose plot (or angle histogram chart) **(Fig. 3B.9)**, it is seen that, ~46% of the cells divided within a 30° wide sector with respect to their longest axis. In ~35% of cell divisions, the difference between the longest axis and the axis of cell division was between 30° and 60°. Owing to the large statistics, we are also able to distinguish a relatively small percentage of the population (~19%) that exhibited a difference of more than 60° between longest axis and the axis of cell division.

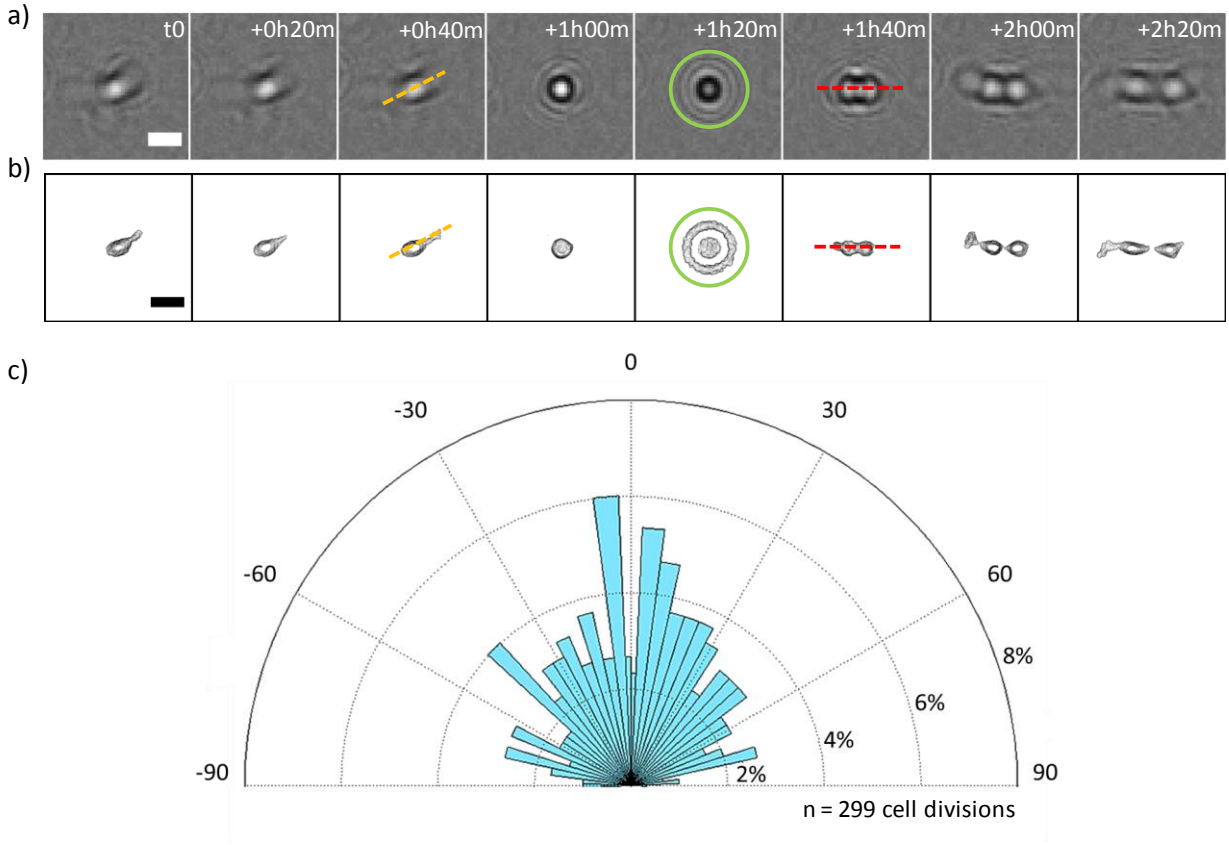

Figure 3B.9: Cell division orientation

(a) Time-lapse raw lensfree holograms obtained from a dividing hMSC obtained over 02h20m. Yellow dotted line at t = t0+0h40m denotes the longest axis prior to cell rounding. The green circle at t0+1h20m indicates the rounded, partially detached metaphase cell. The red dotted line at t = t0+1h40m shows the cell division axis. Scale bar 50µm.

(b) Holographic reconstruction and segmentation of (a). Note that the change in the distance between the cell and the imaging sensor during mitotic cell rounding (t =

t0+1h20m) was not taken in to account while performing holographic reconstruction. This resulted in artifacts around the cell observed in the holographic reconstruction at t = t0+1h00m. Scale bar 50µm.

(c) Rose plot showing the difference in angles between the longest axis and the cell division axis calculated from 299 cell divisions over a period of 4 days.

3B.3 DISCUSSION

Lensfree video proliferation assay serves as a simple and a direct method to count dividing cells in a cell population ranging from few hundred cells to ~4000 cells. Since the system is placed inside standard incubator for time-lapse imaging, there is no need for specialized chambers, as required by standard video-microscopy, to maintain ambient conditions for the cells. Cell populations can be monitored from a few hours to several days for the purpose of defining cell proliferation kinetics, on the basis of which factors that would induce or inhibit cell proliferation can be tested. Here we demonstrated the effect of different concentrations of ActD, a well-known cell proliferation inhibitor, on cell populations for a period of 5-7 hours. From the results we could observe that even though the concentration of ActD administered differed considerably, cell populations reacted the same by suffering a large inhibition of cell division within the first three hours following the addition of ActD; the difference in the concentration of the drug (10µg/ml, 5µg/ml and 2.5µg/ml) only had a negligible impact. We could also observe some cells that were in the process of division during the addition of the drug, abandoned cell division and remained round and detached from the substrate until the end of experiment **(Fig. 3B.10)**. However, when the concentration was further reduced to 1µg/ml and 0.5µg/ml, the impact was less pronounced with only a 50% decrease in the number of dividing cells compared to ~80% reduction induced by elevated concentrations.

The acquired raw image can be reconstructed to obtain minute details. However, since the changes in cell shape and cell-substrate adhesion are well exhibited in the raw image, holographic reconstruction is not necessary for the detection of dividing cells. Nevertheless, it is a promising tool to further analyze single cell divisions with greater detail, for example we measured cell division orientation. By being able to detect and follow cell divisions longitudinally, lensfree video microscopy provides an apt platform to perform a detailed study on the factors influencing the orientation of cell division. To our knowledge, such a high-throughput, label-free, measurement has not been proposed before without the utilization cell localization techniques. Here, we computed the difference between longest axis and cell division axis without introducing any constraint on the cells. However, by using micro-patterned substrates (Théry et al., 2005) or by integrating microfluidic platforms, cells can be exposed to mechanical, or environmental stress. The influence of these factors on the axis of cell division, frequency of cell division (number of cell divisions/period of observation) and the time taken from cell rounding to separation of daughter cells can be analyzed using lensfree video microscopy.

In addition, We have tested the approach with various other cell types such as Vero, U87, RPE1, RWPE1, primary human fibroblasts, Mesenchymal stem cells, PC3, HUVEC, MCF10A cells in both 2D and 3D cell culture conditions **(Fig. 3B.11)** and shown that the method is applicable to numerous cell types in 2D cell culture. Since the cells in 3D cell culture do not show enhanced substrate adherence as in 2D, the change in the holographic pattern is less pronounced. The approach is not applicable to floating cells such as hematopoietic cells, but it is to be noted that majority of the cell types are adherent to the substrate in nature.

As with the lensfree video microscope, not any label or fluorescent reporter is needed and because the system does not use lasers, concerns about photo-toxicity for the cells or photo bleaching of reporters are avoided. Using our prototype 3 **(chapter 2: Fig. 2.3.1c),** we performed 1-minute interval image acquisitions of a BJ cell **(Fig.3B.12)**. Apart from detecting dividing cells, with increased temporal resolution (1 image every 1 minute), analysis on cell division could be performed through label-free tracking of thousands of single cells from cell retraction until separation of daughter cells, providing an entirely new perspective on cell division that includes determination of time taken from cell retraction until the separation of daughter cells.

For the work presented here, we could monitor in parallel up to 3 culture plates (35mm diameter) with 3 lensfree video microscopes having imaging sensor of dimensions (5.7 mm x 4.2 mm). The throughput can be dramatically increased by multiplexing 96 smaller sensors to read 96-well plates (Haguet, Obeïd, Griffin, Freida, & Gidrol, 2013), which would be an ideal setting for drug screening applications. The method could also be exploited to monitor cell behavior in a bioreactor.

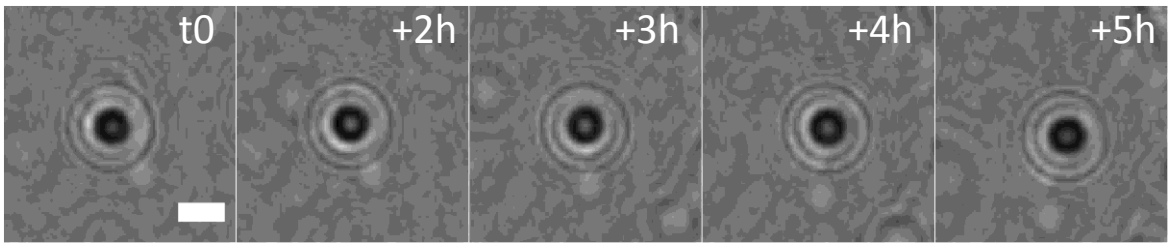

Figure 3B.10: Unsuccessful cell division. A cell that was in the process of cell division, remained round and detached until the end of the experiment, due to the effect of the drug (t0 marks the moment of drug administration). Scale bar: 50μm.

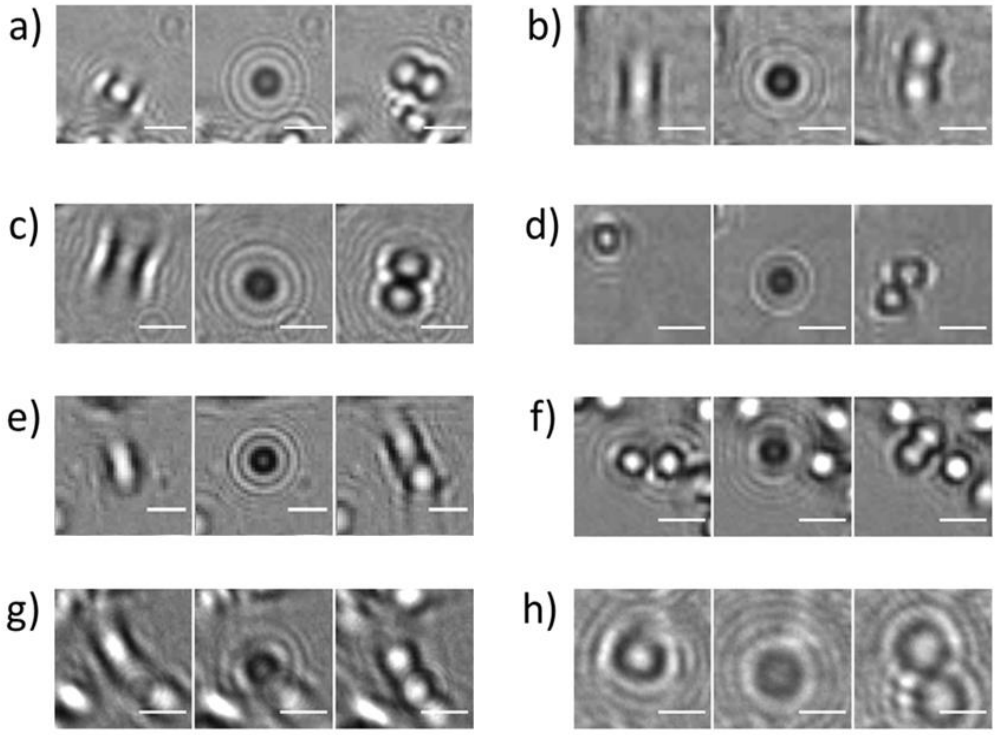

Figure 3B.11: Applicability to other cell types. Other cell types exhibiting similar holographic pattern during cell division (a) MCF10A, (b) RPE1, (c) U87 cells, (d) RWPE1, (e) Mesenchymal stem cells, (f) PC3, (g) HUVEC, (h) RWPE1 in 3D cell culture. Scale bar: 50μm.

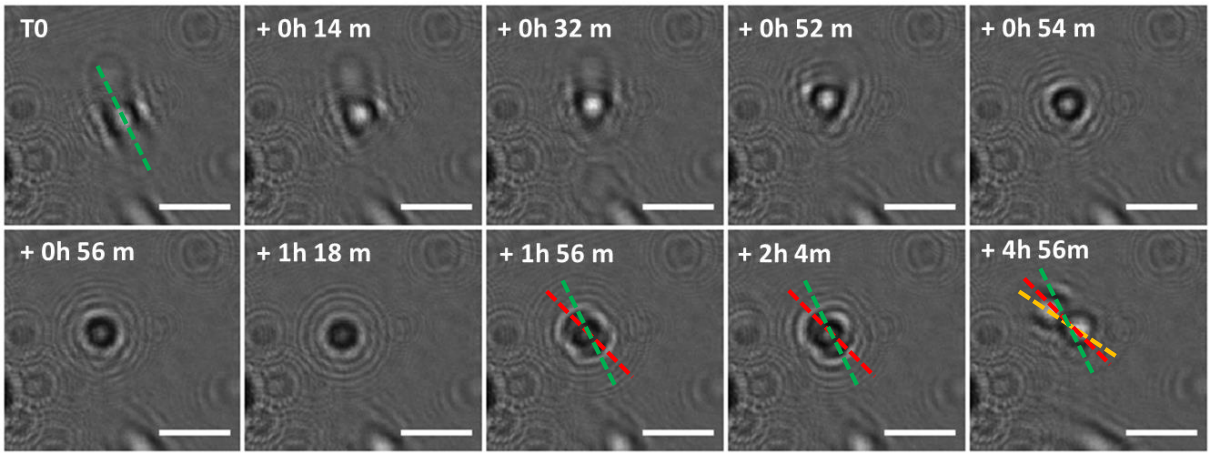

Figure 3B.12: Increased temporal resolution. BJ cells were monitored with a temporal resolution of 1image every minute. Temporal images of interest from real-time monitoring of a BJ cell showing the change in cell shape and cell adhesion taking place during cell division. Cell retraction and rounding can be observed in images obtained from T0 until T0 + 0h54m. Reduced cell substrate adhesion leading to signature holographic pattern of a dividing cell can be seen in images T0 + 0h56m and T0 + 1h18m. Cytokinesis and separation of daughter cells can be seen from T0 + 1h56m until T0 + 4h56m. Diagonal (dotted) green line indicates the longest axis of the cell prior to cell division. Red line denotes the cell division axis during cytokinesis. Yellow line denotes the axis of separation

of daughter cells. The cell in this case, has divided along the longest axis prior to cell division. Scale bar: 100µm.

3B.4 METHODS

3B.4.1 Computational methods

3B.4.1.1 Pattern recognition of dividing cells

Dividing cells and floating cells exhibit similar holographic patterns. Therefore, pattern recognition of dividing cells is performed using the same approach detailed in section (chapter 3A.4.1) based on normalized cross-correlation.

3B.4.1.2 Determination of longest axis and cell division axis

Once a dividing cell is detected based on pattern recognition, the position of the cell in the image is used as reference to find the same cell in previous and subsequent image frames, i.e., the same cell before and after cell rounding. The cell detected before and after cell rounding is segmented in order to obtain the longest axis and the axis of cell division respectively. In case of inability to find the longest axis or the orientation axis, the cell is not considered. The axes are determined using orientation function available in Matlab **(Fig. 3B.13)**.

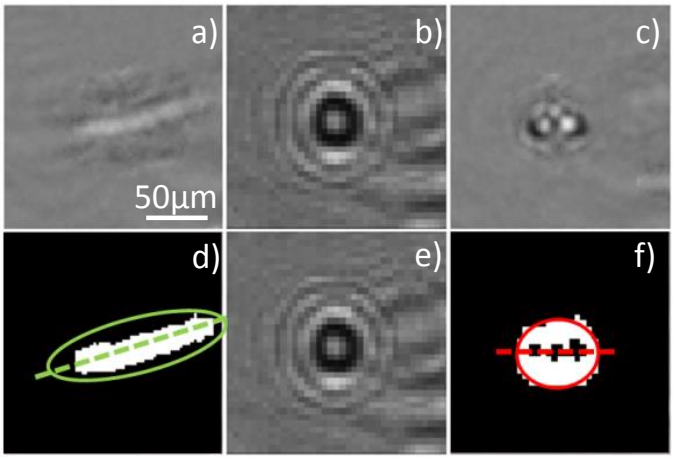

Figure 3B.13: Automated detection of cell division orientation. Once the pattern of a dividing cell is detected (b), the coordinates of the cell is used to search for the cell before and after cell rounding, in previous (a) and subsequent (c) image frames. First, the cell is detected in previous image frame, after the cell is found, using gray-level differentiation and appropriate thresholding, the debris are removed, and the segmented binary image of the cell is obtained (d). From the binary image the orientation is determined using Matlab, by drawing an ellipse that best fits the segmented object (d, green). Similarly, from the subsequent image frame, the dividing cell is segmented and the axis or orientation is determined (f, red). If the cell is still round in the image, the subsequent image frame is considered.

3B.4.2 Cell culture experiments

The murine NIH3T3 fibroblasts were obtained from the American Type Culture Collection (ATCC) and were grown in (DMEM) supplemented with 10% newborn calf serum (PAN Biotech) and 1% antibiotics (penicillin and streptomycin) (Gibco). Primary cultures of human fibroblasts prepared from skin biopsies performed on healthy donors (male 30-39 years) which were established in DME-Glutamax (Invitrogen) supplemented with 20% FCS and used at passage 2. Nemo -/- (seeding density: 30,000 cells) cells are SV40 immortalized human fetal female fibroblasts immortalized with a mutant NEMO gene (a gift from Dr A. Smahi). Vero cells (a gift from F. Barre-Sinoussi's lab) (seeding density: 26,000 cells) are kidney cells from Cercopithecusaethiops. Cells (Nemo, Vero, 343) were grown in DMEM Glutamax plus 10% SVF.

3B.4.2.1 Comparison of lensfree video proliferation assay with standard EdU proliferation assay

Standard 35mm culture dish was filled with 2.5ml of culture media at a cell density of $2.5x10^4$ cells/ml. For cell incubation with EdU, cells were seeded on day 1 in DMEM supplemented culture media with 10% FCS. Cells were treated on day 2 with 10µM EdU (Click iT® EdU Invitrogen) followed by 2.5-hour incubation. The culture dish was imaged with lensfree video microscope during EdU incubation period. Following the incubation period, EdU was removed through three washes in PBS and cells were transferred in tubes

after trypsin (Gibco) treatment. According to manufacturer's recommendation, cells were fixed in 1 ml 1% formaldehyde (Sigma). After 15 minutes, cells were washed once in PBS/ 1% BSA. Then, cells were treated for 30 minutes with 1X saponin solution for membrane permeabilization. After washing once in PBS containing 1% BSA, cells were centrifuged at 500G for 5 minutes and supernatant was eliminated. Cells were incubated for 30 minutes at room temperature, in the dark in presence of the click cocktail reaction buffer containing the fluorescent dye (Invitrogen). After washing and centrifugation at 500G for 5 minutes, cells were harvested and stored at 4°C until FACS analysis.

3B.4.2.2 Inhibiting cell proliferation using ActD

Standard 35mm culture dish was filled with 2.5ml of culture media at a cell density of $2.5x10^4$ cells/ml. Cells were seeded in 3 culture dishes on day 1. On day 2, ActD was added at concentrations 0µg/ml (untreated control), 5µg/ml and 10µg/ml. The culture dishes were imaged simultaneously by 3 lensfree video microscopes immediately following the administration of the drug for a period of 6.5 hours. Similarly, 3 culture dishes were prepared in parallel adhering to the same protocol for EdU proliferation assay. EdU was added for the final 2.5 hours without changing the concentration of ActD.

3B.4.2.3 Monitoring cell proliferation kinetics

Standard 35mm culture dish was filled with 2.5ml of culture media at a cell density of $2.5x10^4$ cells/ml. Cells were seeded on day 1. On day 2, Cells were imaged using lensfree video microscope from approximately 4.5 hours before the addition of ActD (at 2.5µg/ml, 1µg/ml and 0.5µg/ml) until approximately 4.5 hours following the addition of the drug.

3B.4.2.4 FACS analysis

EdU-incorporated cells were analyzed using a BD LSR II two lasers flow cytometer (BD Biosciences). The red laser (633nm) is used for the detection of Alexa Fluor® 647. Sample measurements were performed with DIVA® software (BD Biosciences). Cell debris and aggregates were excluded from the analysis using an appropriate threshold (~30000).

REFERENCES

Al-Nasiry, S., Geusens, N., Hanssens, M., Luyten, C., & Pijnenborg, R. (2007). The use of Alamar Blue assay for quantitative analysis of viability, migration and invasion of choriocarcinoma cells. *Human Reproduction (Oxford, England)*, *22*(5), 1304–9. doi:10.1093/humrep/dem011

Ansar Ahmed, S., Gogal, R. M., & Walsh, J. E. (1994). A new rapid and simple non-radioactive assay to monitor and determine the proliferation of lymphocytes: an alternative to [3H]thymidine incorporation assay. *Journal of immunological methods*, *170*(2), 211–24. Retrieved from http://www.ncbi.nlm.nih.gov/pubmed/8157999

Baker, J., & Garrod, D. (1993). Epithelial cells retain junctions during mitosis. *Journal of cell science*, *104*, 415–425. Retrieved from http://www.ncbi.nlm.nih.gov/pubmed/7685036

Berridge, M. V, Herst, P. M., & Tan, A. S. (2005). Tetrazolium dyes as tools in cell biology: New insights into their cellular reduction. *Biotechnology annual review*, *11*(05), 127–52. doi:10.1016/S1387-2656(05)11004-7

Boucrot, E., & Kirchhausen, T. (2008). Mammalian cells change volume during mitosis. *PloS one*, *3*(1), e1477. doi:10.1371/journal.pone.0001477

Clark, A. G., & Paluch, E. (2011). *Cell Cycle in Development*. (J. Z. Kubiak, Ed.) (Vol. 53, pp. 31–73). Berlin, Heidelberg: Springer Berlin Heidelberg. doi:10.1007/978-3-642-19065-0

Cramer, L. P., & Mitchison, T. J. (1997). Investigation of the mechanism of retraction of the cell margin and rearward flow of nodules during mitotic cell rounding. *Molecular biology of the cell*, *8*(1), 109–19. Retrieved from http://www.pubmedcentral.nih.gov/articlerender.fcgi?artid=276063&tool=pmcentrez&rendertype=abstract

Crouch, S.P.M., Kozlowski, R., Slater, K.J. & Fletcher, J. (1993). Use of ATP as a measure of cell proliferation and cell toxicity.pdf.

Friedrichs, J., Legate, K. R., Schubert, R., Bharadwaj, M., Werner, C., Müller, D. J., & Benoit, M. (2013). A practical guide to quantify cell adhesion using single-cell force spectroscopy. *Methods (San Diego, Calif.)*, *60*(2), 169–78. doi:10.1016/j.ymeth.2013.01.006

Giaever, I., & Keese, C. R. (1984). Monitoring fibroblast behavior in tissue culture with an applied electric field. *Proceedings of the National Academy of Sciences of the United States of America*, *81*(12), 3761–3764. Retrieved from http://www.pubmedcentral.nih.gov/articlerender.fcgi?artid=345299&tool=pmcentrez&rendertype=abstract

Gillies, T. E., & Cabernard, C. (2011). Cell division orientation in animals. *Current biology : CB*, *21*(15), R599–609. doi:10.1016/j.cub.2011.06.055

Gratzner, H. (1982). Monoclonal Antibody to 5-Bromo- and 5-Iododeoxyuridine : A New Reagent for Detection of DNA Replication Placental Mononuclear Phagocytes as a Source of Interleukin-1. *Science*, *218*, 474–475.

Greenbaum, A., Luo, W., Su, T.-W., Göröcs, Z., Xue, L., Isikman, S. O., … Ozcan, A. (2012). Imaging without lenses: achievements and remaining challenges of wide-field on-chip microscopy. *Nature Methods*, *9*(9), 889–895. doi:10.1038/nmeth.2114

Haguet, V., Obeïd, P., Griffin, R., Freida, D., & Gidrol, X. (2013). Parallelized lensfree time-lapse microscopy. *Conference NanoBioEurope, p. 30, Toulouse, France, June 10-12, 2013.*, 2013.

Harder, N., Mora-Bermúdez, F., Godinez, W. J., Wünsche, A., Eils, R., Ellenberg, J., & Rohr, K. (2009). Automatic analysis of dividing cells in live cell movies to detect mitotic delays and correlate phenotypes in time. *Genome research*, *19*(11), 2113–2124. doi:10.1101/gr.092494.109

Held, M., Schmitz, M. H. a, Fischer, B., Walter, T., Neumann, B., Olma, M. H., … Gerlich, D. W. (2010). CellCognition: time-resolved phenotype annotation in high-throughput live cell imaging. *Nature methods*, *7*(9), 747–754. doi:10.1038/nmeth.1486

Heng, Y.-W., & Koh, C.-G. (2010). Actin cytoskeleton dynamics and the cell division cycle. *The International Journal of Biochemistry & Cell Biology*, *42*(10), 1622–1633. doi:10.1016/j.biocel.2010.04.007

Hollstein, U. (1973). Actinomycin. Chemistry and Mechanism of Action. *Chemical Reviews*, *74*(May), 625–652.

Hong, J., Kandasamy, K., Marimuthu, M., Choi, C. S., & Kim, S. (2011). Electrical cell-substrate impedance sensing as a non-invasive tool for cancer cell study. *The Analyst*, *136*(2), 237–245. doi:10.1039/c0an00560f

Jones, L. J., Gray, M., Yue, S. T., Haugland, R. P., & Singer, V. L. (2001). Sensitive determination of cell number using the CyQUANT cell proliferation assay. *Journal of immunological methods*, *254*(1-2), 85–98. Retrieved from http://www.ncbi.nlm.nih.gov/pubmed/11406155

Kemper, B., Bauwens, A., Vollmer, A., Ketelhut, S., Langehanenberg, P., Müthing, J., … von Bally, G. (2013). Label-free quantitative cell division monitoring of endothelial cells by digital holographic microscopy. *Journal of biomedical optics*, *15*(3), 036009. doi:10.1117/1.3431712

Kunda, P., Pelling, A. E., Liu, T., & Baum, B. (2008). Moesin Controls Cortical Rigidity, Cell Rounding, and Spindle Morphogenesis during Mitosis. *Current biology : CB*, *18*(2), 91–101. doi:10.1016/j.cub.2007.12.051

Lancaster, O. M., Le Berre, M., Dimitracopoulos, A., Bonazzi, D., Zlotek-Zlotkiewicz, E., Picone, R., … Baum, B. (2013). Mitotic Rounding Alters Cell Geometry to Ensure Efficient Bipolar Spindle Formation. *Developmental cell*, *25*(3), 270–283. doi:10.1016/j.devcel.2013.03.014

Maddox, A. S., & Burridge, K. (2003). RhoA is required for cortical retraction and rigidity during mitotic cell rounding. *The Journal of cell biology*, *160*(2), 255–265. doi:10.1083/jcb.200207130

Melo, J., & Toczyski, D. (2002). A unified view of the DNA-damage checkpoint. *Current Opinion in Cell Biology*, *14*(2), 237–245. doi:10.1016/S0955-0674(02)00312-5

Minc, N., Burgess, D., & Chang, F. (2011). Influence of cell geometry on division-plane positioning. *Cell*, *144*(3), 414–26. doi:10.1016/j.cell.2011.01.016

Murray, A. W. (1992). Creative blocks: cell-cycle checkpoints and feedback controls. *Nature*, *359*, 599–604.

O'Connell, M. J., Nancy, C., & Carr, A. M. (2000). The G2-phase DNA-damage checkpoint. *Trends in Cell Biology*, *10*(07), 296–303.

Salic, A., & Mitchison, T. J. (2008). A chemical method for fast and sensitive detection of DNA synthesis in vivo. *Proceedings of the National Academy of Sciences of the United States of America*, *105*(7), 2415–20. doi:10.1073/pnas.0712168105

Siegers, M. P., Schaer, J. C., Hirsiger, H., & Schindler, R. (1974). Determination of rates of DNA synthesis in cultured mammalian cell populations. *The Journal of cell biology*, *62*(2), 305–315. Retrieved from http://www.pubmedcentral.nih.gov/articlerender.fcgi?artid=2109404&tool=pmcentrez&rendertype=abstract

Sigoillot, F. D., Huckins, J. F., Li, F., Zhou, X., Wong, S. T. C., & King, R. W. (2011). A time-series method for automated measurement of changes in mitotic and interphase duration from time-lapse movies. *PloS one*, *6*(9), e25511. doi:10.1371/journal.pone.0025511

Sobell, H. M. (1985). Actinomycin and DNA transcription. *Proceedings of the National Academy of Sciences of the United States of America*, *82*(16), 5328–5331. Retrieved from http://www.pubmedcentral.nih.gov/articlerender.fcgi?artid=390561&tool=pmcentrez&rendertype=abstract

Stenman, S., Wartiovaara, J., & Vaheri, A. (1977). Changes in the distribution of a major fibroblast protein, fibronectin, during mitosis and interphase. *The Journal of cell biology*, *74*(33), 453–467.

Stewart, M. P., Helenius, J., Toyoda, Y., Ramanathan, S. P., Muller, D. J., & Hyman, A. a. (2011). Hydrostatic pressure and the actomyosin cortex drive mitotic cell rounding. *Nature*, *469*(7329), 226–230. doi:10.1038/nature09642

Suzuki, K., & Takahashi, K. (2003). Reduced cell adhesion during mitosis by threonine phosphorylation of beta1 integrin. *Journal of cellular physiology*, *197*(2), 297–305. doi:10.1002/jcp.10354

Théry, M., & Bornens, M. (2006). Cell shape and cell division. *Current opinion in cell biology*, *18*(6), 648–57. doi:10.1016/j.ceb.2006.10.001

Théry, M., & Bornens, M. (2008). Get round and stiff for mitosis. *HFSP journal*, *2*(2), 65–71. doi:10.2976/1.2895661

Théry, M., Racine, V., Pépin, A., Piel, M., Chen, Y., Sibarita, J.-B., & Bornens, M. (2005). The extracellular matrix guides the orientation of the cell division axis. *Nature cell biology*, *7*(10), 947–53. doi:10.1038/ncb1307

Tyson, D. R., Garbett, S. P., Frick, P. L., & Quaranta, V. (2012). Fractional proliferation: a method to deconvolve cell population dynamics from single-cell data. *Nature methods*, *9*(9), 923–8. doi:10.1038/nmeth.2138

Upadhyay, P., & Bhaskar, S. (2000). Real time monitoring of lymphocyte proliferation by an impedance method. *Journal of immunological methods*, *244*(1-2), 133–137. Retrieved from http://www.ncbi.nlm.nih.gov/pubmed/11033025

Xiao, C., Lachance, B., Sunahara, G., & Luong, J. H. T. (2002). Assessment of cytotoxicity using electric cell-substrate impedance sensing: concentration and time response function approach. *Analytical chemistry*, *74*(22), 5748–5753. Retrieved from http://www.ncbi.nlm.nih.gov/pubmed/12463358

CHAPTER 3C

MONITORING CELL DIFFERENTIATION

Pg. 89	**CELL DIFFERENTIATION**
Pg. 92	**QUANTIFICATION OF ADIPOGENIC DIFFERENTIATION OF hMSCs** **Kinetics: Gradual filling of cell body with lipid droplets**
Pg. 98	**QUANTIFICATION OF NEURONAL DIFFERENTIATION OF hMSCs** **Kinetics: Varied concentrations of β-mercaptoethanol (BME)**

3C. MONITORING CELL DIFFERENTIATION

3C.1 INTRODUCTION

One of the most unique characteristics of stem cells is their ability to differentiate in to other cell types. Cell differentiation is how generic cells become specialized cells to satisfy varied functional needs. Understanding stem cell differentiation is of prime importance because of the potential that it possesses in therapeutic research. Various factors and protocols that induce or inhibit stem cell differentiation are highly researched (Bianco, Robey, & Simmons, 2008; Chen et al., 2001; Dezawa et al., 2005; Murphy, Moncivais, & Caplan, 2013; Prockop, 1997; Wei et al., 2013). However, one of the bottle-necks of this research is the limitations posed by quantification methods. Methods that are used to quantify cell differentiation are invasive, label-dependent, labor-intensive, time-consuming and especially non-continuous.

Using lensfree video microscopy these limitations are overcome. Here, we demonstrate the ability of lensfree video microscopy to quantify adipogenic and neuronal differentiation of human mesenchymal stem cells (hMSCs). As cells differentiate, there is usually a vast change in cellular properties (e.g.: size, shape, etc.) depending on their associated functions. By detecting these changes, using lensfree video microscope, we perform label-free, continuous, non-invasive quantification of cell differentiation.

3C.1.1 Adipogenic differentiation

Adipogenic differentiation of hMSCs is a process where they differentiate into adipocytes. During the process of adipogenic differentiation, the stem cells increase in size, become relatively circular and the cell body is filled with lipid droplets **(Fig. 3C.1).**

The differentiation process is triggered by the addition of differentiation media – a well-established protocol (Vemuri, Chase, & Rao, 2011). Several factors that induce or inhibit the adipogenic differentiation of hMSCs are being researched (Scott, Nguyen, Levi, & James, 2011), mainly for therapeutic applications.

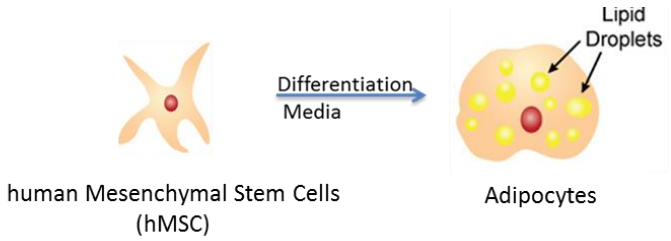

Figure 3C.1: Adipogenic differentiation and associated changes. Schematic diagram showing the changes in the structure of a cell during adipogenic differentiation. The elongated hMSC becomes round and filled with lipid droplets.

Qualitative analysis of adipogenic differentiation is performed by quantifying adipogenic specific gene expression using real-time PCR or by quantifying PPARY. The major limitation is that the absolute percentage of adipocytes is not known by using the techniques. One of the most commonly used methods involves staining adipocytes (using oil red O) followed by quantification using a standard lens-based microscope by manually counting the number of adipocytes and the number of non-differentiated MSCs (Gorjup, Peter, Wien, von Briesen, & Schmitt, 2009). Apart from being a laborious end-point assay, there is an unquantifiable bias introduced by manual counting. Moreover, the field of view

is restricted requiring an extrapolation of results thereby introducing an additional bias. Even with automated counting the method remains invasive and incapable for following the dynamics (Gorjup et al., 2009; Lo Surdo, Millis, & Bauer, 2013). In all the cases, there is a substantial loss of both spatial and temporal information. None of the above mentioned methods can follow the kinetics of cell differentiation, primarily due to their invasiveness. In order to follow the kinetics, several end point assays are performed at different time points, using cell populations subjected to same treatment. The end result is a mere spatial and temporal extrapolation that is unlikely to provide precise information on kinetics of heterogeneous cell populations.

3C.1.2 Neuronal differentiation

Neuronal differentiation of hMSCs is a process where hMSCs are differentiated in to neurons usually characterized by reduction in cell body area, and outgrowth of neuritis **(Fig. 3C.2)**. Neuronal differentiation of hMSC and in vitro cultivation of neurons are of major importance because of its promising therapeutic potential for neuro-degenerative diseases (Benvenuti et al., 2006; Lee et al., 2010; Murphy et al., 2013; Xuan, Luo, Ji, & Long, 2009).

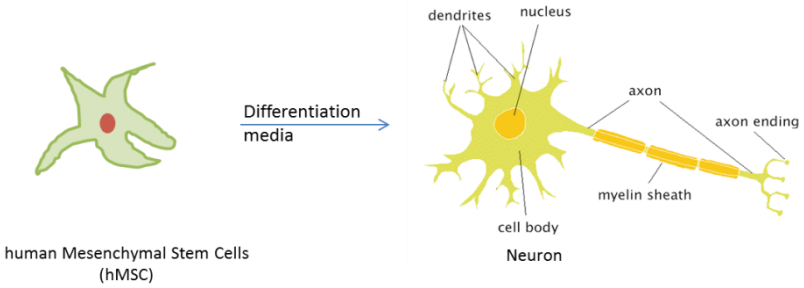

Figure 3C.2: Neuronal differentiation and associated changes. Schematic diagram showing the changes in the structure of hMSC during neuronal differentiation. The elongated hMSC becomes round with neurite (axons, dendrites, etc.) outgrowth.

Methods that are currently used to detect/quantify neuronal differentiation in vitro mainly involve, gene expression analysis using RT-PCR or flow cytometry analysis combined with labeling of cells with appropriate fluorescent antibody. The methods are labor-intensive, label-dependent, highly invasive, and particularly non-continuous. Video microscope may be used to visualize neuronal differentiation in real-time. However, high cost, complexity in manipulating culture dishes during the experiment, restricted field of view are some of its major limitations. In all the cases, there is a substantial loss of spatial and temporal information that is crucial for any quantification method.

Using lensfree video microscope with associated image analysis techniques, we overcame the limitations and deduced the kinetics of both adipogenic and neuronal differentiation of hMSCs.

3C.2 RESULTS

3C.2.1 Adipogenic differentiation

As mentioned earlier, during adipogenic differentiation the interior of the cell body is filled with lipid droplets. Diffraction of light by these lipid droplets changes the holographic interference pattern obtained from the cell **(Fig. 3C.3).** The gradual process of this change is illustrated in **Fig. 3C.4.** From the raw images, based on gray value changes, the differentiated and non-differentiated cells can be identified and segmented **(Fig. 3C.5).**

Comparison of lens-based and lensfree microscope is shown in **Fig. 3C.6.** The difference in the holographic pattern **(Fig. 3C.6b)** between non-differentiated and differentiated cells is well correlated with the standard lens-based microscopic images **(Fig. 3C.6a).** Although significant difference was readily observed in the raw lensfree holographic

patterns **(Fig. 3C.4, 3C.5, 3C.6),** we reconstructed the patterns to obtain precise information about the size and the shape of adipocytes. The marker-free reconstructed and segmented image **(Fig. 3C.6d)** correlated well with the fluorescent image of adipocytes **(Fig.3C.6c: adipocytes stained with AdipoRed)**

The size and the shape of adipocytes are obtained from the holographic reconstruction of the raw image **(Fig 3C.6c, 3C.7b, methods)**. Holographic reconstruction also permits precise segmentation of adipocytes to calculate the number of adipocytes in an image and also the surface covered by adipocytes **(Fig. 3C.7c, methods)**. By determining percentage relative surface area covered by adipocytes (relative to the surface covered by non-differentiated cells just before addition of differentiation media) **(Fig. 3C.8)** for each image frame at different time points, we followed the kinetics of adipogenic differentiation.

We followed cell populations from 4 days post addition of differentiation media. A differentiation phase and a saturation phase could be observed from the plot **(Fig. 3C.8).** Initially, the surface area covered by adipocytes increased considerably for ~ 14 days (from 20±10% to 75±10%) post differentiation trigger, before attaining a saturation point. By 24 days, the relative surface area covered reached values greater than 80%. The number of cells monitored (cell count of the population before the addition of differentiation media) were n~1820 **(Fig. 3C.8, blue)**, n~1852 **(Fig. 3C.8, black)**, n~2466 **(Fig. 3C.8, red).**

Fig. 3C.9 shows a gradual process of adipogenic differentiation of a single hMSC, clearly visible from the reconstructed image. From our experiments, we observed that during adipogenic differentiation, initially a few lipid droplets form along the border of the cell

and gradually over time the entire cell becomes filled with lipid droplets. It can be observed that the differentiation process commenced at t0 + 4 days, with formation of few lipid droplets along the border of the cell (lipid droplets are seen as dark spots in the reconstructed image **Fig. 3C.9**). At this time point, the interior remained relatively bright denoting that it was not filled with lipid droplets **(Yellow arrow Fig. 3C.9 at t0 + 4 days, t0 + 6.5 days)**. However, by the end of 12 days post addition of differentiation media, the interior of the cell is seen completely filled with lipid droplets, with lower gray value compared to initial image at t0+4 days.

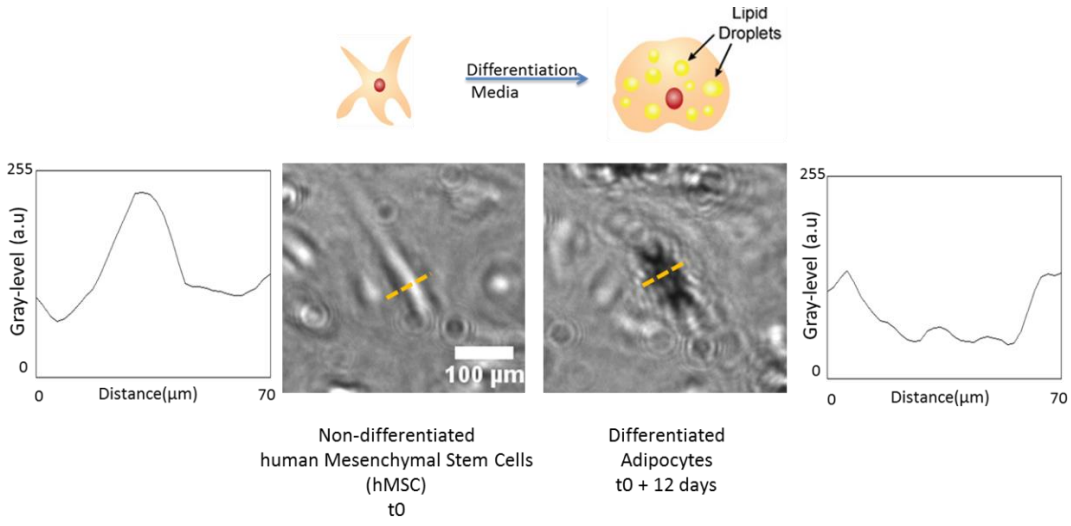

Figure 3C.3: hMSC and differentiated adipocyte. The change in the holographic pattern due to distinct diffraction of light by the lipid droplets inside the adipocytes. Profile plots show the difference in the gray-level intensity before (t0) and after differentiation (t0 + 12 days). Yellow dotted lines denote regions from where gray-level profiles were determined.

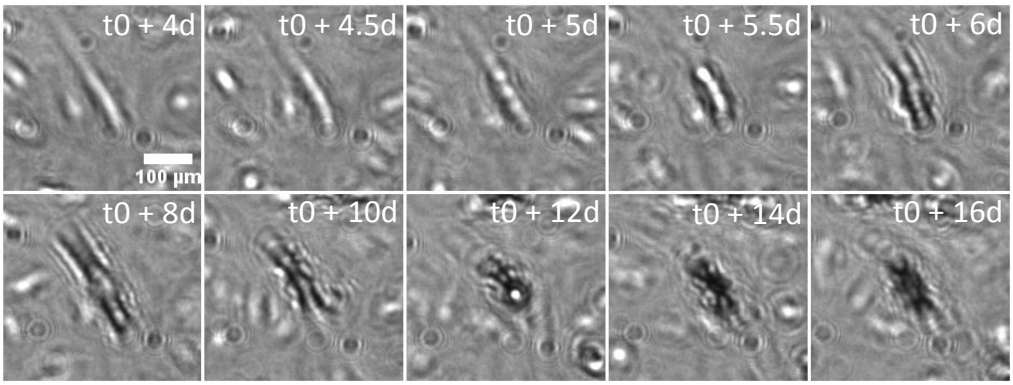

Figure 3C.4: Adipogenic differentiation of single hMSC. Cell Differentiation of a single cell observed over a period of 12 days. Time t0 marks the addition of cell differentiation media. Note the gradual change in the holographic pattern of the cell as it differentiates in to adipocyte over time.

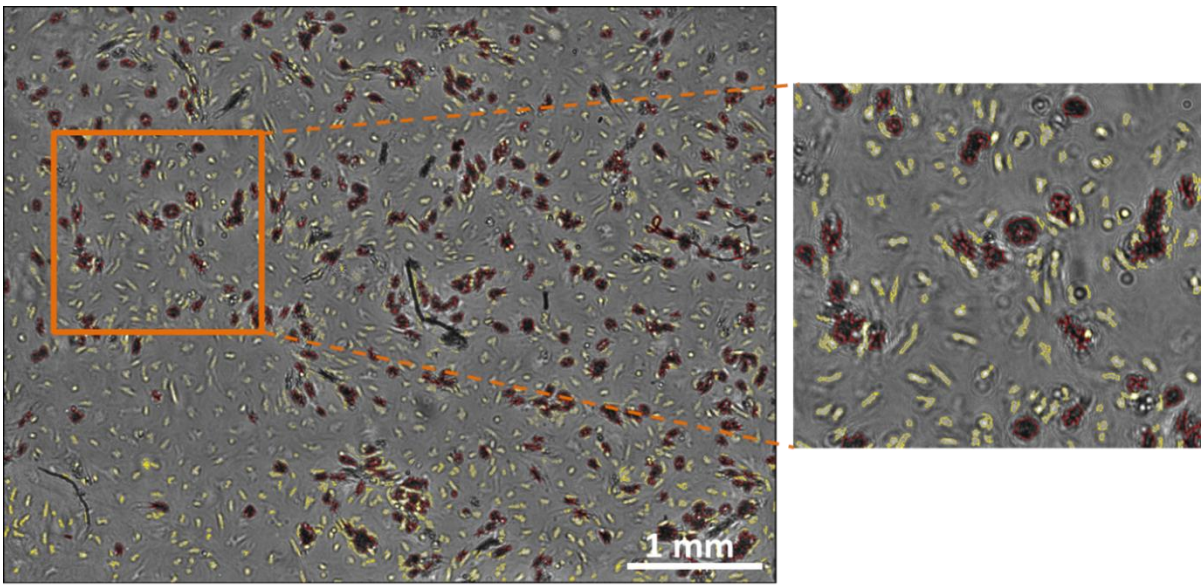

Figure 3C.5: Gray-level based detection of differentiated and non-differentiated cells. Full FOV image containing thousands of cells obtained using lensfree video microscope. Image shows a mixed population of differentiated and non-differentiated cells at the end of the experiment (t0 + 22 days). By using gray-level intensity difference, non-differentiated and differentiated cells are discriminated and are outlined in yellow and red respectively.

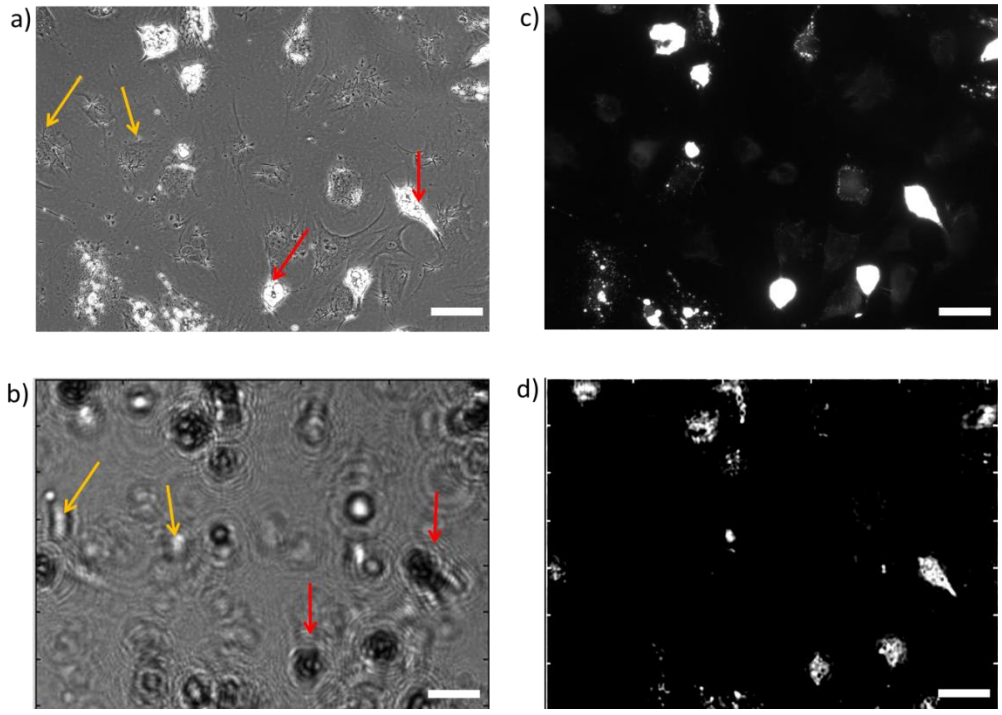

Figure 3C.6: Comparison with standard lens-based microscopic images. Scale bar: 100µm

a) Standard lens-based microscopic image (Yellow and red arrow marks denote non-differentiated and differentiated cells respectively)

b) Same region of interest observed by lensfree video microscope (Yellow and red arrow marks denote holographic patterns of non-differentiated and differentiated cells respectively)

c) Fluorescent image obtained using lens-based microscope showing adipocytes stained with oil red O.

d) Marker-free reconstruction and segmentation of lensfree image showing the adipocytes. The size and the shape of the reconstructed adipocytes compares well with the fluorescent image (c).

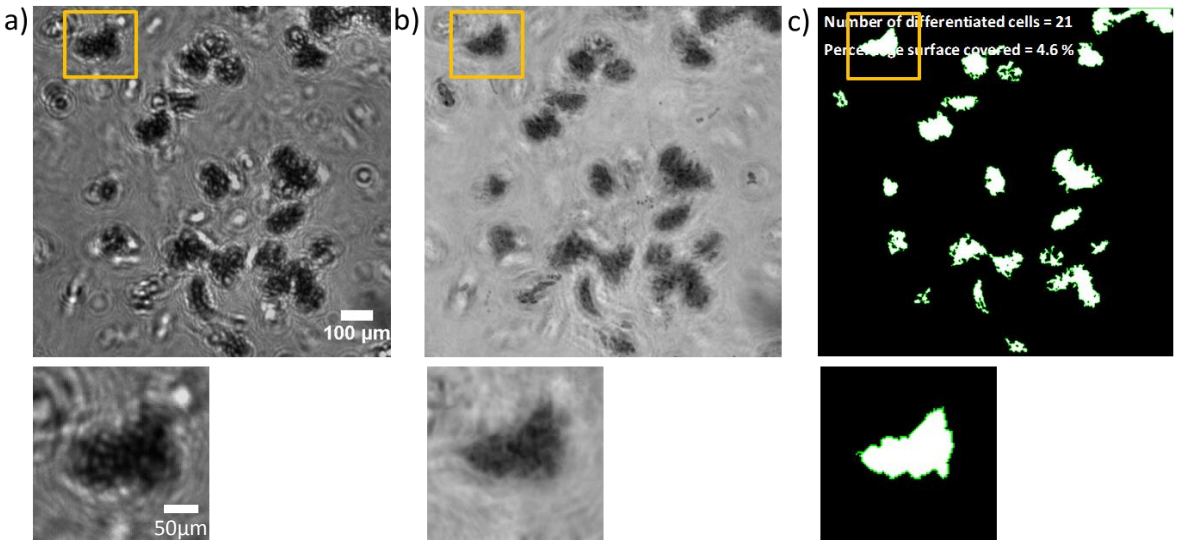

Figure 3C.7: Reconstruction and segmentation of differentiated adipocytes.

a) Lensfree raw hologram

b) Amplitude reconstruction of (a)

c) Segmentation based on gray-level thresholding of (b)

Images at the bottom are digital magnifications of regions of interest marked by yellow squares in (a), (b) and (c).

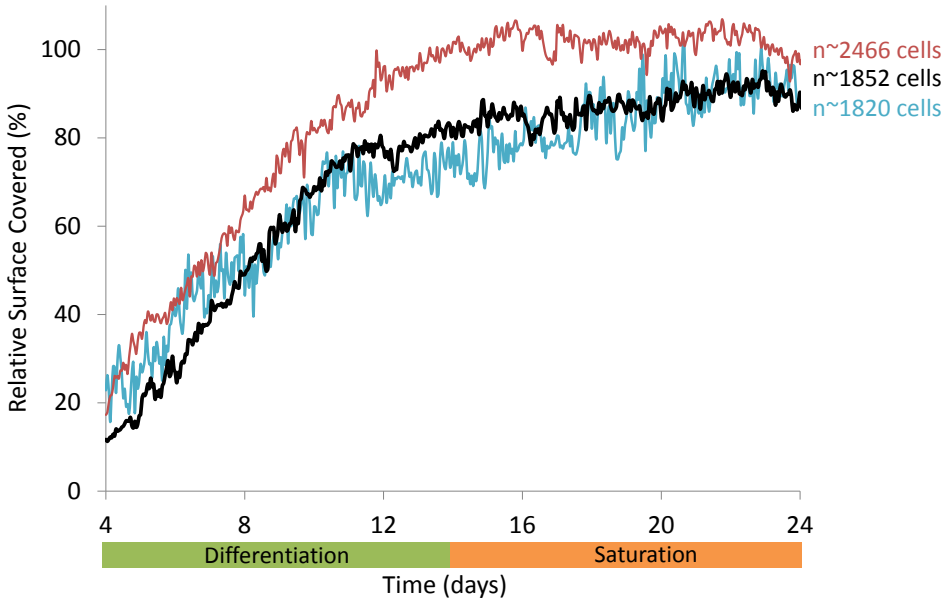

Figure 3C.8: Kinetics of adipogenic differentiation. Kinetics obtained by determining the relative surface covered by the adipocytes. Three culture dishes were observed from 4 days post addition of differentiation media. Initially, the surface area covered by adipocytes increased considerably for ~ 14 days (from 20±10% to 75±10%) post

differentiation trigger, before attaining a saturation point. By 24 days, the relative surface area covered reached values greater than 80%. The number of cells monitored (cell count of the population before the addition of differentiation media) were n~1820 (blue), n~1852 (black), n~2466 (red).

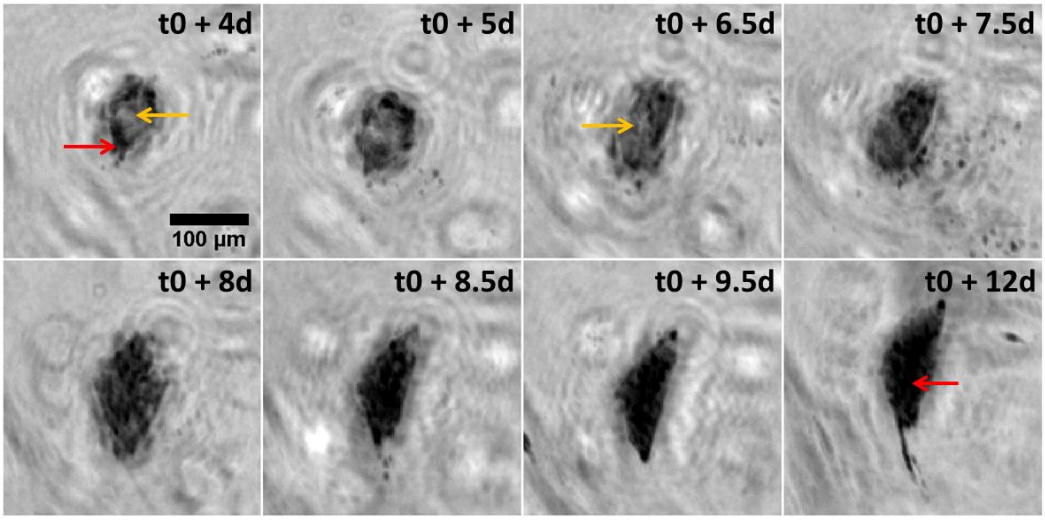

Figure 3C.9: Different stages of adipogenic differentiation. Image reconstruction permits the observation of different stages of adipogenic differentiation. The dark spots correspond to lipid droplets. Time t0 marks the addition of differentiation media. For the cell in consideration, differentiation started at t0 + 4 days (note the few dark spots along the border of the cell denoted by red arrow, while the interior of the cell remained to be filled: yellow arrow) and gradually progressed over the following 10 days. At t0 + 12 days, the cell was entirely filled with lipid droplets (red arrow t0 + 12 days).

3C.2.2 Neuronal differentiation

Neuronal differentiation process is accompanied by change in structure of the cell along with neurite outgrowth (axons, dendrites) as shown in **Fig. 3C.2.** Neuronal differentiation was triggered in 2 steps, by adding 2 differentiation culture media at t0 and t0 + 24 hours **(methods)**. The time-lapse lens-based video microscopic images of neuronal differentiation are shown in **Fig. 3C.10.** The reduction in size of the cell body is evident along with neurite formation **(Fig 3C.10. red arrow)**. A similar process is also seen from both raw lensfree holographic patterns **(Fig. 3C.11a)** and from reconstructed images **(Fig. 3C.11b).** The resolution of lensfree video microscope ~5µm and hence fine structures such as neuritis **(<2µm)** cannot be resolved. However, the differentiation can be visualized through the change in the structure of the cell. The reduction in area of the

cell body during neuronal differentiation is clearly observed by means of lensfree video microscope **(Fig. 3C.11).**

We followed neuronal differentiation kinetics of 3 different conditions (1mM, 5mM, and 7.5mM β-mercaptoethanol (BME) by following the reduction in the area of cell body **(Fig. 3C.12)**. As mentioned earlier, the differentiation process was triggered in 2 steps. The first step is the addition of 1mM BME 24 hours after cell seeding. The second step is the addition of 1mM, 5mM, or 7.5mM BME to the culture dishes, 24 hours after the addition of differentiation media 1. We followed the reduction in mean area of cell body, of a population of 800 ± 100 cells (S.D. of number of cells present in the field of view from N = 3 experiments), with respect to the concentration of BME. After the addition of differentiation media 1, the area of the cell body reduces from 740μm^2 ± 10 μm^2 to 670μm^2 ± 10μm^2 (S.D., is the deviation in the mean area of cell body of n~800 cells from N=3 experiments) for all the cases. After the addition of differentiation media 2, the area of cell body decreases only by ~10μm^2 for 1mM BME, but for 5mM and 10mM BME, the area of cell body decreases by ~ 60μm^2 in ~16 hours and reaches a stable value of 590μm^2 (±5μm^2: local variations in mean area of the cell body after the population has reached stability).

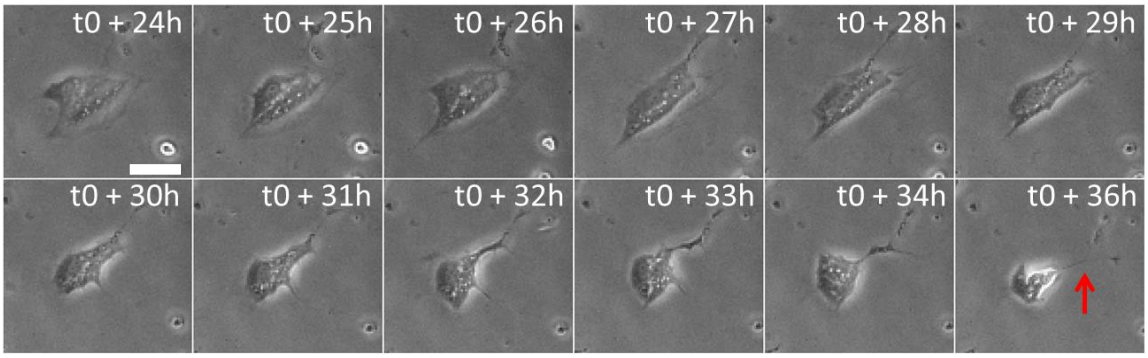

Figure 3C.10: Time-lapse lens-based microscopic image of neuronal differentiation.Images show the changes in structure of a cell during neuronal differentiation. The elongated cell (t0 + 24h) becomes highly circular (t0 + 36h) accompanied by fine neurite outgrowth (t0 + 36h red arrow). Time t0 denotes the addition of differentiation media 1, and t0 + 24h denotes the addition of differentiation media 2. Scale bar: 50µm.

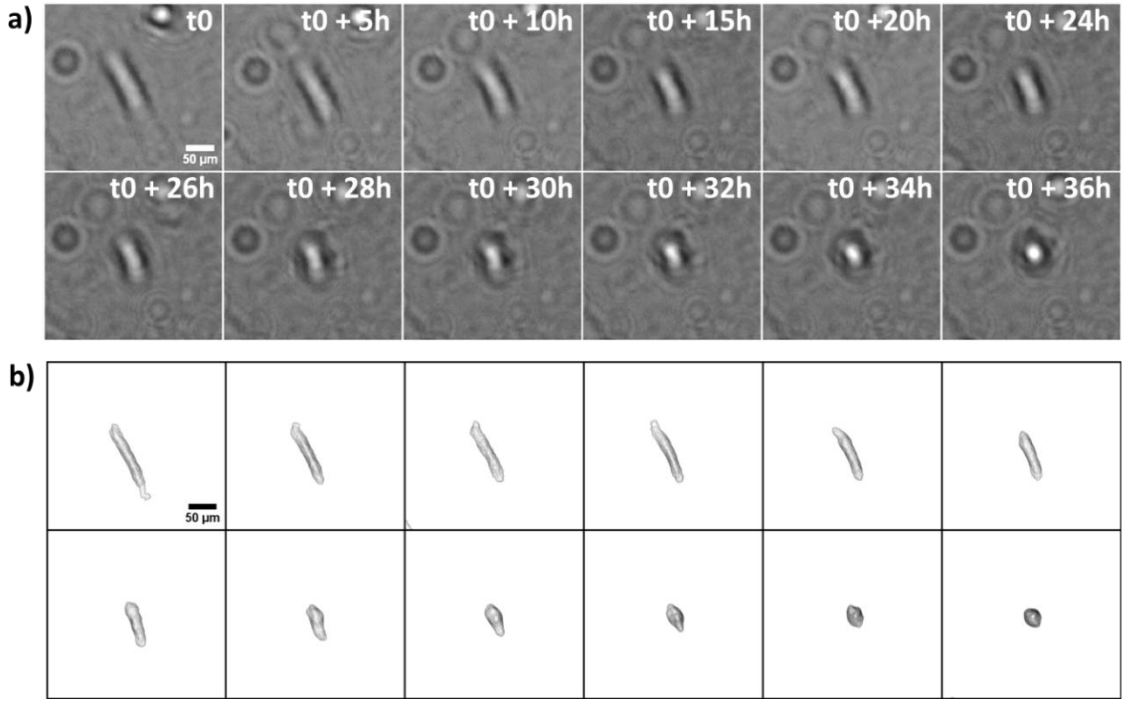

Figure 3C.11: Neuronal differentiation of a single hMSC. Change in structure of the cell during neuronal differentiation is evident from both raw lensfree holographic patterns (a) and reconstructed images (b). Time t0 marks the addition of differentiation media. The area of cell body of this particular cell reduced from 2345µm² to 645µm² in 36 hours following the addition of differentiation media.

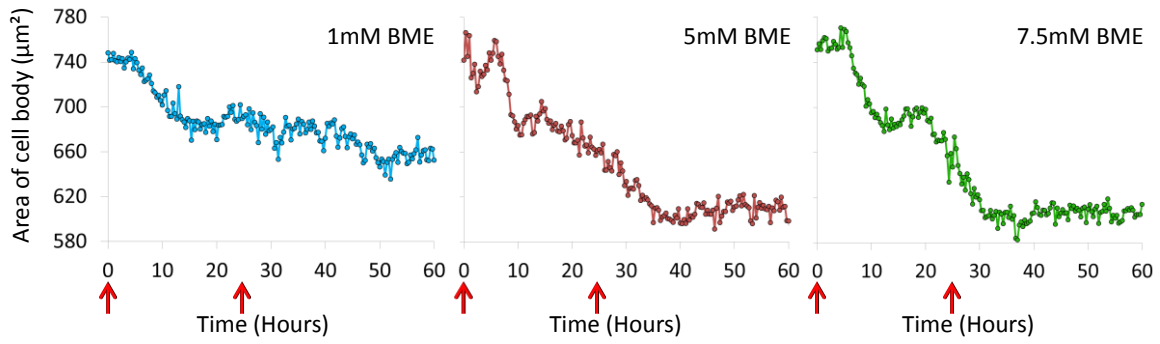

Figure 3C.12: Kinetics of neuronal differentiation. Reduction in mean area of cell body (n = 800 ± 100 cells, S.D. resulting from difference in counted number of cells in the field of view), with respect to the concentration of BME. The red arrows indicate the moment of addition of differentiation media 1 and 2, at 0h and 24h respectively (Time 0h denotes the addition of differentiation media 1 and not to be confused with the moment of cell seeding). The differentiation media 1 has the same concentration of 1mM BME. Differentiation media 2, has different BME concentrations of 1mM, 5mM, and 7mM. After the addition of differentiation media 1, the area of the cell body reduces from 740µm²± 10 µm² to 670µm²± 10µm² (S.D., is the deviation in the mean area of cell body of n~800 cells from N=3 experiments) for all the cases. After the addition of differentiation media 2, the area of cell body decreases only by ~10µm² for 1mM BME, but for 5mM and 7.5mM BME, the area of cell body decreases by ~ 60µm² in ~16 hours and reaches a stable value of 590µm² (±5µm² local variations in mean area of the cell body after the population has reached stability)

3C.3 DISCUSSION

Cahan et al., discusses about the myriad possible transitions between cellular states and their potential applications in drug screening and regenerative medicine (Cahan et al., 2014). However, to bring this to reality, firstly, cell differentiation mechanisms need to be clearly understood and several factors that influence cell differentiation need to be studied extensively, to which robust quantification methods are a prerequisite. By performing real-time, label-free, high-throughput monitoring of cell differentiation, lensfree video microscope and dedicated image processing provides an alternative perspective to cell differentiation. Unlike other quantification assays where destroying of differentiated cells for end-point label-dependent quantification is inevitable, our approach remains entirely non-invasive which, is highly beneficial in cell differentiation

experiments that often involve rare and expensive cell types. Also, non-invasiveness of the method implies that the cells that are differentiated may be used for further manipulations: live monitoring of differentiation followed by de-differentiation of the same population is an exciting prospect.

With our lensfree video microscope we have demonstrated quantification of adipogenic and neuronal differentiation. Visualizing adipogenic differentiation would appear facile since cells undergo vast change during the process. However, it is to be noted that, our method visualizes also the gradual formation of droplets inside the cell body with intracellular resolution **(Fig. 3C.9).** In both cases, neuronal and adipogenic differentiation, using changes in structure of the cell, we observed the kinetics of both single cells and entire population. In the case of neuronal differentiation, we were able to discriminate the effect based on concentrations of BME. The difference in concentration is clearly observed between 1mM, and the rest. However, the difference was not observed between 5mM and 7.5mM. This could be due to (i) absence of significant effects between the 2 concentrations, or (ii) limitation of our approach to demarcate the effects. Further experiments that are foreseen by using different concentrations of BME could explain.

Since change of structure is a major step in most types of cell differentiation **(Fig. 3C.13)**, we envisage the possibility of applying lensfree video microscope along with dedicated image analysis to detect and quantify other types of cell differentiation as well.

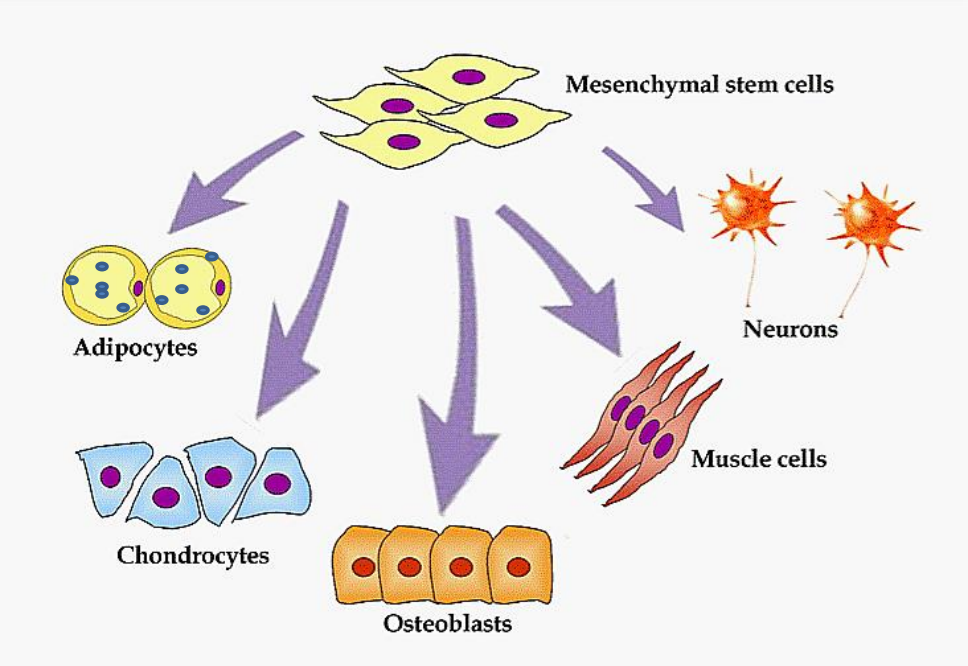

Figure 3C.13: Mesenchymal stem cell differentiation to other types. Schematic diagram show some examples of MSC differentiation to other types. As depicted in the schematic diagram, there is a change in structure, shape associated with differentiation process, which could be means to detect differentiation using lensfree video microscope. Schematic diagram reproduced from (Meregalli, Farini, & Torrente, 2011)

3C.4 METHODS

3C.4.1Computational methods

Reconstruction of lensfree holographic pattern is performed as explained earlier (chapter 2). The amplitude reconstruction of single Fresnel back-propagation yields the size and shape of the differentiated adipocytes as shown in **Fig. 3C.7b**. From the reconstructed image **(Fig. 3C.7b)**, adipocytes are segmented based on gray value thresholding **(Fig. 3C.7c)**, and relative percentage surface area covered (relative to the percentage covered by non-differentiated cells, before the addition of the differentiation media) is determined **(Fig. 3C.7c).**

For neuronal differentiation, reconstruction of the raw image and segmentation of the cells are performed as mentioned above. Mean area of the cell body is obtained from segmented image.

3C.4.2 Cell culture methods

HMSCs were cultured adhering to the same protocol mentioned in chapter 3A.4.2.

For adipogenic differentiation, hMSCs were incubated in petri dish at the density of $5x10^3$ cells/cm2 in the proliferation media. When, the confluency of cells were attained 70-80%, the media of proliferation were removed and the differentiation media consisting of Dubelcco's modified Eagle's medium (DMEM) with 1g/L glucose (Invitrogen) supplemented with 20% FBS, 60µM Indomethacin, 0.5mM 3-Isobutyl-1-methylxanthtine and 10-6M dexamethasone (Sigma Aldrich) were added. The media was replaced every 3-4 days.

For neuronal differentiation, hMSC were maintained in culture dish in proliferation media supplemented with 1mM β-mercaptoethanol (BME) (differentiation media 1) during 24h. The media was changed with a differentiation media (differentiation media 2) consisting of DMEM supplemented with 1-7.5mM of BME (Black & Woodbury, 2001).

REFERENCES

Arnulf, B., Lecourt, S., Soulier, J., Ternaux, B., Lacassagne, M.-N., Crinquette, a, … Larghero, J. (2007). Phenotypic and functional characterization of bone marrow mesenchymal stem cells derived from patients with multiple myeloma. *Leukemia*, *21*(1), 158–63. doi:10.1038/sj.leu.2404466

Benvenuti, S., Saccardi, R., Luciani, P., Urbani, S., Deledda, C., Cellai, I., … Peri, A. (2006). Neuronal differentiation of human mesenchymal stem cells: changes in the expression of the Alzheimer's disease-related gene seladin-1. *Experimental cell research*, *312*(13), 2592–604. doi:10.1016/j.yexcr.2006.04.016

Bianco, P., Robey, P. G., & Simmons, P. J. (2008). Mesenchymal stem cells: revisiting history, concepts, and assays. *Cell stem cell*, *2*(4), 313–9. doi:10.1016/j.stem.2008.03.002

Black, I. B., & Woodbury, D. (2001). Adult rat and human bone marrow stromal stem cells differentiate into neurons. *Blood cells, molecules & diseases*, *27*(3), 632–6. doi:10.1006/bcmd.2001.0423

Cahan, P., Li, H., Morris, S. A., Lummertz da Rocha, E., Daley, G. Q., & Collins, J. J. (2014). CellNet: Network Biology Applied to Stem Cell Engineering. *Cell*, *158*(4), 903–915. doi:10.1016/j.cell.2014.07.020

Chen, J., Li, Y., Wang, L., Zhang, Z., Lu, D., Lu, M., & Chopp, M. (2001). Therapeutic Benefit of Intravenous Administration of Bone Marrow Stromal Cells After Cerebral Ischemia in Rats. *Stroke*, *32*(4), 1005–1011. doi:10.1161/01.STR.32.4.1005

Dezawa, M., Ishikawa, H., Itokazu, Y., Yoshihara, T., Hoshino, M., Takeda, S., … Nabeshima, Y. (2005). Bone marrow stromal cells generate muscle cells and repair muscle degeneration. *Science (New York, N.Y.)*, *309*(5732), 314–7. doi:10.1126/science.1110364

Gorjup, E., Peter, L., Wien, S., von Briesen, H., & Schmitt, D. (2009). Automated microscopic quantification of adipogenic differentiation of human gland stem cells. *Annals of anatomy = Anatomischer Anzeiger : official organ of the Anatomische Gesellschaft*, *191*(1), 13–22. doi:10.1016/j.aanat.2008.09.003

Lee, H. J., Lee, J. K., Lee, H., Shin, J., Carter, J. E., Sakamoto, T., … Bae, J. (2010). The therapeutic potential of human umbilical cord blood-derived mesenchymal stem cells in Alzheimer's disease. *Neuroscience letters*, *481*(1), 30–5. doi:10.1016/j.neulet.2010.06.045

Lo Surdo, J. L., Millis, B. a, & Bauer, S. R. (2013). Automated microscopy as a quantitative method to measure differences in adipogenic differentiation in preparations of human mesenchymal stromal cells. *Cytotherapy*, *15*(12), 1527–40. doi:10.1016/j.jcyt.2013.04.010

Meregalli, M., Farini, A., & Torrente, Y. (2011). Mesenchymal Stem Cells as Muscle Reservoir. *Journal of Stem Cell Research & Therapy*, *01*(02), 1–9. doi:10.4172/2157-7633.1000105

Murphy, M. B., Moncivais, K., & Caplan, A. I. (2013). Mesenchymal stem cells: environmentally responsive therapeutics for regenerative medicine. *Experimental & molecular medicine*, *45*(11), e54. doi:10.1038/emm.2013.94

Prockop, D. J. (1997). Marrow Stromal Cells as Stem Cells for Nonhematopoietic Tissues. *Science*, *276*(5309), 71–74. doi:10.1126/science.276.5309.71

Scott, M. a, Nguyen, V. T., Levi, B., & James, A. W. (2011). Current methods of adipogenic differentiation of mesenchymal stem cells. *Stem cells and development*, *20*(10), 1793–804. doi:10.1089/scd.2011.0040

Vemuri, M. C., Chase, L. G., & Rao, M. S. (2011). *Mesenchymal stem cell assays and applications.Methods in molecular biology (Clifton, N.J.)* (Vol. 698, pp. 3–8). doi:10.1007/978-1-60761-999-4_1

Wei, X., Yang, X., Han, Z., Qu, F., Shao, L., & Shi, Y. (2013). Mesenchymal stem cells: a new trend for cell therapy. *Acta pharmacologica Sinica*, *34*(6), 747–54. doi:10.1038/aps.2013.50

Xuan, a G., Luo, M., Ji, W. D., & Long, D. H. (2009). Effects of engrafted neural stem cells in Alzheimer's disease rats. *Neuroscience letters*, *450*(2), 167–71. doi:10.1016/j.neulet.2008.12.001

CHAPTER 3D

MONITORING CELL DEATH

Pg. 108	**EXISTING CELL VIABILITY ASSAYS**
Pg. 112	**CELL DEATH: CELL DETACHMENT** **siCellDeath transfection of U2OS cells**
Pg. 116	**CELL DEATH: CHANGES IN CELL SHAPE** **siCellDeath transfection of human Mesenchymal Stem Cells (hMSCs)**
Pg. 120	**APLICABILITY TO DIFFERENT SUBSTRATES AND CELL TYPES**

3D. MONITORING CELL DEATH

3D.1 INTRODUCTION

Premature termination or uncontrolled prolongation of a cell's life is directly responsible for degenerative disorders, auto-immune diseases, and cancer. Hence, factors that play a role in causing or counteracting cell death and the various mechanisms involved in cell death are extensively studied (Bano, Zanetti, Mende, & Nicotera, 2011; Barski, Michel, & Ba, 2014; Chiong, Quest, Lavandero, & Stutzin, 2005; Crews & Masliah, 2010; Hitzmann & Ueffing, 2013; Jellinger, 2001; Mc, Zenteno, Chávez, & Lascurain, 2009; Orrenius, Nicotera, & Zhivotovsky, 2011; Reed & Pellecchia, 2012; Reed, 2011; Rønn et al., 2000; Surova & Zhivotovsky, 2012; Tyson, Garbett, Frick, & Quaranta, 2012; Yuan & Kroemer, 2010; Zeng et al., 2014; Zhang et al., 2009). Cell viability assays are imperative to perform these studies. Particularly, real-time monitoring is essential to study the time-dependent kinetics of cell death. A review of cell viability assays from O. Kepp et al., discusses about combination of various assays and technological platforms that are currently used (Kepp, Galluzzi, Lipinski, Yuan, & Kroemer, 2011)**(Table 3D.1)**. Out of these, only 2 platforms allow real-time monitoring of cell death, which are lens-based time-lapse video microscopy, and impedance reader. Limited field of view, cost, complexity and requirement of labels are limitations of video microscopy. Inability to visualize the cells and being indirect are the limitations of substrate impedance techniques. Hence partial kinetics of cell death is mostly derived from series of end-point measurements. End-point measurements using cytometer requires cell harvesting. Cell harvesting is complicated to perform, because during cell death, due to associated cell detachment, not all the cells in the population have same degree of attachment to the substrate.

Method	Technological platform	Main advantages	Main disadvantages	Recommended for HTS*
ATP consumption	Luminometer	Rapid and highly sensitive	• Highly sensitive to metabolism-related ATP fluctuations • Cannot identify cell death modes	1
Autophagic flux	Luminometer	Rapid	• Expensive	2
	Fluorescence microscopy	Allows real-time monitoring	• Different inducers might influence the pH of the lysosomes	2
	Immunoblotting	Assessed by routine methods	• Time-consuming	N/A
Autophagosome quantification	Electron microscopy	Provides precise ultrastructural information	• Expensive and time-consuming	N/A
	Fluorescence microscopy	Rapid and inexpensive	• Cannot distinguish between increased autophagy and decreased degradation	1
Caspase activation (fluorescent substrates or FRET constructs)	Cytofluorometry	Allows automated analyses on a per-cell basis	• Caspase activation may occur in cell death-unrelated settings • Fluorescent substrates may emit upon unspecific degradation	2
	Fluorescence reader	Rapid		1
	Fluorescence microscopy	Can be coupled with other cell-death markers		1
Cell detachment	Impedance reader	Allows real-time monitoring	• Unable to discriminate between different cell death modes	2
$\Delta\psi_m$ dissipation	Cytofluorometry	Rapid, inexpensive and no need for permeabilization	• Temporary $\Delta\psi_m$ dissipation may occur in cell death-unrelated settings • Fixable probes are suitable for end-point determinations only	2
	Fluorescence microscopy	Non-fixable probes allow for real-time $\Delta\psi_m$ monitoring		1
Extracellular release of proteins	Absorbance reader	Inexpensive	• Unable to discriminate between different cell death modes	1
	Fluorescence microscopy	Allows the study of late events and is applicable to real-time monitoring	• Detection might be aggravated by morphological changes of dying cells	1
Immunological methods	Cytofluorometry	Allows automated analyses on a per-cell basis	• Rely heavily on the performance of primary antibodies • Poorly expressed antigens may be under-detected or undetected • Antigens may get denatured during sample processing	2
	Electron microscopy	Irreplaceable for precise colocalization studies		N/A
	Fluorescence microscopy	Compatible with sample fixation and storage		1
	Immunoblotting	Allows the study of early biochemical parameters		N/A
	Light microscopy	Allows the detection of early cell death-related events		N/A
IMS protein release	Fluorescence microscopy	Release of fusion proteins can be followed in real-time	• Release of more than one IMS protein must be assessed to avoid false positive results	N/A
	Immunoblotting	Subcellular fractionation allows the detection of multiple proteins		1
LC3 lipidation	Immunoblotting	Assessed by routine methods	• Expensive and time-consuming	N/A
Mitochondrial swelling	Absorbance reader	Allows the study of mitochondria in the absence of metabolic interference	• Laborious and time-consuming	N/A
Morphological determinations	Electron microscopy	Provides precise ultrastructural information	• Expensive	N/A
	Fluorescence microscopy	Inexpensive and fixable dyes available	• Morphological alterations can be caused by cell death-independent mechanisms	N/A
	Light microscopy	Rapid and inexpensive, can be used for monitoring cell cultures	• Prone to underestimation, unsuitable for quantitative studies	1
PS exposure	Cytofluorometry	Rapid, specific for an early event of apoptosis execution	• PS exposure can occur independently of apoptosis	2

Method	Technological platform	Main advantages	Main disadvantages	Recommended for HTS*
ROS overgeneration	Cytofluorometry	Inexpensive	• ROS generation can occur independently of cell death	N/A
	Fluorescence microscopy			N/A
Tetrazolium salt conversion	Absorbance reader	Rapid and inexpensive	• Cannot discriminate between cytotoxic and antiproliferative effects	1
Translocation of cell death mediators	Fluorescence microscopy	Applicable for live cell monitoring	• Detection might be complicated by morphological changes of dying cells	1
Detection of DNA-strand breaks	Cytofluorometry	Useful in co-staining protocols; compatible with long term sample storage	• TUNEL positivity can derive from sample processing • Expensive	N/A
	Fluorescence microscopy			N/A
	Light microscopy	Seen as the gold standard for detecting cell death *in situ* (in tissues slides) by IHC		N/A
Vital dyes	Cytofluorometry	Routinely employed in co-staining protocols	• Unable to discriminate between different cell death modes	1
	Fluorescence microscopy	Facilitates the identification of dead cells by visual inspection		1

Table 3D.1: Cell viability assays. Table reproduced from (Kepp et al., 2011) with permission (Annex), lists currently used cell viability assays. Out of these, only 2 platforms allow real-time monitoring (boxed in blue), fluorescence video microscope, and impedance reader.

3D.2 RESULTS

As a preliminary example, we can observe the cell death of NIH3T3 Cells adhered to micro-patterns (Cytoo™), from the perspective of lensfree video microscope **(Fig. 3D.2)**. Massive changes in the cell population are evident from raw lensfree holograms. Usually, cell death is accompanied by intense changes that occur in the size, shape and structure of the cell, including also changes related to cell-substrate adhesion. Lensfree video microscope and associated metrics monitors these changes, considering them as natural markers, to pronounce death of cells.

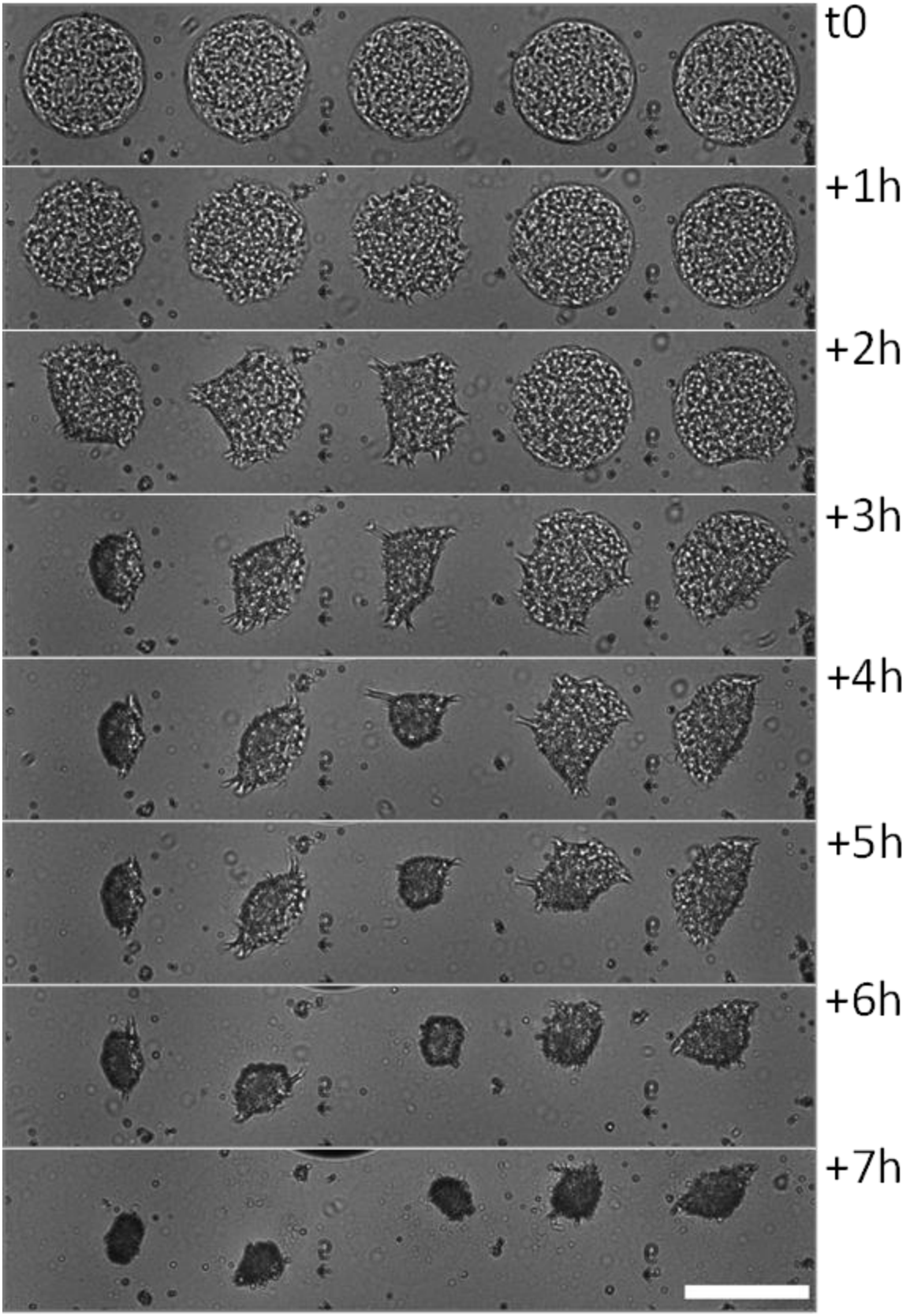

Figure 3D.2: Cell death observed by lensfree video microscopy. Real-time observation of cell death of NIH3T3 cells adhered to disc shaped Cytoo™ micro-patterns. Cells were subjected to 45°C for a period of ~7 hours. Scale bar: 500µm.

In order to monitor more subtle effects of cell death at single cell level, we introduce 2 metrics for the detection of cell death using lensfree video microscope. The first metric monitors cell death by detecting the changes in the gray value associated with cell detachment. The method is applied on raw image and does not require holographic reconstruction. The second method employs holographic reconstruction to detect the changes in cell morphology to monitor cell death. We followed cell death kinetics on 2 different cell types: U2OS, and hMSC. In both the cases, cell death was induced by forward transfection using the positive cell death phenotype control siRNA (siCellDeath) **(Methods).**

3D.2.1 Cell death of U2OS cells

A comparison of regions of interest, comprising live and dead cells, imaged by lens-based and lensfree microscopy are seen in **Fig. 3D.3**. The difference in the gray-level of the hologram obtained from floating and adhered cell can be observed. As stated earlier (chapter 3A), the gray value at the center of the hologram obtained from a floating cell is much lower compared to that of an adherent cell. Thus change in zero-order gray value is expected when cells detach during cell death. We observe this in **Fig. 3D.4a**, where a single U2OS cell experiences cell death, upon transfection of siCellDeath. At t = t0+35h, the gray value of the cell changes instantaneously as it detaches from the substrate. **Fig 3D.4b** shows the change in the gray value of 10 U2OS cells during cell death. The transfection was performed at t = t0. After 28 hours, the gray values plummeted from 211 ± 40 gray-levels (S.D. n = 10 single cells) to 70 ± 20 gray-levels (S.D. n = 10 single cells) emphasizing the detachment of the cells from the substrate.

It is further illustrated in a much larger scale from the scatter plot of the entire population containing more than 900,000 measurements from 3506 ± 228 cells (S.D. resulting from

local variation in cell counting over the period of observation before the onset of cell detachment) over a period of 90 hours **(Fig. 3D.4c).**The scatter plot represents the cell population from the time of cell plating to the time of cell death. Initially at t = t0-20h, the cells were afloat with gray values between 60 and 100 gray-levels **(Fig.3D.4c: region A).** Within first 10 hours (from t = t0-20h to t =t0-10h), more than 75% of the cells adhered to the substrate, as shown by the increase in gray values. T = t0 marks the moment of transfection **(Fig.3D.4c: region B).** The effect of transfection is visible in **(Fig.3D.4c: region C)**, from t = t0+22h. At this stage, nearly 15% of the cells experienced cell death demonstrated by the accumulation of values between 60 gray-levels and 100 gray-levels in the scatter plot. A predominant change is observed only from t = t0+30h, when more than 50% of the cells experienced cell death. At t =t0+40h, the distribution completely reversed compared to t = t0 (immediately after transfection) as ~80% of the cells detached taking gray values between 65 gray-levels and 110 gray-levels. Within the duration of 18h (± 4h) (S.D., n~3500 cells) post transfection, starting from t0+22h (± 1h) (S.D., n~3500 cells) until t0+40h (± 3h) (S.D., n~3500 cells), nearly 80% of the population suffered cell death, testifying the effectiveness of siCellDeath. It is to be noted that the distribution at the start of the experiment (t = t0-20h) and at the end of the experiment (t = t0+70h) are similar. This shows that the gray value of live floating cells is equal to the gray value of dead detached cells. Also,**(Fig.3D.4c: region C)** shows that the detached cells did not reattach to the substrate as long as 20 hours after detachment.

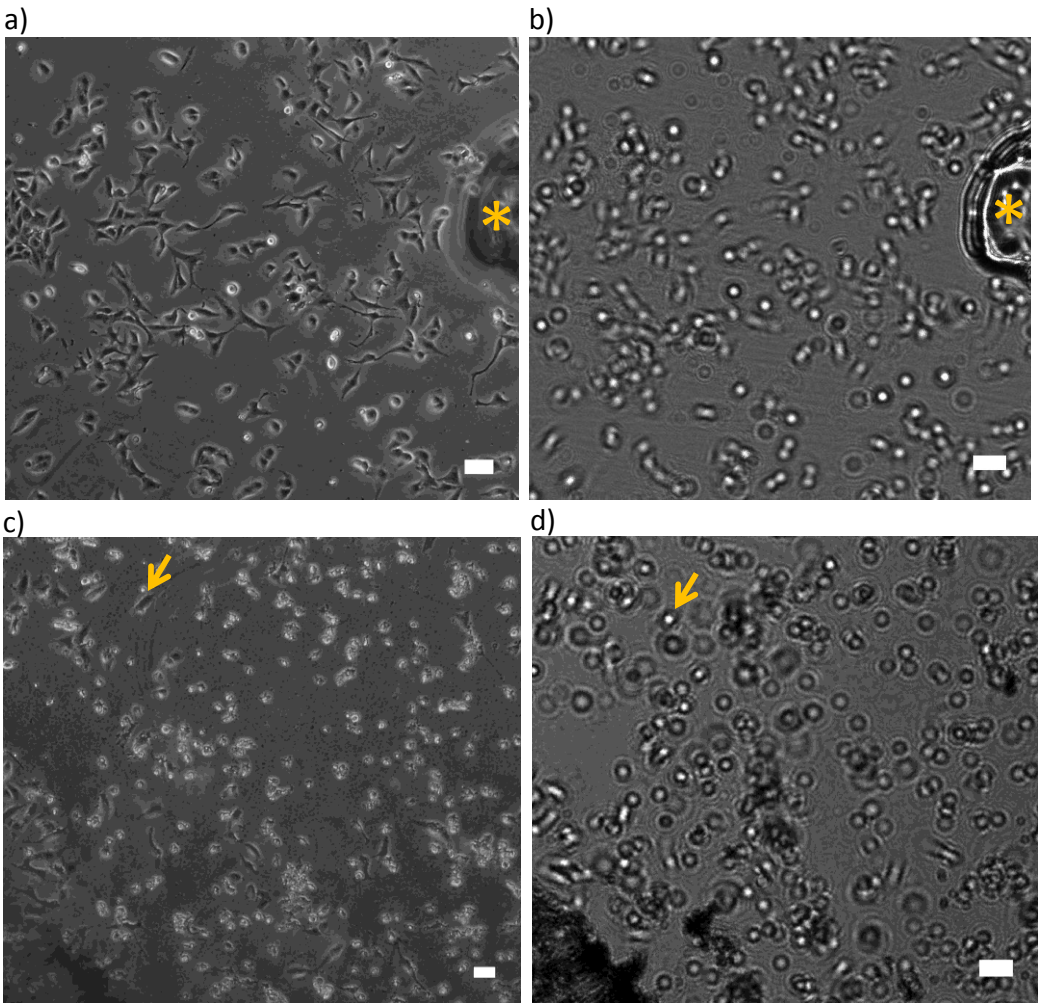

Figure 3D.3: Comparison with lens-based microscopy

(a) Lens-based microscopic image showing U20S cells adhered to the surface.

(b) Corresponding lensfree image showing the same region of interest. The holographic patterns obtained from adhered cells have larger gray values (~200 gray-levels with a background of ~70 gray-levels).

(c) Lens-based microscopic image showing mostly detached dead U2OS cells (cells are mostly round).

(d) Corresponding lensfree image showing detached cells. As cells detach, the gray values of their holographic patterns decrease.

Yellow arrow mark denotes a cell that remained attached to the surface. Note that the attached cells are easier to distinguish from their bright lensfree holographic patterns.

The yellow asterisk symbols show the ink mark for facilitated comparison. Scale bar: 100 µm.

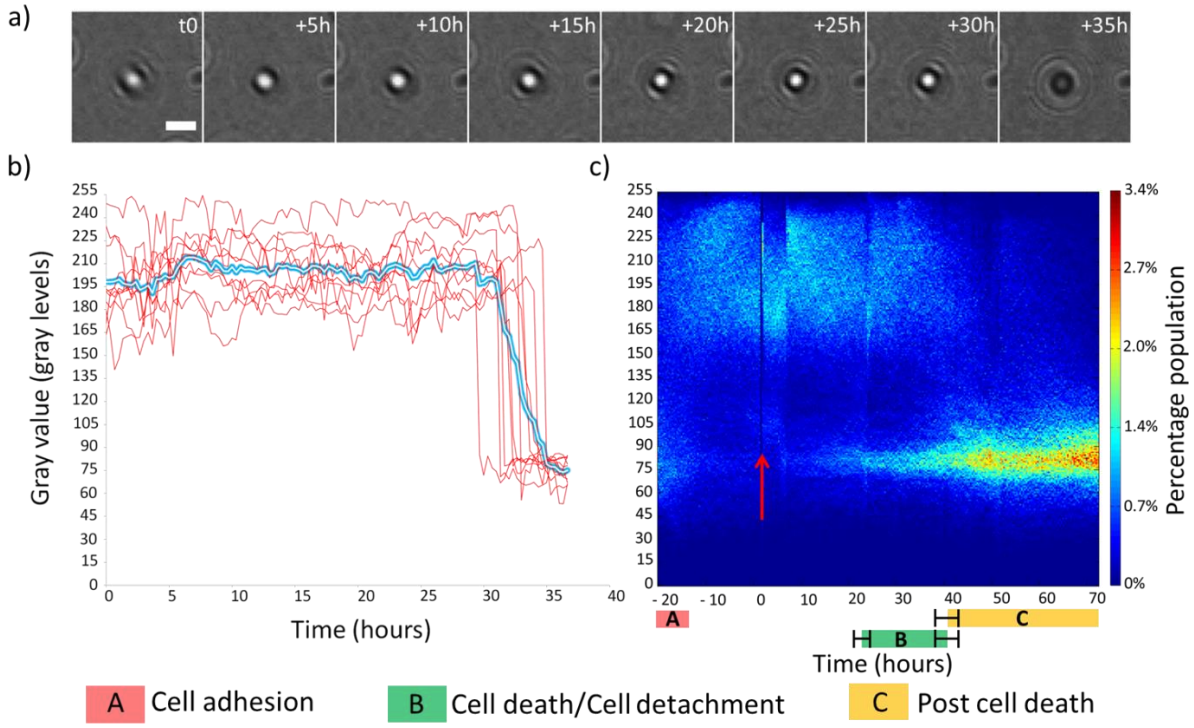

Figure 3D.4: Cell death – human Osteo Sarcoma (U2OS) cells

(a) Time-lapse lensfree holograms obtained from a dying U2OS cell. The cell detaches from the substrate at t = t0+35h (t0 = immediately after transfection), visible from the change in the gray value. Scale bar 50µm.

(b) Change in gray value associated with cell death of 10 U2OS cells along with its mean. siRNA transfection was performed at t = 0h(red arrow).

(c) Scatter plot containing >900,000 gray values obtained from 3506 ± 228 cells over a period of 90 hours. Red arrow denotes the moment of siRNA transfection. Region B denotes the time taken for more than 80% of the cell population to die. Region C shows that the detached cells did not reattach to the substrate. The error margin in regions B, C, is the standard deviation resulting from the local fluctuations in the cell population. Local fluctuation in the population corresponds to the small variation in gray value, ~30 gray-levels, when the cell population is stable (n ~ 3500 cells). This might be due to cell-cell variability or due to automated calculation of gray values.

3D.2.2 Cell death of human Mesenchymal Stem Cells (hMSCs)

We reproduced the same approach to quantify cell death induced by siCellDeath on hMSCs (**Fig. 3D.5a,b)** shows the holograms obtained from a dying hMSC and the reconstructed images, respectively. It is notable from **Fig. 3D.5a** that the change in the gray value associated with cell death was not as significant as it was observed in U2OS cell death **(Fig. 3D.4a).** Although hMSCs retracted from the substrate and became circular, they did not completely detach from the substrate upon cell death (remaining subtly attached). As a consequence, the gray value remained high throughout and did not provide a precise reflection of cell death**.** This is evident from the measurement of gray value from the entire population **(Fig 3D.6)**. Though we see a disturbance in the graph resulting from cell detachment at t0 + 38h **(Fig. 3D.6 blue arrow)**, cell detachment does not result in a significant difference in gray value as it was observed with U2OS cells. For this reason, we measured the change in the aspect-ratio (ratio of minor axis length to the major axis length) of the cells in order to efficiently quantify cell death in the case of hMSCs **(Methods).** Measuring aspect-ratio of cells (from the reconstructed image) provided information on the change in the morphology of cells during cell death. **Fig. 3D.5b** shows the morphological change (rounding) endured by a dying hMSC, clearly visible from the reconstructed images. At t = t0, the cell was well spread with an aspect-ratio close to 0.4 a.u. As the cell became circular due to cell death, the aspect-ratio gradually reached a value close to 0.9 a.u. at t = t0+60h.

A similar effect was observed in the entire population containing 3699 ± 215 cells (S.D., resulting from local variation in cell counting over the period of observation before onset of cell retraction and rounding) **(Fig.3D.5c)**.The cells were monitored from cell plating until cell death for a period of 7.5 days. Due to large population of cells and significant

diversity, mean (of the scatter plot) did not provide an accurate description of cell death. Hence, we segregated the aspect-ratio values from 0.0 to 0.1 a.u. in to 10 ranges. We computed the most populated range (bin corresponding to the max value of the histogram, i.e., the mode value) at each frame ('max plot') **(Fig. 3D.5d).**Initially after cell plating (t = t0-90h), more than 60% of the cell population had an aspect-ratio greater than 0.8 a.u. As the cells spread, the distribution of cell aspect-ratios changed gradually **(Fig. 3D.5c, d: region A)**. The 'max plot' reached 0.4 a.u and remained stable with fluctuations of ± 0.1 a.u (S.D., n ~ 3700 cells. Fluctuations are the differences in aspect-ratio values between subsequent images when the cell population is stable. This may result from cell segmentation and aspect-ratio calculation or from subtle cell-cell differences). siCellDeath transfection was performed at t = t0 **(Fig. 3D.5c, d: red arrow, Methods).** The aspect-ratio values changed gradually from t = t0+23h **(Fig. 3D.5c, d: Region B)**. The rise time of the plot corresponds to the rounding time of dying cells i.e. to the kinetics of cell death. The rise time commenced at t = t0+28h (± 2h) (S.D., n ~ 3700 cells) hours post transfection and reached the final value (~0.9 a.u.) at t = t0+49h (± 3h), lasting 23 ± 3 hours**.** At this stage, it can be observed that more than 70% of the population had an aspect-ratio of 0.8 ± 0.1a.u (S.D., n ~ 3700 cells).**Region C in Fig. 3D.5c, d** shows that the aspect-ratio values did not descend back denoting that the cell rounding due to cell death was irreversible.

It is noteworthy that the distribution towards the end of the experiment is similar to the distribution at the start of the experiment. This states that, in general, the average aspect-ratio is the same, 0.9 ± 0.1 a.u. for both, just adhered living cells and loosely attached dead cells. The decay time and the rise time provided the time taken for the values to descend from 0.9 a.u. to 0.4 a.u. during spreading and then from 0.4 a.u. back to 0.9 a.u. during cell

death. The spreading time of living cells (following cell plating) was 17 ± 2 hours from t = t0-88 h to t = t0-71h (± 2h) (S.D., n ~ 3700 cells) **(Fig. 3D.5c,d: region A).** The rounding time of dying cells was 23 ± 3 h (S.D., n ~ 3700 cells) **(Fig. 3D.5c,d: region B).**

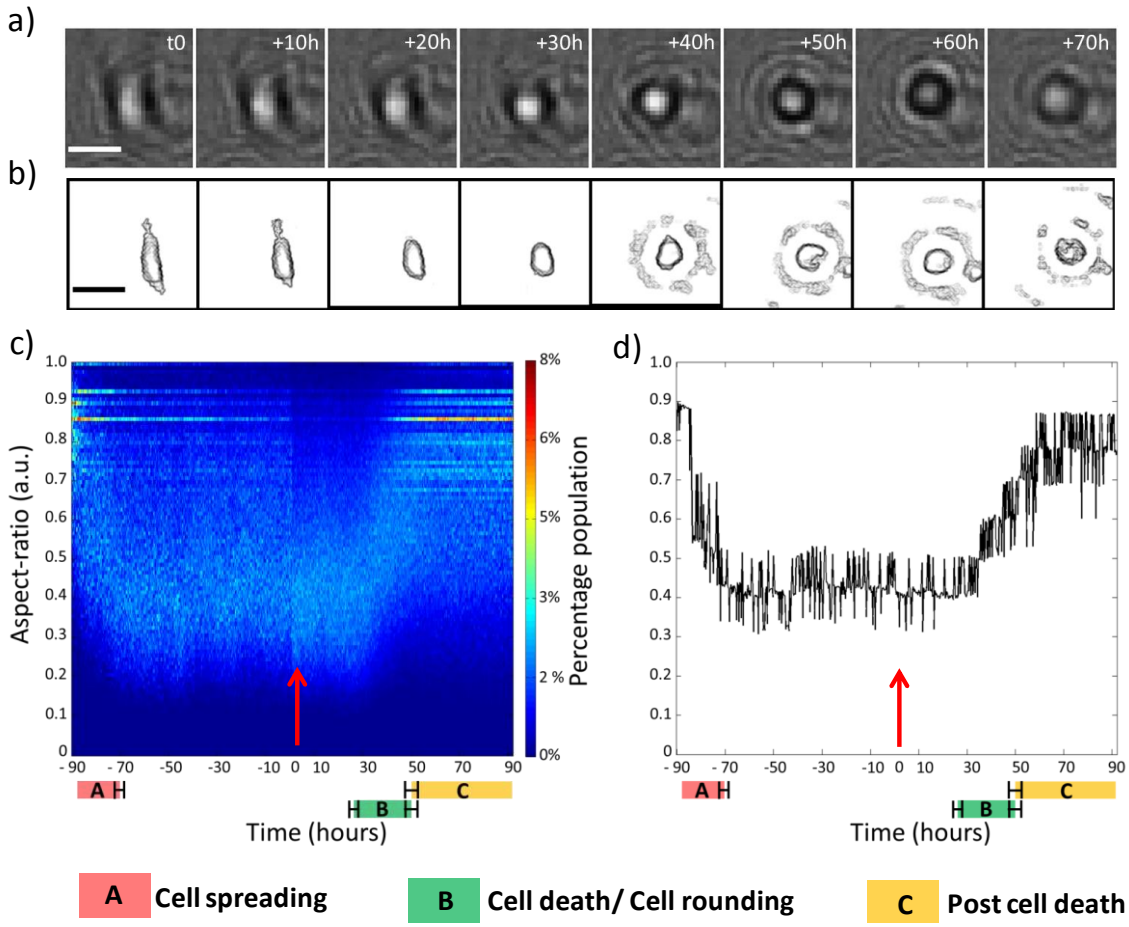

Figure 3D.5: Cell death - hMSCs

(a) Time-lapse lensfree holograms obtained from a dying hMSC. Time t0 marks the moment of transfection. Scale bar 50µm.

(b) Holographic reconstruction and segmentation of (a). Note that the change in the distance between the cell and the imaging sensor that may have occurred from (t = t0+40h until t = t0+70h) was not taken in to account while performing holographic reconstruction. Scale bar 50µm.

(c) Scatter plot showing the changes in the aspect-ratio of 3699 ± 215 cells over 180 hours. Region A and region B shows the time taken for cell spreading and cell death/ cell rounding respectively.

(d) 'max plot' showing the most populated range with an interval of 0.1 a.u.

Error margins in region A, B, C is the standard deviation resulting from the local fluctuation of aspect-ratio values in the cell population (n ~ 3700 cells). These fluctuations may result from automated segmentation and aspect-ratio calculation or from subtle cell-cell variations.

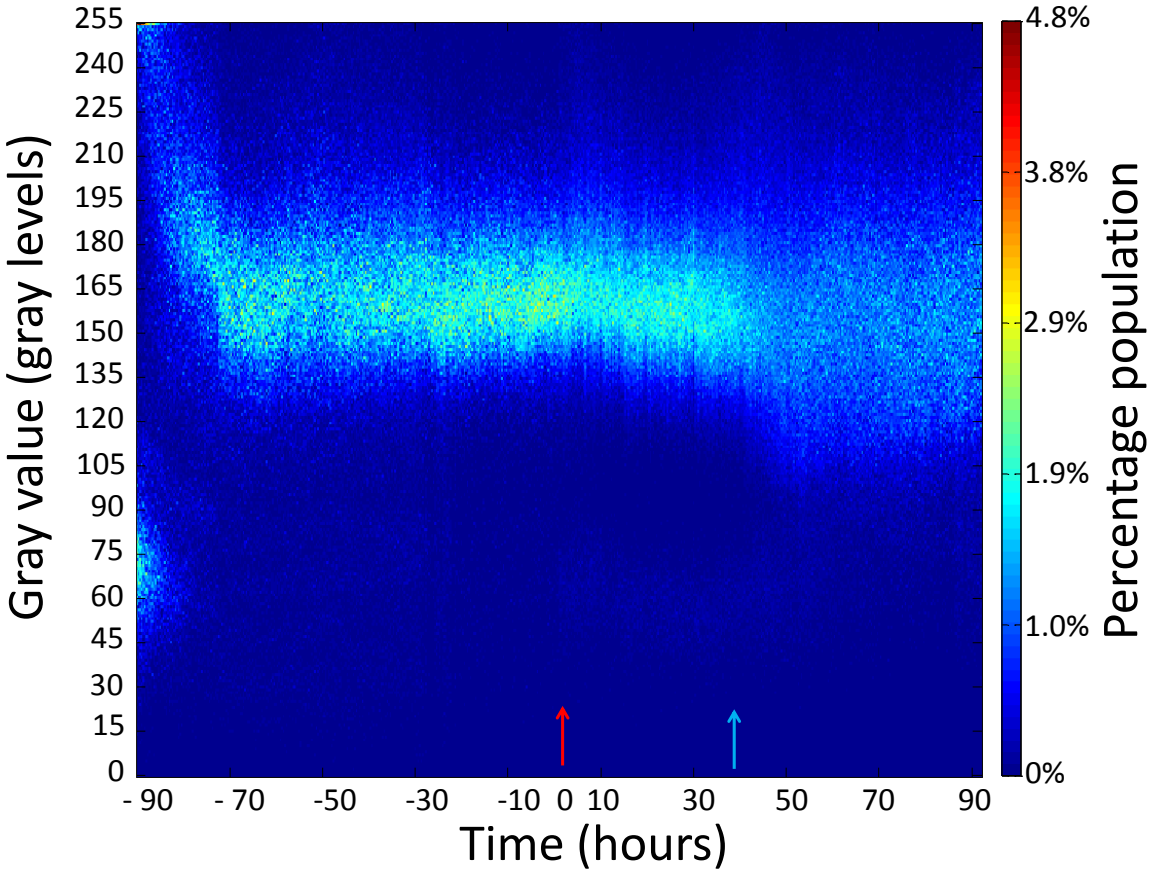

Figure 3D.6: Change in gray value during cell death of hMSCs. Scatter plot showing change in gray value associated with cell death of hMSCs resulting from siRNA transfection (red arrow). Though we see a disturbance in the graph resulting from cell detachment at t0 + 38h (blue arrow), cell detachment does not result in a significant difference in gray value as it was observed with U2OS cells.

3D.2.3 Other cell types and substrates

Cell types such as PC3, DU145 exhibit a change in gray value during cell death **(Fig. 3D.7)**. However, since the cells do not spread well as hMSCs, the aspect-ratio of the cells does not exhibit a major change. Hence like, U2OS cells, cell death can be detected by the loss of cell-substrate adhesion, in other words, by the change in gray value of the pattern.

Whereas, cell types such as NIH3T3 fibroblasts exhibit both change in gray value and change in aspect-ratio during cell death **(Fig. 3D.8)**. The cells exhibit an elongated morphology, and become circular before detaching from the substrate.

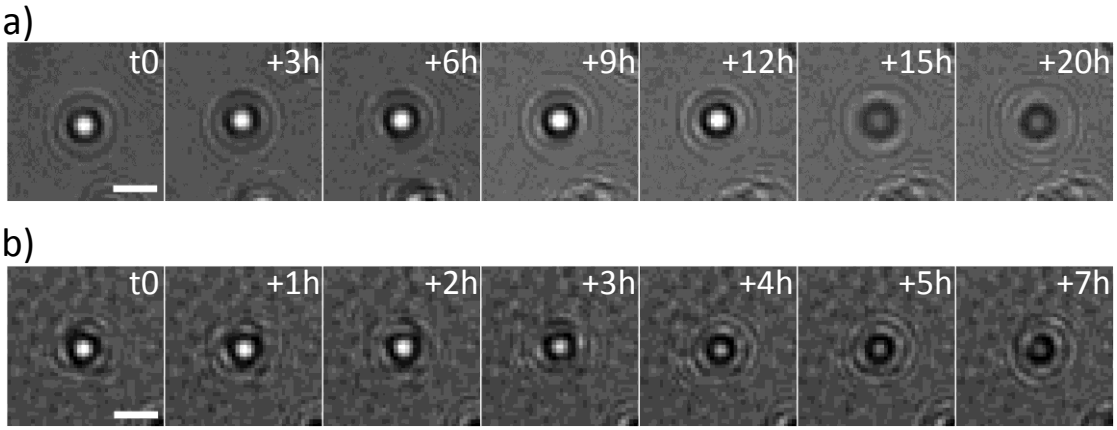

Figure 3D.7: Cell death of DU145 and PC3. We monitored cell death due to siCellDeath transfection, and Straurosporin addition in (a) DU145 cells, and (b) PC3 cells, respectively. In both cases, we observed a change in gray value as cells detached from the substrate. The cells possess a rounded morphology and hence, the change in the shape of the cells is not evident. Cell death can be monitored by the change in gray value. Time t0 marks the moment of siRNA transfection or drug administration. Scale bar 50µm.

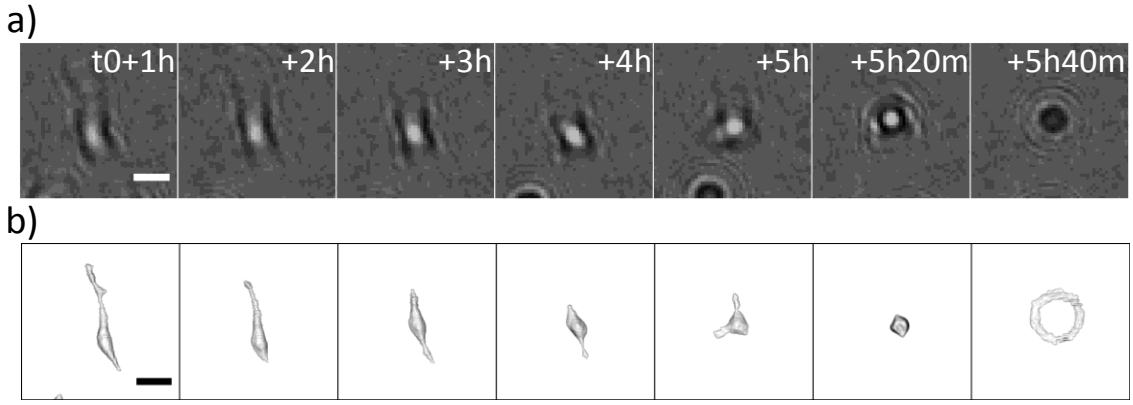

Figure 3D.8: Cell death of NIH3T3 cells

Due to their elongated morphology, changes in both gray-level and aspect-ratio can be observed. Time t0 marks the administration of ActinomycinD (50µg/ml). Scale bar 50µm.

(a) The change in gray-level is observed from the raw holograms, at t0+5h40m, as the cell detaches from the substrate.

(b) From the reconstructed images, we can also observe the change in the aspect-ratio starting from t0 + 1h and lasting until the detachment of the cell at t0+5h40m. Note that the change in the distance between the cell and the imaging sensor that occurred at t0+5h40m, was not taken in to account while performing holographic reconstruction. Hence we do not observe the cell, but the diffraction pattern.

We also tested our approach by changing the substrate. Cells can be tightly packed in a small area of the substrate. This is seen in **Fig. 3D.2, 3D.9**, where NIH3T3 cells are closely packed in a small fibronectin coated micro-patterned (disc shaped Cytoo™ micro-patterns) substrate surround by non-adherent substrate. Detecting or reconstructing single cells in these closely packed clusters can be complicated due to the increased cell density and interference from neighboring cells. However, cell death can be clearly observed by the significant changes in the area of the cell cluster. By measuring the reduction of the cell cluster area, we monitor cell death **(Fig. 3D.9)**.

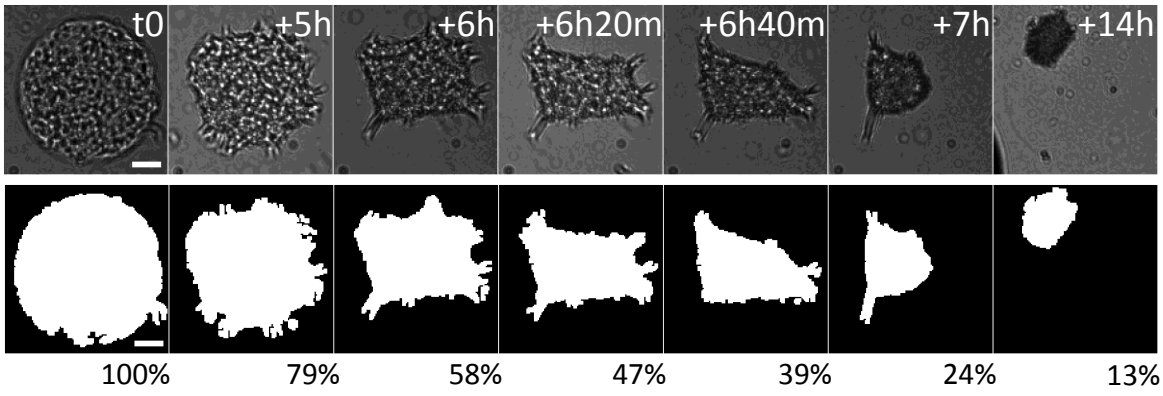

Figure 3D.9: Cell death on micro-patterns. Highly dense NIH3T3 cells on Cytoo™ micro-patterns were subjected to continuous exposure of elevated temperature (45°C). The disc shaped micro-pattern was initially filled with cells at t0. However, as cell started to die, the area of the cell cluster decreased to ~10% of the initial value. Scale bar 50µm.

3D.3 DISCUSSION

As mentioned earlier, cell death is accompanied by distinct changes in both raw and reconstructed images which can be used for real-time monitoring. We used 2 metrics to monitor cell death gray value measurement, and aspect-ratio measurement to provide information on cell detachment and cell rounding respectively. The kinetics is observed from the scatter plot from which the percentage of live and dead cells at any desired point in time can be obtained. Importantly, in the case of gray value measurement, there is 3σ significance in differentiating dead cell with an average gray value of 70 gray-levels and a live cell with an average gray value of 210 gray-levels. In the case of U2OS cells, measurement of gray value was sufficient. Whereas, in the case of hMSCs aspect-ratio measurement was needed. We tested the approach with PC3, DU145, and NIH3T3 cells. Similar to U2OS cells, PC3 and DU145 cells showed only difference in the gray-level, and not in aspect-ratio owing to its rounded morphology. Whereas, NIH3T3 fibroblast cells showed changes in both aspect-ratio, and gray-level. We also visualized cell death of densely packed NIH3T3 cells, on Cytoo™ micro-patterns. During cell death, the surface of the micro-patterns, occupied by the cells, reduced significantly due to shrinking of the cell body.

We monitored the effect of siCellDeath, Staurosporin, and elevated temperature, which are well known to induce cell death. However, several other siRNAs, drugs, environmental conditions could be tested to determine their efficacy in killing the cells. Along with the ability to follow the kinetics of cell death, recognizing the different types of cell death (apoptosis, necrosis, autophagy) is an interesting prospect. For example, it is known that the morphological modifications that occur during apoptosis and necrosis are different. Apoptosis is characterized by retraction of pseudopodia, detachment from substrate,

whereas, necrosis is characterized by increase in translucency of cytoplasm, swelling of cytoplasmic organelles, etc (Kepp, Galluzzi, Lipinski, Yuan, & Kroemer, 2011). These differences could lead to difference in the holographic pattern from the respective cells. The study remains an object of future interest.

3D. 4 METHODS

3D.4.1 Computational methods

3D.4.1.1 Measurement of gray value

Once the cells are detected, the mean zero-order gray value is obtained from a smaller circular region of interest of 16μm diameter surrounding the detected cells, on the raw image.

3D.4.1.2 Measurement of aspect-ratio

Similar to **section 3A**, the adherent cells are segmented from the reconstructed image. The segmented objects (cells) are subjected to the measurement of aspect-ratio, which is the ratio of minor-axis length to major-axis length of the ellipse that best fits the shape of individual segmented cells.

3D.4.1.3 Measurement of surface-area covered

Using gray value difference, the background is eliminated from the image leaving a binary image consisting only the surface area covered by the cells (both viable and dead).

3D.4.2 Cell culture methods

HMSCs were cultured using the same protocol mentioned in chapter 3A.4.2.

Human osteosarcoma U2OS cells were cultured in high glucose Dulbecco's modified Eagle's medium (DMEM; Life Technologies™), supplemented with pyruvate and 10% fetal bovine serum.

For cell death experiments involving U2OS and hMSCs, cell death was induced by forward transfection using the positive cell death phenotype control siRNA (siCellDeath = AllStars Hs Cell Death siRNA, Ref SI04381048; Qiagen) and the Lipofectamine RNAiMAX transfection reagent (Life Technologies™). For transfection, Lipofectamine RNAiMAX (3µL) and siCellDeath (20nM final concentration) were separately diluted in Opti-MEM media, combined together then added to culture dishes after 10 minutes of incubation.

REFERENCES

Arnulf, B., Lecourt, S., Soulier, J., Ternaux, B., Lacassagne, M.-N., Crinquette, a, … Larghero, J. (2007). Phenotypic and functional characterization of bone marrow mesenchymal stem cells derived from patients with multiple myeloma. *Leukemia*, *21*(1), 158–63. doi:10.1038/sj.leu.2404466

Bano, D., Zanetti, F., Mende, Y., & Nicotera, P. (2011). Neurodegenerative processes in Huntington ' s disease, 1–7. doi:10.1038/cddis.2011.112

Barski, E., Michel, U., & Ba, M. (2014). ROCK2 is a major regulator of axonal degeneration , neuronal death and axonal regeneration in the CNS, 1–12. doi:10.1038/cddis.2014.191

Chiong, M., Quest, A. F. G., Lavandero, S., & Stutzin, A. (2005). Mechanisms of cell death : molecular insights and therapeutic perspectives, 1449–1456. doi:10.1038/sj.cdd.4401738

Crews, L., & Masliah, E. (2010). Molecular mechanisms of neurodegeneration in Alzheimer ' s disease, *19*(1), 12–20. doi:10.1093/hmg/ddq160

Hitzmann, B., & Ueffing, M. (2013). Retinitis pigmentosa : rapid neurodegeneration is governed by slow cell death mechanisms, 1–8. doi:10.1038/cddis.2013.12

Jellinger, K. a. (2001). Cell death mechanisms in neurodegeneration. *Journal of cellular and molecular medicine*, *5*(1), 1–17. Retrieved from http://www.ncbi.nlm.nih.gov/pubmed/12067447

Kepp, O., Galluzzi, L., Lipinski, M., Yuan, J., & Kroemer, G. (2011). Cell death assays for drug discovery. *Nature reviews. Drug discovery*, *10*(3), 221–37. doi:10.1038/nrd3373

Mc, A. A., Zenteno, E., Chávez, R., & Lascurain, R. (2009). Cell Death Mechanisms Induced by Cytotoxic Lymphocytes, *12*(February).

Orrenius, S., Nicotera, P., & Zhivotovsky, B. (2011). Cell death mechanisms and their implications in toxicology. *Toxicological sciences : an official journal of the Society of Toxicology*, *119*(1), 3–19. doi:10.1093/toxsci/kfq268

Reed, J. C. (2011). Cancer. Priming cancer cells for death. *Science (New York, N.Y.)*, *334*(6059), 1075–6. doi:10.1126/science.1215568

Reed, J. C., & Pellecchia, M. (2012). Ironing Out Cell Death Mechanisms. *Cell*, *149*(5), 963–965. doi:10.1016/j.cell.2012.05.009

Rønn, L. C., Ralets, I., Hartz, B. P., Bech, M., Berezin, a, Berezin, V., … Bock, E. (2000). A simple procedure for quantification of neurite outgrowth based on stereological principles. *Journal of neuroscience methods*, *100*(1-2), 25–32. Retrieved from http://www.ncbi.nlm.nih.gov/pubmed/11040363

Surova, O., & Zhivotovsky, B. (2012). Various modes of cell death induced by DNA damage. *Oncogene*, (October), 1–9. doi:10.1038/onc.2012.556

Tyson, D. R., Garbett, S. P., Frick, P. L., & Quaranta, V. (2012). Fractional proliferation : a method to deconvolve cell population dynamics from single-cell data. *Nature methods*, *9*(9), 923–928. doi:10.1038/Nmeth.2138

Yuan, J., & Kroemer, G. (2010). Alternative cell death mechanisms in development and beyond. *Genes & development*, *24*(23), 2592–602. doi:10.1101/gad.1984410

Zeng, W., Zhang, J., Qi, M., Peng, C., Su, J., Chen, X., & Yuan, Z. (2014). αNAC inhibition of the FADD-JNK axis plays anti-apoptotic role in multiple cancer cells. *Cell death & disease*, *5*, e1282. doi:10.1038/cddis.2014.192

Zhang, D.-W., Shao, J., Lin, J., Zhang, N., Lu, B.-J., Lin, S.-C., … Han, J. (2009). RIP3, an energy metabolism regulator that switches TNF-induced cell death from apoptosis to necrosis. *Science (New York, N.Y.)*, *325*(5938), 332–6. doi:10.1126/science.1172308

CHAPTER 3E

CELL MIGRATION AND ITS ALTERATIONS

Pg. 128	**CLASSIFYING CELL MIGRATION**
Pg. 129	**CELL MIGRATION ON 2D SUBSTRATES**
Pg. 137	**CELL MIGRATION ON 3D SUBSTRATES** **Network formation of acini structures**
Pg. 143	**CELL MIGRATION AT 3D/2D INTERFACE** **Exploratory migration**
Pg. 144	**REVERSIBLE AND IRREVERSIBLE ALTERATION OF CELL MIGRATION** **Associated to division, differentiation, quiescence, and death**

3E. CELL MIGRATION AND ITS ALTERATIONS

As stated by Franz. Et al. cell migration plays a central role in the development and maintenance of multi-cellular organisms(Franz, Jones, & Ridley, 2002). Be it embryogenesis where complex migration ensures proper tissue formation, wound healing where the cells migrate to cover the wound, immune response where leukocytes migrate into lymph nodes and inflamed tissue, or even metastasis where cancer cells migrate to colonize neighboring areas, cell migration plays distinct and specific roles. Studying cell migration is hence of prime importance.

By analyzing data from 20,000 hours of lensfree video microscopy time-lapse imaging, containing thousands of cells in every frame, of different conditions (2D, 3D, reduced temperature, etc.) and cell types (primary human fibroblasts, human mesenchymal stem cells, RWPE1, Hela, Vero, etc.), we witnessed different types of cell migration, and more interestingly, its alteration (temporary change, arrest or permanent halt). In particular, we monitored how migration is linked to major cell functions, thereby to the fate of the cell.

Based on our observation, we broadly classified cell migration in to 4 very broad categories, (i) random to semi-ordered migration - majorly observed with cell culture cultivated in-vitro on a substrate, (ii) directed cell migration – observed in 3D cell culture, (iii) exploratory migration observed at the interface of 3D and 2D, (iv) altered migration – alteration in response to the constraints connected to major cell functions: division, differentiation, quiescence and death.

Studying the types of migration, would lead us to better understand migration and its intrinsic role in deciding the fate of the cell. However, from an experimental perspective, this study is complex. Because unlike other functions, such as cell-division, or cell-death, where kinetics can be extrapolated by series of end-point flow cytometry assays, live monitoring is indispensable to study cell migration. The following advantages offered by lensfree video microscope make it a unique platform to perform such a study: (i) ability to perform real-time monitoring for extended time period (few weeks) (ii) possibility of quantifying not just cell migration but also other events (cell division, differentiation, etc.) that occur simultaneously, (iii) ability to provide both macroscopic and microscopic information, in order to observe cell population and single cells, (iv) being entirely free from markers and any kind of photo- or cyto-toxicity.

3E.1 CELL MIGRATION ON 2D SUBSTRATES

We observe that a large majority of the cells (90% of the population) that are cultured on 2D surfaces are motile (with an arbitrary threshold of 0.2µm/min below which the cells are considered stationary: typical cell velocity, in our observation, ranged between 0.3µm/min and 3µm/min). In most cases, this cell migration does not have a particular goal or destination. It is entirely random and starts immediately as the cells adhere to the substrate (in case of 2D). Unlike, cell differentiation or cell death, we do not have to activate signaling pathways, control cell culture environment, and/or modify their metabolism to trigger cell migration, in order to observe the same. Most of the cells are motile in nature, and cell motility is observed as the cells adhere to the substrate.

Unlike a normal displacement with an intention of reaching point B from point A, most cells in culture (on substrate) display cell migration that is highly random. In majority of the cell types, we observe that the cell migration starts from the moment the cell adheres to the substrate and continues for time period extending to several days, and is only interrupted when the culture reaches confluence. As stated earlier, this constant displacement does not occur with a motive to reach a destination, but with a motive to keep moving giving equal importance to all directions by changing frequently the direction of motion, which can be described in terms of Brownian motion with very low directional persistence **(Fig. 3E.1, 3E.2)**. Although this kind of a migration is observed in a majority of cell types (e.g.: fibroblasts, RPE1, Vero, etc.), we have also observed other types of cell migration, where the displacement is comparatively more predictable and ordered.

In this regard, a second type of cell migration is where cells that are in a cluster, move in a circular manner around the group **(Fig. 3E.3)**. This is observed in RWPE1 cells in 2D. We have observed multiple such occurrences in clusters located closely to one another. But, from our videos (> 100 hours imaging), we did not observe a cell that moved from one cluster to another. These clusters grow in size as the cells in the cluster divide.

The third type of movement that we observed was displayed by keratinocyte cells. Similar to RWPE1 cells, we observe several cell clusters. However, here the cells move in a rectilinear fashion, towards the exterior surface of the cluster, with an objective to cover the surface and expand **(Fig. 3E.4)**. This movement is assisted majorly by cell division, increasing the number of cells in the cluster, as the cells cover the entire substrate area. Keratinocyte migration **(Fig. 3E.4)** can be compared to the growth of bacteria, and also to

wound-healing **(Fig. 3E.5)**, where cells divide and move forward, to cover the wounded portion.

The 3 above mentioned types of migration stop when the culture reaches complete confluence. This is clearly illustrated in **figure 3E.6**, where the mean velocity of fibroblast cells descends to <0.1μm/min **(Fig. 3E.6: Region C)**, due to increase in the number of cells in the population (from ~2000 to ~5000 cells). It is interesting that even at this stage of very low cell migration and complete confluence, we observe a subtle movement (<0.1μm/min) in the population using Particle Image Velocimetry (PIV) analysis **(Fig. 3E.7)**. PIV analysis is performed based on cross-correlation of sub-regions of 2 consecutive images in order to determine the displacement of the objects in between the 2 images (Deforet et al., 2012; Westerweel, 1993). This movement within the cell monolayer, could be due to the mechanical force/ pressure generated within the monolayer of cells (Campàs et al., 2014; Krieg et al., 2008).

On the contrary to all the above mentioned types of migration, there exists a fourth type of migration, which has not been described before, a type of migration that never stops, according to our observation – the migration exhibited by hMSCs, is pertinent (> 0.2μm/min) even at confluence. In order to move at exceedingly larger cell densities, hMSCs align themselves parallel to one another to engage in this motion resembling 'Optical Flow', either in the same or in opposing directions with respect to their neighbors **(Fig. 3E.8a)**. We monitored highly confluent culture of hMSCs (> 95% surface covered with cells, n~5000 cells in 24mm^2 FOV) for 35 hours. We observed that the mean cell velocity of the culture remained at ~0.5μm/min **(Fig. 3E.8b)** despite the increased density, compared to that of RPE1 and fibroblast cells, which decreased to less than 0.1μm/min.

Cell migration on 2D substrates, though random, is linked to the size, shape and level of adhesion of single cells in the population. By observing the migration of single cells (n ~2000 cells) along with the cell's parameters, we observed a trend. The cell velocity increased proportionally with the length of the cells **(Fig. 3E.9a)**. From the scatter plot **(Fig. 3E.9a)**, it can be observed that majority of the population had a major axis length between 5µm and 50µm. However, there were a few cells in the population that were longer (~30% of the population of ~2500 cells, with major axis length between 50 µm and 100 µm). This sub-population moved relatively faster (0.7 µm/min compared to 0.4 µm/min by the rest of the population). However, we did not observe significant variation in velocity with respect to the aspect-ratio and the level of adhesion of the cells **(Fig. 3E.9b,c)**.

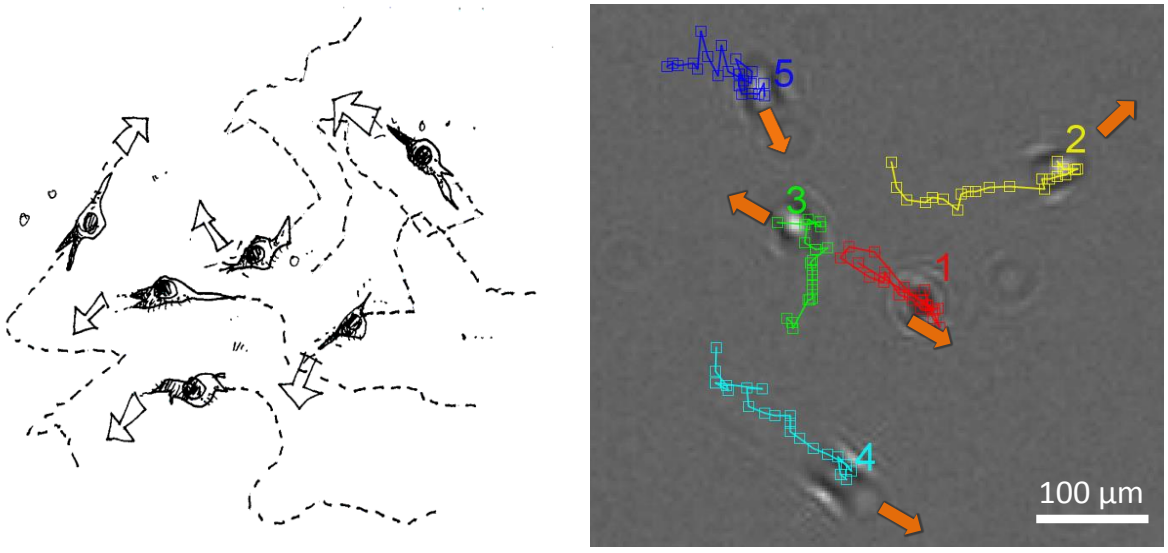

Figure 3E.1: Random cell migration of NIH3T3 cells on 2D substrates

(a) Schema explaining the random cell migration on 2D surface.

(b) ROI illustrating the schema, where the tracks show random migration of NIH3T3 cells. Arrows indicate the direction towards which the respective cells are headed.

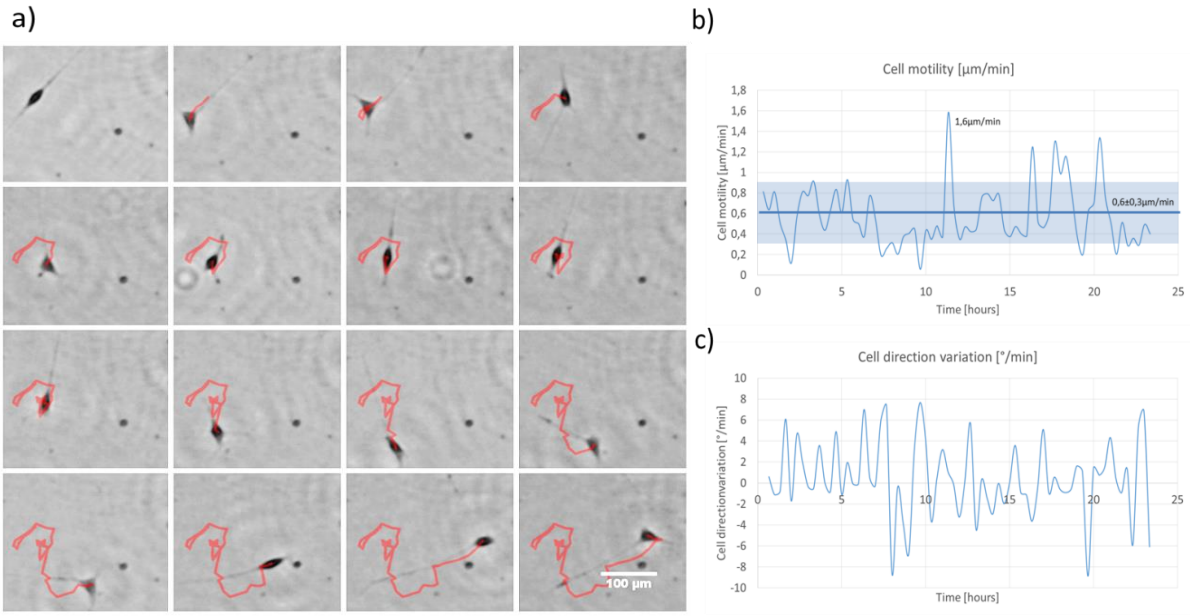

Figure 3E.2: Random cell migration of a single neuron on 2D substrates

(a) Track of a neuron followed during 24 hours.

(b) Motility is plotted as a function of time at intervals of 20 minute. Mean motility is 0.6µm/min with a maximum of 1.6µm/min

(c) Variation in direction is plotted as a function of time. It shows a low direction persistence which results into a Brownian-like migration as depicted in (a).

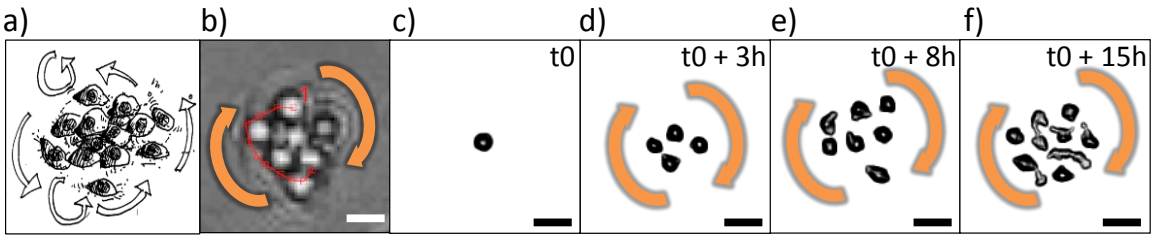

Figure 3E.3: Circular cell migration: RWPE1 cells on 2D substrate

(a) Schema describing circular cell migration;

(b-f) ROI showing a cell cluster of RWPE1 cells in 2D, composed of ~9 cells. The track shows circular movement exhibited in the cluster. Scale bar: 20 µm.

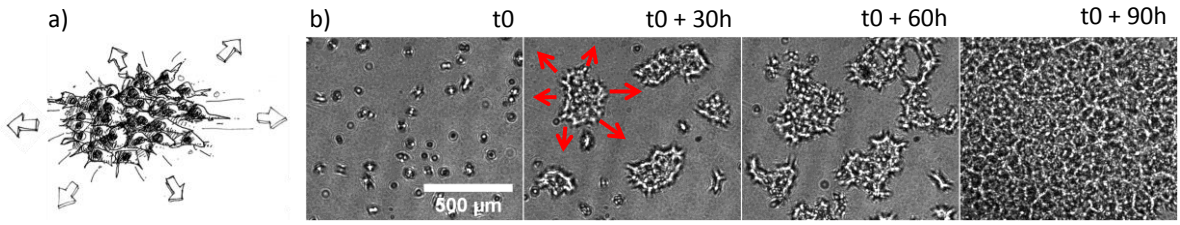

Figure 3E.4: Directed rectilinear cell migration of keratinocytes on 2D substrate

(a) Schema representing directed rectilinear cell migration on 2D substrates exhibited by keratinocytes.

(b)Raw time-lapse images obtained from lensfree video microscope exemplifying rectilinear migration of keratinocytes, with a motive to cover the entire substrate. Red arrows indicate the directions of cell migration.

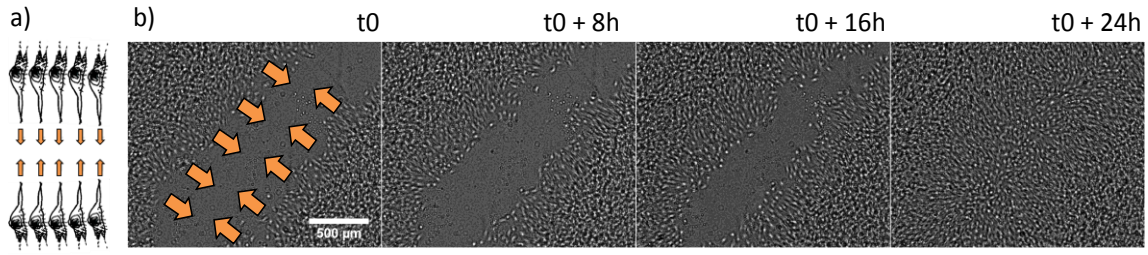

Figure 3E.5: Directed migration on 2D substrate – Wound healing

(a) Schema representing directed cell migration in the case of wound-healing on 2D surfaces.

(b) NIH3T3 cells display a directed cell migration (orange arrows) to cover the gap in the surface. The gap of ~650µm is covered in 24 hours.

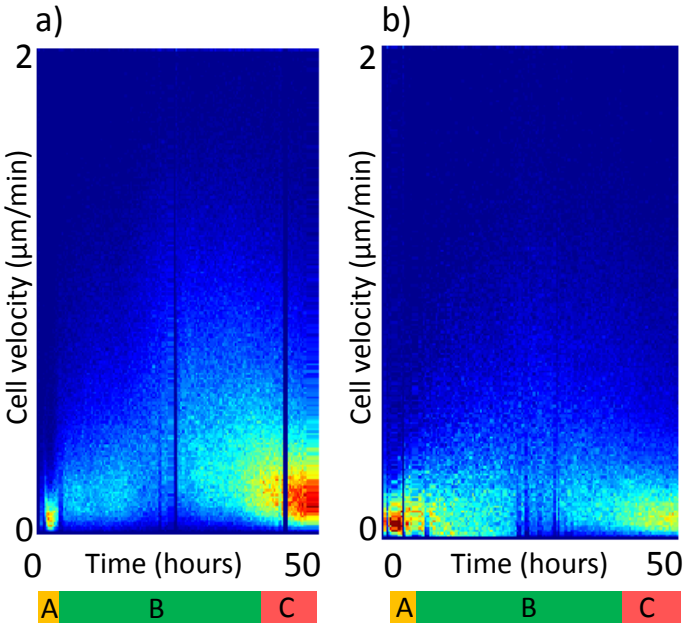

Figure 3E.6: Cell velocity in relation to confluence. Cell migration observed for a time-period of 50 hours from cell seeding until confluence of 2 different cultures of fibroblasts (a), (b). During initial adhesion to the substrate (yellow region A), the cell migration is low. The cells start to spread and migrate (green region B), resulting in increased cell velocity (~0.4µm/min, average n~2000 cells). The cells keep moving constantly until the culture approaches confluence, at which point cell migration is decreased, (red region C) to cell velocity of ~0.1µm/min (average n~5000 cells). Change in field of view during addition of culture media has caused some discontinuities.

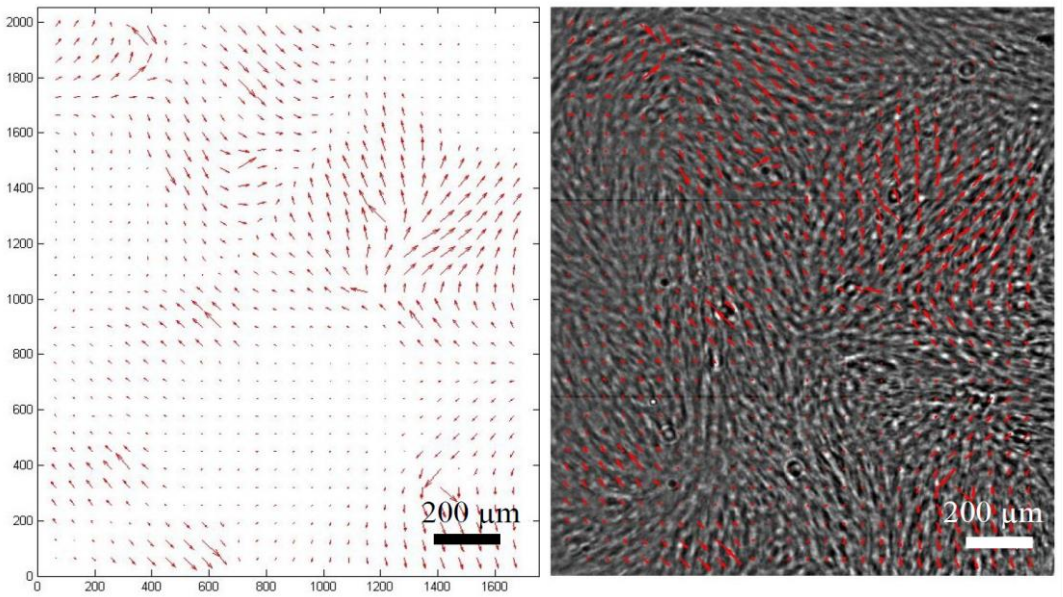

Figure 3E.7: Cell migration at confluence – RPE1 cells. Lensfree time-lapse images were analyzed using PIV. PIV analysis is used to find the displacement of the objects in two successive image frames. It is based on cross correlation of sub-regions in successive

images. Lensfree image (right) shows a confluent cell culture, where ~98% of the surface is covered by cells. It can be seen that even at exceedingly high cell density, the cells display subtle movement (left). The cell velocity during this period is very low (< 0.1µm/min)

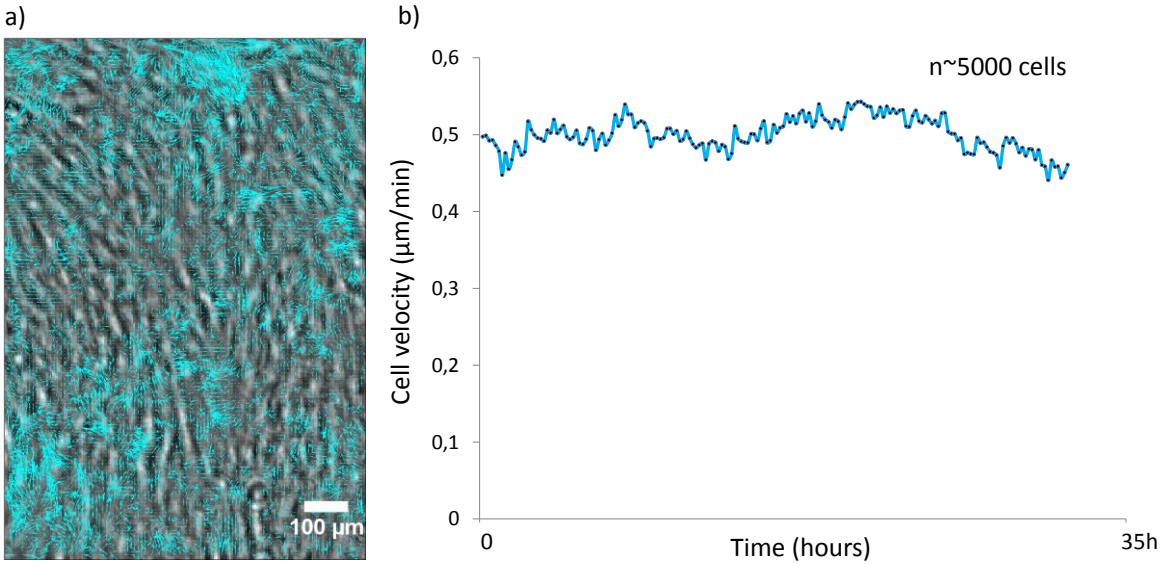

Figure 3E.8: Cell migration at confluence - hMSCs

(a) PIV analysis of hMSC migration at increased cell density (> 95% of surface covered with cells, n~5000 cells)

(b) Average cell velocity of n~5000 stem cells during 35-hour long observation. Note that the average cell velocity is ~0.5µm/min, even at this highly confluent state.

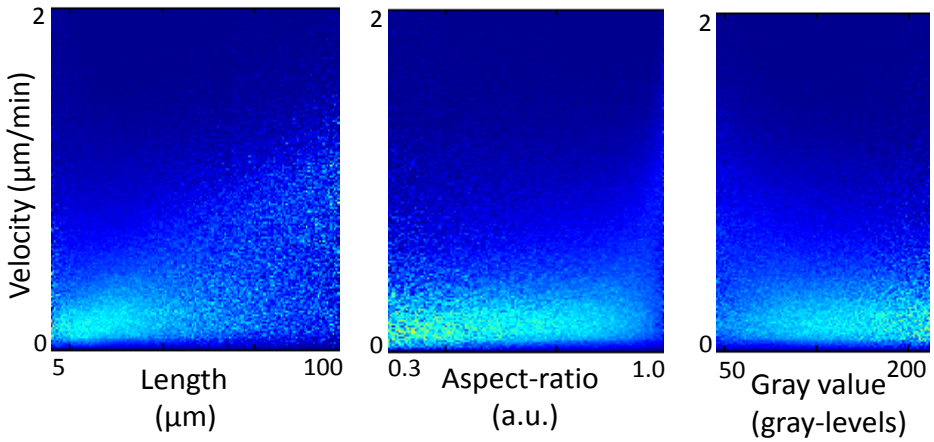

Figure 3E.9: Velocity as a function of (a) length of the cells, (b) aspect-ratio of the cells, and (c) adhesion of the cells. Note that the velocity distribution with respect to the length of the cells shows a clear trend: longer cells moved faster comparatively.

3E.2 CELL MIGRATION ON 3D SUBSTRATES: Network formation between 3D acini structures

We monitored cells cultured in a 3D Matrigel environment. 3D cell culture promises a closer resemblance to conditions in-vivo compared to 2D cell culture (Abbott, 2003). Hence 3D cell culture is being increasingly used. We demonstrate the applicability of lensfree video microscope platform to 3D cell culture imaging, by studying the network formation of RWPE1 prostate epithelial cell structures (acini) constituting secretory epithelium.

So far we listed the types of migration that we detected in 2D cell culture, where cells adhere to the substrate and do not have the freedom to move in the z-direction. As one could expect, 3D cell culture in Matrigel, resulted in an entirely different kind of migration, which has not been observed before at a larger scale. Up to now, in 2D cell culture, we observed different types of migration, always connected to the cell population. We did not observe any directed migration at the level of individual cells that varies from one cell to another. Here in 3D cell culture, we witnessed the most directed migration of single cells from one point A to point B separated by varying distances in the order of hundreds of micrometers. RWPE1 cells in 3D migrate in an effort to bridge the gap between these distantly placed points (objects), with a directional persistence close to 90% (ratio of traveled distance to actual distance). It is to be noted that the RWPE1 cells in 2D did not show this kind of behavior.

We filmed the RWPE1 3D cell culture for a period of 6 days. Using real-time imaging combined with large field of view, we were able to visualize the network formation between several acini 3D structures. **Figure 3E.10** shows the time-lapse lensfree images obtained at t0 and t0 + 6 days. It can be observed that initially at t0, the 3D acini structures

can be observed with no network between one another. After 6 days, several networks were observed. We analyzed the formation of each of the networks **(Fig. 3E.11, 3E.12, 3E.13, 3E.14, 3E.15, and 3E.16)**. We observed single-cell ejections that initiated branching **(Fig. 3E.11)**, collective migration of a train of cells **(Fig. 3E.11 through Fig. 3E.16)**, close-gap branching **(Fig. 3E.15)**, aborted connection leading to back-forth cell migration between acini structures **(Fig. 3E.12)**.

We observed a single RWPE1 cell that initiated the establishment of networks. We observed migration of one cell then several single cells following the same track in Matrigel and then forming a chain of cells that transforms into tubule-like structure. In **Fig. 3E.11**, the first cell that established the connection between acini D and acini C, traveled at a speed of 0.9μm/min. The cells that closely followed had an increased speed of 1.1μm, and the train of cells that subsequently followed traveled at 1.3μm/min. We could hypothesize that the degradation of the Matrigel by the first cell facilitated the movement of subsequent cells. It is interesting to note that in this case, the distraction of another acini did not deter the directed cell migration. In other words, we observed cells that migrated from one acini at point D to another acini at point C situated at a distance of ~750μm, while bypassing a third acini B which was 3 times closer to point D.

Similarly we observed different kinds of both successful migrations leading to establishment of network and more notably unsuccessful migration where the cells returned to the departure point, traveling exactly the same path backwards, at almost the same velocity as the onward journey. Surprisingly, all the cells that departed, without any exception, returned back **(Fig. 3E.12)**.

We measured trajectories of 18 different branching **(Fig. 3E.16)** and calculated the directional persistence of nearly 90% when the traveled distance is below 350 µm.

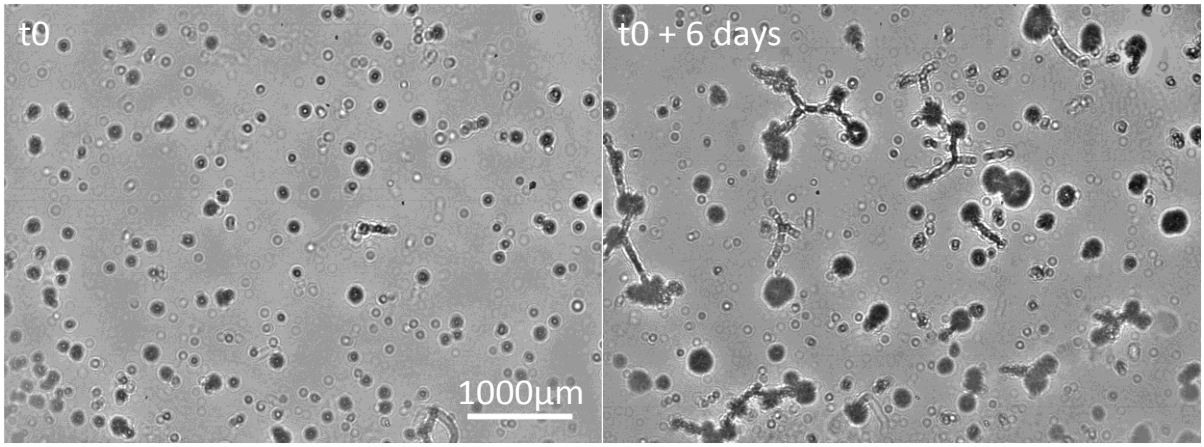

Figure 3E.10: Directed migration on 3D – acini network formation. Time-lapse image from lensfree video microscope showing 3D RWPE1 cell culture at t0 and t0 + 6 days. Single acini without network can be seen from the image at t0, whereas several networks between acini structures can be observed from the image at t0 + 6 days. Time t0 marks the commencement of time-lapse imaging.

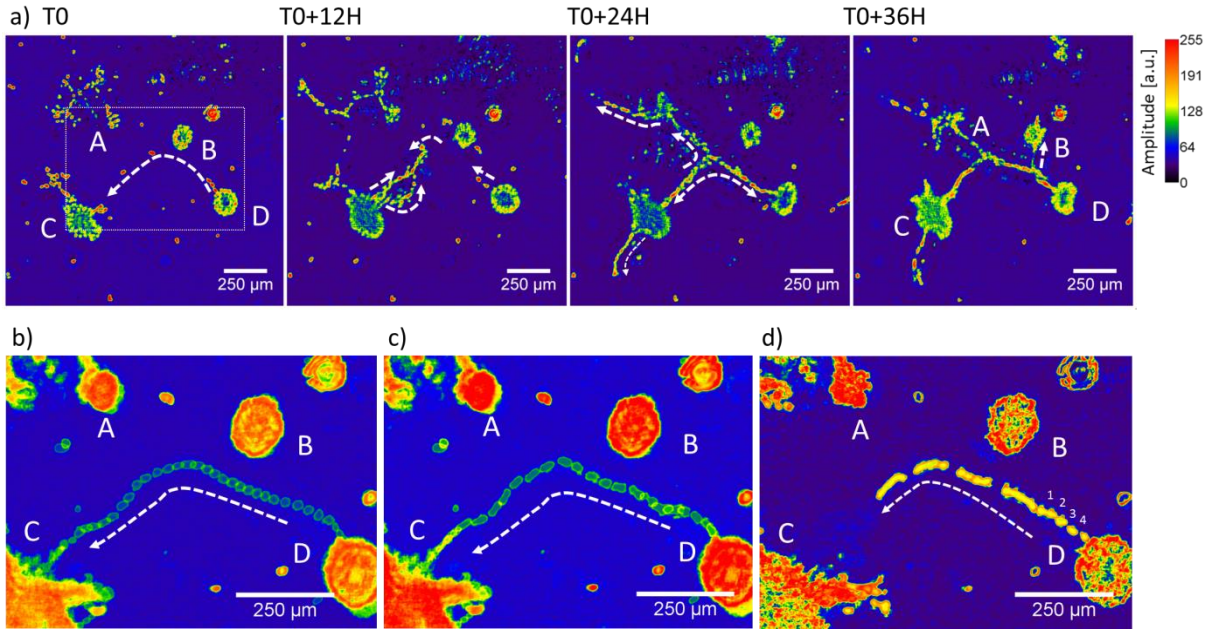

Figure 3E.11: Formation of network between 4 acini structures. The network was formed after the initiation of connection, when a single cell moved from acini D to acini C. It is to be noted that it bypassed acini B, which was closer. This single cell was followed by a couple of cells, and later by a group of cells. Within 24 hours, a network was formed between acini D and C, which further extended to acini A and B. After 36 hours, a connection was established between the 4 acini structures. (b) The first RWPE1 cell that initiated the connection. (c) Couple of cells that followed the first cell, (c) Train (~4 cells)

that later followed the same path. Time T0 marks the commencement of the formation of this particular network and not to be confused with t0 – commencement of time-lapse imaging.

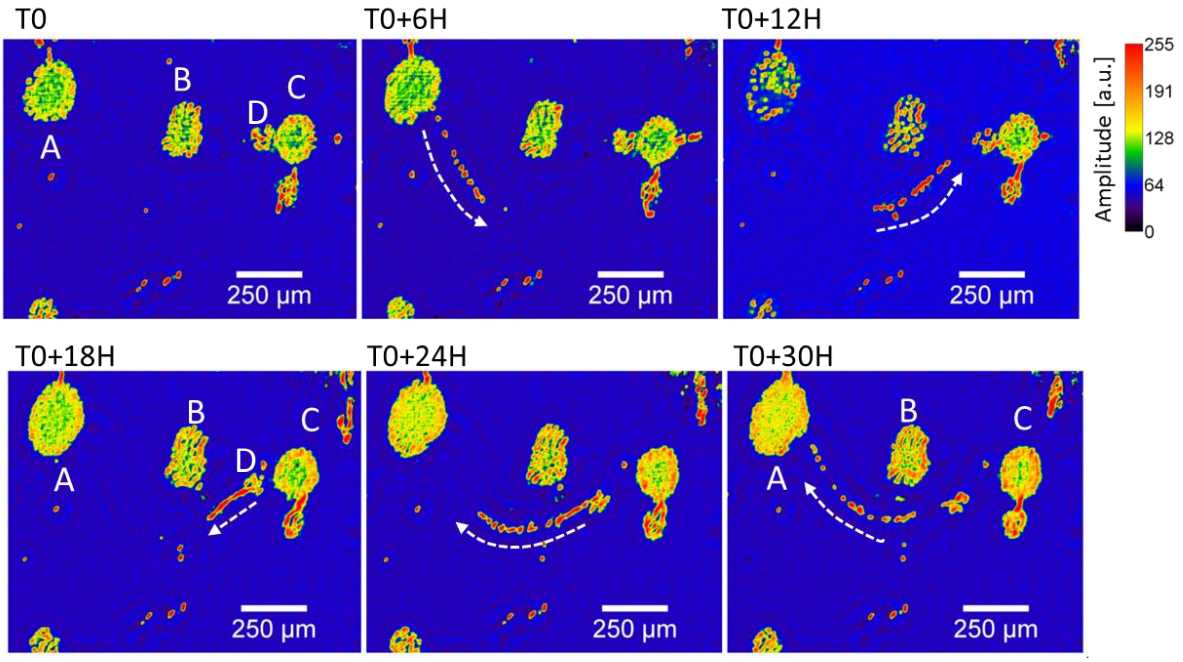

Figure 3E.12: Failed Connection. Time-lapse (30H) imaging shows the collective migration of a batch of ~15 cells between two acini (A and C), bypassing a third acini B. The track is as long as 990µm and the cell migration last about 13 hours (1.26µm/min). But the cells do not dock to acini C and all 15 cells move backwards to acini A at about the same velocity, taking almost the same path. Doing so they move with them a small acini D of 80µm in diameter that was first attached to acini C. Time T0 marks the commencement of the formation of this particular network and not to be confused with t0 – commencement of time-lapse imaging.

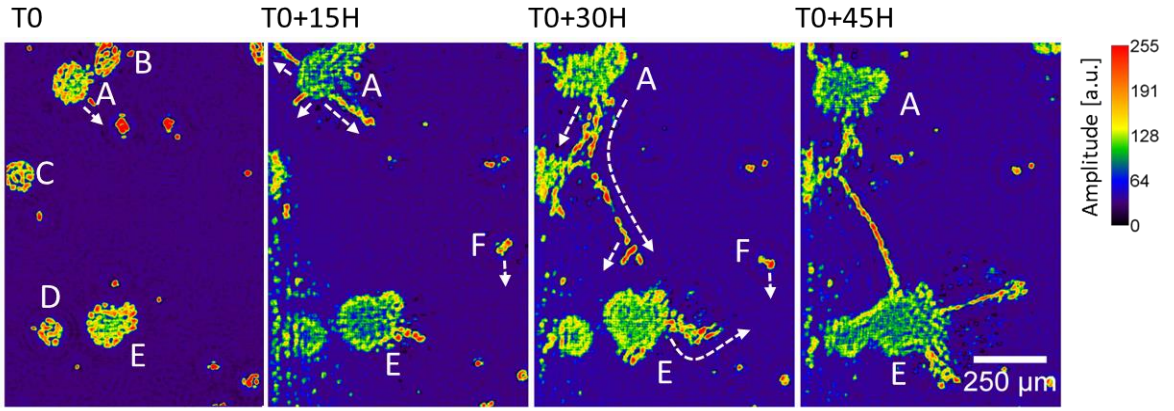

Figure 3E.13: Formation of network between 3 acini structures. 45h time-lapse imaging s hows the construction of a network between the three acini A, C and E. Acini C and E

are respectively 920µm and 420µm apart from acini A. At T0, a first branch initiated by a ci-ni A moves towards a cell aggregate located at a distance of 200µm. Connection occurs at T+15H (track of 175µm, 0.6µm/min, distance/route=0.86) and the branch further exte nds through acini C in the direction of acini E (T0+30H, track of 550µm 0.79µm/min, dist ance/route=0.78). Then the tip of the branch then divides in two parts that will connect t o the two bumps of acini E. At T0+45H a three acini network is finally formed between ac ini A, C and E. One can also observe a branch connecting the acini E and the cell aggregat e F at a distance of 310 µm (0.98µm/min, distance/route=0.96).

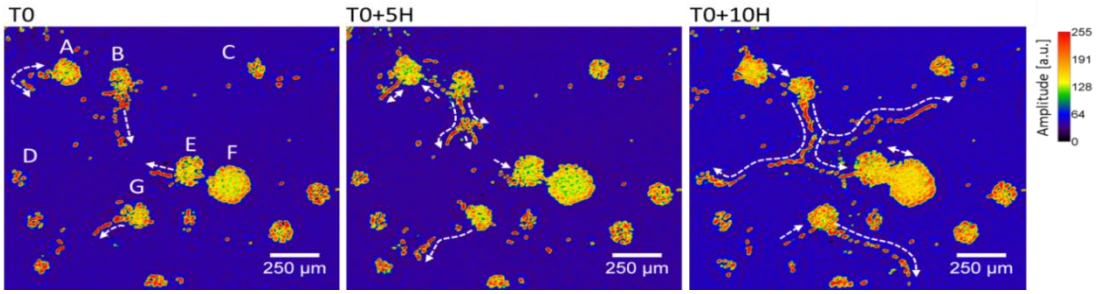

Figure 3E.14: Multiple branching. 10H time-lapse imaging shows the development of several branching. In particular acini B is attempting to connect via branching to four acini, i.e. A ,C, D and E that are at distances of 220µm, 690µm, 805µm and 660µm respectively. At first,a branch evolves from acini B which divides into three other branches at T0+5H. The three branches go towards acini C, D and E. From these branches, only (B,E) connection is achieved at T0+10H (track of 537µm, 0.9µm/min, distance/route=0.37). Another connection is achieved between acini B and D but results from a sub-branches of the (B,D) connection (track of 515µm, 0.8µm/min, distance/route=0.65). Meanwhile close-gap branching occurs between acini A and B, and acini E and F. One can also observe acini G initiating two branches but fail to connect (the two branches will finally retract).

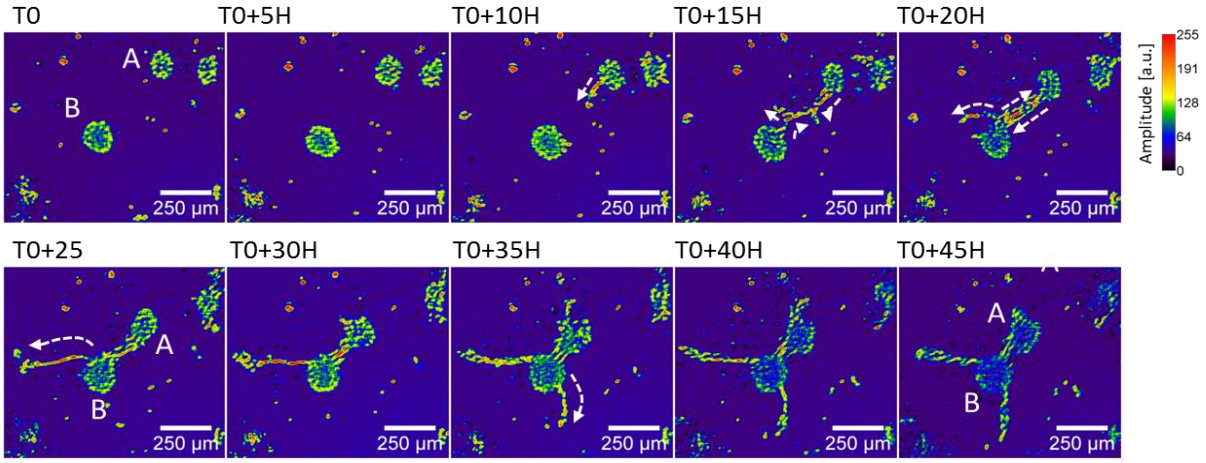

Figure 3E.15: Close-gap branching. 45H time-lapse imaging show in details a close-gap branching between acini A and B that are initially 250µm apart. At T0+10H, a branch starting from acini A goes towards acini B. At T0+15 two branches going opposite

directions are connecting acini A and B. Then the two acini are mutually attracted and get closer at a speed of about 0.16µm/min. One can also observe at T0+20H that the branch starting from acini A is connected to acini B and moves further in the direction of a cell aggregate 450µm away. The latter is connected to the acini network at T0+30H (0.9µm/min, distance/route=0.75). Another branch emerges from B at T0+35H and elongates 250µm at T0+45H. But this branch fails at connecting and will finally retract itself.

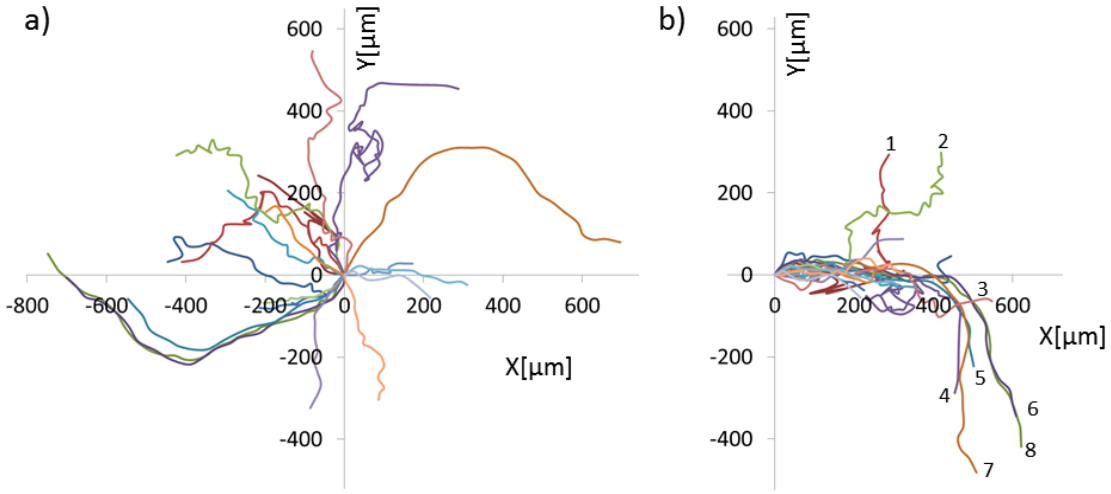

Figure 3E.16: Trajectories.

(a) The graph depicts the trajectories of 18 different branching connecting acini to acini or acini to cell aggregates. Trajectories are measured by following the tip of the branching position relative with the first position as origin. From over 436 positions, we have calculated an average speed of 0.9±0.4µm. We can define the connection efficiency as the percentage ratio between the effective distance and the travelled distance. We measure a pretty high efficiency of 78±16% and larger than 90% if the travelled distance is below 350µm.

(b) The graph shows trajectories rotated so that initial direction taken in the first 100µm matches with the X-axis. This representation shows that branching takes at first a straight direction till it encounters another object, e.g. an acini or a cell aggregate. At this point, depending on the surrounding object, the trajectory could be modified. In most cases, when branching connection occurs between two objects, it is straightforward and not a random migration.

3E.3 EXPLORATORY MIGRATION: 3D/2D INTERFACE

As we stated earlier, cell migration is inherent to cell culture on a substrate (2D), i.e., a default random cell migration without out any evident quest. Here we illustrate another type of migration with a directed goal: to sense the environment and explore. We exposed the cells in 3D environment to the 2D environment. In other words, we placed sections of tissue, biopsy samples in a culture dish. We observed cells moving out from the tissue in an effort to sense the external environment, using their pseudopodia **(Fig. 3E.17)**. The pseudopodia communicate with the environment by using focal adhesion points **(Fig. 3E.17b Focal adhesion point green arrows)**, which contain more than 100 proteins (Riveline et al., 2001). Cells that are inside the tissue or fibers, searches for anchoring points to adhere and propel forward. Cells continue to move in this fashion, from an anchorage to another, while sensing and exploring the environment for suitable conditions to further proliferate and colonize. This behavior was observed in (i) human skin biopsy where fibroblasts migrate from the tissue to the culture dish **(Fig. 3E.17b)**, and (ii) isolated muscle fibers where satellite cells migrate from the muscle fibers to the culture dish, proliferate and colonize **(Fig. 3E.17c)** (chapter 4.4.2). Cell migration in this case is aimed at accomplishing one goal – to explore.

The cell that exits and starts to explore, continues to explore responding successively to signals from neighboring favorable sites. The cell migrates from one site to another, more like the default random continuous cell migration that was first explained; simultaneously the cells divide and colonize.

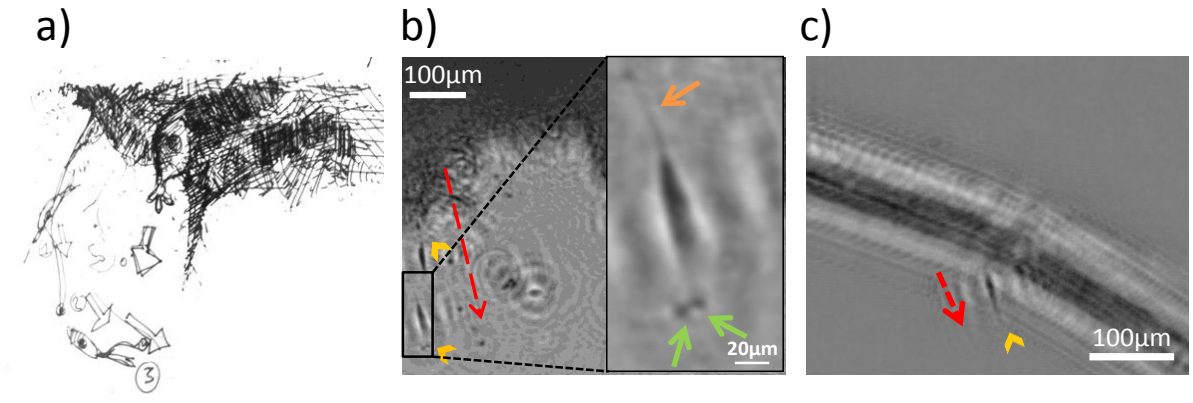

Figure 3E.17: Exploratory migration.

(a) Schema of a cell exiting the tissue sample, to sense the external 2D environment.

(b) ROI from reconstructed lensfree image showing single cells that exit human skin biopsy. Yellow arrow heads denote the single cells that exit the tissue, and red arrow shows the path taken by the cells. Picture inset is magnification of a single cell, which shows the cell's focal adhesion points (green arrows), and trailing edge (orange arrow).

(c) ROI from reconstructed lensfree showing the first satellite cell that exits the muscle fiber. Yellow arrow heads denote the single satellite cell and red arrow shows the path taken by the cell.

3E.4 REVERSIBLE AND IRREVERSIBLE ALTERATION IN CELL MIGRATION

Based on our observation, we further monitored and quantified reversible and irreversible alteration in cell migration. Especially, to carry out some functions that are directly linked to the fate of the cell, such as cell division, differentiation, etc., migration is reduced, temporarily arrested or permanently brought to a halt. As stated earlier, cell migration is achieved at the expense of metabolic energy of the cell. Hence, cells must stop moving to carry out other functions, i.e. division, differentiation, and death. The cells must control migration and should know when to stop moving, in order not to compromise e.g.: cell division. So far we have not observed the occurrence of other events in cell's life while the cell is constantly moving. This emphasizes on the existence of a formidable connection between cell migration and cell fate.

3E.4.1 Cell migration and division

In 2D cell cultures, during cell division, cell migration is arrested and the cell-substrate adhesion is greatly reduced. The stationary parent cell divides, re-attaches to the substrate, after which the daughter cells start to move **(Fig. 3E.18)**. We have observed more than 10 different cell types and have observed > 3000 single cell divisions, and in almost all the cases, we observe the momentary arrest in cell migration during division. Only in some rare cases, particularly in myoblasts, we have observed cell displacement of detached dividing cell **(Fig. 3E.19)**.

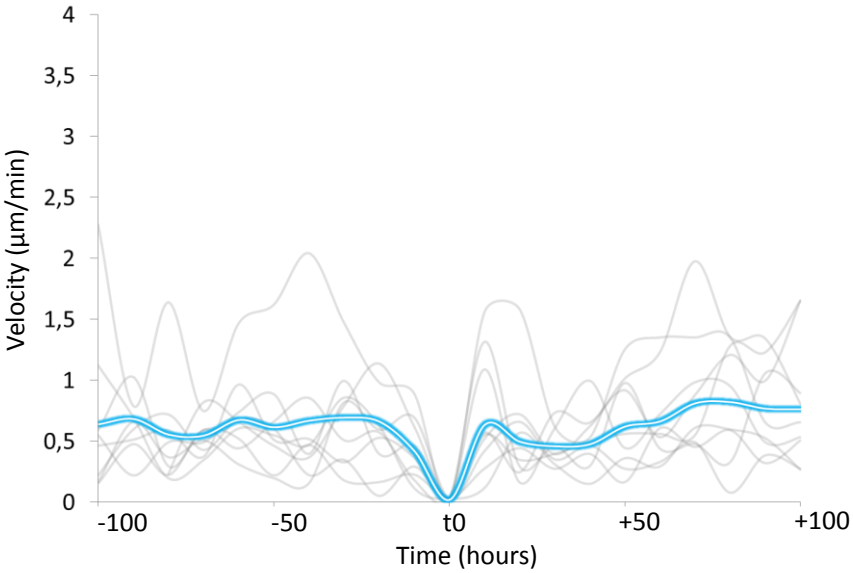

Figure 3E.18: Cell migration and cell division. Alteration in cell velocity of 10 cells (of independent experiments) seen before during, and after cell division. Time t0 marks the moment of cell division. Note that the cell division of the culture is not synchronized, as it is depicted in the graph. The time of division was adjusted manually for better visualization. The velocity drops to zero as the cell divides, after which cell migration continues in the same fashion (after division only one of the daughter cells is tracked).

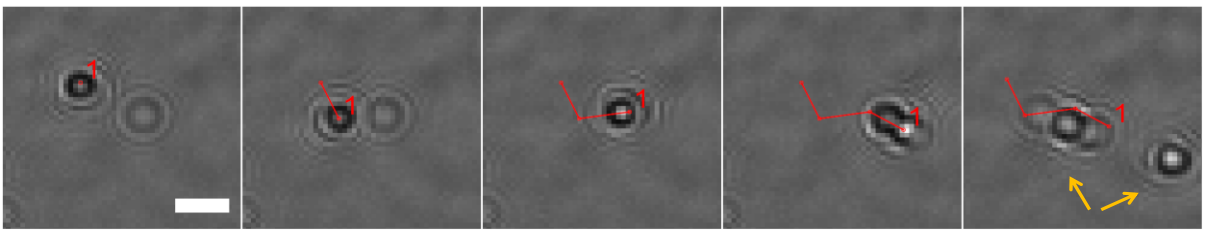

Figure 3E.19: Myoblasts cell migration during cell division. 100-minute time-lapse images showing cell migration during cell division observed in myoblasts. Each frame is separated from its subsequent frame by 20 minutes. The tracked parent cell (red track) moved with a velocity of 0.5µm/min during division. Yellow arrows in the last frame denote the daughter cells. Scale bar: 100µm.

3E.4.2 Cell migration and differentiation

Similarly during cell differentiation (neuronal cell differentiation), we observe reduction in cell migration. On the contrary to migration alteration during division, we do not have a 'V' like curve. In other words, the divided daughter cell behaved like its parent in terms of cell migration, whereas, the differentiated cell did not exhibit significant migration compared to its migration before differentiation. The neuronal cell differentiation of hMSCs was triggered after 28h30m post seeding. The differentiation was realized in 2 steps, as stated in section 3.3. The first differentiation media (culture media supplemented with 1mM β-mercaptoethanol) was added at t0 (24 hours post cell seeding). The second differentiation media (culture media supplemented with 5mM β-mercaptoethanol) was added 24 hours after the first (t0 + 24h). It is interesting to observe that the average cell velocity (n = ~500 cells) gradually decreased from 0.35±0.1 µm/min to less than 0.1 µm/min **(Fig. 3E.20, Fig. 3E.22)**, in 17 hours post addition of the first culture media (t0 + 17h), that is 7 hours prior to the addition of the second culture media **(Fig. 3E.20)**. However, complete neuronal differentiation occurred only at t0 + 36h, as seen by reduction in the size of cell body **(Fig. 3E.21)** and neurite outgrowth, that is 12 hours post addition of second culture media. This shows that change in cell migration is a prerequisite for cell differentiation **(Fig. 3E.22).**

The differentiated cells (neurons) did not regain their earlier cell velocity, indicating in this case, an irreversible alteration in cell migration. However, it is to be noted that the behavior of the cell post-differentiation would depend on the type of differentiation.

Hence it is imaginable that with some other type of differentiation, the cell velocity might increase after differentiation is completed. For example in the neuronal differentiation of PC12 cells, the differentiated neurons migrated with a velocity of ~0.6um/min **(Fig: 3E.2)**.

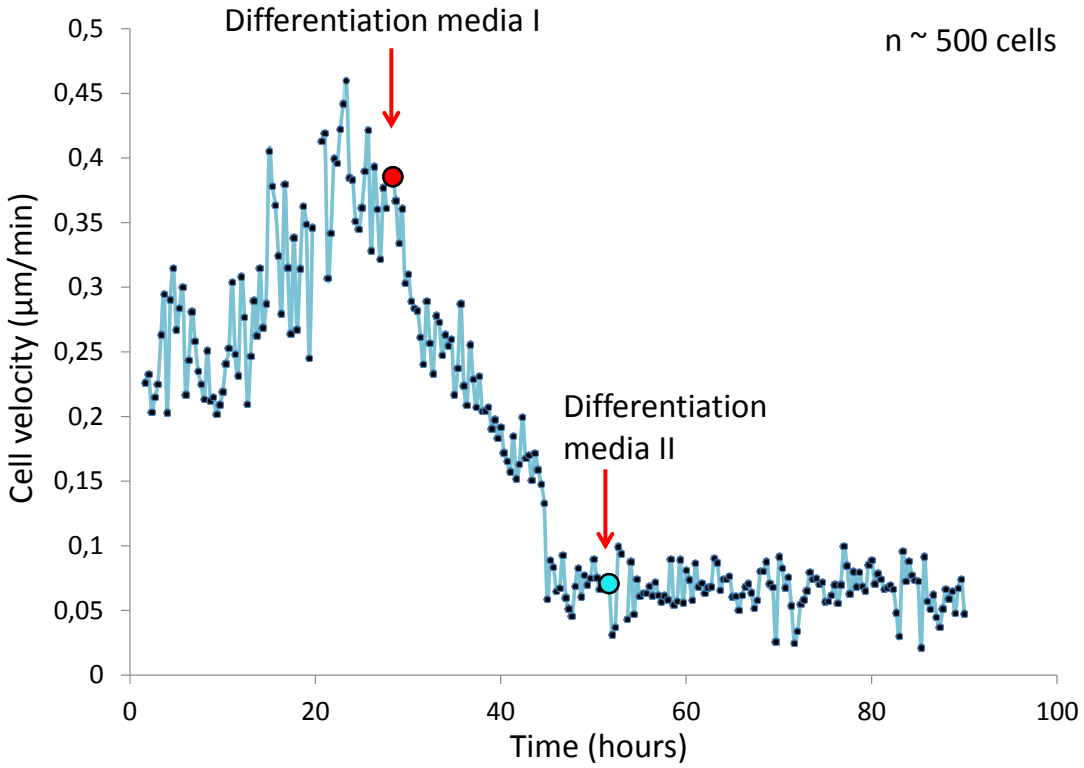

Figure 3E.20: Reduction in cell velocity during neuronal differentiation. Red and blue dots mark the addition of first and second cell differentiation culture media. Note that the cell velocity was significantly reduced well before the addition of second culture media and remained constant thereafter.

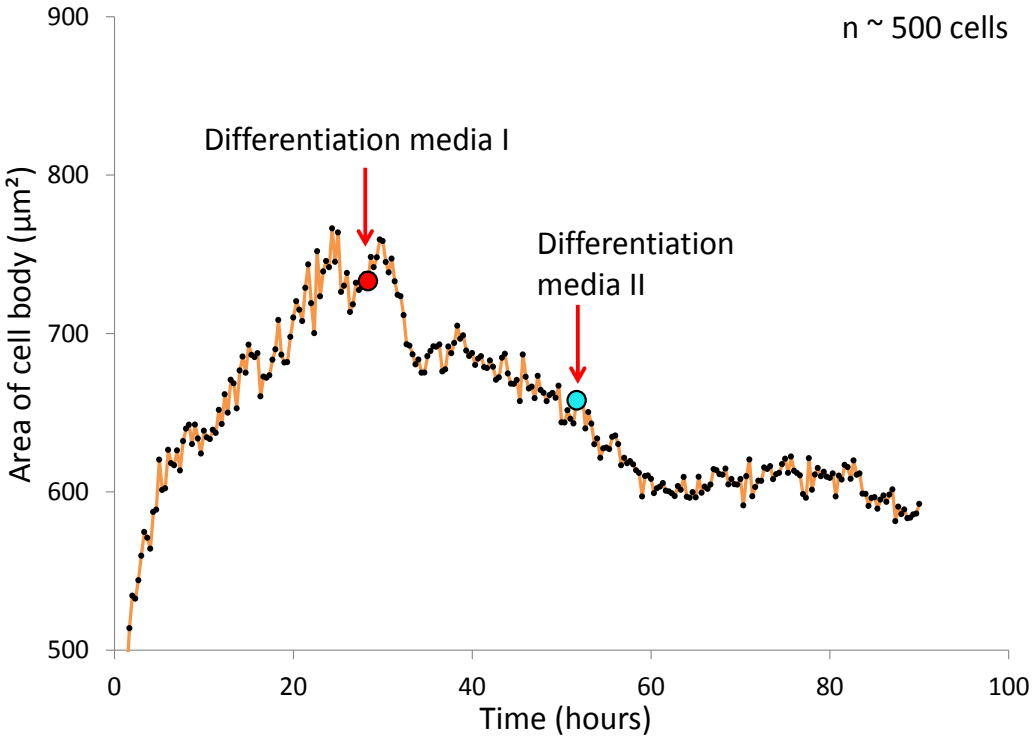

Figure 3E.21: Reduction in area of cell body during neuronal differentiation. Reduction in cell body is used as a way to quantify neuronal cell differentiation. Red and blue dots (along with red arrows) mark the addition of first and second cell differentiation culture media. Unlike cell velocity, the cell body reached its minimum area only ~12 hours after the addition of second culture media.

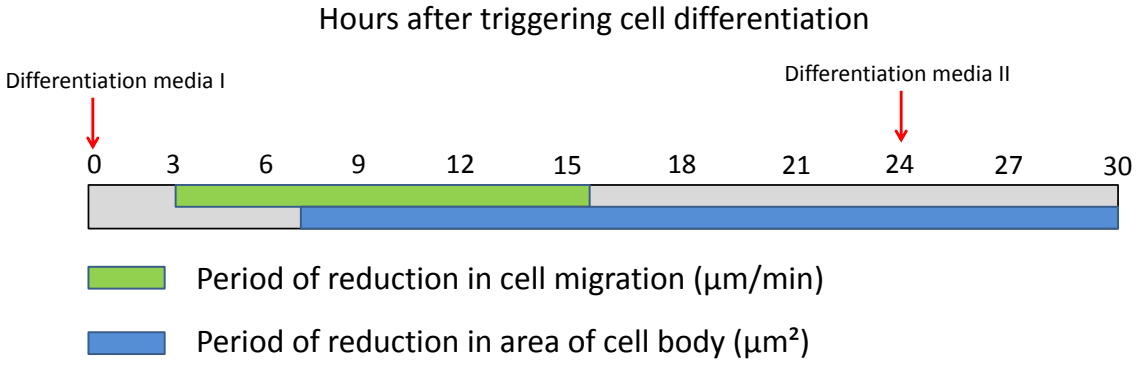

Figure 3E.22: Chronograph - cell differentiation. Chronograph showing reduction in cell motility and cell body area after triggering neuronal differentiation of hMSCs.

3E.4.3 Cell migration and death

Observation of fibroblasts from cell adhesion until cell death, showed us a definite reduction in cell motility during cell death resulting from elevated temperature **(Fig. 3E.23)**. To observe it more clearly, we transfected hMSCs with siCellDeath (siRNA known to induce cell death) to show that the loss of migration of the entire cell population is observed before cell shrinkage and well before the detachment of cells during cell death **(Fig. 3E.24, Fig. 3E.25, Fig. 3E.26)**. Cells were transfected with siCellDeath at t0, loss of cell motility is seen at t0 + 28h **(Fig. 3E.24)** as percentage of motile cells started to decrease (cells with velocity less than 0.2µm/min are considered stationary). The effect of cell shape (i.e. aspect-ratio) is seen only from t0 + 28h **(Fig. 3E.25a)**, and cell detachment is observed only from t0 + 38h **(Fig. 3E.25b)**.

It is known that many genes that are closely connected to PCD (Programmed Cell Death) play equally important role in other cell functions, including energy production, cell division, etc. (Gether, Asmar, Meinild, & Rasmussen, 2002; Karnik, Gogonea, Patil, Saad, & Takezako, 2003). Hence, it is conceivable that initiation of cell death mechanism rapidly results in the loss of cell migration. However, it is also probable that the loss of migration initiates cell death. In other words, is reduction in cell migration an early symptom of cell death or is it the one of the reasons for cell death? Directed individual cell migration is the backbone of collective migration, which is necessary for morphogenesis, regeneration, and cancer (Friedl & Gilmour, 2009). When a cell fails to move efficiently, it starts to exert a localized mechanical tension affecting the neighboring cells and the entire group, therefore counteracting the collective movement. If we consider that the alteration of cell migration initiates PCD, then molecular signals and actors need to be identified, which will link mechanical tension to cell death via genetic pathways. This type of connection

has been shown to exist. For example, it is known that contact inhibition initiates apoptosis in epithelial cells (Eisenhoffer & Rosenblatt, 2014). Similarly Frish et al. have shown alteration in cell-matrix interaction as potential PCD inducing factor (Francis, 1994; Frisch, 1996). Hood et al. provided a comprehensive list of proteins, which links the localized mechanical tension and PCD. Based on these observations, we postulate the probability that loss of cell migration might initiate PCD. For example, in cell death of hMSCs due to siRNA transfection, we observed a small percentage of the population (< 5% of the population containing ~5000 cells) that remained viable **(Fig. 3E.27)**. We observed that these cells did not stop migrating. This can be seen in **Fig. 3E.27**, where 52h after siRNA transfection, only few cells remained adhered and viable. Tracking one such cell showed us that the cell never stopped moving (average speed of 0.5μm/min until the end of experiment, 50h after transfection) **(Fig. 3E.27b,c)**. These rare events, encourages us to hypothesize if the persistence of cell migration was a predominant reason for these sub-population of cells to stay alive while its neighbors did not. It would be interesting to test if suppression of migration can cause cell death. Further experiments are needed to evaluate the interesting hypothesis.

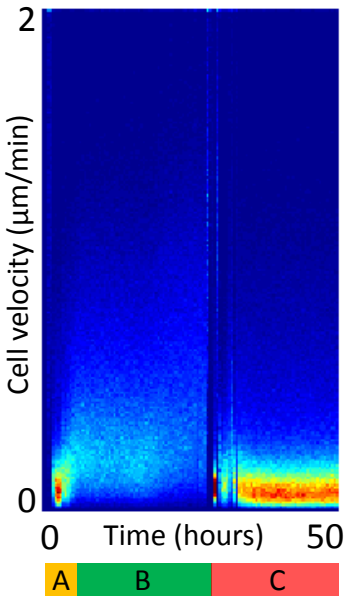

Figure 3E.23: Cell migration and cell death – Fibroblasts. Fibroblast cell death due to increased temperature. Change in cell velocity during cell death of fibroblasts is shown. Initially during cell adhesion (yellow region A), the cell velocity was less than 0.2 µm/min. After adhesion to the substrate, the cells started to migrate with an average velocity of ~0.4µm/min (n = ~2000 cells, green region B). However, the cell velocity decreased to less than 0.2µm/min due to cell death caused by elevated temperature >40°C (red region C).

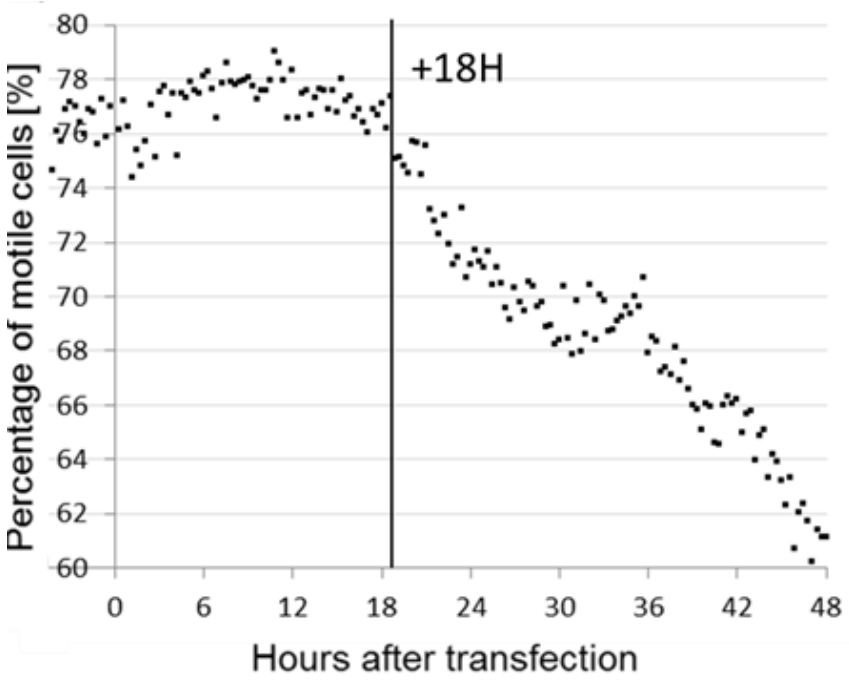

Figure 3E.24: Cell migration and cell death – hMSCs. Cell death of hMSCs due to siCellDeath transfection. The change in cell migration during cell death of hMSCs is shown. With a

threshold of 0.2µm/min for a cell to be considered moving, we calculated the percentage of motile cells. The percentage starts to decrease 18 hours post siRNA transfection.

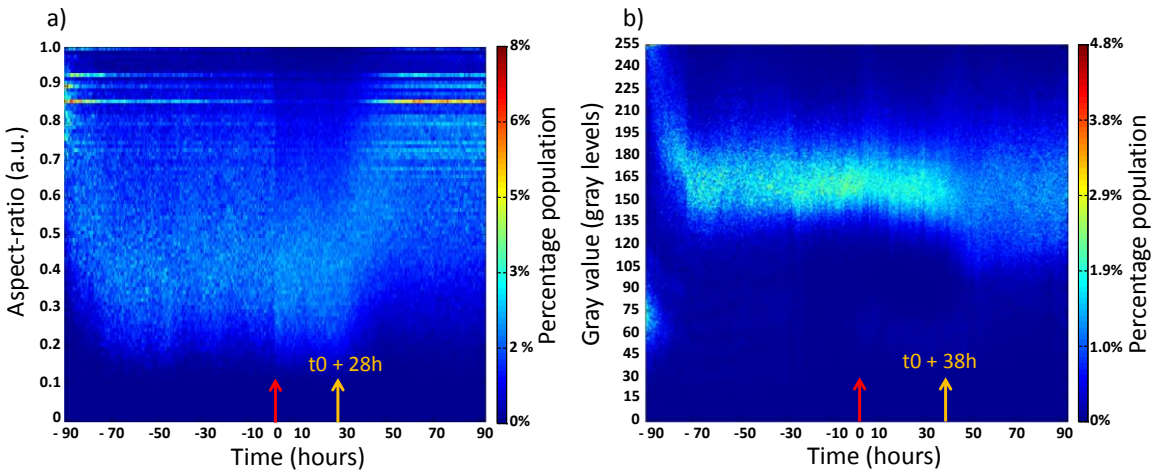

Figure 3E.25: Cell size and cell adhesion during cell death.

(a) Change in cell size (aspect-ratio) following siCellDeath transfection. The cells start to shrink at ~t0 + 28hours (yellow arrow), where t0 marks the moment of siRNA transfection (red arrow).

(b) Change in cell adhesion (gray value) as cells detach from the substrate (yellow arrow) at t0 + 38 hours, due to cell death induced by siCellDeath transfection (red arrow).

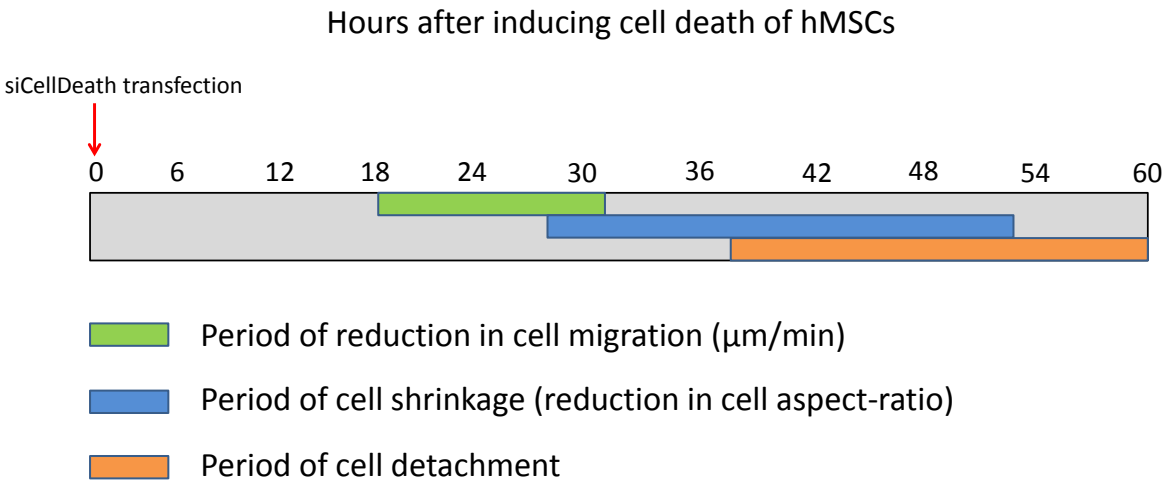

Figure 3E.26: Chronograph – cell death. Chronograph of the effects of siCellDeath on a population of mesenchymal stem cells, showing reduction in cell migration well before cell shrinkage and cell detachment from the substrate.

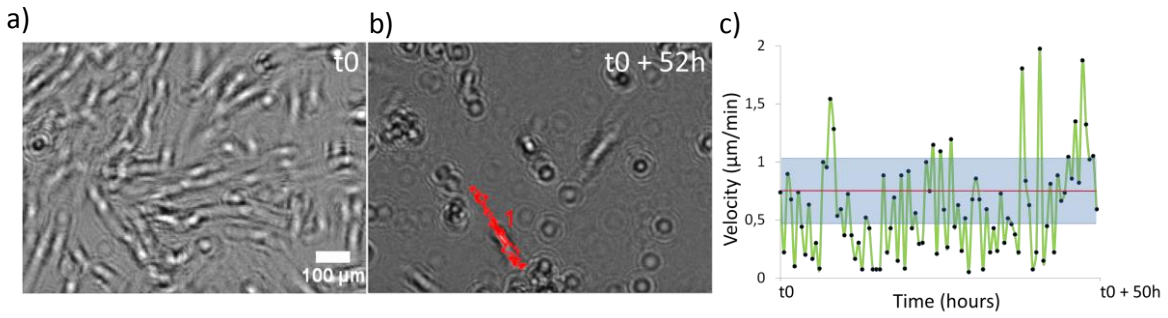

Figure 3E.27: Single migrating hMSC during cell death

(a) ROI of lensfree time-lapse image obtained immediately after transfection (t0), showing densely populated cells.

(b) Same ROI after t0 + 52hours, showing a vacant region due to cell death and detachment. There are a few cells (< 5%) that remain adherent. One such cell was tracked (red track).

(c) The cell constantly moved while its neighbors stopped and died. Perhaps this constant movement of the cell delayed its death. The cell remained viable until the end of the experiment.

3E.4.4 Quiescence and cell migration

Quiescence is a state where cells retain their energy by reducing their metabolic activity exceedingly. At this state, the cells are no longer in cell cycle. Cells enter the state of quiescence in order to protect themselves from harsh environmental conditions, absence of nutrients, etc. In a non-conducive environment, in order to prolong the existence, the cells reduce their metabolic energy almost entirely, by arresting all the cell functions, and by exiting from the cell cycle. Latil et al. have demonstrated extended quiescence of nearly 17 days, seen in satellite stem cells (Latil et al., 2012). Here, we show the entry and exit, of fibroblast cells, from the cell cycle, while being subjected to decreased temperature, using in-vitro scratch assay.

In vitro scratch assay is considered as a convenient and inexpensive method for analysis of cell migration in-vitro (Hulkower & Herber, 2011; Liang, Park, & Guan, 2007). The method involves creation of a gap in confluent monolayer. The cells on either side of the gap move towards each other, closing the gap. By imaging the closure of the gap/or wound, the time taken for the process, and thereby the rate of cell migration can be quantified. The major advantages of the method are that, (i) it is been shown to mimic cell migration in-vivo (Liang et al., 2007), (ii) it does not disrupt the cell-ECM, or cell-cell interaction, and (iii) it is very simple to perform and the process can be followed using live-imaging. The simplicity and FOV of our lensfree video microscope provides an innovative and a convenient platform to study scratch assay along with flexibility to follow the assay in different experimental conditions. Fig. 3E.27 shows the wound healing process of NIH3T3 monolayer. We show the difference in the rate of wound closure at different temperatures. The difference is attributed to cell's entry to quiescence.

We performed scratch assay of NIH3T3 cells at 4°C, and at 37°C. After creating the scratch, the entire process of healing was filmed using lensfree video microscope by taking images once every 20 minutes **(Fig. 3E.28)**. The obtained images were analyzed using imageJ **(Fig. 3E.29).**The background of the image is subtracted, and a binary mask is created using the image. From the mask, using appropriate threshold, all the smaller particles are eliminated, leaving the wound (or gap), and the outline of the wound is generated. From the outline, the area of the wound is calculated. The process is repeated for all the images **(Fig. 3E.30)**.

Monolayer of NIH3T3 cells was subjected to scratch wound and was placed inside the standard incubator. The initial wound area covered 20% of the FOV of the image. From the obtained images, we calculated the wound area at every frame in order to determine

the time taken for the closure. We calculated the fall time of the graph, i.e. the time taken to cover 90% of the wound surface starting from 10%. The process of wound healing started at t0 + 3h20m (considering 10% as the starting point), and 90% of the wound was covered in 18h40m **(Fig. 3E.31, green circles)**.

A similar experiment was performed, creating a wound of approximately the same area. Immediately after creating the wound, the culture dish was placed at 4°C. The culture dish was monitored for a time period of 31 hours. It can be seen that after 32 hours, the wound remain unclosed **(Fig. 3E.31, blue circles)**. In this case, the cell migration was completely brought to a halt, with a displacement of less than 5µm for the entire period of observation of 31 hours.

After 31 hours, we placed the culture dish inside the standard incubator, and the culture media was renewed (preheated to 37°C). Unlike the initial case **(Fig. 3E.31, green circles)**, where 10% of the surface was covered in t0 + 3h20m, here the commencement of the wound healing process was delayed by a factor of 4. Only at t0 + 12h, 10% of the surface was covered. Nevertheless, 90% of the wound surface was covered in t0 + 32h (Fig. 3E.30, red circles).

The closure of the wound is due to combination of cell migration and cell proliferation. However, both these processes involve high metabolic rates. At 37°C, with proper nutrients, cells are active. However, when they are subjected to diverse conditions, in order to survive, cells may enter a state of quiescence. Quiescent cells are widely reported to exhibit reduced size, nucleotide synthesis, and metabolic activity (Coller, Sang, & Roberts, 2006; Glauche et al., 2009; Gray et al., 2004; Larue et al., 2004; White et al., 2014).

In our experiment, we observed NIH3T3 cells' entry in to quiescence due to prolonged exposure to reduced temperature (4°C). Although there was a wound, cell migration, and cell proliferation was arrested, and the wound remained open. It is to be noted that the state of quiescence is characterized by cell's reversible exit from the cell cycle. In other words, upon re-introducing the cells to ambient conditions, the cells may re-enter cell cycle. In order to observe this, we placed the culture dish that was subjected to 4°C for 32 hours, inside the standard incubator. We changed the culture media (with culture media preheated to 37°C). We observed that the cells entered cell cycle, proliferated, migrated and covered the wound. However, the process of wound healing did not start for nearly 12 hours inside the standard incubator. The delay might be attributed to the time taken for the cells to re-enter the cell cycle after being quiescent for ~31 hours.

Immediately (in < 40 minutes) after being exposed to 4°C, the fibroblasts exited from the cell cycle and entered the state of quiescence. The cells remained in the state of quiescence during the entire period with displacement less than 5um (during the period of observation of 32 hours), and re-entered in to the cell cycle after having been exposed to standard ambient conditions. In this case, the change in cell migration was entirely reversible. The cells that re-entered the cell cycle after temporary exit, migrated similar to the cells exposed to normal conditions.

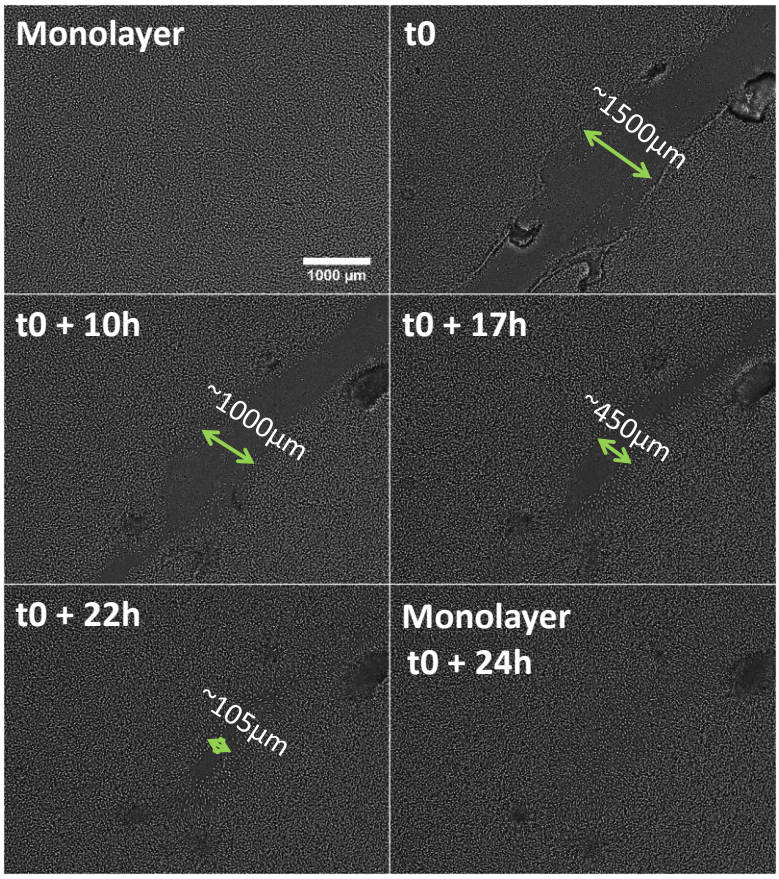

Figure 3E.28: Scratch assay. In vitro scratch assay followed temporally using Lensfree Video Microscope. Time t0 marks the creation of the scratch (green arrow). The wound of ~1500µm was closed in ~18h.

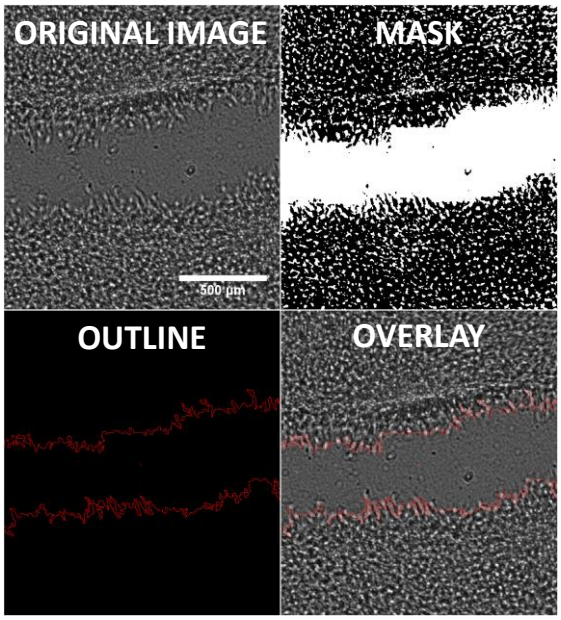

Figure 3E.29: Computational analysis. ROI showing computational analysis using ImageJ. The original image is used to create a binary mask. All the smaller particles in the binary

mask are eliminated, and the larger wound is outlined, and is overlaid on the original ima ge. The area of the wound is calculated from the outlined image.

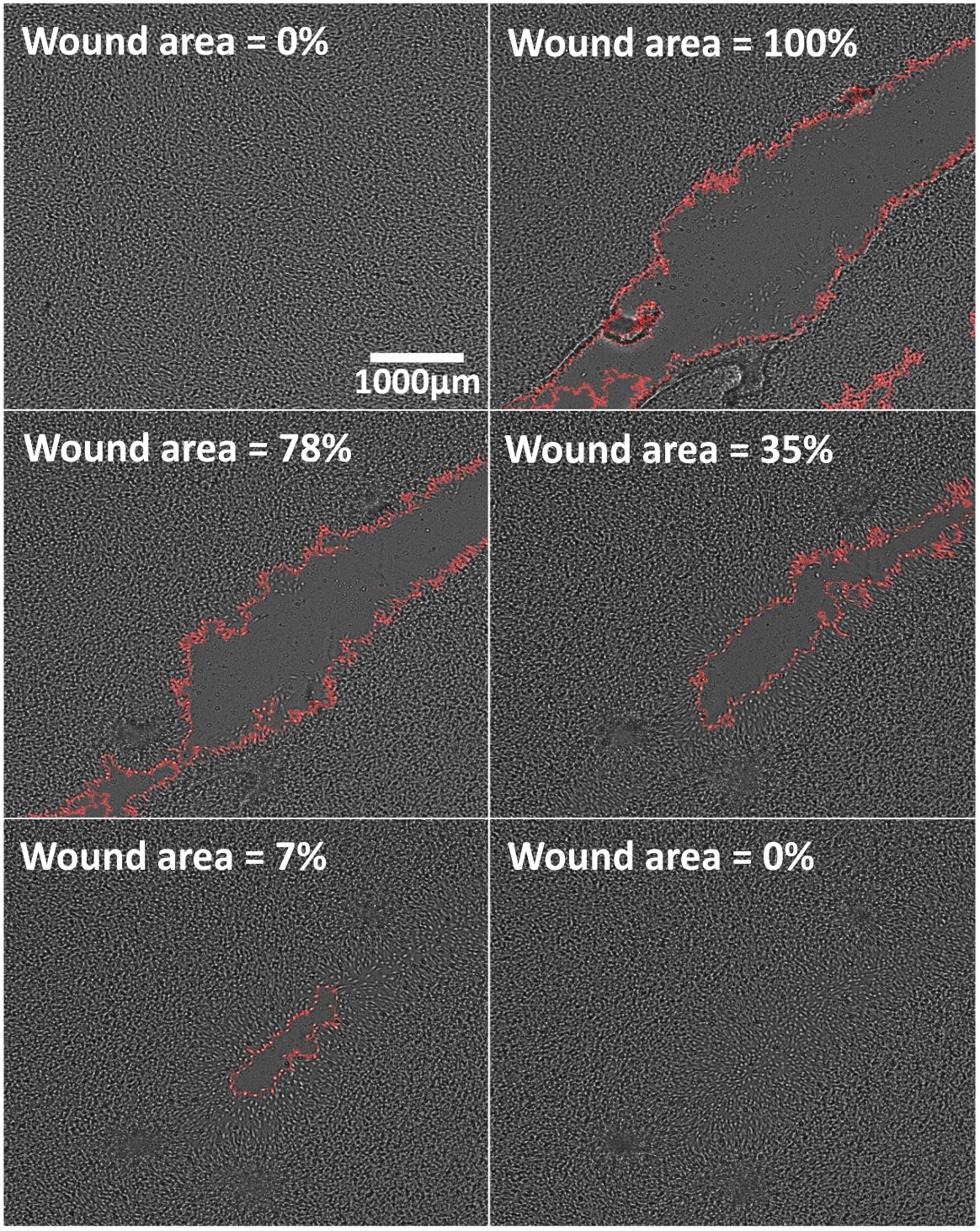

Figure 3E.30: Wound area measurement. Analysis of raw images to obtain wound-area and rate of healing.

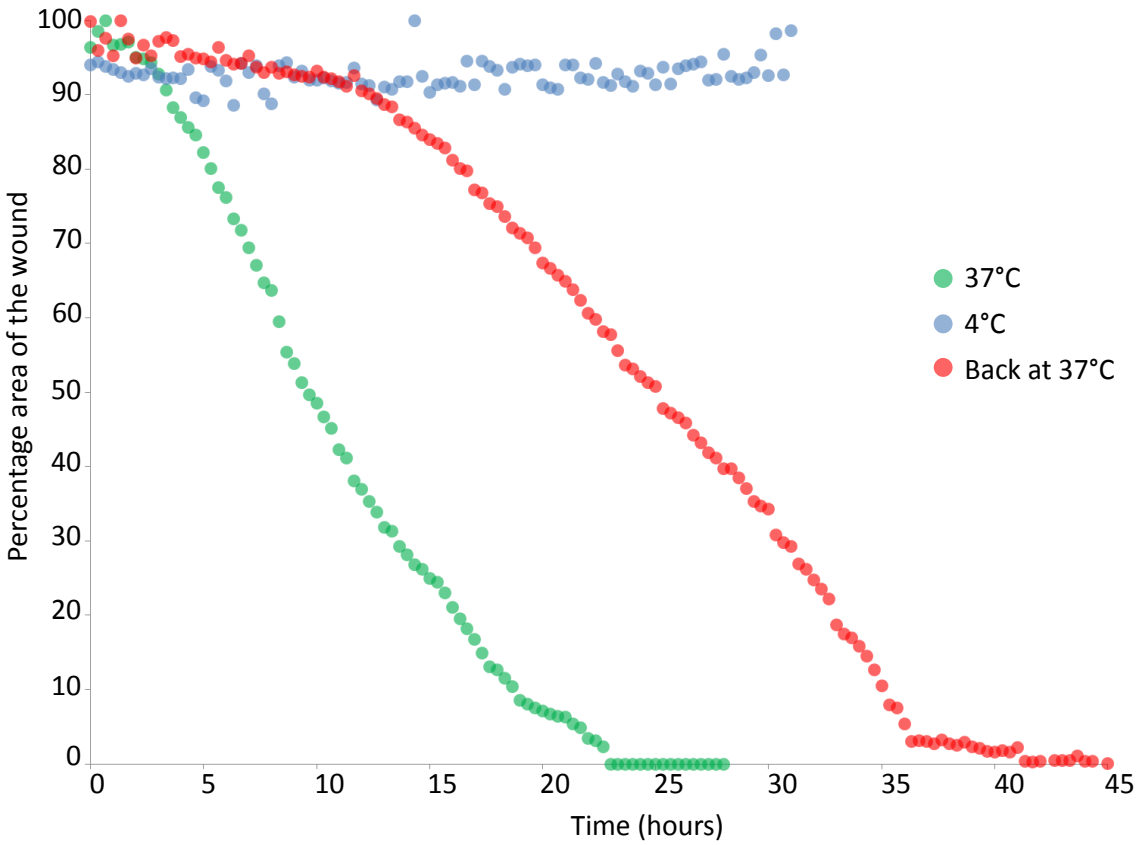

Figure 3E.31: Rate of wound healing at different temperatures. Initially at 37°C (green circles), at 4°C (blue circles), and culture dish that was at 4°C placed back at 37°C (red circles). In the first condition, the wound healing was faster, and 90% of the wound area was covered in 18h40m. At 4°C, due to arrested migration and proliferation, the wound remained open for 32 hours. After 32 hours, the culture dish was placed back in the incubator at 37°C. The cells started to migrate and proliferate, resulting in wound closure. In this case, 90% of the wound was closed in 35 hours.

3E.5 DISCUSSION

Using lensfree video microscope, we exhaustively monitored, classified and quantified cell migration. By analyzing data acquired from varied cell types and experimental conditions, we observed significant relation between cell migration and cell fate, opening a wider question, whether alteration in cell migration is a pre-requisite for these functions to be carried out or, in some cases like cell death, if alteration in cell motility the cause. This question needs to be answered through series of experiments, where cell migration needs to be intentionally altered to observe the effect on other functions. To the best of our knowledge, lensfree video microscope is an apt choice to perform these experiments since it can observe all the major cell functions and also quantify cell migration of both cell population and single cells, without the need for cell harvest, or markers that would perturb the continuity of the experiment.

REFERENCES

Abbott, A. (2003). Biology ' s new dimension. *Nature*, *424*(August), 870–872.

Campàs, O., Mammoto, T., Hasso, S., Sperling, R. a, O'Connell, D., Bischof, A. G., … Ingber, D. E. (2014). Quantifying cell-generated mechanical forces within living embryonic tissues. *Nature methods*, *11*(2), 183–9. doi:10.1038/nmeth.2761

Coller, H. a, Sang, L., & Roberts, J. M. (2006). A new description of cellular quiescence. *PLoS biology*, *4*(3), e83. doi:10.1371/journal.pbio.0040083

Deforet, M., Parrini, M. C., Petitjean, L., Biondini, M., Buguin, A., Camonis, J., & Silberzan, P. (2012). Automated velocity mapping of migrating cell populations (AVeMap). *Nature methods*, *9*(11). doi:10.1038/NMETH.2209

Eisenhoffer, G. T., & Rosenblatt, J. (2014). Bringing balance by force: live cell extrusion controls epithelial cell numbers. *Trends in Cell Biology*, *23*(4), 185–192. doi:10.1016/j.tcb.2012.11.006.Bringing

Francis, S. M. F. and H. (1994). Disruption of Epithelial Cell-Matrix Interactions Induces Apoptosis. *The Journal of cell biology*, *124*(4), 619–626.

Franz, C. M., Jones, G. E., & Ridley, A. J. (2002). Cell Migration in Development and Disease. *Developmental cell*, *2*, 153–158.

Friedl, P., & Gilmour, D. (2009). collective cell migration for morphogenesis, regeneration and cancer. *Nature Publishing Group*, *10*(7), 445–457. doi:10.1038/nrm2720

Frisch, S. M. (1996). Control of Adhesion-dependent Cell Survival by Focal Adhesion Kinase. *The Journal of cell biology*, *134*(3), 793–799.

Gether, U., Asmar, F., Meinild, A. K., & Rasmussen, S. G. F. (2002). Structural Basis for Activation of G-Protein-Coupled Receptors. *Pharmocology and Toxicology*, *91*, 304–312.

Glauche, I., Moore, K., Thielecke, L., Horn, K., Loeffler, M., & Roeder, I. (2009). Stem cell proliferation and quiescence--two sides of the same coin. *PLoS computational biology*, *5*(7), e1000447. doi:10.1371/journal.pcbi.1000447

Gray, J. V, Petsko, G. A., Johnston, G. C., Ringe, D., Singer, R. A., & Werner-washburne, M. (2004). " Sleeping Beauty ": Quiescence in Saccharomyces cerevisiae †. *Microbiology and Molecular Biolody Reviews*, *68*(2), 187–206. doi:10.1128/MMBR.68.2.187

Hulkower, K. I., & Herber, R. L. (2011). Cell migration and invasion assays as tools for drug discovery. *Pharmaceutics*, *3*(1), 107–24. doi:10.3390/pharmaceutics3010107

Karnik, S., Gogonea, C., Patil, S., Saad, Y., & Takezako, T. (2003). Activation of G-protein-coupled receptors: a common molecular mechanism. *Trends in Endocrinology and Metabolism*, *14*(9), 431–437. doi:10.1016/j.tem.2003.09.007

Krieg, M., Arboleda-Estudillo, Y., Puech, P.-H., Käfer, J., Graner, F., Müller, D. J., & Heisenberg, C.-P. (2008). Tensile forces govern germ-layer organization in zebrafish. *Nature cell biology*, *10*(4), 429–36. doi:10.1038/ncb1705

Larue, K. E. A., Khalil, M., Freyer, J. P., Larue, K. E. A., Khalil, M., & Freyer, J. P. (2004). Microenvironmental Regulation of Proliferation in Multicellular Spheroids Is Mediated through Differential Expression of Cyclin-Dependent Kinase Inhibitors Microenvironmental Regulation of Proliferation in Multicellular Spheroids Is Mediated through Diffe. *Cancer research*, *64*, 1621–1631.

Latil, M., Rocheteau, P., Châtre, L., Sanulli, S., Mémet, S., Ricchetti, M., … Chrétien, F. (2012). Skeletal muscle stem cells adopt a dormant cell state post mortem and retain regenerative capacity. *Nature communications*, *3*(may), 903. doi:10.1038/ncomms1890

Liang, C.-C., Park, A. Y., & Guan, J.-L. (2007). In vitro scratch assay: a convenient and inexpensive method for analysis of cell migration in vitro. *Nature protocols*, *2*(2), 329–33. doi:10.1038/nprot.2007.30

Riveline, D., Zamir, E., Balaban, N. Q., Schwarz, U. S., Ishizaki, T., Narumiya, S., … Bershadsky, A. D. (2001). Focal Contacts as Mechanosensors : Externally Applied Local Mechanical Force Induces Growth of Focal Contacts by an mDia1-dependent and. *The Journal of cell biology*, *153*(6), 1175–1185.

Westerweel, J. (1993). Digital Particle Image Velocimetry.pdf. *Delft University Press*.

White, a C., Khuu, J. K., Dang, C. Y., Hu, J., Tran, K. V, Liu, a, … Lowry, W. E. (2014). Stem cell quiescence acts as a tumour suppressor in squamous tumours. *Nature cell biology*, *16*(1), 99–107. doi:10.1038/ncb2889

CHAPTER 4

CASE STUDIES

Pg. 165	**TEMPERATURE MEDIATED CELL DETACHMENT – USING PNIPAM GRAFTED SUBSTRATES**
Pg. 175	**3D CELL CULTURE RWPE1 CELL POLARITY**
Pg. 180	**3D CELL CULTURE ENDOTHELIAL NETWORK FORMATION**
Pg. 185	**NORMAL AND REDUCED TEMPERATURES NORMOXIC AND ANOXIC CONDITIONS**

4. CASE STUDIES

Typically cell culture experiments are performed inside standard incubator at 37°C, in the presence of 20%O_2, 5%CO_2, and 95% of relative humidity, and in majority of the cases the experiments are performed in 2D cell culture conditions. However, certain experiments require tailored conditions, such as reduced temperatures, decreased O_2 content, etc. In particular, recently the use of 3D cell culture has increased as it is believed to closely mimic the conditions in-vivo. Time-lapse microscopes are mainly designed to perform experiments in the ambient condition mentioned above, and do not provide the option of having different experimental conditions. Also, it is difficult to monitor 3D cultures using time-lapse microscopes due to constant unpredictable variations in Z. ECIS (Electrical Cell Substrate Impedance Sensing) have also not been shown to operate at different conditions, and since the cells do not adhere to the substrate in 3D culture, ECIS cannot be used to monitor cell culture in 3D conditions. Hence, researchers who need to monitor cell culture at diverse conditions are in search of platforms that could offer them the required flexibility. Because of its simplicity, our lensfree video microscope offers flexibility that was so far lacking. Monitoring cell culture in diverse conditions resulted in new observations.

4.1 TEMPERATURE MEDIATED CELL DETACHMENT – USING PNIPAM GRAFTED SUBSTRATES

Experiments performed in collaboration with SBSC, CEA, Grenoble
Collaborator: Fabien Abeille (PNIPAM grafting, characterization, experiments)

4.1.1 Introduction

Adherent cell culture often involves harvesting of cells by detaching them from culture surfaces. Cell detachment is usually achieved through the use of enzymes (i.e. trypsin, accutase, collagenase, etc.) which degrade the extra-cellular matrix (ECM), cell-cell junctions and membrane surface protein receptors (Muranova, Shvyrkova, Arkhipov, & Rykunova, 1998)

Poly(N-isopropylacrylamide) (PNIPAM) has been shown to offer an interesting alternative for cell harvesting by preserving the integrity of the cells (Tamura, Kobayashi, Yamato, & Okano, 2012). Cell detachment is mediated by temperature to which PNIPAM responds. Above a lower critical solution temperature (LCST), usually about 32°C, PNIPAM chains are in a poor solvent state exhibiting rather hydrophobic interactions enabling cell adhesion. Below the LCST, PNIPAM chains behave the opposite: they are in a good solvent state and show hydrophilic interactions, cell detachment is triggered. Different studies, both theoretical and experimental, are aimed at understanding the mechanism, and increasing the efficiency of cell detachment on PNIPAM brushes(Halperin & Kröger, 2012; Okano, Yamada, Okuhara, & Sakai, 1995; Xue, Choi, Choi, Braun, & Leckband, 2012; Yamato et al., 1999), particularly by regulating the thickness and the density of the polymer chains (Halperin & Kröger, 2012)

The cell detachment efficiency of PNIPAM brushes is quantified based mainly on the percentage of cells that detach from the substrate upon decreasing the temperature.

Typically, cells are grown on PNIPAM coated culture dishes inside the incubator for 24 hours. During this time period, the cells are not monitored. After 24 hours, the culture dish is placed outside the incubator and the detachment is monitored. Lens-based microscopes are majorly used for the study. In most cases, images are obtained manually at stipulated time periods. The limitations of this approach are restricted FOV, subjective selection, by the user, of the regions of the culture dish for monitoring, subjective discrimination of floating and adherent cells. The restricted FOV offers visibility of at best few tens of cells. As mentioned in section 3A, discriminating floating and adherent cells based on microscopic images is difficult. In some cases, only cell rounding (or cell shrinkage) is considered as a marker for cell detachment, by calculating the area and circularity of the cells. However, cell rounding does not mean that the cell has detached from the substrate. Alternatively, another method involves withdrawing the media supernatant to count the number of detached cells. When detached cells are collected by aspiration of the supernatant, the hydrodynamic shear stress induced, even low, may contribute to detachment of cells that are weakly attached (Ernst, Lieske, Jäger, Lankenau, & Duschl, 2007). This shear stress is obviously variable since it is operator-dependent, adding unquantifiable experimental bias to the quantification.

In order to evaluate the PNIPAM surface, we need a better quantification method. Large FOV, and simplicity in discriminating floating and adherent cells, make lensfree video microscope an efficient platform for this study. Using our microscope, we performed a preliminary analysis of temperature controlled cell detachment of PNIPAM grafted substrates.

4.1.2 Results

As explained in section 3A, the difference in gray value between floating and adherent cells was exploited to quantify cell detachment. We used pattern recognition and gray-level differentiation to calculate the percentage of detached cells.

We studied the temperature mediated detachment of NIH3T3 cells, on PNIPAM coated substrates of thickness 38nm ± 5nm. The reduction in temperature was achieved by (1) placing the culture dish at room temperature (2) Placing the culture dish at room temperature and adding room temperature culture media. In the former case, the temperature decrease was gradual **(Fig. 4.1.1)**, and the culture media descended below LCST in 6 minutes. Whereas, in the latter, the temperature decrease was instantaneous as the culture media at 37°C was replaced with a culture media of 23°C.

In a typical experiment, we observed control (glass substrate), PNIPAM (w/o media change – Slow cooling), and PNIPAM (media change – Fast cooling), outside the incubator for a period of 1h20m, with temporal resolution of 20 minutes.

The results are plotted in Figure for bare glass slides (i.e. control substrates, without PNIPAM) and PNIPAM-grafted glass slides. The control experiments yielded reproducible results compared to PNIPAM substrates. It can be noted that the average percentage of cell detachment (N = 3 independent experiments) is close to 20% in all the cases **(Fig. 4.1.2)**. The cell detachment did not vary between control and PNIPAM grafted substrates (with and without media change). This poor difference motivated us to hypothesize that PNIPAM properties have been lost due to repetitive usage. We performed contact angle measurements to verify if the temperature dependent hydrophilic and hydrophobic properties of PNIPAM, necessary for cell detachment, are intact after repetitive usage.

From contact angle measurements, performed on recycled substrates, we found that PNIPAM chips lost their thermo-sensitivity **(Fig. 4.1.3)**, a case not reported so far. This is further illustrated in **Fig. 4.1.4**, showing the results obtained using lensfree video microscope. During the first usage, about 70% of the cells detached from the substrate, whereas, subsequent usage produced only 20% of cell detachment.

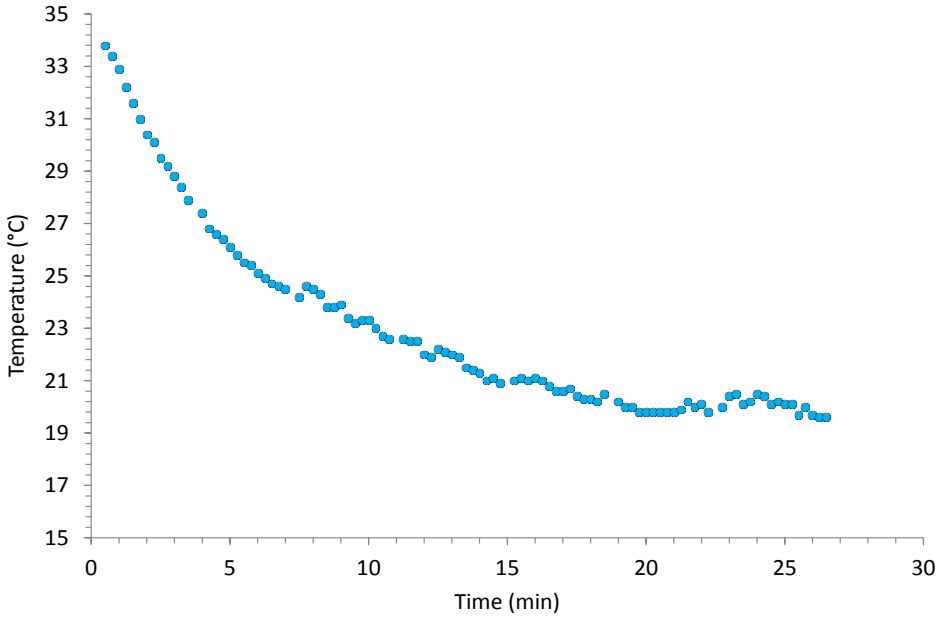

Figure 4.1.1: Time-taken to descend below LCST. Cooling of the culture media inside cult ure dish (Cytoo™ chamber) characterized by a thermal infrared camera (FLIR A20). Afte r 24-hour incubation at 37°C, the Cytoo™ chamber was left to cool in room temperature.

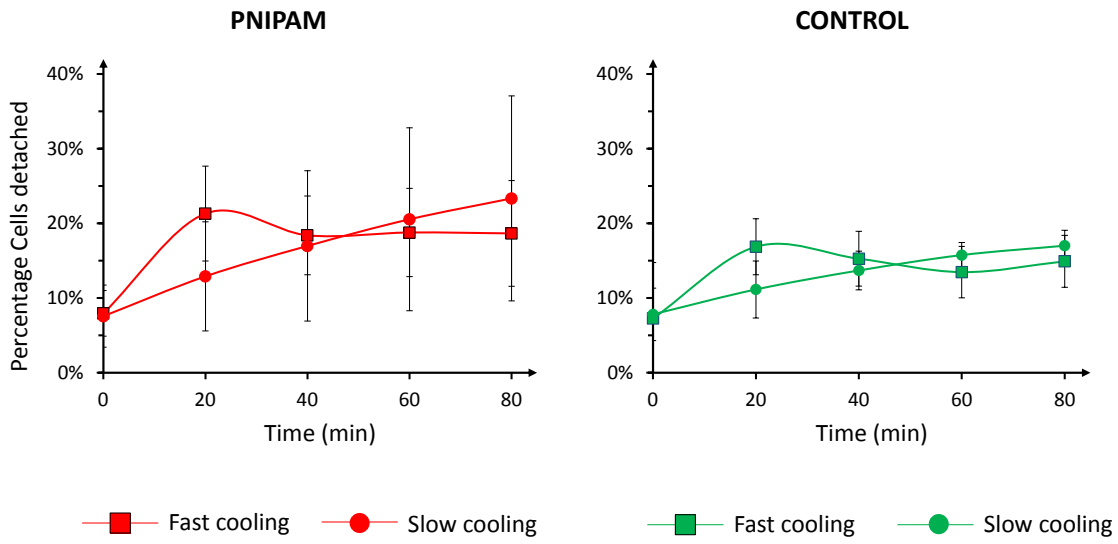

Figure 4.1.2: Percentage of cell detachment. Cell detachment on PNIPAM grafted substrates and control (non-coated glass substrates) were quantified using lensfree video microscope, in 2 conditions, fast cooling (media change), and slow cooling (no media change). Error bars: S.D. from 3 independent experiments.

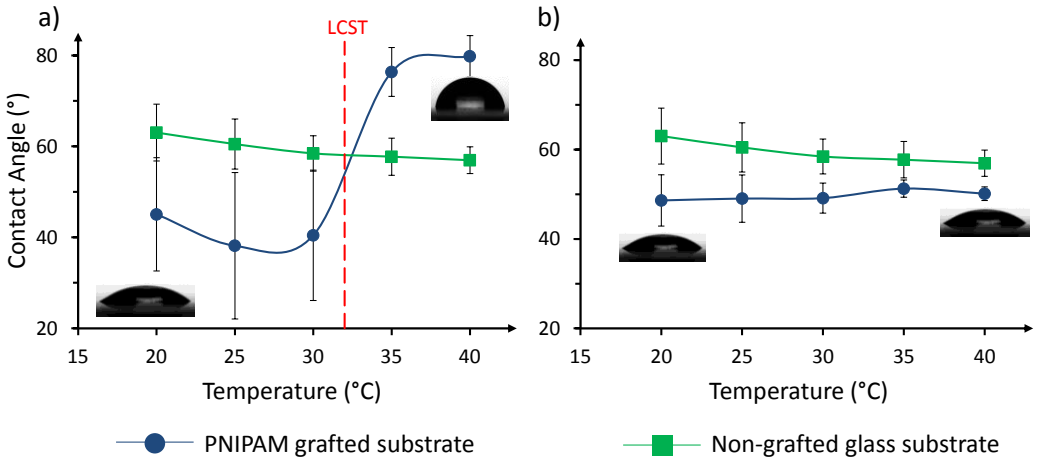

Figure 4.1.3: Static contact angle variation with respect to temperature.

(a) Variation in static angle before the first use and

(b) after several use, of PNIPAM grafted substrates and non-grafted glass substrates.

Picture insets show the water droplet illustrating the thermal sensitivity. Error bar: S.D. from 3 independent experiments.

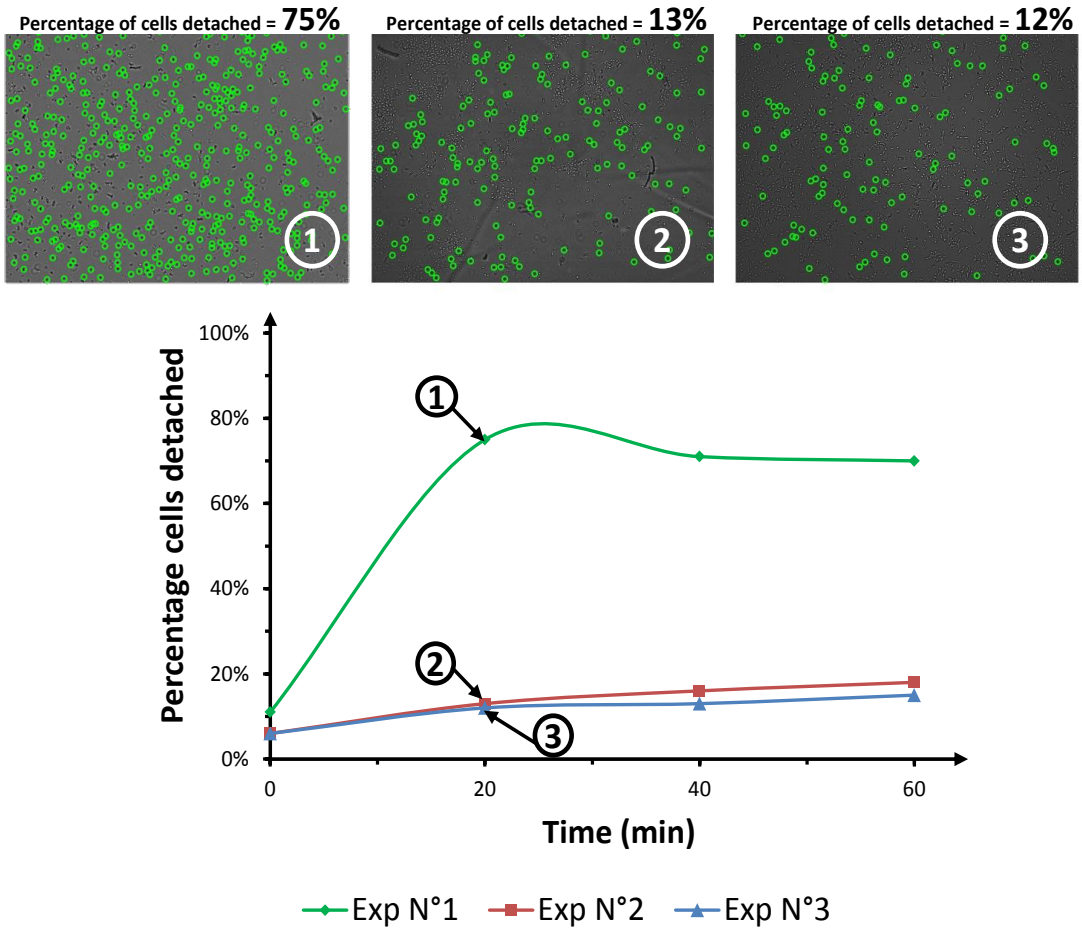

Figure 4.1.4: Loss of cell detachment efficiency. Reduction in cell detachment percentage on a PNIPAM substrate with successive thermal detachment experiments. Numbers correspond to the number of the experiment. Images show cell detachment after initial 20 minutes below LCST.

4.1.3 Discussion

The results do not show a significant difference between PNIPAM grafted substrates and control **(Fig. 4.1.3)**. This is not expected since PNIPAM substrates have been shown to produce significantly higher percentage of cell detachment compared to control non-coated substrates. This smaller difference could be due to larger field of view and also due to the way in which the floating and adherent cells are discriminated. If we consider cell rounding as a criterion and not complete cell detachment, perhaps we could have a higher percentage. Nevertheless, cell rounding cannot be considered as cell detachment since the

cell is still physically adhered to the substrate. Also, since PNIPAM coating may be non-uniform, certain regions of the substrate might yield larger detachment percentage compared to its neighbors. In these circumstances, if evaluation of the substrate is based on smaller field of view of microscope, the results could certainly be misleading. Our results demonstrate that proper care is required in quantifying these substrates, taking a larger field of view to encompass several regions and thousands of cells (n∼1000 to 3000 cells), and a proper way to discriminate floating and adherent cells.

Also we showed the degradation of PNIPAM properties over time **(Fig. 4.1.4).** This might be due to the left-over proteins coming from cell cultures. It is known that the cells are known to detach with the majority of their ECM (Kumashiro, Yamato, & Okano, 2010), but not all, since some components (i.e. proteins) of that ECM could be found on PNIPAM substrates after cell lift-off (Canavan et al., 2007). Perhaps this is the reason for varied results due to repetitive usage. By varying the substrate thickness of the PNIPAM coated substrates, and also by varying the cell types, the efficiency of PNIPAM on cell detachment and its usage-dependent degradation can be evaluated.

4.1.4Methods

4.1.4.1 Poly(N-isopropylacrylamide) grafting

The grafting of PNIPAM brushes on microscope glass slides and diced silicon wafers was proceeded as depicted in **Fig. 4.1.5**. i) silanization of the glass and SiO2 surfaces followed by, ii) covalent attachment of a surface initiator which eventually promoted, and iii) PNIPAM grafting by atom transfer radical polymerization (ATRP).

i) Silanization: Glass slides and silicon chips surfaces were hydroxylated and cleaned in an O_2 plasma reactor (AST products, Inc.) under a flow of 20 sccm for 5 min and 80 W RF power. Hydroxylated surfaces were immersed for 1 min into $5x10^{-4}$ M aqueous solution of APTES filtered through a 0.22µm filter (Acrodisc® PSF syringe filter, Pall®Life Science). Time of immersion determined the further density of PNIPAM. Slides and chips were rinsed with deionized water and dried.

ii) Polymerization initiator grafting: After silanization substrates were immersed for 30 seconds in a 25ml dichloromethane solution containing 1.25ml of TEA and 250µl of BIBB (surface initiator). Substrates were rinsed in dichloromethane then ethanol, then deionized water and eventually dried.

iii) PNIPAM grafting: NIPAM was recrystallized 2 times before use in n-hexane. A 20 mL aqueous solution with 0.5g of NIPAM and 150µl of PMDETA was stirred and bubbled in a balloon under argon for 30 min. It was then transferred to another balloon containing 12 mg of CuCl also under argon atmosphere and stirring. Eventually substrates were immersed for 3 min. The time of immersion determined the chain length of the polymer brushes.

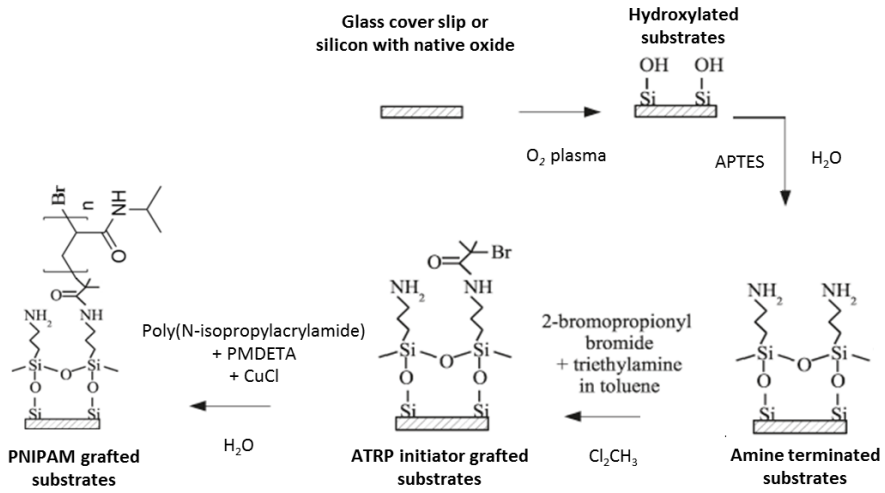

Figure 4.1.5: PNIPAM grafting procedure

4.1.4.2 Poly(N-isopropylacrylamide) grafting: Ellipsometry

To obtain the dry thickness of PNIPAM which is the thickness of the collapsed chain above the LCST, the grafted silicon chips were analyzed by a custom-built rotating compensator ellipsometer with a 632nm wavelength laser and a 70° angle of incidence. A refractive index of 1.46 was considered for SiO2 and 1.47 for PNIPAM. A Si/SiO2/PNIPAM multilayer was assumed. Measurements were performed in 3 different locations of the chips.

4.1.4.3 Cell culture methods

NIH3T3 cells were cultured following the same protocol mentioned in chapter 3A.4.2.

4.1.4.4 Cell detachment monitoring

Protocol schematic of cell detachment monitoring is depicted in **figure 4.1.6**. Glass slides (20 x 20mm), with and without PNIPAM were sanitized by immersion in 70% ethanol for overnight. The non-coated glass substrate and 2 PNIPAM coated substrates were then attached to 3 Cytoo™ chambers. Cells were seeded in the Cytoo™ chambers at a concentration of 10^4 cells/cm², and were cultured for 24 hours in the 5% CO_2 incubator at 37 °C prior to cell detachment experiment.

For cell detachment monitoring at room temperature: The Cytoo™ chambers were monitored in parallel, using 3 lensfree video microscopes. A total of five images were acquired at a rate of one image per 20 minutes.

PNIPAM substrates were immersed in 1ml of trypsin-EDTA for 10 minutes at 37°C to remove the remaining cells followed by two washes with 1mL of PBS. 1ml of trypsin-EDTA was dispensed afterwards on the substrates for 10min at room temperature and finally they were rinsed with 1ml of PBS. PNIPAM substrates were stored wet (PBS) in 4°C between each cell culture experiments.

Percentage of cell detachment was quantified based on pattern recognition, and gray-level differentiation, on raw image, as mentioned in chapter 3A.4.1

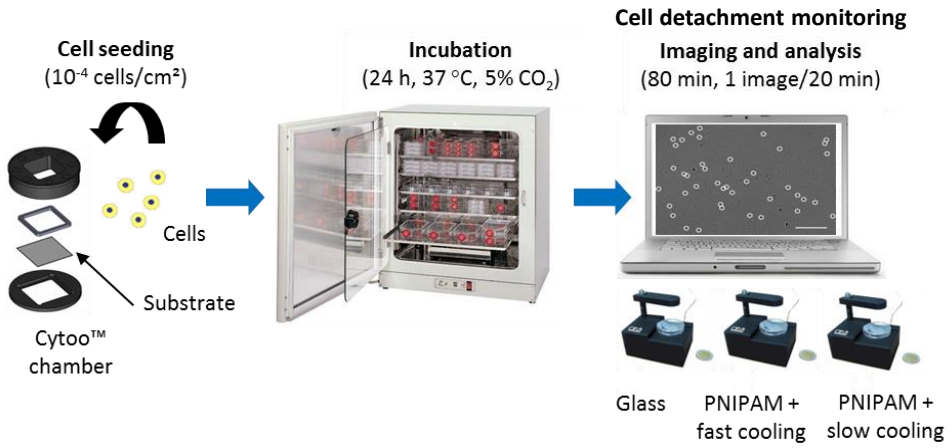

Figure 4.1.6: Protocol schematic of a cell detachment experiment. The substrates (with and without PNIPAM) are attached to Cytoo™ chambers. The cells are seeded into the chambers, and are cultured inside the standard incubator for 24h. After 24h, the chambers are imaged outside the incubator for cell detachment using 3 lensfree video microscopes in parallel.

4.2 3D CELL CULTURE: RWPE1 CELL POLARITY

Experiments performed in collaboration with DSV, Biomics, CEA
Collaborators: Monika E. Dolega, Sophie Gerbaud, Frédérique Kermarrec, Xavier Gidrol, Nathalie Picollet-D'Hahan(3D cell culture preparation and experiments, data analysis)

4.2.1 Introduction

Although the majority of the experiments are being performed in 2D cell culture environment, recent studies question the significance of 2D cell culture, stating that it does not mimic the in-vivo conditions (Pampaloni, Reynaud, & Stelzer, 2007)(Abbott, 2003)(Maltman & Przyborski, 2010). 3D cell culture on the other hand is shown to be closer to the conditions in-vivo. In fact, certain cellular functions that are present in 3D environment are never to be seen in 2D cell culture (Fraley et al., 2010; Pampaloni et al., 2007). Therefore, the growth of 3D cell culture utilization is expanding since 2003.

Unlike lens-based microscopes, imaging using Lensfree video microscope is not hindered by the displacement in Z direction associated with 3D cell cultures. Using lensfree video microscope, we studied the 3D organization of RWPE1 prostate epithelial cells in Matrigel environment. We studied acini–3D structures constituting secretory epithelium. These 3D acini structures are characterized by their apical and basal polarities. During tumor progression, the apical polarity of the acini is lost, transforming them in to spheroids. To differentiate between the acini and spheroids, currently marker-dependent, time-consuming, immunostaining approaches are used. By reading the optical signatures obtained from both these structures –acini and spheroids – we were able to differentiate them in real-time, without using markers.

4.2.2 Results

The full FOV image obtained from RWPE1 3D cell culture is shown in **Fig. 4.2.1**. Many 3D acini structures can be visualized, along with few single cells. The diffraction pattern obtained from the single cells and from the 3D acini structures are different compared to that of single cells.

We studied RWPE1 and WPE1-NB26 cell types. The optical confocal sections of DAPI-stained cells after 8 days of growth in Matrigel show that the non-tumorigenic RWPE1 formed acini with well-polarized cells and a distinct lumen, whereas, characteristic to their increased malignancy, WPE1-NB26 cells did not differentiate efficiently, forming spheroids.

By comparing the two different 3D cell cultures, we found that our lensfree holographic patterns showed significant differences between acini and spheroids. The lensfree holograms of spheroids exhibited a very bright spot in the middle compared to the darker pattern obtained from acini with lumens. The difference in the gray-level intensity in the center of these two holograms is approximately 100 out of 255 gray levels.

We also filmed the growth, in size, of acini structures over a period of 3 days. Cells that form the acini structures divide resulting in the growth of the structure, from ~10µm to ~100µm in 72 hours.

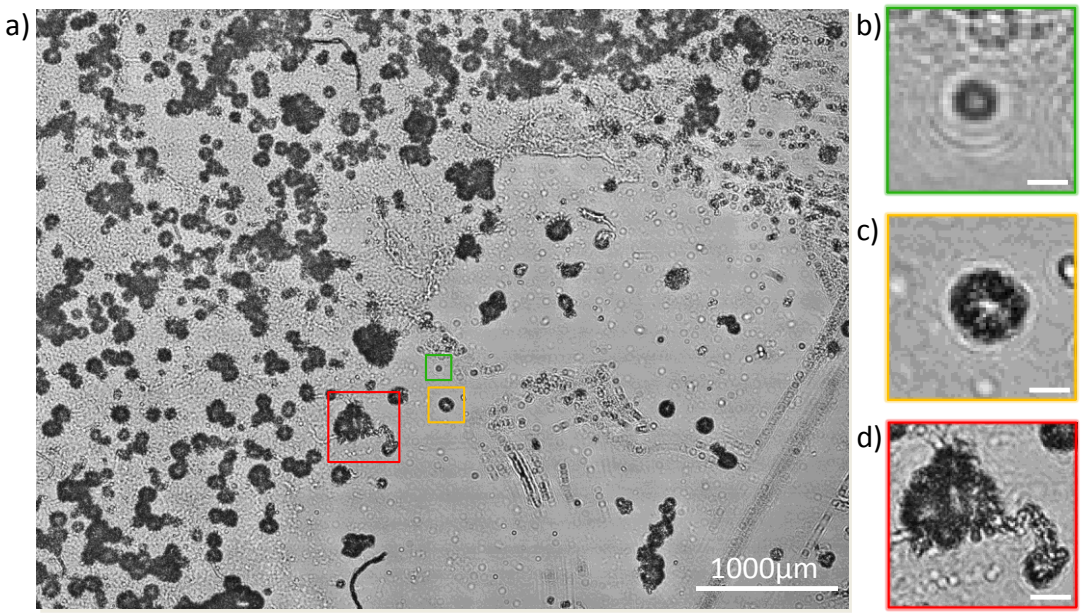

Figure 4.2.1: Lensfree imaging of 3D cell culture. a) Lensfree imaging of an 8-well Lab-Tek slide chamber filled with a 3D culture of RWPE1 epithelial cells. The magnified R OI (b), (c), (d) show single RWPE1 cell, single acini, and merged acini respectively. Scale bar for magnified ROI: 50µm

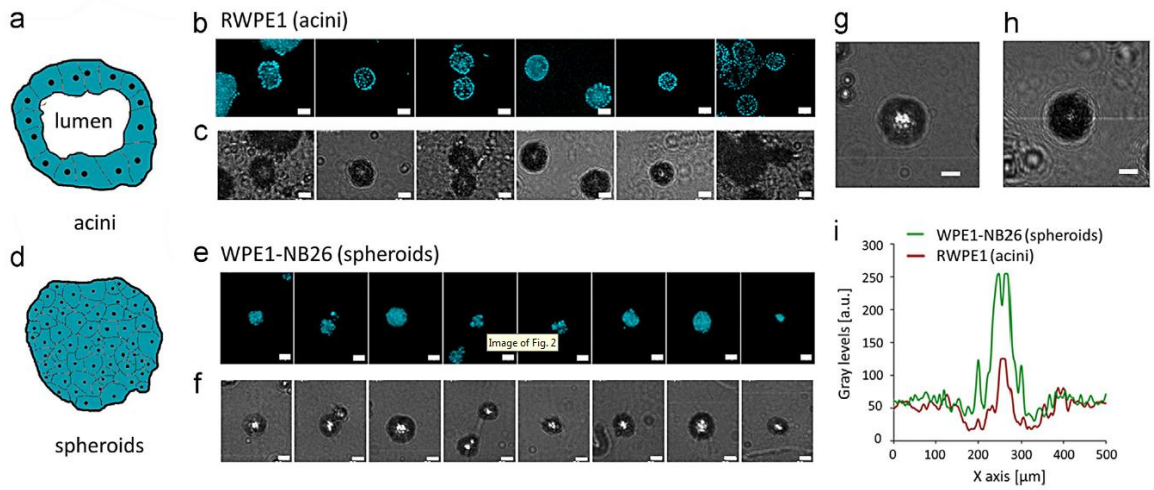

Figure 4.2.2: Discriminating acini and spheroids from lensfree holographic patterns. Lensfree and fluorescence microscopy images of acini with lumen and spheroids. Hoechst-stained 3D cell cultures after 8 days of growth in Matrigel of (a-b) RWPE1 and (d-e) WPE1-NB26 cells (20x magnification, scale bar 50µm). The lensfree holograms of the acini with lumen and the spheroids, whose schematics are depicted in (a) and (d) respectively present significant difference (scale bar: 50µm). At the center of the pattern, the difference in gray-levels yields a value of 100 (on a scale of 255). The value is largely above the background noise of lensfree image (~ 5 gray-levels S.D.), and well above the mean gray value of 50 gray-levels. Typical lensfree holograms of WPE1-NB26 cells (spheroids) (g) and RWPE1 cells (acini) (h) (scale bar: 50µm). Intensity profiles measured

on lensfree holograms showing the main axis of the WPE1-NB26 cells (spheroids, in green) and the RWPE1 cells (acini, in red) (i).

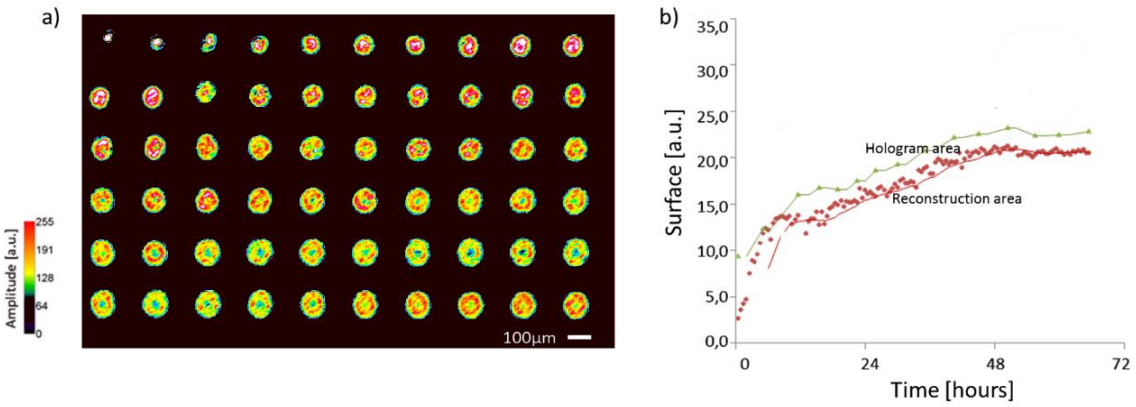

Figure 4.2.3: Growth of acini.

(a) Time-lapse observations showing the development of a prostatic acinus over 72 hours, with 1 hour between two frames. The reconstructed amplitude indicated as a grey/yellow/red lookup table allows to outline the acinus, but the value cannot be correlated to e.g. absorption or thickness and is given for information only.

(b) The relative dimensions of the acinus is measured over time by measuring both the raw hologram area (green), and also by measuring reconstructed image area (red). The latter parameter gives the dimension of the 2D projection of the acinus figure and can be related to the diameter of the 3D volume of the acinus provided that it is spherical.

4.2.3 Discussion

Monitoring of 3D cell cultures is currently performed using lens-based microscopes, and immunofluorescence. However, quantitative measurement over a period of time is hampered as described in (Yue, Cárdenas-Mora, Chaboub, Lelièvre, & Cheng, 2012). ECIS (Electric Cell Substrate Impedance Sensing) cannot be used in studying 3D structures due to the absence of adherence of the cells to the substrate. Lensfree video microscope is an alternative technique to perform label-free, real-time, continuous monitoring in 3D cell culture conditions that is certainly not hindered by the Z directional movement of the objects. In this study we observed epithelial 3D structures. The study demonstrates for the first time, the use of lensfree imaging as a new methodology to discriminate polarized

(acini), and non-polarized architectures. The maintenance of polarity is a critical criterion in development and morphogenesis. By further extending our experiment, we monitored the growth of acini structures over 72 hours. Using lensfree video microscope several conditions that alter the cell-ECM interaction can be studied to understand its influence in the biological processes including polarity maintenance, network formation, growth etc.

4.2.4 Methods

4.2.4.1 3D Cell culture methods

The RWPE1 human prostate epithelial cells (ATCC CRL-11609) were cultured in 3D with KSFM (Life Technologies, ref.17005-075) supplemented with 50ng/ml EGF and 2% fetal bovine serum (FBS). Briefly, the 3D culture was grown in Matrigel (BD Biosciences, San Jose, CA, ref.356231) according to the top-coat protocol (Lee, Kenny, Lee, & Bissell, 2010). For polymerization, Matrigel was incubated for 30 minutes at 37°C. Cells were seeded in half the final volume and allowed to adhere for approximately 45 minutes. The top coat layer containing 8% Matrigel was slowly poured over the attached cells. The culture media was changed every other day. The Labtek plate was placed in an incubator at 37°C with humidified atmosphere and 5% CO_2. Acini growth was monitored starting day 4 when nice polarized structures are already formed. Acquisitions were performed with a temporal resolution of 1 image per hour.

4.2.4.2 Computational methods

The holographic patterns obtained from acini structures were reconstructed using the reconstruction technique mentioned in chapter 2.3.2, assuming 2D projection recorded from 3D objects, to obtain the diameter of the acini structures.

4.3 3D CELL CULTURE: ENDOTHELIAL NETWORK FORMATION

Experiments performed in collaboration with Grenoble Institute of Neurosciences.
Collaborators: C. Di Natale, L. Hamard, B. van der Sanden, D. Wion (Conceptualization, experimentation, analysis)

4.3.1 Introduction

Angiogenesis is the process by which endothelial cells grow and disassemble into functional blood vessels. It is the sprouting of microvessels to form new capillary networks. Angiogenesis occurs by endothelial cell migration away from existing vasculature after degradation of the surrounding basement membrane, and endothelial cell proliferation. Angiogenesis plays major role in morphogenesis, wound-healing, and also in tumor-formation and metastasis. Hence studies are conducted to understand the mechanism of angiogenesis and especially to control it by growth inhibiting factors in cancer therapy (Eilken & Adams, 2010; Grange et al., 2011; Potente, Gerhardt, & Carmeliet, 2011; Saunders & Hammer, 2011; Shojaei, 2012).

4.3.2 Results

Using our lensfree video microscope, we visualized the kinetics of the network formation of endothelial cells **(Fig. 4.3.1)**. We monitored the formation of network over a period of 24 hours. The architecture of the HUVEC network was analyzed with ImageJ using an angiogenesis analyzer plug-in (Angiogenesis Analyzer by Gilles Carpentier) **(Fig. 4.3.2)** to calculate several parameters of the network, including the number of branches, nodes and meshes, and then plot them as a function of time **(Fig. 4.3.3)**. During the first 4 hours, the network is in formation: the number of meshes increases, and so do the number of segments, junctions and nodes. Following this, for 6 hours, the network remains stable. Towards the end, the meshes merge to form larger meshes. After 24 hours, the networks present the following architecture: total meshes area of 9mm^2, with 60 meshes, with an

average size of 0.15mm². Overall, we were able to define three different steps for the network formation: initiation, a stabilization period and then the fusion of meshes **(Fig 4.3.3)**.

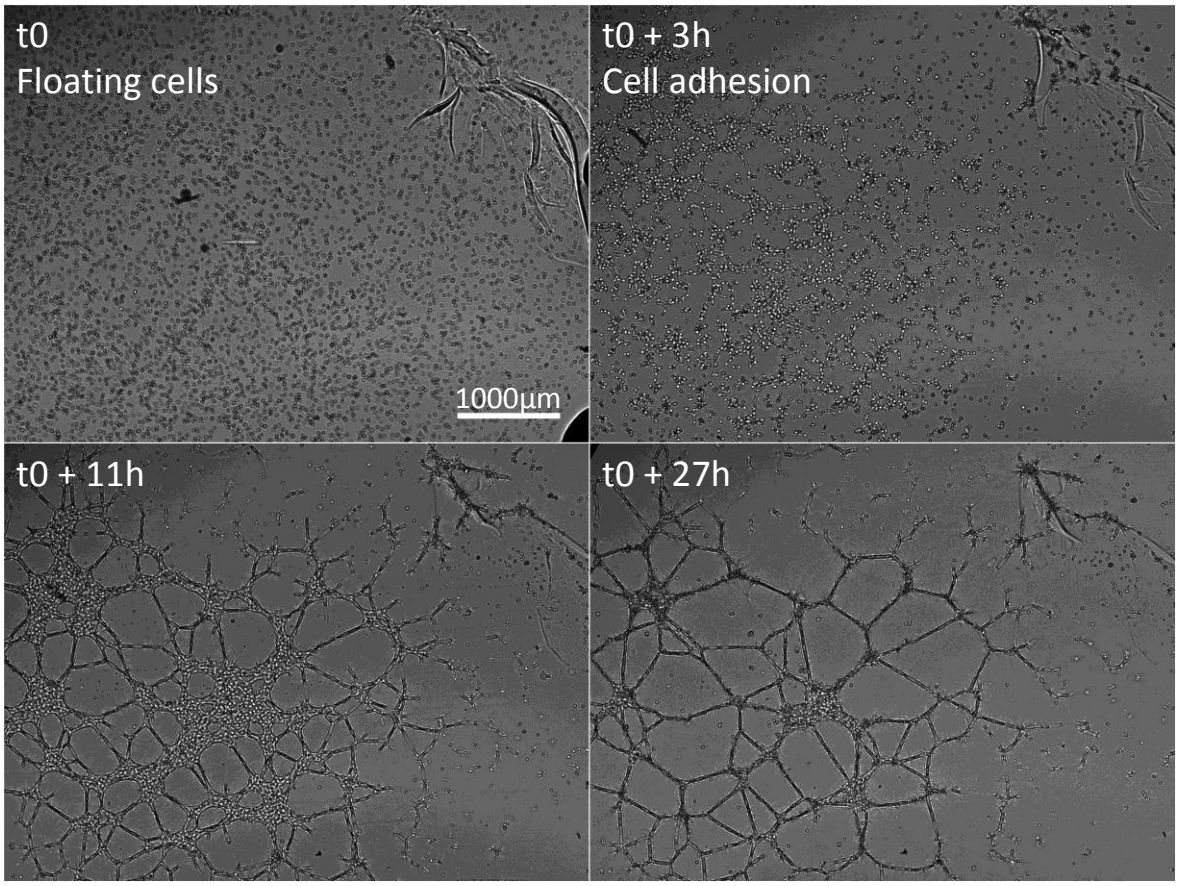

Figure 4.3.1: HUVEC angiogenesis observed using lensfree video microscope. Cell adhesion is observed at t0 + 3h, and a well-established network is seen at t0 + 24h. Time t0 marks cell plating.

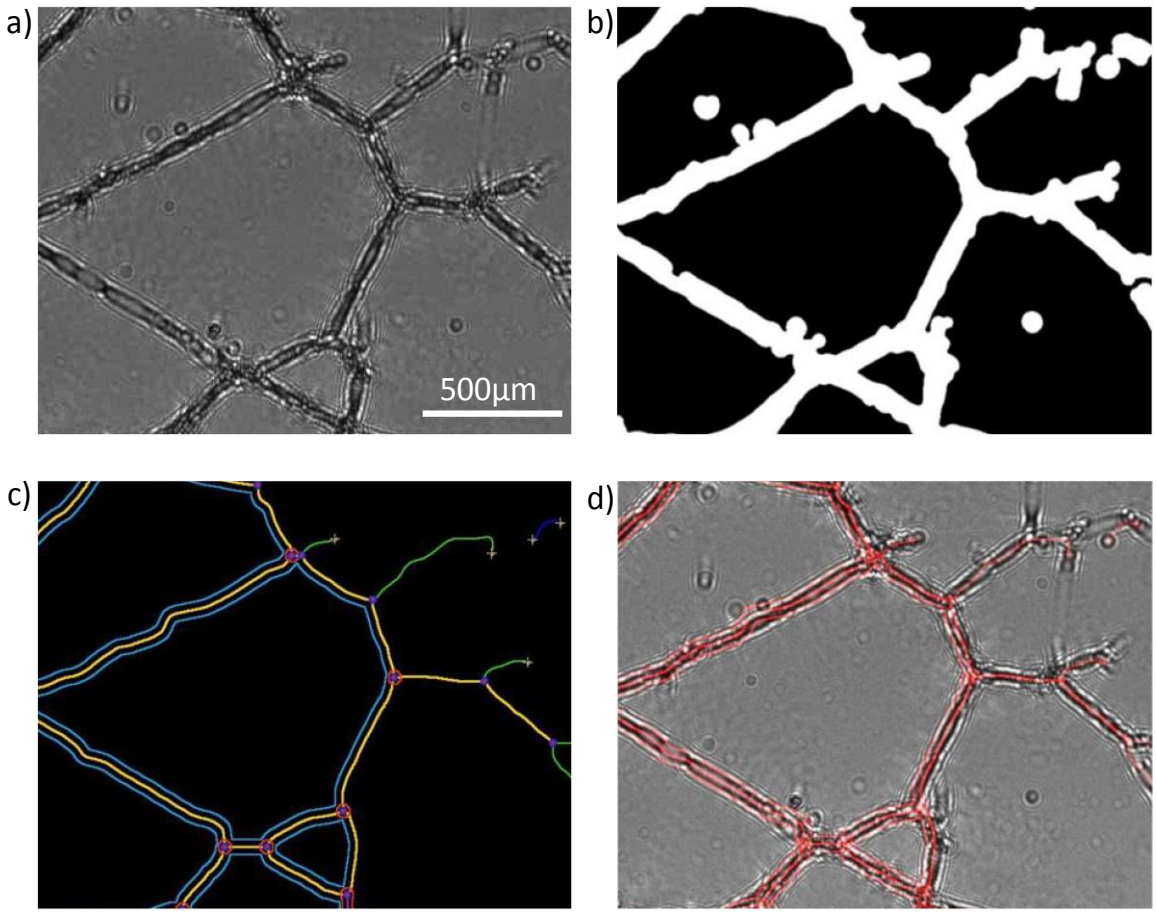

Figure 4.3.2: Analysis of HUVEC angiogenesis. Image analysis of the acquired images using ImageJ: plugin angiogenesis analyzer. (a) ROI from raw lensfree image. (b) Image after binarization. (d) Image after the application of 'angiogenesis analyzer' algorithm. Segments are in yellow, branches in green, red points are nodes, meshes (closed structures, also called tube-like-structures) are in cyan, and isolated structures are in blue. (e) Outline of the analysis is superimposed on raw image. Analysis by C. Di Natale.

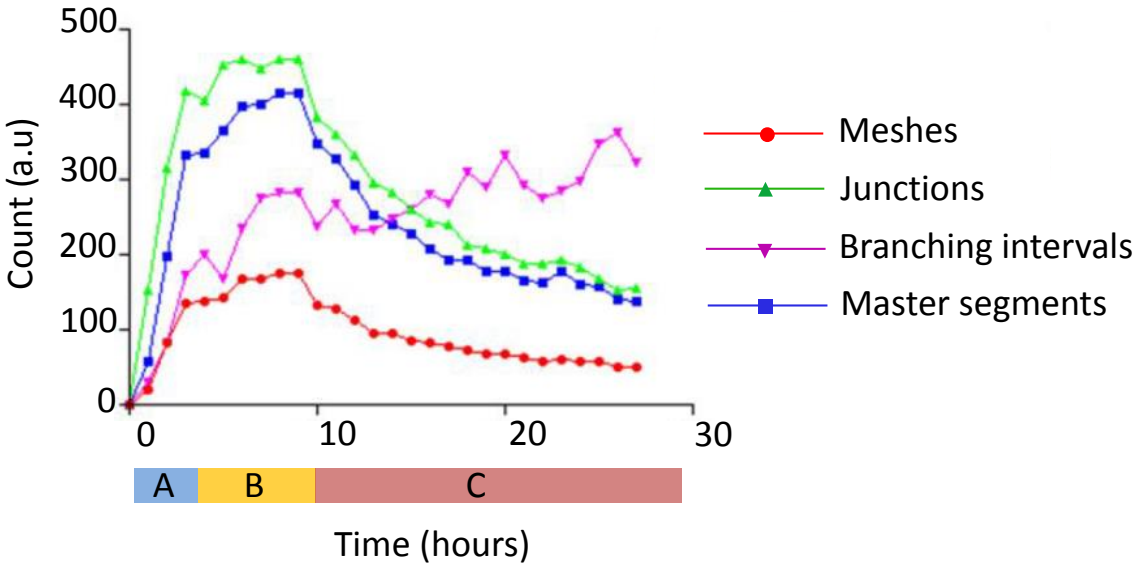

Figure 4.3.3: Analysis of the kinetics of HUVEC network: meshes (red), junctions (green), branching intervals (pink) and master segments (blue). The bars A, B, C denote the three phases that was identified in the network formation: initiation phase (A), stable phase (B), and fusion phase (C). Analysis by C. Di Natale.

4.3.3 Discussion

Angiogenesis is inevitable for tumor growth and metastasis, since it is the way for the tumor cells, to access necessary nutrients and O_2 from blood vessels. Endothelial cells involved in vasculogenesis and angiogenesis are key targets in cancer therapy. We studied the network formation kinetics of endothelial cells using lensfree video microscope and characterized the in-vitro network formation in to 3 stages, initiation, stabilization, fusion of meshes. The kinetic information that is provided by our microscope is certainly an added asset to the study. The network formation in-vitro is studied by using 3D (Matrigel) environment, in order to better mimic the conditions in-vivo. Indeed the cells went through the Matrigel by about 300µm during the network formation process. Our methodology was not able to identify this degradation of Matrigel environment by HUVEC cells during network formation. However, this information can be obtained by using 2-photon microscopy or a similar setup. Hence the kinetic information from lensfree video

microscope and the high-resolution 3D end-point information from lens-based microscopic techniques can complement one another to provide a deeper insight. Different experimental conditions and its influence on network formation could be analyzed. For example, studies (Nissou et al., 2013) show that the normoxia condition in many areas of the brain is close to 3% O_2 and not 20% O_2 that is used in the standard incubator. Lensfree video microscope can be placed inside the incubator set to 3% O_2, and the network formation kinetics can be monitored.

4.3.4 Methods

4.3.4.1 Cell culture methods

Human Umbilical Vein Endothelial Cells (HUVEC) (Gibco C0035C, Pays) were cultured in EGM2 medium (5Lonza CC-3024) completed with hEGF, hydrocortisone, GA100, FBS (Fetal Bovine Serum), VEGF, hFGF-b, heparin,R3, IGF-1 and ascorbic acid at 20% of O_2.

For the experiments, in the center of 35mm culture dishes, a hole of 1 cm in diameter was drilled and sealed at the bottom with a quartz lamella. 75µl of liquid Matrigel at 5 °C was added in the drilled hole and allowed to solidify in an incubator at 37°C for 20 minutes. Cells were then seeded at a density of $5x10^4$cells (per culture dish), on Matrigel (BD Biosciences) and incubated at 37°C.

4.3.4.2 Computational methods

Image analysis was performed on the raw lensfree images. The obtained images were binarized, filled for holes, and were subjected to analysis using Angiogenesis Analyzer plugin by Gilles Carpentier as seen in **Fig. 4.3.2**

4.4 NORMAL AND REDUCED TEMPERATURES IN NORMOXIC AND ANOXIC CONDITIONS

Experiments performed in collaboration with Institute Pasteur.
Collaborator: Pierre Rocheteau (Conceptualization, experiments)

4.4.1 Introduction

M. Latil et al. showed that stem cells adopt a dormant cell state post mortem, retaining regenerative capacity (Latil et al., 2012). They demonstrated that the stem cell viability and regenerative capacity, which are thought to decline 2 days post-mortem (Erker, Azuma, Andrew Y Lee, & Guo, 2010; Perentesis, Watson, Lasky, Steinberg, & Filipovich, 2014), can in fact be extended to as long as 17 days post-mortem. By depriving the muscle stem cells (satellite cells) of nutrients and especially oxygen, they described the culture conditions that force the stem cells to exit the cell cycle and adopt a state of quiescence. This state of quiescence however is reversible upon providing necessary nutrients and ambient culture conditions, similar to wound-healing at different conditions as demonstrated in section 3E.4.

Extreme experimental conditions such as 4°C, 0% O_2 make it impossible (or exceedingly difficult) to image the status of the cells, using lens-based microscopes. Static time-point images cannot be obtained as well, as it might result in breaking the continuity. However, with lensfree video microscope, we succeeded in filming satellite cells and myoblasts at 4°C in anoxia.

4.4.2 Results

Majority of satellite cells remain quiescent in developed and undamaged muscles. However in the event of mechanical strain and damage, the satellite cells become activated. When active, satellite cells proliferate in to myoblasts, which fuse to form

myofibers by the process of myogenesis (Bentzinger, Wang, & Rudnicki, 2012). This is a vital step in development and also in muscle regeneration.

Using our lensfree video microscopy platform, we filmed isolated single fibers, from which dormant satellite cells exit. Upon exit, we observed colonization and proliferation of satellite cells forming myoblasts **(Fig. 4.4.1)**. We calculated the kinetics of proliferation of satellite cells by counting the number of cells. We observed an initial lag phase before the satellite cells became active. For the initial ~45 hours following the placement of single fibers in the culture dish, satellite cells did not proliferate as shown by the stable cell count **(Fig. 4.4.2)**. Following this period, we observed steady increase in cell count showing satellite cell proliferation.

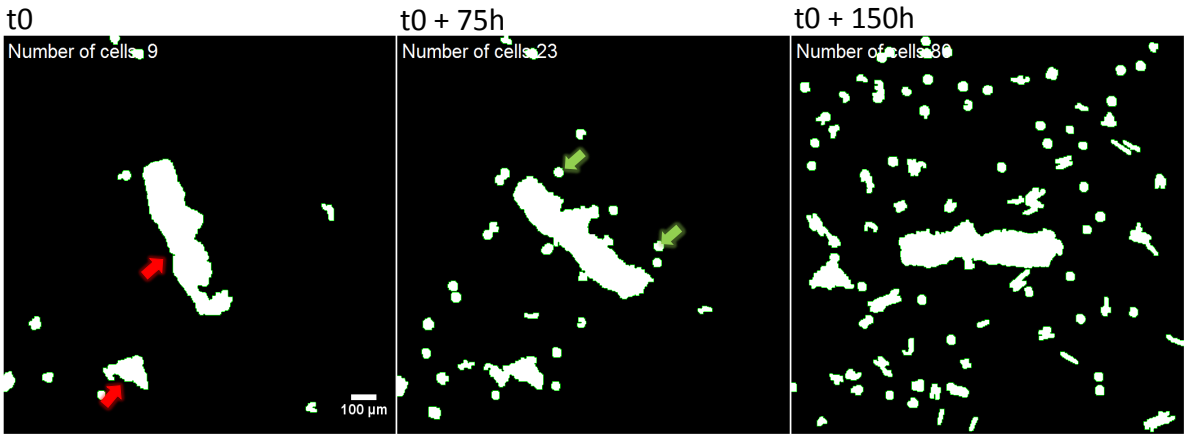

Figure 4.4.1: Single fibers. Processed ROI of time-lapse lensfree video microscopy images showing satellite cells that exit the single fibers, and colonize. Red arrows show the single fibers and the green arrows show a couple of satellite cells that exit the single fibers. The satellite cells proliferate upon exiting from the single fibers.

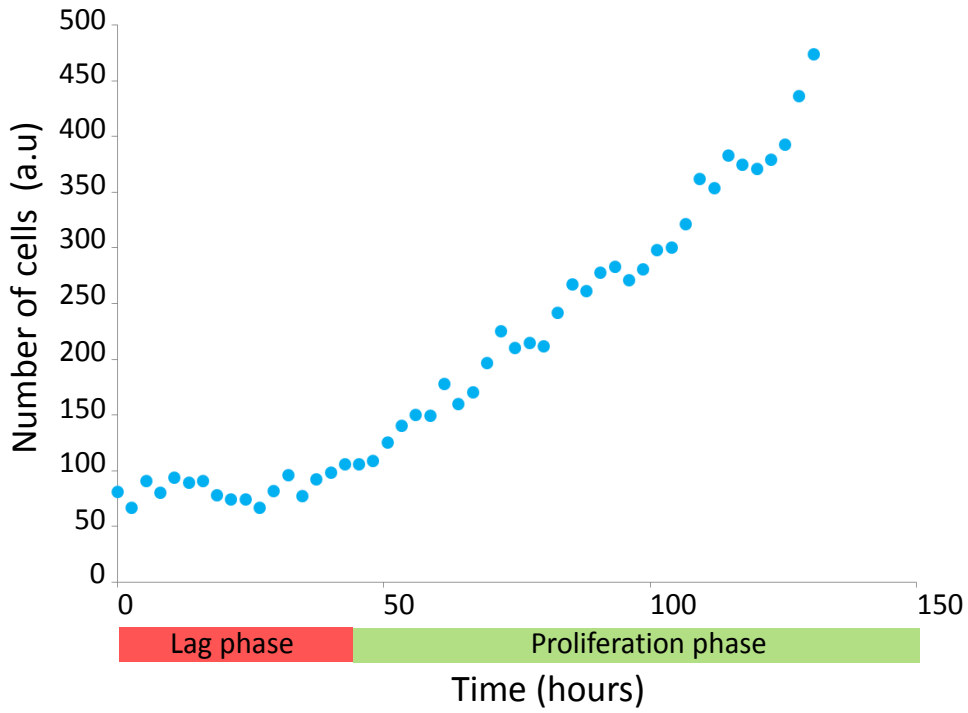

Figure 4.4.2: Proliferation of satellite cells that exit from single fibers. Single fibers are placed in a culture dish at t = 0h, inside standard incubator. Satellite cells exit from the single fibers and proliferate. It can be noted that the proliferation of satellite cells did not commence for the first ~45 hours.

4.4.2.1 Myoblasts at standard culture conditions (37°C, 20%0_2)

We monitored in-vitro cultures of myoblasts in normoxic and anoxic conditions at 37°C inside standard incubator and at 4°C respectively.

Myoblasts at 37°C showed increased motility. From 625 time points, we calculated an average speed of 1.4 ± 0.5 µm/min **(Fig. 4.4.3)**, and the cell migration was random. The percentage ratio between the effective distance and the traveled distance is 21 ± 8 %. Also, we observed that several cells stopped moving abruptly in the middle of the experiment and remained stationary until the end of the experiment. This is illustrated in **Fig. 4.4.4**, showing a tracked cell that divides. The daughter cells were motile initially, after ~ 4 hours, their motility was permanently arrested. Similarly another cell **(Fig. 4.4.5)** became stationary after moving for ~13 hours with an average velocity of 1.3 (± 0.3) µm/min.

Nearly 50% of the tracked cells exhibited similar kind of behavior. It is to be noted that the cell motility stopped at different time points for different cells, indicating cell to cell variability.

The cell count increased from 202 ± 14 to 448 ± 14 cells, over a period of 60 hours at standard conditions **(Fig. 4.4.6)**, indicating a very little cell proliferation compared to standard doubling time of ~24 hours.

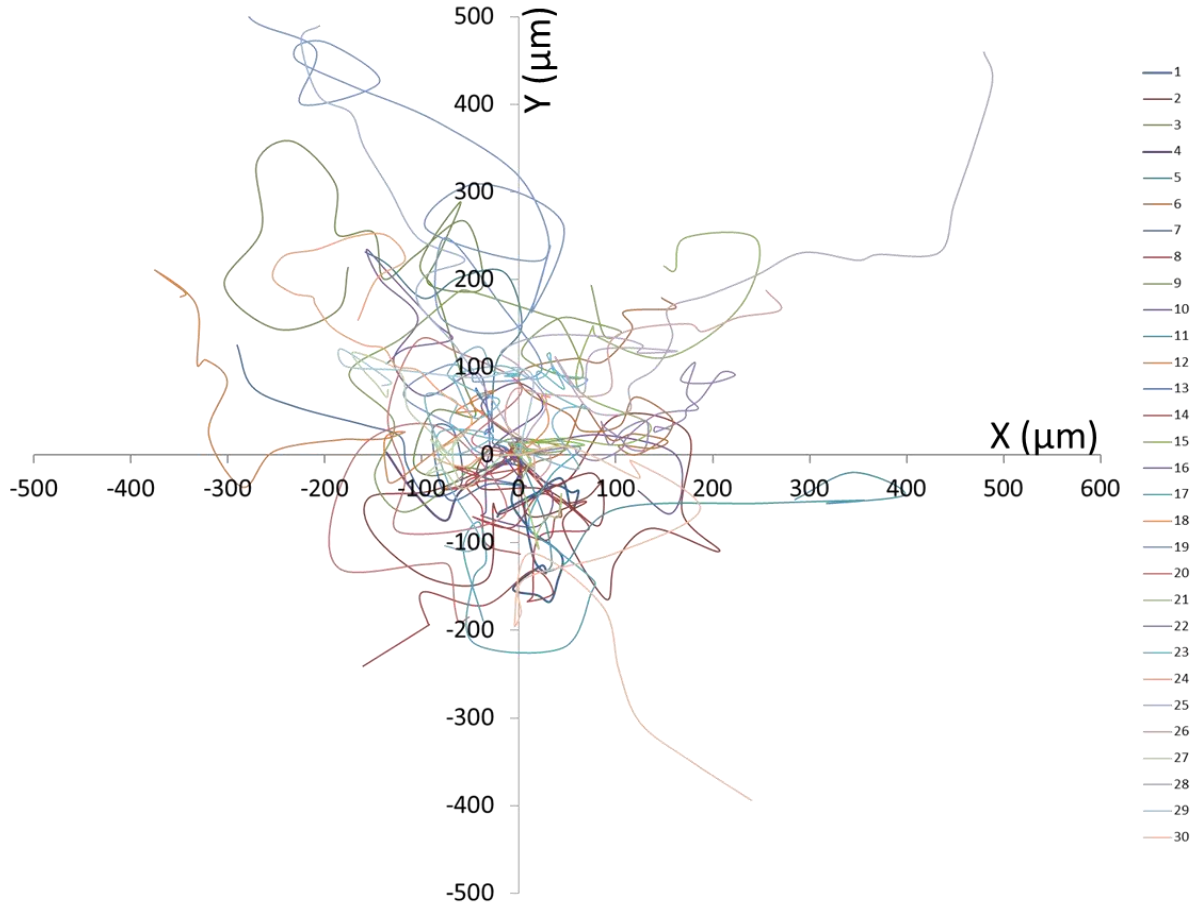

Figure 4.4.3: Myoblast trajectories. Trajectories of 30 myoblast cells inside standard incubator. From 625 time points, we calculated an average speed of 1.4 ± 0.5 µm/min. The average length covered by cells was 810 ± 501 µm (n = 30 cells). The percentage ratio between the effective distance and the traveled distance is very low, 21 ± 8 %, indicating a random displacement.

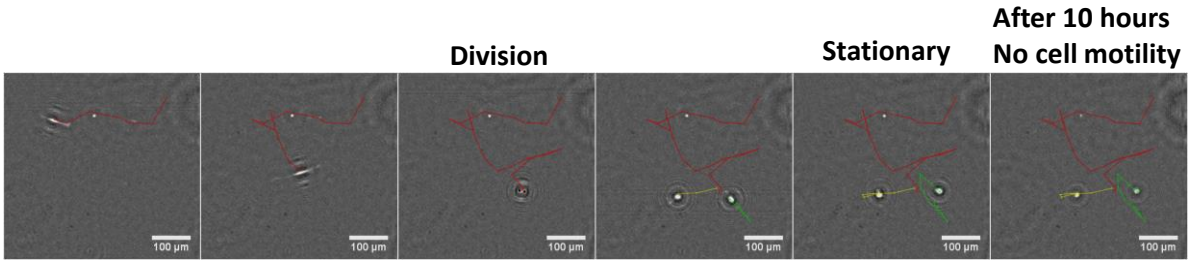

Figure 4.4.4: Cell migration of myoblast. A tracked cell (red) divides giving 2 daughter cells (tracks yellow, green). The daughter cells become immobile after ~4 hours of displacement. The cells remained stationary until the end of the experiment.

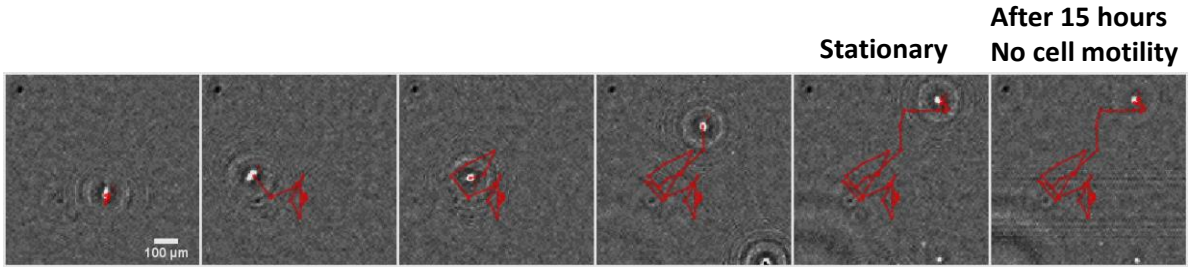

Figure 4.4.5: Cell migration of myoblast. Similar behavior exhibited by another cell, which stops moving after ~13 hours of displacement. The cell remained stationary until the end of the experiment.

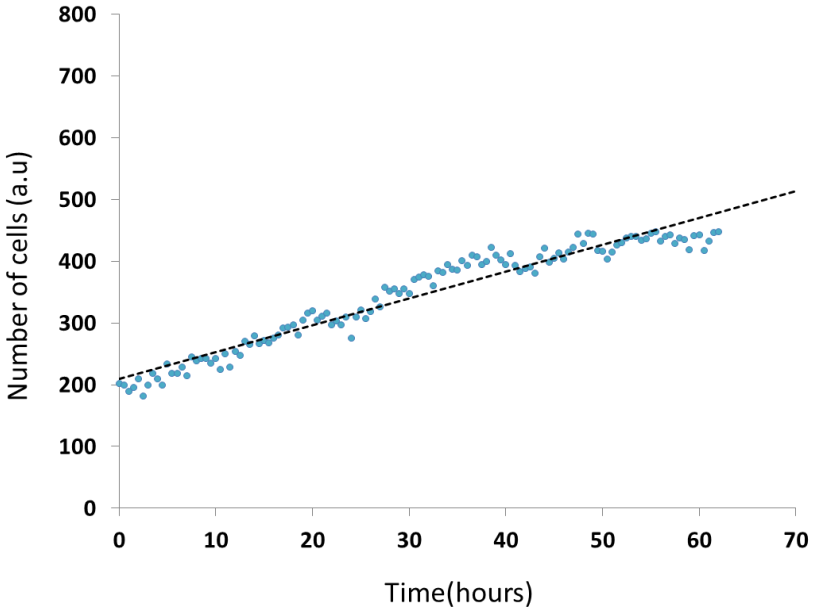

Figure 4.4.6: Proliferation of myoblasts at 37°C normoxia. Inside standard incubator, the cell count increased from 202 ± 14 to 448 ± 14 cells (S.D. resulting from local variations in cell counting) in 60 hours.

4.4.2.2 Myoblasts at 4°C 0%O_2

The behavior of myoblasts subjected to 4°C and anoxia, was completely different, compared to its behavior in standard conditions. We performed Z-projection of the time-lapse images in order to observe the displacement of the cells. From **figure 4.4.7**, it can be seen that all the cells (green arrows) were stationary for the entire period of observation, indicating a displacement of <5μm in 92 hours. Immediately after placing the culture dish at 4°C and 0% O_2, we observed cell shrinkage, which was evident even from the raw image **(Fig. 4.4.7b)**. Also, we observed that most of the cells detached temporarily and then re-attached (or sedimented) to the substrate, characterized by the change in the gray value of the holographic patterns **(Fig. 4.4.8)**.

Also, the number of cells in the population remained constant, at 364 ± 14 cells, during the entire period of observation **(Fig. 4.4.9)**, indicating that the cells did not proliferate at all.

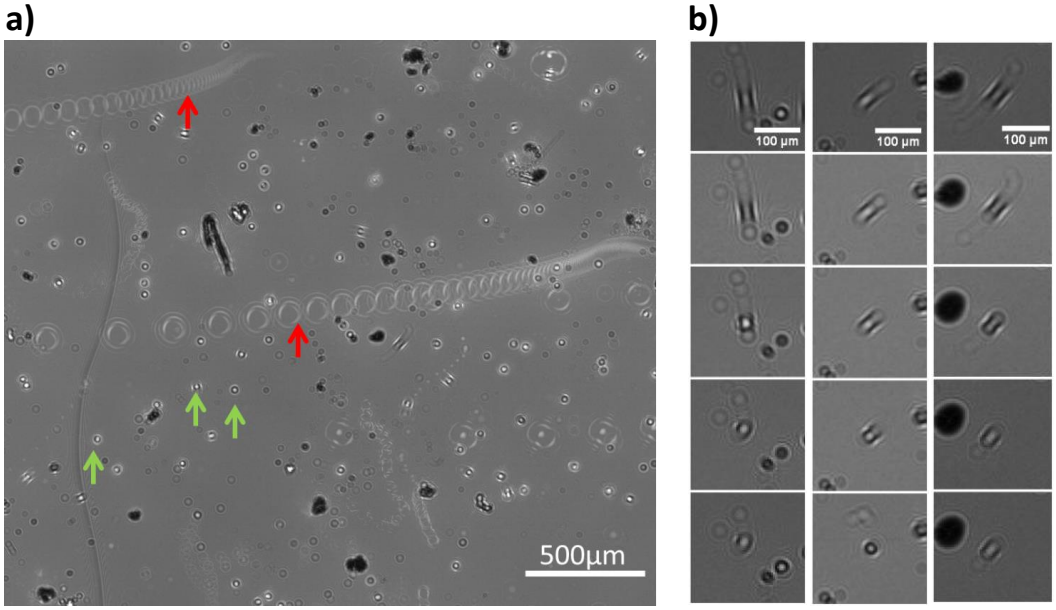

Figure 4.4.7: Cell migration and cell shrinking of myoblasts at 4°C anoxia.

(a) Z-projection of time-lapse images obtained from myoblasts over a period of 92 hours at 4°C, 0% O_2. The image shows complete absence of cell displacement. Red arrows indicate floating debris, and its trail. Green arrows indicate few examples of cells that have no trails indicating very low displacement (< 5µm in 92 hours of observation).

(b) Few examples showing the shrinkage of myoblasts visible from the raw image.

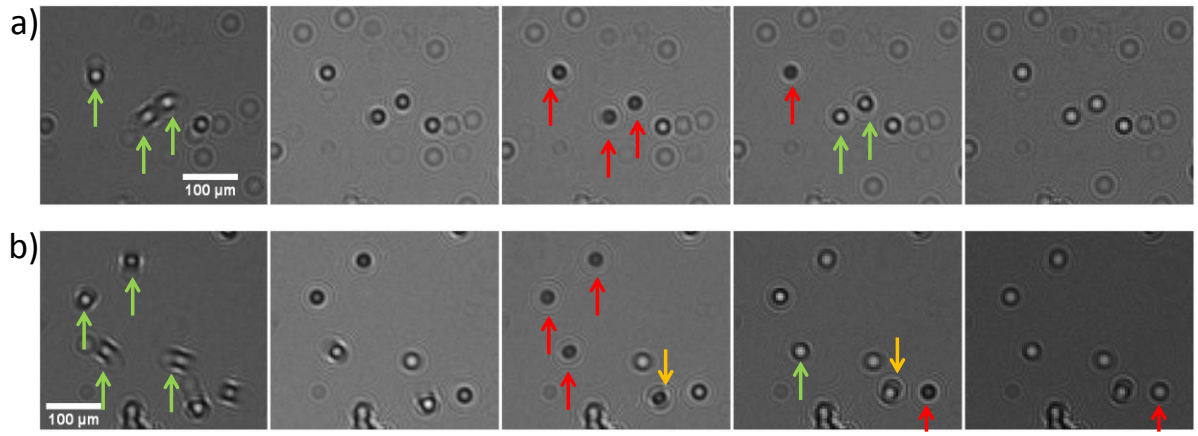

Figure 4.4.8: Cell detachment of myoblasts at 4°C anoxia. (a), (b) Region of interests showing temporary cell detachment undergone by most of the cells. Initially the cells seem adhered to the substrate (green arrows). However, momentary cell detachment (red arrows) is observed at different time points, followed by re-attachment to the substrate (green arrows). We also observed a very rare cell division (yellow arrow).

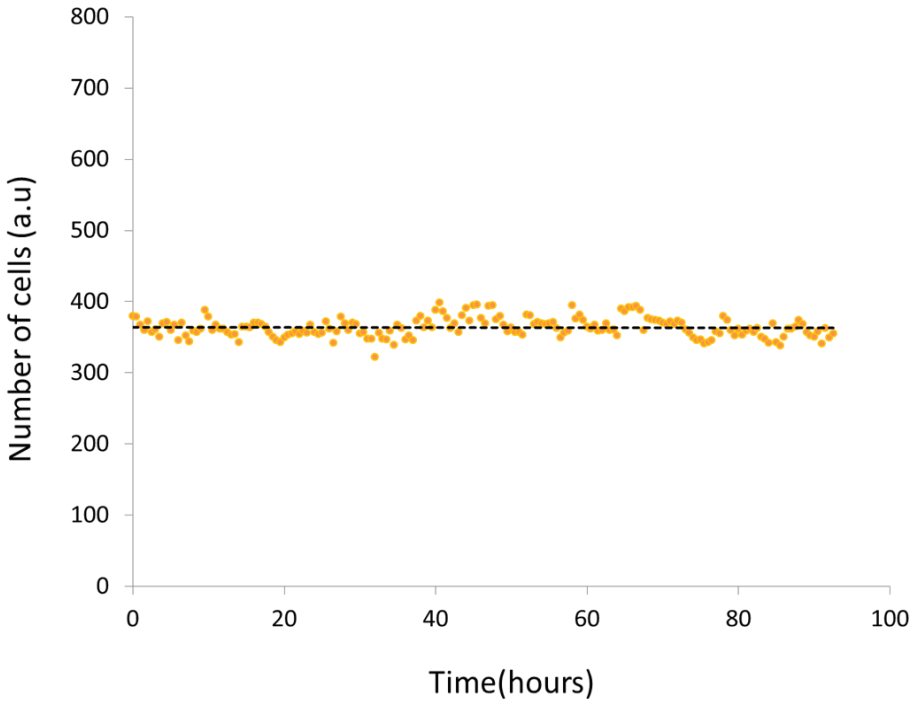

Figure 4.4.9: Cell proliferation of myoblasts at 4°C anoxia. The cell count remained unchanged at 314 cells with a very little standard deviation of 14 cells.

4.4.3 Discussion

We observed proliferation of satellite cells forming myoblasts. Also we monitored exceeding difference in behavior shown by myoblasts at 37°C, 20% O_2 and 4°C, 0% O_2. In the former condition, cell migration and proliferation were observed and quantified. In the latter case, we observed, complete lack of cell motility and proliferation, and temporary cell detachment. With our images, we are unable to quantify cell viability. This assessment can be performed by placing the cells back in normal conditions, and monitoring them to see if they migrate and proliferate (similar to chapter 3E.4). Further, a similar experiment needs to be performed with satellite cells at 4°C 0% O_2, followed by 37°C 20% O_2, to test if they re-enter cell cycle.

REFERENCES

Abbott, A. (2003). Biology ' s new dimension. *Nature*, *424*(August), 870–872.

Bentzinger, C. F., Wang, Y. X., & Rudnicki, M. a. (2012). Building muscle: molecular regulation of myogenesis. *Cold Spring Harbor perspectives in biology*, *4*(2). doi:10.1101/cshperspect.a008342

Canavan, H. E., Graham, D. J., Cheng, X., Ratner, B. D., Castner, D. G., Uni, V., … No, F. (2007). Comparison of Native Extracellular Matrix with Adsorbed Protein Films Using Secondary Ion Mass Spectrometry †. *Langmuir : the ACS journal of surfaces and colloids*, (6), 50–56.

Eilken, H. M., & Adams, R. H. (2010). Dynamics of endothelial cell behavior in sprouting angiogenesis. *Current opinion in cell biology*, *22*(5), 617–25. doi:10.1016/j.ceb.2010.08.010

Erker, L., Azuma, H., Andrew Y Lee, & Guo, C. (2010). Therapeutic liver reconstitution with murine cells isolated long after death. *Gastroenterology*, *139*(3), 1019–1029. doi:10.1053/j.gastro.2010.05.082.Therapeutic

Ernst, O., Lieske, A., Jäger, M., Lankenau, A., & Duschl, C. (2007). Control of cell detachment in a microfluidic device using a thermo-responsive copolymer on a gold substrate. *Lab on a chip*, *7*(10), 1322–9. doi:10.1039/b708619a

Fraley, S. I., Feng, Y., Krishnamurthy, R., Kim, D.-H., Celedon, A., Longmore, G. D., & Wirtz, D. (2010). A distinctive role for focal adhesion proteins in three-dimensional cell motility. *Nature cell biology*, *12*(6), 598–604. doi:10.1038/ncb2062

Grange, C., Tapparo, M., Collino, F., Vitillo, L., Damasco, C., Deregibus, M. C., … Camussi, G. (2011). Microvesicles released from human renal cancer stem cells stimulate angiogenesis and formation of lung premetastatic niche. *Cancer research*, *71*(15), 5346–56. doi:10.1158/0008-5472.CAN-11-0241

Halperin, A., & Kröger, M. (2012). Theoretical considerations on mechanisms of harvesting cells cultured on thermoresponsive polymer brushes. *Biomaterials*, *33*(20), 4975–87. doi:10.1016/j.biomaterials.2012.03.060

Kumashiro, Y., Yamato, M., & Okano, T. (2010). Cell attachment-detachment control on temperature-responsive thin surfaces for novel tissue engineering. *Annals of biomedical engineering*, *38*(6), 1977–88. doi:10.1007/s10439-010-0035-1

Latil, M., Rocheteau, P., Châtre, L., Sanulli, S., Mémet, S., Ricchetti, M., … Chrétien, F. (2012). Skeletal muscle stem cells adopt a dormant cell state post mortem and retain regenerative capacity. *Nature communications*, *3*(may), 903. doi:10.1038/ncomms1890

Lee, G. Y., Kenny, P. A., Lee, E. H., & Bissell, M. J. (2010). Three-dimensional culture models of normal and malignant breast epithelial cells. *Nature methods*, *4*(4), 359–365. doi:10.1038/nmeth1015.Three-dimensional

Maltman, D. J., & Przyborski, S. a. (2010). Developments in three-dimensional cell culture technology aimed at improving the accuracy of in vitro analyses. *Biochemical Society transactions*, *38*(4), 1072–5. doi:10.1042/BST0381072

Muranova, T., Shvyrkova, I., Arkhipov, V., & Rykunova, A. (1998). Anti-adhesive property of the plasmin / plasminogen system : the use of plasmin (ogen) for cell d e t a c h m e n t and disaggregation in cell culture technique. *Fibrinolysis and Proteolysis*, *12*, 23–32.

Nissou, M.-F., El Atifi, M., Guttin, A., Godfraind, C., Salon, C., Garcion, E., … Wion, D. (2013). Hypoxia-induced expression of VE-cadherin and filamin B in glioma cell cultures and pseudopalisade structures. *Journal of neuro-oncology*, *113*(2), 239–49. doi:10.1007/s11060-013-1124-4

Okano, T., Yamada, N., Okuhara, M., & Sakai, H. (1995). Mechanism of cell detachment from hydrophobic polymer surfaces. *Biomaterials*, *16*(4), 297–303.

Pampaloni, F., Reynaud, E. G., & Stelzer, E. H. K. (2007). The third dimension bridges the gap between cell culture and live tissue. *Nature reviews. Molecular cell biology*, *8*(10), 839–45. doi:10.1038/nrm2236

Perentesis, P., Watson, V., Lasky, C., Steinberg, E., & Filipovich, H. (2014). Successful donor cell engraftment in a recipient of bone marrow from a cadaveric donor. *Blood*, *67*, 1655–1660.

Potente, M., Gerhardt, H., & Carmeliet, P. (2011). Basic and therapeutic aspects of angiogenesis. *Cell*, *146*(6), 873–87. doi:10.1016/j.cell.2011.08.039

Saunders, R. L., & Hammer, D. A. (2011). Assembly of Human Umbilical Vein Endothelial Cells on Compliant Hydrogels. *Cell Molecular Bioengineering*, *3*(1), 60–67. doi:10.1007/s12195-010-0112-4.Assembly

Shojaei, F. (2012). Anti-angiogenesis therapy in cancer: current challenges and future perspectives. *Cancer letters*, *320*(2), 130–7. doi:10.1016/j.canlet.2012.03.008

Tamura, A., Kobayashi, J., Yamato, M., & Okano, T. (2012). Temperature-responsive poly(N-isopropylacrylamide)-grafted microcarriers for large-scale non-invasive harvest of anchorage-dependent cells. *Biomaterials*, *33*(15), 3803–12. doi:10.1016/j.biomaterials.2012.01.060

Xue, C., Choi, B.-C., Choi, S., Braun, P. V., & Leckband, D. E. (2012). Protein Adsorption Modes Determine Reversible Cell Attachment on Poly(N-isopropyl acrylamide) Brushes. *Advanced Functional Materials*, *22*(11), 2394–2401. doi:10.1002/adfm.201103056

Yamato, M., Okuhara, M., Karikusa, F., Kikuchi, A., Sakurai, Y., Okano, T., & Information, A. (1999). Signal transduction and cytoskeletal reorganization are required for cell detachment from cell culture surfaces grafted with a temperature-responsive polymer. *Journal of biomedical materials research. Part A*, *4636*(199901), 3–5. doi:10.1002/(SICI)1097-4636(199901)44

Yue, S., Cárdenas-Mora, J. M., Chaboub, L. S., Lelièvre, S. a, & Cheng, J.-X. (2012). Label-free analysis of breast tissue polarity by Raman imaging of lipid phase. *Biophysical journal*, *102*(5), 1215–23. doi:10.1016/j.bpj.2012.01.023

5. CONCLUSION AND FUTURE PERSPECTIVES

The technological advancements in the field of microscopy have changed the way cells and molecules are examined (Rosenthal, 2009). While recent advances have been mainly focused on improving the resolution (Egner & Hell, 2005; Hell, 2007; Sengupta, Van Engelenburg, & Lippincott-Schwartz, 2012), we developed a 'Lensfree video microscope' as an alternative to increased cost, complexity, bulkiness and reduced field of view – the limitations faced by majority of modern-day microscopes. We demonstrated in-vitro cell culture monitoring and quantification using our lensfree video microscope.

In-vitro cell culture monitoring and quantification are indispensable to understand biological processes at cellular level, to elucidate reaction of the cell population to environment, siRNAs, drugs, etc. Commonly used techniques for in-vitro monitoring and quantification include, (i) Flow cytometry, (ii) Time-lapse microscopy and (iii) recently advancing method Electric Cell Substrate Impedance Sensing (ECIS). Flow cytometry can quantify but not monitor longitudinally. Time-lapse microscopes can monitor but not perform high-throughput quantification. ECIS can monitor and quantify certain cell functions, however, the cells are not visualized, cell heterogeneity is lost, and also cell culture practices needs to be altered (special culture dishes with gold electrodes are required for the measurement of impedance).

Our lensfree video microscope overcomes the limitations and combines the strongest advantages of the three above mentioned techniques by performing, high-throughput, real-time, label-free monitoring and quantification of cellular events with resolution extending to single cells.

Lensfree video microscope is simple, cost-effective, robust, and compatible to cell culture practices

Our lensfree video microscope has only 4 components: LED, Pinhole, CMOS imaging sensor, and heat sink (chapter 2). The relatively expensive component is CMOS imaging sensor (~500 $), and the fabrication cost of the entire system is well under 1000$. The Simplicity of the system makes it robust (> 20,000h of imaging thus far) and compatible to the standard cell culture practices. It does not necessitate the cells to be grown on specific substrates, or with particular culture media for improved acquisition, or any other requirements that would alter the standard cell culture practices. Any culture dish of interest can be placed on our microscope which is installed inside the incubator.

Lensfree video microscope is adaptable

In addition to being compatible to standard practices of 2D cell culture, lensfree video microscope is also applicable to 3D cell culture conditions. Imaging techniques to monitor 3D cell culture is not developing as fast as 3D cell culture systems (Dolega et al., 2013). By successfully performing 3D cell culture imaging using lensfree video microscope, we demonstrated discrimination of acini and spheroids (chapter 4.2), and more importantly, we imaged the network formation of acini structures and HUVEC (chapter 3E,4.3), which were rendered possible solely due to the combination of advantages (large FOV, no focalization required, time-lapse imaging capability) offered by lensfree video microscope. Also, our microscope offers the flexibility to be installed not only in standard incubator conditions, but also at reduced temperatures (4°C to 37°C), reduced oxygen concentrations (anoxia, hypoxia, normoxia), etc. Depending on the experiments, our lensfree video microscope can be placed in any setting with different combinations of temperature, oxygen, humidity, CO_2 levels. This opens new possibilities to monitor cell cultures in non-standard conditions, which was so far difficult or even impossible. It is to

be noted that recently studies are aimed at understanding cell behavior in non-standard conditions (Latil et al., 2012; Nissou et al., 2013). In chapter 4, we have demonstrated the applicability of our microscope to diverse conditions. This makes our lensfree video microscope a pioneer in live imaging systems, which is capable of real-time imaging in all the above mentioned conditions, especially 4°C in anoxia (chapter 4.4).

Lensfree video microscope is high-throughput

In spite of the need for markers and the obligation for cell harvesting, flow cytometry is highly favored over time-lapse microscopy for in-vitro quantification. One of the major reasons is the high-throughput. With ultra-wide field of view of 24mm^2 and ability to longitudinally monitor cells in culture for extended time periods (> 1 month), lensfree video microscope offers similar throughput as flow cytometry. This ensures the statistical significance of the results obtained and the credibility of the conclusion drawn from the experiments. For instance, the cellular events quantified in chapter 3, involved high-throughput monitoring of ~500 – 4000 cells for 1 – 20 days.

Lensfree video microscope is label-free (non-invasive)

Most of the cell-based assays depend on markers, some of which are expensive and even radioactive (BrdU). Although markers are tested for cytotoxicity before its widespread application, their integrity is often questioned (Evdokimov et al., 2006; Katayama, Yamamoto, Mizushima, & Yoshimori, 2008; Marx, 2013; Wang, Henning, & Heber, 2010). Care must be taken particularly when another external chemical agent is used in the experiment along with the markers. Even though the role of markers cannot be substituted in super-resolution imaging (Nienhaus & Nienhaus, 2014), the use of markers can certainly be reduced or even eliminated in basic cell culture assays e.g. cell proliferation assay, cell death assay, etc. Using lensfree video microscopy and quantitative

image analysis, we have demonstrated that, richness in temporal and spatial information can replace markers and provide necessary information regarding the cell culture in observation. In chapter 3, we have demonstrated label-free monitoring of major cell functions. The non-invasiveness of our microscope makes it particularly suitable for rare cell types (primary cells, stem cells, etc.).

Lensfree video microscope is real-time and continuous

Understanding the kinetics of cellular occurrences is important to test the time-dependent effects of external stimulus (Kaup et al., 2001; Mir, Bergamaschi, Katzenellenbogen, & Popescu, 2014). While innovative methods and techniques are being demonstrated to acquire cell population kinetics based on time-lapse microscopy and ECIS (Dykstra et al., 2006; Mir et al., 2014; S. a Patel et al., 2012; S. Patel, Pine, & Rameshwar, 2013), flow cytometry is still majorly used for deduction of kinetics owing to the established labeling protocols, feasibility, and high-throughput. However, to obtain kinetics using flow cytometry based assays, one has to perform series of temporally separated end-point assays using cell populations that are treated to similar conditions. In addition to being labor-intensive the measurements cannot be called continuous because the cell population is not the same. Label-free, non-invasive approach of lensfree video microscope offers real-time and continuous measurement from few minutes to several days (> 1 month). For example, to the best of our knowledge, to perform the experiment shown in Fig. 3D.4c, 3D.5d, where the same population is monitored from cell adhesion until cell death, is simply not possible with any of the flow cytometry approaches that exist today.

Lensfree video microscope preserves cell-cell variability

Lukas Pelkman precisely discusses the negligence of cell-cell variability and its potential in uncovering novel cellular processes (Pelkmans, 2012; Snijder & Pelkmans, 2011). Heterogeneity in cell population has been shown to exist; however, it is often ignored due to the lack of ways to explore it (Pelkmans, 2012). Lensfree video microscope provides high-throughput data about the cell population, while preserving cell-cell variability. Firstly, with lensfree video microscope, it is more probable to observe cell-cell variability considering the thousands of cells that are observed in the field of view, and the temporal information that is available. Secondly, from the images, cell-cell variability is detected and reflected in the output. In chapter 4, we have shown a single cell that was viable and was moving constantly when ~95% of its neighboring cells died due to siRNA transfection of siCellDeath, which prompted us to question whether the arrest in cell migration a symptom of cell death or the cause. The scatter plots (chapter 3) containing 25,000 – 900,000 measurements show the trend of the population taking every single cell in consideration. From the scatter plot, those cells that behave differently can be observed, and using the coordinates (spatial, temporal) from the plot, the cell could be accessed and visualized from the time-lapse images to validate the result if needed and also to get further insight about the cell.

To the best of our knowledge, lensfree video microscope introduced in this thesis is the only imaging system that combines all the advantages listed above. These advantages make our microscope highly application-oriented and readily acceptable by biologists. For example, status of the cell culture, at any instant, can be obtained without even the minimum necessity of having to access the culture dish. Our lensfree video microscopy prioritized simplicity and adherence to standard cell culture practices over resolution and

fluorescence. Although the setup cannot resolve fine lamellipodial and filopodial extensions (~3-5 μm), shape and the size of single cells are well reconstructed and segmented. Also, we clearly demonstrated that many important measurements can be performed without requiring sub-cellular resolution or fluorescence. We have demonstrated wide-spread applications of our microscope in chapter 3, by monitoring major cell events: cell substrate adhesion, spreading, division, division orientation, differentiation, migration, quiescence, and death. Unlike commonly used assays that can monitor only one cell function at a given condition, our platform and associated metrics can follow all the mentioned cell functions simultaneously in the same cell culture in observation. This paves way to assess combination of cell functions hampered or enhanced by a particular scenario. Taking advantage of this possibility, for the first time, we measured, from the same population, the reduction in cell migration that preceded cell differentiation and cell death (chapters 3E.4.2, 3E.4.3). Unlike lens-based microscopy and cytometry, our setup provides the feasibility to perform direct measurements with simplicity, and therefore helps to address biological issues that were not accessible before.

Future Perspectives

Our lensfree video microscope is well received by biologists, which laid foundation for our collaborations. A start-up company is created based on the PhD work. This will certainly diversify the applications of our microscope in near future.

Improving resolution and integrating fluorescence would certainly widen the reach of our microscope. Methods to improve resolution and acquire fluorescence using lensfree imaging have been demonstrated before (Coskun, Sencan, Su, & Ozcan, 2010, 2011; Hennequin et al., 2013; Mudanyali et al., 2013). These techniques can be integrated with

our microscope. However, care must be taken in order not to compromise the simplicity of the setup. Also, by multiplexing several imaging sensors together, multi-well plates can be monitored (Haguet, Obeïd, Griffin, Freida, & Gidrol, 2013) and the throughput of the system can be dramatically increased.

In addition to the cell events that were monitored in chapter 3, several other occurrences can be followed quantitatively. Most cellular events (cell differentiation, cell death, etc.) cause changes in cell shape and functions. Through time-lapse images, these changes can be quantified and the entire process can be followed. For example, Epithelial Mesenchymal Transition (EMT), the process which is integral in development, wound-healing, and cancer (Lamouille, Xu, & Derynck, 2014), can be followed by lensfree video microscope. EMT involves change in shape, motility, and function of the cells, similar to cell differentiation. Also, our lensfree video microscope could be extended to monitor floating cells.

Overall, with the results presented here, we demonstrate that our lensfree video microscopy and associated metrics give new perspectives to cell culture monitoring and have high potential to provide new means for the quantification of cell behavior in cell culture conditions.

REFERENCES

Coskun, A. F., Sencan, I., Su, T.-W., & Ozcan, A. (2010). Lensless wide-field fluorescent imaging on a chip using compressive decoding of sparse objects. *Optics express*, *18*(10), 10510–23. Retrieved from http://www.pubmedcentral.nih.gov/articlerender.fcgi?artid=2898750&tool=pmcentrez&rendertype=abstract

Coskun, A. F., Sencan, I., Su, T.-W., & Ozcan, A. (2011). Wide-field lensless fluorescent microscopy using a tapered fiber-optic faceplate on a chip. *The Analyst*, *136*(17), 3512–8. doi:10.1039/c0an00926a

Dolega, M. E., Allier, C., Vinjimore Kesavan, S., Gerbaud, S., Kermarrec, F., Marcoux, P., … Nathalie, P.-D. (2013). Label-free analysis of prostate acini-like 3D structures by lensfree imaging. *Biosensors & bioelectronics*, *49C*, 176–183. doi:10.1016/j.bios.2013.05.001

Dykstra, B., Ramunas, J., Kent, D., Mccaffrey, L., Szumsky, E., Kelly, L., … Jervis, E. (2006). High-resolution video monitoring of hematopoietic stem cells cultured in single-cell arrays identifies new features of self-renewal. *Proceedings of the National Academy of Sciences of the United States of America*, *103*, 8185–8190.

Egner, A., & Hell, S. W. (2005). Fluorescence microscopy with super-resolved optical sections. *Trends in cell biology*, *15*(4), 207–15. doi:10.1016/j.tcb.2005.02.003

Evdokimov, A. G., Pokross, M. E., Egorov, N. S., Zaraisky, A. G., Yampolsky, I. V, Merzlyak, E. M., … Chudakov, D. M. (2006). Structural basis for the fast maturation of Arthropoda green fluorescent protein. *EMBO reports*, *7*(10), 1006–12. doi:10.1038/sj.embor.7400787

Haguet, V., Obeïd, P., Griffin, R., Freida, D., & Gidrol, X. (2013). Parallelized lensfree time-lapse microscopy. *Conference NanoBioEurope, p. 30, Toulouse, France, June 10-12, 2013.*, 2013.

Hell, S. W. (2007). Far-field optical nanoscopy. *Science (New York, N.Y.)*, *316*(5828), 1153–8. doi:10.1126/science.1137395

Hennequin, Y., Allier, C. P., McLeod, E., Mudanyali, O., Migliozzi, D., Ozcan, A., & Dinten, J.-M. (2013). Optical Detection and Sizing of Single Nanoparticles Using Continuous Wetting Films. *ACS nano*, (9), 7601–7609. doi:10.1021/nn403431y

Katayama, H., Yamamoto, A., Mizushima, N., & Yoshimori, T. (2008). GFP-like Proteins Stably Accumulate in Lysosomes. *Cell Structure and Function*, *33*, 1–12.

Kaup, B., I, S., Knupfer, H., Sclenzka, A., Prieb, R., & Knupfer, M. . (2001). Time-dependent Inhibition of Glioblastoma Cell Proliferation by Dexamethasone. *Journal of neuro-oncology*, *51*(2), 105–110.

Lamouille, S., Xu, J., & Derynck, R. (2014). Molecular mechanisms of epithelial-mesenchymal transition. *Nature reviews. Molecular cell biology*, *15*(3), 178–96. doi:10.1038/nrm3758

Latil, M., Rocheteau, P., Châtre, L., Sanulli, S., Mémet, S., Ricchetti, M., … Chrétien, F. (2012). Skeletal muscle stem cells adopt a dormant cell state post mortem and retain regenerative capacity. *Nature communications*, *3*(may), 903. doi:10.1038/ncomms1890

Marx, V. (2013). Is super-resolution microscopy right for you? *Nature methods*, *10*(12), 1157–63. doi:10.1038/nmeth.2756

Mir, M., Bergamaschi, A., Katzenellenbogen, B. S., & Popescu, G. (2014). Highly sensitive quantitative imaging for monitoring single cancer cell growth kinetics and drug response. *PloS one*, *9*(2), e89000. doi:10.1371/journal.pone.0089000

Mudanyali, O., Mcleod, E., Luo, W., Greenbaum, A., Coskun, A. F., Hennequin, Y., & Allier, C. P. (2013). Wide-field optical detection of nanoparticles using on-chip microscopy and self-assembled nanolenses, *254*(February), 2013. Retrieved from http://dx.doi.org/10.1038/nphoton.2013.49

Nienhaus, K., & Nienhaus, G. U. (2014). Fluorescent proteins for live-cell imaging with super-resolution. *Chemical Society reviews*, *43*(4), 1088–106. doi:10.1039/c3cs60171d

Nissou, M.-F., El Atifi, M., Guttin, A., Godfraind, C., Salon, C., Garcion, E., … Wion, D. (2013). Hypoxia-induced expression of VE-cadherin and filamin B in glioma cell cultures and pseudopalisade structures. *Journal of neuro-oncology*, *113*(2), 239–49. doi:10.1007/s11060-013-1124-4

Patel, S. a, Ramkissoon, S. H., Bryan, M., Pliner, L. F., Dontu, G., Patel, P. S., … Rameshwar, P. (2012). Delineation of breast cancer cell hierarchy identifies the subset responsible for dormancy. *Scientific reports*, *2*, 906. doi:10.1038/srep00906

Patel, S., Pine, S., & Rameshwar, P. (2013). Time-Lapse Video Microscopy for Assessment of Self-Renewal and Division Kinetics. *Protocol Exchange*, *6*, 1–3.

Pelkmans, L. (2012). Cell Biology. Using cell-to-cell variability--a new era in molecular biology. *Science (New York, N.Y.)*, *336*(6080), 425–6. doi:10.1126/science.1222161

Rosenthal, C. K. (2009). Milestones in light microscopy. *Nature cell biology*, *11*(10), 1165.

Sengupta, P., Van Engelenburg, S., & Lippincott-Schwartz, J. (2012). Visualizing cell structure and function with point-localization superresolution imaging. *Developmental cell*, *23*(6), 1092–102. doi:10.1016/j.devcel.2012.09.022

Snijder, B., & Pelkmans, L. (2011). Origins of regulated cell-to-cell variability. *Nature reviews. Molecular cell biology*, *12*(2), 119–25. doi:10.1038/nrm3044

Wang, P., Henning, S. M., & Heber, D. (2010). Limitations of MTT and MTS-based assays for measurement of antiproliferative activity of green tea polyphenols. *PloS one*, *5*(4), e10202. doi:10.1371/journal.pone.0010202

ANNEX

COMMUNICATIONS

1. High-throughput monitoring of major cell functions by means of lensfree video microscopy
S. Vinjimore Kesavan, F. Momey, O. Cioni et al.
Nature Scientific Reports 4, 5942 doi:10.1038/srep05942 (Aug 2014)

2. Real-time label free detection of dividing cells by means of lensfree video microscopy
S. Vinjimore Kesavan**,** F. Navarro, M. Menneteau, et al.
Journal of Biomedical Optics Vol. 19(3) doi:10.1117/1.JBO.19.3.036004 (Mar 2014)

3. Real-time cell culture monitoring by means of lensfree video microscopy
S. Vinjimore Kesavan, C. Allier, F.Momey et al.
Optical Society of America (Conference paper) doi.org/10.1364/BIOMED.2014.BT3A.21 (Mar 2014)

4. Video lensfree microscopy of 2D and 3D culture of cells
C.P. Allier, S. Vinjimore Kesavan**,** JG. Coutard, et al.
Proceedings of SPIE Vol. 8947, doi:10.1117/12.2038098 (Jan 2014)

5. Multi-scale high-throughput cell culture monitoring by lensfree imaging
S. Vinjimore Kesavan**,** C.P. Allier, F. Navarro, et al.
Molecular Imaging and Biology (conference proceedings of WMIC) Volume 15, Issue 1 Supplement, pp 1585-1587 (Dec 2013)

6. Label-free analysis of prostate acini-like 3D structures by lensfree imaging
M. Dolega, C. Allier, S. Vinjimore Kesavan, et al.
Biosensors and Bioelectronics Vol. 49, doi: 10.1016/j.bios.2013.05.001 (Nov 2013)

7. Lensless Imaging system to quantify cell proliferation
S. Vinjimore Kesavan, C.P. Allier, F. Navarro, et al.
Proceedings of SPIE Vol. 8587, doi:10.1117/12.2001826 (Feb 2013)

PATENTS

- Method and System for Reconstructing Optical Properties of Diffracting Objects Immersed in a Liquid Medium
  Publication Number: WO2014009519 A1 (16 Jan 2014)
  Inventors: C. Allier, S. Vinjimore Kesavan
- Procédé et système de caractérisation d'un état d'adhésion de particules, telles que des cellules
  DD 14896 CLG (Deposited in France)
  C. Alier, S. Vinjimore Kesavan.

ELSEVIER LICENSE
TERMS AND CONDITIONS

Oct 22, 2014

This is a License Agreement between Srikanth Vinjimore Kesavan ("You") and Elsevier ("Elsevier") provided by Copyright Clearance Center ("CCC"). The license consists of your order details, the terms and conditions provided by Elsevier, and the payment terms and conditions.

All payments must be made in full to CCC. For payment instructions, please see information listed at the bottom of this form.

Supplier	Elsevier Limited The Boulevard,Langford Lane Kidlington,Oxford,OX5 1GB,UK
Registered Company Number	1982084
Customer name	Srikanth Vinjimore Kesavan
Customer address	50 avenue general Leclerc, FRANCE st martin le vinoux, 38950
License number	3494110948071
License date	Oct 22, 2014
Licensed content publisher	Elsevier
Licensed content publication	Methods
Licensed content title	A practical guide to quantify cell adhesion using single-cell force spectroscopy
Licensed content author	Jens Friedrichs,Kyle R. Legate,Rajib Schubert,Mitasha Bharadwaj,Carsten Werner,Daniel J. Müller,Martin Benoit
Licensed content date	1 April 2013
Licensed content volume number	60
Licensed content issue number	2
Number of pages	10
Start Page	169
End Page	178
Type of Use	reuse in a thesis/dissertation
Portion	figures/tables/illustrations
Number of figures/tables/illustrations	1
Format	both print and electronic
Are you the author of this Elsevier article?	No
Will you be translating?	No
Title of your thesis/dissertation	Cell culture monitoring by means of lensfree video microscopy

Expected completion date	Dec 2014
Estimated size (number of pages)	190
Elsevier VAT number	GB 494 6272 12
Permissions price	0.00 EUR
VAT/Local Sales Tax	0.00 EUR / 0.00 GBP
Total	0.00 EUR
Terms and Conditions	

NATURE PUBLISHING GROUP LICENSE
TERMS AND CONDITIONS

Oct 22, 2014

This is a License Agreement between Srikanth Vinjimore Kesavan ("You") and Nature Publishing Group ("Nature Publishing Group") provided by Copyright Clearance Center ("CCC"). The license consists of your order details, the terms and conditions provided by Nature Publishing Group, and the payment terms and conditions.

All payments must be made in full to CCC. For payment instructions, please see information listed at the bottom of this form.

License Number	3494181162262
License date	Oct 22, 2014
Licensed content publisher	Nature Publishing Group
Licensed content publication	Nature Reviews Drug Discovery
Licensed content title	Cell death assays for drug discovery
Licensed content author	Oliver Kepp, Lorenzo Galluzzi, Marta Lipinski, Junying Yuan and Guido Kroemer
Licensed content date	Mar 1, 2011
Volume number	10
Issue number	3
Type of Use	reuse in a dissertation / thesis
Requestor type	academic/educational
Format	print and electronic
Portion	figures/tables/illustrations
Number of figures/tables/illustrations	1
High-res required	no
Figures	Table 1
Author of this NPG article	no
Your reference number	None
Title of your thesis / dissertation	Cell culture monitoring by means of lensfree video microscopy
Expected completion date	Dec 2014
Estimated size (number of pages)	190
Total	0.00 EUR
Terms and Conditions	